Optical nanofibers interfacing cold toms. A tool for quantum optics

Baptiste Gouraud

UPMC SORBONNE UNIVERSITÉS

Laboratoire Kastler Brossel
Physique quantique et applications

THÈSE DE DOCTORAT
DE L'UNIVERSITÉ PIERRE ET MARIE CURIE

Spécialité : Physique

École doctorale : "Physique en Île-de-France"

réalisée

au Laboratoire Kastler Brossel

présentée par

Baptiste GOURAUD

pour obtenir le grade de :

DOCTEUR DE L'UNIVERSITÉ PIERRE ET MARIE CURIE

Sujet de la thèse :

Optical Nanofibers Interfacing Cold Atoms
A Tool for Quantum Optics

soutenue le 11 Février 2016

devant le jury composé de :

M.	Arno Rauschenbeutel	Rapporteur
M.	Thierry Chanelière	Rapporteur
M^{me}	Sylvie Lebrun	Examinateur
M.	Rémi Carminati	Examinateur
M.	Simon Bernon	Examinateur
M.	Julien Laurat	Directeur de thèse

Contents

Introduction

Learning, is one of my favorite human experiences. During the past few years - which were probably the last years I was still considered as a student - it has been part of my life on a day-to-day basis in many new ways. This was mostly due to the challenge that was proposed to me by Julien Laurat: building a new experiment as part of his research team.

Why did I get involved in this particular experience? After having been taught physics away from experiments, I was first mostly attracted by theoretical physics. But my personal experiences as a student at ENS got me interested in more technical and experimental aspects of science. A large part of this interest came from discovering computer science through the free software community. This was soon followed by an interest in open-source hardware stimulated by my close friendship with the founder of Hackens: the hackerspace of ENS students. With those stimulations, I had to put my hands at work on an advanced experiment. Additionally, I was in the ENS physics department environment, where experimenting with quantum theory, or with matter cooled almost to absolute zero are commonplace, but were still technical mysteries in my mind. I thus got involved in starting from scratch a new quantum physics experiment based on cold atoms and nanophotonics. This choice was perfect to unravel these mysteries and soon proved to be a rich source of learning.

In the beginning of 2012, when I started to work in the team, my role was the following: combine into a new experiment knowledge from the international research community and knowledge from the team's experience. On one hand, the international community was bringing in optical nanofibers, a tool for guiding and focusing light. Optical nanofibers had brought much interest in the past decade and, as detailed in the beginning of chapter 1, they were already starting to prove their potential in the context of atom physics. On the other hand, the LKB team was contributing with its knowledge on how to use cold atomic ensembles as a tool for manipulating and storing the quantum state of light.

The first and largest part of my PhD was to learn from those sources and prepare the experiment. With the valuable help of Dominik Maxein, Adrien Nicolas and Julien, I could design it, gather the required materials and gradually build the experimental setup. All this was done in very close relation with the other and earlier experiment of the quantum memory team (a quantum optics experiment based on a cold cesium ensemble), involving during my stay in the lab Lambert Giner [Giner13b], Lucile Veissier [Veissier13], Adrien Nicolas [Nicolas14], Dominik Maxein, Alexandra Sheremet, Christophe Arnold, Valentina Parigi, Pierre Vernaz-Gris, Elisabeth Giacobino and Julien Laurat. Much of the new experiment is based on this previous and

parallel works.

My work started with a nanofiber production setup, then, after one year, we started to build the vacuum system where the cold atoms would be prepared. This was soon followed, during the second year, with the implementation of the laser system required to manipulate the cesium atoms. The second part of my PhD started from March 2014. During that month, we managed to transfer our first optical nanofiber in an operational atomic physics setup. From that moment, my personal experience changed from something mostly based on learning from other people's experience, to a very different and intense way of learning: by running my own experiment. I then worked on showing how this setup could be used in similar protocols than those developed in the team for quantum optics. The main result is that light at the single-photon level tightly confined in an optical nanofiber could be slowed down in electromagnetically induced transparency (EIT) conditions and stored in an atomic ensemble surrounding the fiber.

During the third and last part, my main role has been the transmission of my recently acquired knowledge. The latter involved the writing of an article, my participation in different conferences, the arrival of Neil Corzo-Trejo and Aveek Chandra in the team (who had to learn how to use the tools I had developed), and finally the writing of this thesis.

This manuscript is organized as follows. The first chapter introduces optical nanofibers, or more precisely sub-wavelength optical fibers, and the properties of the light they can guide. In the second chapter I will describe how a cold atom physics setup was built around such a nanofiber. The third chapter will present electromagnetically induced transparency, a quantum interference effect occurring in a 3-level atomic system, and will describe the first experiments based on EIT that we realized with the setup, including the storage of pulses of guided light attenuated to the single-photon level. The final chapter describes how we can trap and manipulate further the cold atoms in the vicinity of a nanofiber, aiming at more experiments in the fields of quantum optics and optomechanics.

Along with this text, I try to give all the numerical information regarding the present work that is easy enough to provide. This information is available on a personal web-page [webpage] and includes:

- code for computing the EIT susceptibility for Zeeman degenerate atoms and any electric field polarization (see subsection 3.1.3),
- source codes for synchronization and acquisition with FPGAs (see Appendix A),
- a few technical 3D drawings,
- translation stage trajectories used for nanofiber pulling,
- sources for all figures of this document.

Chapter 1

Subwavelength optical fibers

After its accelerated development in the 1970s, driven in particular by the rapid growth of telecommunications, optical fibers have become an essential component of modern technologies. The possibility to produce fibers of very thin diameter - at the scale of optical wavelengths - has then rapidly been considered. In the 2000s, improvements in manufacturing processes of such fibers (see for example [Tong03, Brambilla04]), resulted in optical waveguides having a diameter of a few hundred nanometers and an optical transmission close to 100%.

Since then, these nanofibers have been used for various applications taking advantage of their different properties (see [Brambilla10] for a review, and Figure 1.1):

- Strong confinement of the electromagnetic field, going beyond focusing in free space, over the whole fiber length (in free space, confinement is limited in both the transverse and the propagation directions). This allowed for example to observe efficient nonlinear optical effects [Leon-Saval04, Shan13].
- Intense evanescent fields: a significant part of the guided energy is within the evanescent wave located outside of the fiber.
- Flexibility: some manufacturing methods allow to obtain nanofibers directly coupled by a tapered transition to a standard optical fiber. This results in a low loss and rather compact optical component which may be connected directly to fiber networks.

The strong confinement of the electromagnetic field means that a strong interaction between the guided light and matter in the vicinity of the fiber can be obtained. This is where comes into play an intense area of research at the Laboratoire Kastler Brossel: light-matter interaction at a few quanta level, for which strong interaction is a challenging but essential condition. Beyond LKB, this area of research has become very important in recent decades culminating during the beginning of my thesis with the award of the Nobel Prize to two representatives of the field (Serge Haroche and David Wineland). Related to this field of research, two key topics in which the nanofibers are expected to play an interesting role are cavity quantum electrodynamics (QED) and quantum information.

Before detailing the properties of light guided in nanoscale waveguides, let us first consider the nanofibers in the context of atomic physics. They allow interactions

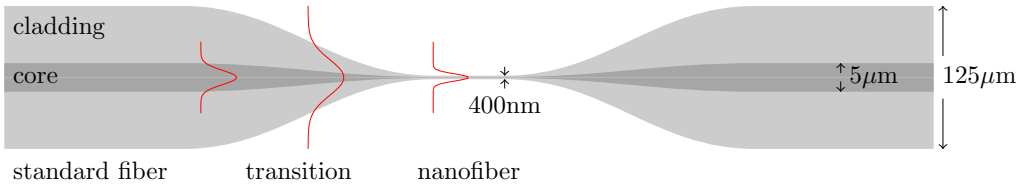

Figure 1.1: Illustration of a typical tapered fiber. The nanofiber, in the center, can guide light with subwavelength confinement and intense evanescent fields. It is coupled adiabatically on both sides to standard optical fibers.

between light guided in the fiber and atoms at a sub-micron distance from the surface. This distance should be compared to an atomic resonance cross section which is on the order of λ^2. An immediate consequence is the modification (an increase) of the spontaneous emission rate of atoms close to the nanofiber and the possibility to collect and guide spontaneous emission into the fiber. On the other hand, a significant fraction of power guided by the nanofiber can be absorbed by a single atom [Chang14].

Following theoretical proposals from Hakuta and co-workers [Balykin04, Patnaik02] starting from 2002, several experimental groups have demonstrated the manipulation of atoms with nanofibers. Many challenging experiments have now been or are being developed based on such a manipulation. With warm atoms, non-linear optics demonstrations were carried out in the USA by S. Spillane *et al.* [Spillane08] and by S. Hendrickson *et al.* [Hendrickson09] showing in particular saturation effects at very low power levels (nanowatts).

In a first series of experiments with cold atoms, atom clouds were prepared with magneto-optical traps (MOT) in the vicinity of nanofibers. This allowed to study the modified atomic spontaneous emission, as well as surface interactions and the possibility to probe the MOT characteristics. Those experiments were carried out by the groups of A. Rauschenbeutel [Sagué07] in Germany/Austria, K. Hakuta in Japan [Nayak09], and Síle Nic Chormaic [Morrissey09] in Ireland/Japan.

Before the beginning of my thesis, the pioneering success in trapping atoms in a nanofiber vicinity by A. Rauschenbeutel's group [Vetsch10] was soon followed by the contribution of Kimble's group [Goban12] in the USA, with a different scheme aiming at the preservation of the internal properties of untrapped atoms. More recent setups aim at collective atomic entanglement [Béguin14] (Béguin *et al.* in Danemark), cavity-QED with additional Bragg mirrors [Kato15] (S. Kato and T. Aoki in Japan), or bringing nanofiber trapped atoms close to superconducting circuits [Lee15] (J. Lee *et al.* in Maryland USA).

In this chapter, I will describe optical nanofibers and their properties. In the first part, I will consider the propagation of light through dielectric optical waveguides, focusing on the simplest case for fibers and nanofibers: a step-index profile with rotational invariance around one axis. I will then describe the fabrication of such fibers by the flame brushing technique we implemented in the lab and discuss some practical considerations when using these nanofibers.

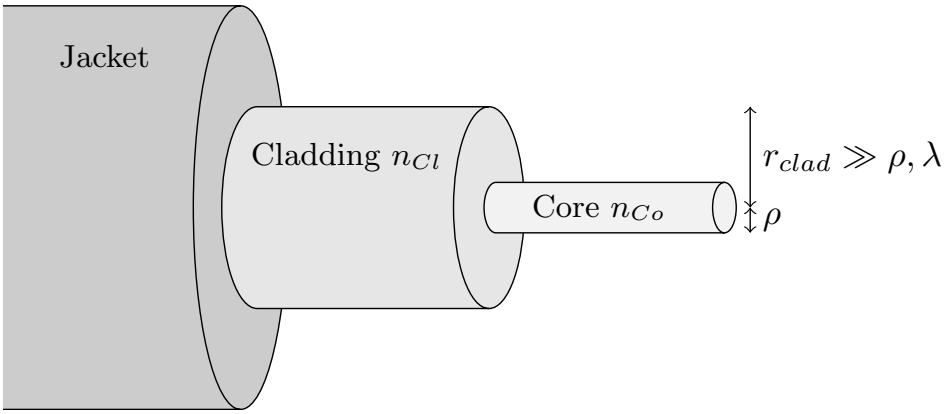

Figure 1.2: A step-index optical fiber. Light is guided in the core by total internal reflection at the core/cladding interface. Standard fibers are usually packaged in a protective acrylate jacket.

1.1 Propagation in optical nanofibers

Propagation in dielectric waveguides can usually be understood in terms of ray optics. Rays propagating in a *core* of refractive index n_{Co} surrounded by a *cladding* of lower refractive index n_{Cl} will be guided by total internal reflection. However, this geometric description is not relevant to describe some properties of single-mode fibers or fibers with variations of the refractive index at the wavelength scale such as optical nanofibers. The full derivation of the problem requires the use of Maxwell equations, and the result is given here in terms of transverse mode functions. As we are dealing with evanescent waves and near-field optics, some usual properties of plane wave propagation in vacuum are not true anymore.

The properties of the electromagnetic field in optical waveguides are described in much details in [Snyder83]. This includes the case of step-index fibers and nanofibers that we will consider here. A shorter summary giving the mode functions for the guided and radiated modes in a nanofiber can be found for example in the appendices of [Le Kien05].

We describe in this section the solution of Maxwell equations for step-index fibers.

1.1.1 Step-index fiber: Derivation of the guided mode properties

A step-index optical fiber (see Figure 1.2) is composed of a cylindrical dielectric core with refractive index n_{Co} and radius ρ, a cladding with smaller refractive index n_{Cl} and radius r_{clad}, and usually a protective jacket. Both the core and cladding are supposed non-absorbing and with magnetic permeability equal to the free-space permeability μ_0.

For the practical examples relevant in this thesis we will consider two configurations of such step-index fibers. One is a standard single-mode or few-mode fiber, made of silica and doped silica. For visible or near infrared light, the core has typically a diameter larger than a few microns with a refractive index ($n \sim 1.5$) slightly higher than the cladding's index (the cladding diameter is usually larger than 100 microns).

The other example is the silica tapered fiber where the cladding is made of air or vacuum ($n \sim 1$). When the diameter of the core is smaller than the wavelength, we call this a subwavelength optical fiber or nanofiber for short.

Notations – The fiber is modeled with a refractive index profile defined by the following equations expressed in the cylindrical coordinates (r,ϕ,z):

$$\begin{aligned} n(r) &= n_{Co}, & 0 \leq r < \rho \\ n(r) &= n_{Cl}, & \rho \leq r < \infty. \end{aligned}$$

In this simple waveguide, the Maxwell equations have exact analytical solutions. Historically, they were studied extensively in the weakly guiding ($n_{Co} \sim n_{Cl}$) and Gaussian approximations, which are adapted to most standard fibers, but not to optical nanofibers. We thus present the general solution here (no approximations).

The following are common notations that will be used in this chapter:

- λ the optical wavelength in vacuum, c the speed of light in vacuum, $k = \frac{2\pi}{\lambda}$ and $\omega = kc$,
- $R = \frac{r}{\rho}$, the radial coordinate normalized to the core radius,
- $V = k\rho\sqrt{n_{Co}^2 - n_{Cl}^2} = 2\pi\frac{\rho}{\lambda}\sqrt{n_{Co}^2 - n_{Cl}^2}$, an essential dimensionless parameter depending on the index contrast and, importantly, on the ratio between the core radius and the wavelength λ,
- β the propagation constant, or wavenumber, for a given guided mode, and the corresponding effective refractive index $n_{\text{eff}} = \beta/k$
- $U = \rho\sqrt{(kn_{Co})^2 - \beta^2}$,
- $W = \rho\sqrt{\beta^2 - (kn_{Cl})^2}$,
- J_ν the Bessel functions of the first kind (ν is an integer),
- K_ν the modified Bessel functions of the second kind (similar to an exponential decay).

The electric and magnetic field for a propagation constant β can be written in the general case as:

$$\begin{aligned} \vec{E}(r,\phi,z,t) &= \vec{e}(r,\phi)\exp[i(-\omega t \pm \beta z)]/2 + c.c. \\ \vec{H}(r,\phi,z,t) &= \vec{h}(r,\phi)\exp[i(-\omega t \pm \beta z)]/2 + c.c.. \end{aligned} \tag{1.1.1}$$

Solutions – There are two families of general solutions, valid for both standard fibers and nanofibers. In the "even" case, the longitudinal components of the electric and magnetic fields are expressed with Bessel functions [Snyder83]:

$$\begin{aligned} e_z &= A\frac{J_\nu(UR)}{J_\nu(U)}\cos(\nu\phi) \quad \text{and} \quad h_z = -B\frac{J_\nu(UR)}{J_\nu(U)}\sin(\nu\phi) \quad \text{for} \quad 0 \leq R < 1 \\ e_z &= A\frac{K_\nu(WR)}{K_\nu(W)}\cos(\nu\phi) \quad \text{and} \quad h_z = -B\frac{K_\nu(WR)}{K_\nu(W)}\sin(\nu\phi) \quad \text{for} \quad 1 \leq R < \infty. \end{aligned}$$

The "odd" solutions are obtained from the "even" solutions with a $\pi/2$ rotation around the fiber axis.

The transverse components (e_x and e_y) can be derived from the longitudinal components using the Maxwell equations. They have a $\pi/2$ phase relative to the longitudinal components. The local polarization is thus in general non-transverse and elliptic. The electric and magnetic fields are not orthogonal, even in the vacuum part in the vicinity of a nanofiber. The "parity" (the term used in [Snyder83]) corresponds to the general orientation of the mode, it plays a role similar to polarization of a propagating mode in vacuum.

The continuity of the tangential components in $R = 1$ gives $\frac{A}{B}$ and three eigenvalue equations for the propagation constant β. Each of these equations leads to a finite number of possible values for β and corresponds to one of three classes of guided modes.

$$\frac{J_1(U)}{UJ_0(U)} + \frac{K_1(W)}{WK_0(W)} = 0, \quad \nu = 0, \text{ TE}_{0m} \text{ modes}$$

$$\frac{n_{Co}^2 J_1(U)}{UJ_0(U)} + \frac{n_{Cl}^2 K_1(W)}{WK_0(W)} = 0, \quad \nu = 0, \text{ TM}_{0m} \text{ modes}$$

and

$$\Big(\frac{J'_\nu(U)}{UJ_\nu(U)} + \frac{K'_\nu(W)}{WK_\nu(W)}\Big)\Big(\frac{J'_\nu(U)}{UJ_\nu(U)} + \frac{n_{Cl}^2 K'_\nu(W)}{n_{Co}^2 WK_\nu(W)}\Big) - \Big(\frac{\nu\beta}{kn_{Co}}\Big)^2\Big(\frac{V}{UW}\Big)^4 = 0.$$

$\nu > 0$, hybrid modes $\text{HE}_{\nu m}$ and $\text{EH}_{\nu m}$

Standard fiber modes: weak guidance and Gaussian approximations – Standard fibers can usually be treated in the weak guidance approximation where $n_{Co} \sim n_{Cl}$. Subsets of the modes introduced above become nearly degenerate in β and can be combined to form transverse and homogeneously linearly polarized (LP) modes. They correspond to the pictures usually available in the fiber optics literature. Their intensity profile are shown in Figure 1.3. They can be approximated with the mode functions of free-space propagating Gaussian beams (Gaussian approximation).

Nanofiber modes: transverse and hybrid modes – For nanofibers, we cannot make the weak guidance approximation and we have to stick to the general solution. The TE modes have a transverse electric field, but have both a transverse and a longitudinal component of the magnetic field. The TM modes have a transverse magnetic field, and have both a transverse and a longitudinal component of the electric field. On the other hand, the HE and EH modes (hybrid modes) have a transverse and a longitudinal component for both fields.

The transverse components of the fields can be significant for the nanofiber modes. This result can be derived from Gauss's law: $\vec{\nabla} \cdot \vec{E} = 0$. Using Eq. (1.1.1) the law reads:

$$\frac{\partial e_x}{\partial x} + \frac{\partial e_y}{\partial y} = \pm i\beta e_z = \pm i n_{\text{eff}} \frac{2\pi}{\lambda} e_z,$$

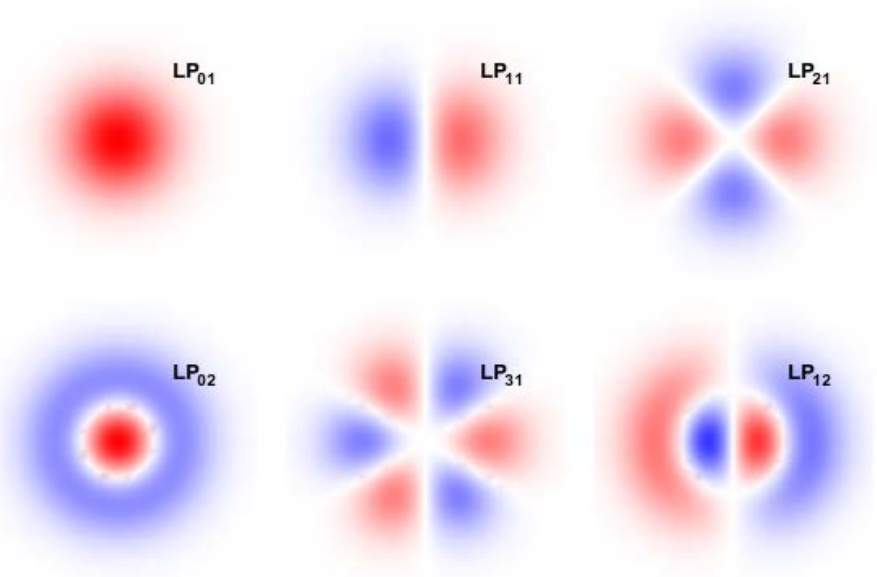

Figure 1.3: Amplitude profiles of linearly polarized modes in standard fibers. These modes are obtained in the weak guidance and Gaussian approximations from combinations of the more general TM, TE, HE and EH modes. More precisely, $\mathrm{LP}_{\nu m}$ modes are derived from $\mathrm{HE}_{\nu+1,m}$ and $\mathrm{EH}_{\nu-1,m}$, where for $\nu = 0$, TE_{0m} and TM_{0m} are identified to EH_{0m}.

where n_{eff} is the effective refractive index for the guided mode. Thus, if the transverse field varies over a length scale l with an amplitude $\mathcal{E}_t$, the longitudinal component of the electric field can have a value

$$\mathcal{E}_z = \pm i \frac{1}{2\pi n_{\mathrm{eff}}} \frac{\lambda}{l} \mathcal{E}_t.$$

It is indeed in phase quadrature with the transverse field and negligible when the mode is not focused to wavelength scale (LP modes) but can be significant otherwise (nanofiber modes). It is zero for nanofiber guided modes only if $\frac{\partial e_x}{\partial x} + \frac{\partial e_y}{\partial y} = 0$ (TE modes).

Dispersion relation – The eigenvalue equations must be solved numerically. Figure 1.4a shows a graphical resolution. Each solution for the wavenumber β corresponds to four degenerate modes with the two possible parities and two propagation directions. The mode index m is a positive integer numbering the values for β in decreasing order $kn_{Cl} < \beta \leq kn_{Co}$.

Figure 1.4b gives the solution as a function of the fiber radius. The dispersion relation for a given mode - β as a function of λ - can be deduced from these curves. Note that the effective refractive index β/k varies from a higher value $n_{Co} = 1.45$ for which the mode is mostly in the bulk silica to a lower value $n_{Cl} = 1$ for which the mode is mostly in the evanescent field outside the fiber.

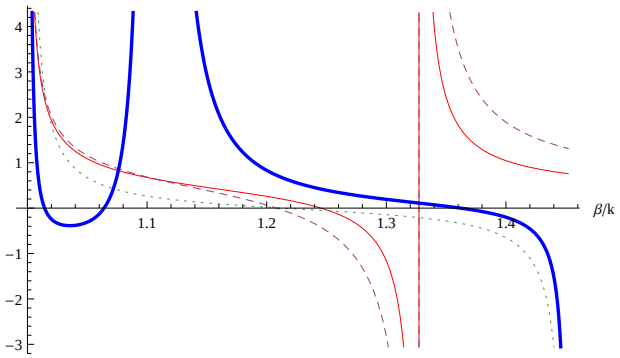

(a) Graphical resolution of the eigenvalue equation for the propagation constant β. Here, the core radius is $\rho = 575$ nm and $\lambda = 852$ nm. The left hand sides of the eigenvalue equations are plotted : thick lines for hybrid $\nu = 1$ modes, thin lines for TE modes, dashed for TM modes and dotted lines for $\nu = 2$ modes. The solutions are given by the intersections with the horizontal axis. The highest value for β is for the fundamental HE_{11} mode, other obtained values are for TE_{01}, TM_{01}, HE_{21}, EH_{11} and HE_{12} modes.

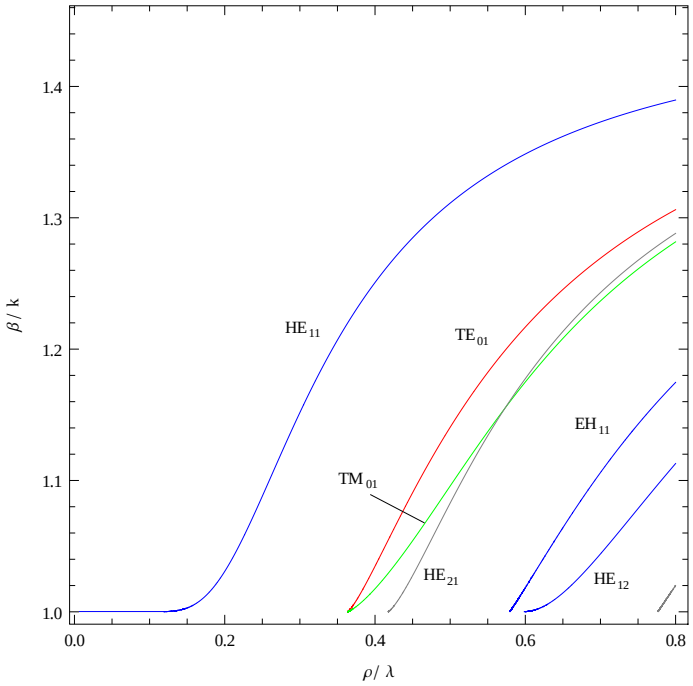

(b) Wavenumber β as a function of the core radius - or equivalently as a function of V. β/k is also the effective refractive index n_{eff} with $n_{Cl} < n_{\text{eff}} < n_{Co}$. When $V < 2.405$, or here $\rho/\lambda < 0.36$, the fiber is single-mode. Otherwise, different modes can co-propagate with different wavenumbers.

Figure 1.4: Resolution of the eigenvalue equations in the nanofiber case with $n_{Co} = 1.45$ and $n_{Cl} = 1$.

Only one solution remains when the diameter approaches zero, this is the fundamental mode HE_{11}. The waveguide is then single-mode[1]. The single-mode condition can be read on Figure 1.4b as $\rho/\lambda < 0.36$ with the chosen refractive indexes or more generally as[2]:

$$0 < V < 2.405.$$

For even smaller diameters, light cannot be guided anymore in the core as explained in [Sumetsky06]. Any bending of the fiber would lead to loss in the radiation modes.

Note that *single-mode* here is a rather imprecise term taking into consideration only the spatial mode function. A continuum of modes with different optical frequencies can indeed be guided. But, when the frequency is fixed, only a finite number of mode functions are enough to describe the guided electromagnetic field. Each of these mode functions is associated with a specific β (or a specific wavelength when propagating in the guide) as mentioned before. And these mode functions actually correspond to 4 different modes of propagations, when considering the 2 possible "parities", and the 2 possible directions of propagation (forward and backward).

Electric field distribution – Figure 1.5 shows the transverse electric field for different modes in a nanofiber. They have complex polarization pattern and are clearly different from the usual LP modes. In subsection 1.1.2 we will focus on the properties of the fundamental HE_{11} mode in a nanofiber.

Energy distribution – Another interesting feature is the energy distribution for the guided modes. The local electric field and magnetic field energy densities are given by[3]:

$$w_E = \frac{1}{4}\epsilon_0 n^2 |\vec{e}|^2 \qquad \text{and} \qquad w_H = \frac{1}{4}\mu_0 |\vec{h}|^2.$$

Note that in evanescent waves, the electromagnetic energy density is not equally distributed between its magnetic field and electric field contributions. Either of them can be dominant depending on the position. However the electromagnetic energy per unit length, i.e. when integrating the density over a transverse plane, is equally distributed.

The guided power is:

$$P = \frac{1}{2}\iint \Re[(\vec{e}\times\vec{h}^*).\vec{z}]dxdy.$$

Again, because we are dealing with evanescent waves, the fraction of electromagnetic intensity ($\frac{1}{2}\Re[(\vec{e}\times\vec{h}^*).\vec{z}]$) inside the core might be different from the fraction of electric field intensity ($I_E \propto cw_E = \frac{1}{4}c\epsilon_0 n^2|\vec{e}|^2$) inside the core.

[1] HE_{11} is thus the usual mode of standard single-mode fibers. In the examples given here though, the refractive indexes and the core size are chosen for the nanofiber case.

[2] Recall that $V = 2\pi\frac{\rho}{\lambda}\sqrt{n_{Co}^2 - n_{Cl}^2}$, and ρ is the core radius.

[3] If silica is supposed dispersive with group index n_g,

$$w_E = \frac{1}{4}\frac{d(\epsilon\omega)}{d\omega}|\vec{e}|^2 = \frac{1}{4}(n^2 + 2n(n_g - n))|\vec{e}|^2$$

.

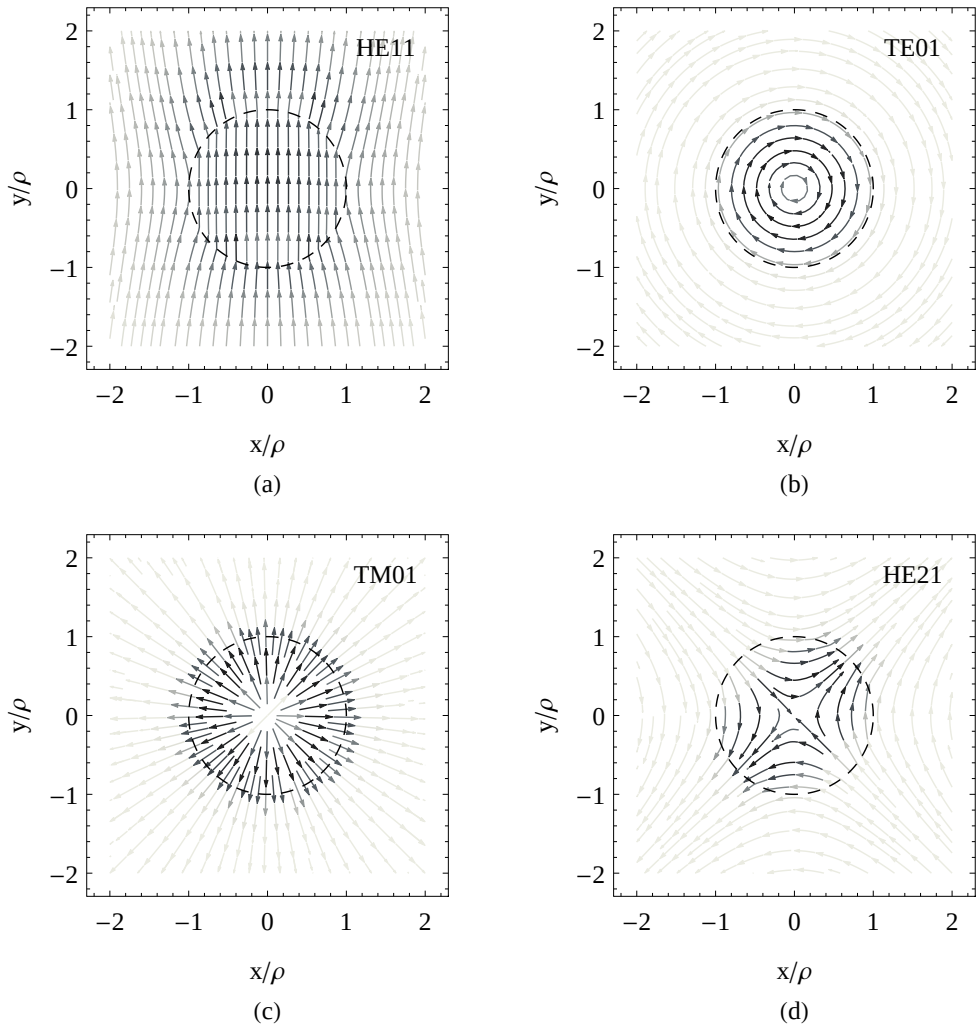

Figure 1.5: Examples of modal shape of the transverse electric field for $\lambda = 852$ nm in nanofibers of different radii. $\rho = 200$ nm (a) corresponds to a single-mode fiber and $\rho = 2\lambda = 1.7$ μm (b,c,d) to a few modes fiber. The refractive indexes are $n_{Co} = 1.45$ and $n_{Cl} = 1$ and the displayed modes are : (a) HE_{11}, (b) TE_{01}, (c) TM_{01}, (d) HE_{21}. The core region is delimited by dashed lines and the transverse electric field amplitude is represented with gray scale while its direction is represented with arrows.

1.1.2 Properties of the fundamental HE_{11} mode in a nanofiber

We now focus on the fundamental HE_{11} mode for a nanofiber. For a 400 nm diameter silica nanofiber and light at 852 nm for instance, with $n_{Co} = 1.45$, $n_{Cl} = 1$ and $V = 1.55$, all the light propagates in the single HE_{11} mode, with only 41% of the electromagnetic energy inside the core. As we will see soon enough, those parameters correspond the optimal single-mode nanofiber when working with the D_2-line of cesium (852 nm) and we use them for all the experiments in this thesis.

More details of the HE_{11} mode electric field distribution, including the longitudinal components, are plotted on Figure 1.6. The chosen parity corresponds here to a

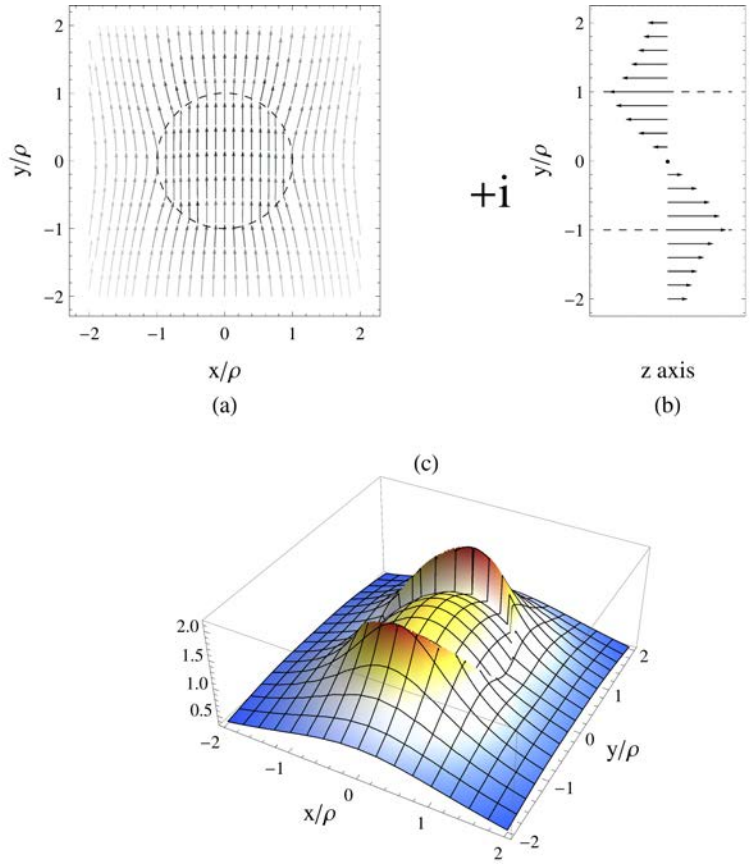

Figure 1.6: Electric field of the HE_{11} *quasi-linearly polarized* along y in a step-index optical fiber of radius $\rho = 200$ nm, refractive indexes $n_{Co} = 1.45$ and $n_{Cl} = 1$ for $\lambda = 852$ nm. The core region is delimited by dashed lines. (a) Transversal component in the $z = 0$ plane, the transverse electric field amplitude is represented with gray scale. (b) Longitudinal component on the $x = z = 0$ line. (c) Electric field intensity in $z = 0$ plane.

general orientation of the electric field along the y-axis, the $x = 0$ plane being a plane of symmetry. The mode with this particular orientation, linked with a linear polarization along y-axis at the fiber input has been referred to in the literature as *quasi-linearly polarized* along y-axis. *This doesn't mean that the polarization is almost linearly polarized* as we detail below. I will use this denomination in the present thesis.

There is a strong discontinuity of the electric field intensity at the surface, as is clear from Figure 1.6 (c). Outside the core, the electric field is maximal in the $x = 0$ plane. In this plane, the polarization is elliptic, rotating around the x axis with opposite directions in the $y > 0$ and $y < 0$ subspaces as illustrated in Figure 1.7, and in more details in Figure 1.8. These opposite rotations on both sides of the fibers have been exploited elegantly in a few experiments recently [Petersen14, Mitsch14a, Mitsch14b]. In Figure 1.8(b)-(d) the polarization is represented as the square of the amplitudes projected in a spherical basis (defined in subsection 3.1.3). These numbers are linked to the probabilities of atomic excitation to a given Zeeman sub-level. For completeness,

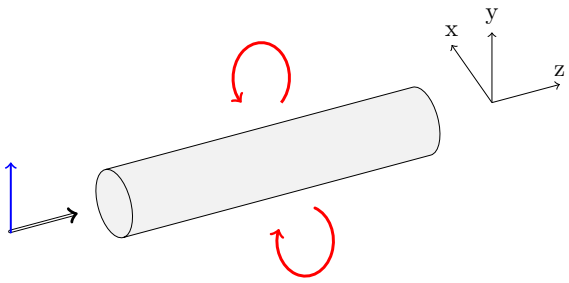

Figure 1.7: Elliptic polarization of the electric field in a nanofiber vicinity. Here the guided mode is quasi-linearly polarized along y. The polarization rotates in opposite directions for $y > 0$ and $y < 0$.

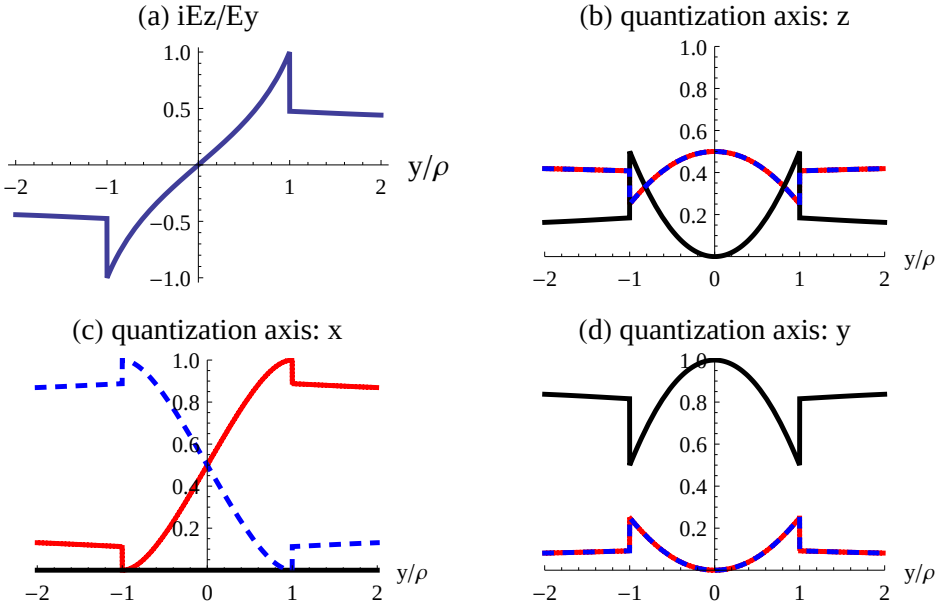

Figure 1.8: Local polarization of the HE_{11} mode quasi-linearly polarized along y, on the $x = z = 0$ line. (a) Ratio of the longitudinal component and the transverse component. (b), (c) and (d) are the corresponding square of the amplitudes of the electric field expressed in spherical bases. σ_+, σ_- and π are represented respectively with red, blue and black curves. The simplest choice of quantization axis is clearly the x-axis, such that there is no π component and σ_+ is almost 90% populated in the evanescent field for positive y values.

this is plotted in Figure 1.8 for different choices of the quantization axis.

The probability for an atom to interact with a photon scales as σ/A where $\sigma = \frac{3\lambda^2}{2\pi}$ is the maximal resonant atomic cross section and A the mode area. This probability gets very significant when $\sigma/A \sim 1$, also corresponding the non-linear phenomena with only a few photons. For nanofiber guided modes, an "effective mode area"[4] can

[4]Note that there are other definitions for a mode area in the realm of optical waveguides.

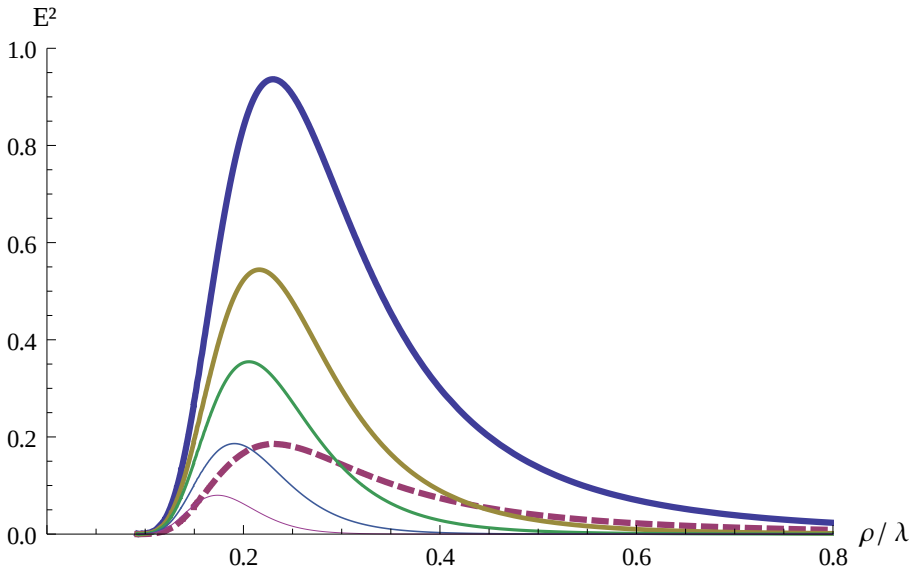

Figure 1.9: Normalized electric field intensity of the quasi-linearly polarized HE_{11} mode as a function of the fiber radius for different positions around the fiber, in units of the inverse maximal atomic scattering cross section $\frac{1}{\sigma} = \frac{2\pi}{3\lambda^2}$. The solid lines are for positions on the quasi-linear polarization axis, from thicker lines to thinner lines at distances 0, $\frac{\rho}{4}$, $\frac{\rho}{2}$, ρ and 2ρ from the surface. The dashed line is for a position on the orthogonal direction, on the fiber surface.

be defined as the inverse of the electric field intensity normalized by the guided power P: $A = \frac{P}{I_E(\vec{r})}$. The electric field intensity is provided as a function of the fiber radius in Figure 1.9, for different positions in the evanescent field. As the plot shows, this effective area can be as small as the scattering cross section. This is obtained for an optimal radius close to $\rho = 0.2\lambda$ depending on the atomic position.

Section summary

We described here the guidance properties of step-index fibers. In particular, the smallest nanofibers are single-mode and they only guide the so-called HE_{11} mode. This highly focused mode has a complex intensity and polarization pattern whose symmetries are determined by the input polarization. For a linear polarization along y-axis at the fiber input, the mode is called *quasilinearly polarized*. It has a stronger intensity along the y-axis, with a strong elliptical polarization in the evanescent field rotating in opposite directions on both sides of the fiber.

In this thesis, we will mostly use nanofibers with a 400 nm diameter, optimal for D_2-line resonant interaction with a cesium atom at the fiber surface. With these parameters only 41% of the input power is guided inside the core.

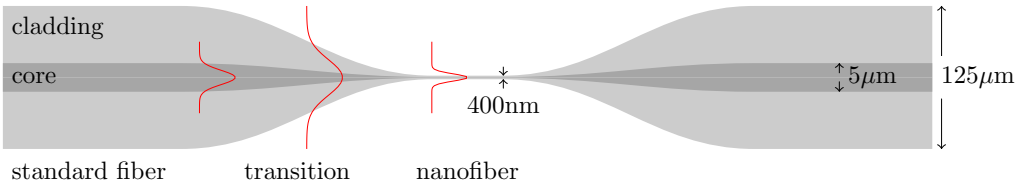

Figure 1.10: Illustration of a typical tapered fiber. Light initially guided at the core-cladding interface is adiabatically coupled to a nanofiber. In the nanofiber the core has vanished and the guidance is at the cladding-air interface, with a large ratio of the guided power located in the evanescent field outside the fiber.

1.2 Producing optical nanofibers

One of the first tasks of my PhD was to learn how to make nanofibers and to set up a production bench in our team. After a first experience with Yves Candéla and Jean Hare in the ENS part of LKB [Candéla11], I studied the different techniques used by different research teams in France and abroad (see [Garcia-Fernandez11] for a review, or the reports on different rigs developed at the time [Wilcut Connolly09, Aoki10], with a careful study of the taper shape in [Stiebeiner10] or the possibility to use a ceramic oven as a heater in [Lu Ding10]). I could then build a nanofiber production rig that is now being used for different experiments in LKB. This new rig is already working well enough for the challenging atom-physics experiments we've been running in the lab so far. It can clearly be improved and there is still much to learn from all the progress that has been done in the community during those few years. For more details, the reader can refer to the various papers published in 2014 from groups producing nanofibers for atom-physics experiment. In [Ravets13] for example, losses via intermodal energy transfers in the tapered transition are studied for optimization of the fabrication process. Similarly, in [Nagai14], the taper shape is optimized, resulting in high transmissions with short tapered transitions. [Sorensen14] refines the modeling and characterization of the heater, while [Hoffman15] uses local Rayleigh scattering for *in situ* imaging of propagation in fiber tapers. The fabrication process is exposed in [Hoffman14] where very high transmissions are reported, with emphasis on the cleanliness required for such results. The full nanofiber fabrication process is also recently reviewed in [Ward14].

The technique we implemented is based on a rather simple idea: a standard optical fiber is softened by heating and pulled until its diameter has reached a target value. The result is illustrated in Figure 1.10. We obtain a nanofiber that is adiabatically connected via tapered regions on both sides to the standard fiber.

Let's describe propagation in this system. Light can be coupled from the left side, in our case usually in a single-mode fiber, with standard techniques. When the guided light reaches the tapered region, the mode area decreases as the diameter of the core decreases. At some point, the mode area increases and the core is soon too small to keep its guiding properties. The light escapes the core, but is reflected at the cladding/air interface (it might be lost here if the tapering angle is too large). At this point the fiber is multi-mode. As the diameter keeps decreasing, the cutoff diameter is reached for different modes one after the other. When the diameter reaches the

last cutoff, the fiber is then single-mode and the light is guided in the fundamental HE_{11} mode. Here, the guided light is already propagating in a sub-wavelength fiber although the diameter might still decrease in order to reach a specific target diameter. After the second tapered region, the guided light couples back into the core. All the input power can be retrieved at the output if the fiber was designed and produced carefully enough. These propagation properties were amazingly demonstrated in *in situ* experiments by Jonathan Hoffman *et al.* [Hoffman15] using high-resolution Rayleigh scattering imaging along the tapered transition.

High transmission through the whole taper is obtained when it meets the so-called adiabaticity criterion. The latter is defined in [Black91] as a limitation on the taper angle relative to the fiber axis. The taper angle should be much smaller than

$$\Omega_c = \frac{\rho(\beta_1 - \beta_2)}{2\pi} = \frac{\rho}{\Lambda},$$

where r is the local fiber radius, β_1 and β_2 are the propagation constants of the fundamental HE_{11} mode and the first excited mode (which both depend on the local fiber radius) and Λ is simply the spatial beatnote between these two modes. If at some point, the taper angle gets closer to ρ/Λ, the higher order mode will be excited and the corresponding power will be lost later when the taper reaches the mode cutoff radius. With our typical parameters, Ω_c is lower (using small angles is thus critical), in the middle of the taper: when the fiber radius ranges from 10 μm to 30 μm, Ω_c is about 10 mrad (see for example [Ravets13]). It increases rapidly for thinner or thicker fibers.

The shape of the tapered region can be derived from volume conservation [Birks92]. If the fiber is heated uniformly over a region of constant width and pulled symmetrically, it will have an exponential shape and the nanofiber will have the same length than the heating width. However, if the heating width is varied during the pulling, any shape of the tapered transition and any length of the nanofiber can be obtained. The specific method that we implemented, the "flame-brushing" technique (illustrated in Figure 1.11), allows such a variation of the heating width. The flame makes back-and-forth movement in order the produce an effective heating zone whose width is defined by the amplitude of the flame oscillations. In our setup, the flame itself does not move, but rather the two pulling stages: their motion is a combination of pulling motion and a synchronized back-and-forth motion.

There are three main constraints for this process to be successful and to obtain tapered fibered with tiny diameters and high transmissions. The first is the cleanliness of the whole process. Also, smooth enough shapes of the tapering regions should be used in order to meet the adiabaticity criterion. Finally, the mechanical motion of the different elements of the process should be well controlled for smooth and reproducible pulling.

A picture of our rig is provided in Figure 1.12[5] and the different elements used summarized in Figure 1.13. The next few paragraphs describe in more details the setup. Table 1.1 summarizes the typical parameters used, while Table 1.2 is a bill of materials.

[5] Figure 2.1 gives a more general point of view together with the rest of the experiment.

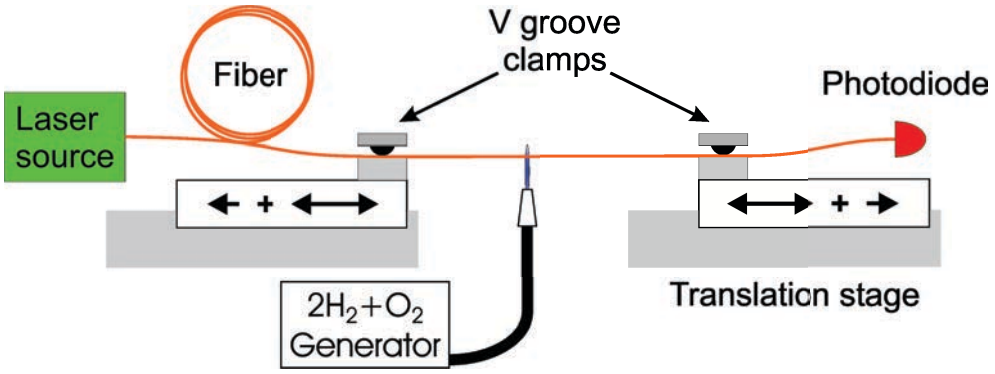

Figure 1.11: Sketch of the flame brushing rig. The fiber is heated by a hydrogen/oxygen flame. It is clamped on the sides to two linear translation stages responsible for both a pulling and a back-and-forth motion. Transmission of a laser beam through the fiber is monitored continuously during the pulling process.

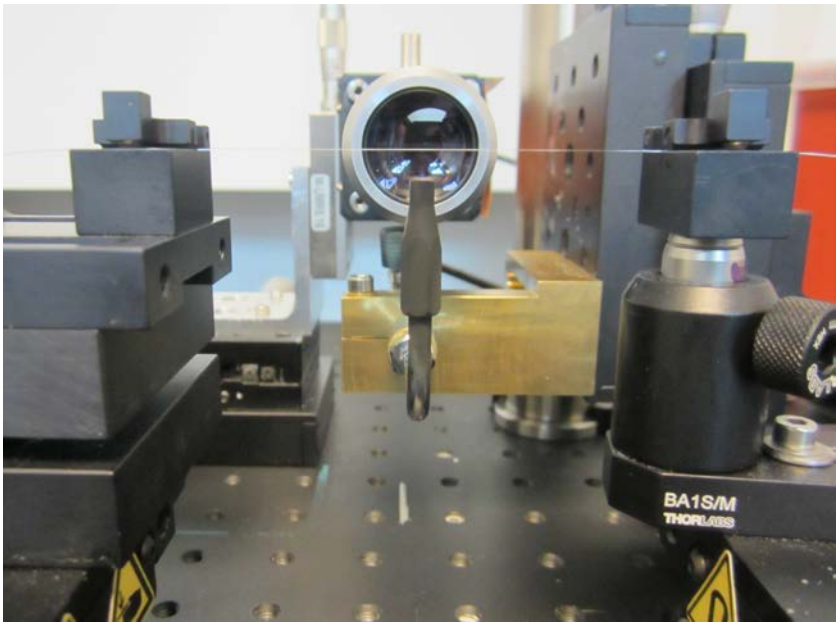

Figure 1.12: Center of the flame brushing setup. On this picture, the flame, the "V-groove" fiber clamps, the translation stages and a microscope objective are visible. The microscope objective is used for example for checking the fiber cleanliness before pulling, or for precise positioning of the torch tip.

1.2.1 Hydrogen/Oxygen flame

In our setup, the fiber is heated using a hydrogen/oxygen flame, which avoids any unclean combustion products (only water is produced here). A stoichiometric mixture of hydrogen and oxygen is produced by electrolysis of water. Since all the produced hydrogen is burned rapidly, any storage in the lab of explosive hydrogen is avoided.

The gas flow is controlled using a mass flow controller for a better stability and

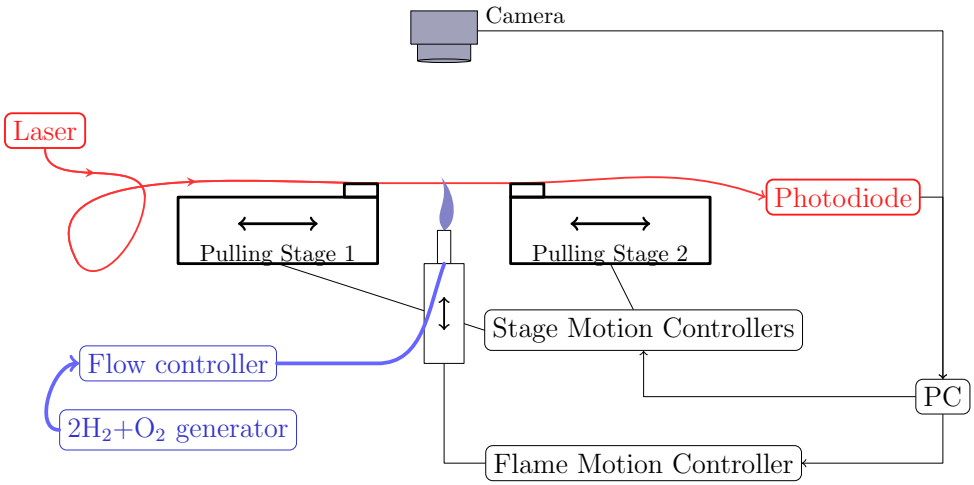

Figure 1.13: Diagram displaying the different elements of our flame-brushing rig. The fabrication itself is handled by the hydrogen/oxygen flame and the two pulling stages. Measuring the transmission of a laser beam through the fiber and imaging with a camera give information for monitoring the process.

reproducibility of the flame. The flow is set to the lowest possible value such that a flame can be continuously fed. In our setup this value is approximatively 280 mls/min (standard milliliters per minute). In order to preserve the flow controller from any damage, the mixture is dried and filtered before going through the flow controller.

The torch tip we have been using so far has a single hole of 0.5 mm diameter. The produced flame has a 0.42 mm effective width. This width is estimated by measurement of the taper shape after a symmetric pull (no brushing) of a fiber: assuming a uniform heating over the flame width, the expected profile is an exponential with decay constant equal to the flame width (which actually depends on other experimental parameters such as the distance from the tip to the fiber).

The flame motion is controlled via a motorized stage. This allows to keep the flame a few centimeters below the fiber before the pulling has started. It is then lifted just before the pulling. The flame height is chosen such that it is high enough to soften the fiber, but low enough such that the fiber doesn't bend. The fiber is at the edge of the flame, it is slightly glowing red, not as brightly as when it is inside the flame. This defines a small interval ($\sim$ 1 mm) which is usually suitable for a controlled pulling process. The height is calibrated using as a reference the position where the torch tip (the flame is turned off for the calibration) is touching an unstripped fiber (this is monitored looking from the side using a microscope objective). A typical value for the distance of the tip from this reference point is 4 mm in our setup. Looking from the top, the flame is centered on the fiber.

After turning on the flame, we wait a few minutes for any contaminant gas to be flushed from the tubings and for the flame to stabilize.

Table 1.1: Typical parameters in our nanofiber fabrication setup.

Parameter	**Experimental value**
Cladding diameter before pulling	diameter: 125 μm
Nanofiber target length	1 cm
Nanofiber target diameter	400 nm
Total taper target length	$<$ 12 cm
Taper shape	taper angle 1.5 mrad. Taper angle: angle between the surface and the fiber axis. Opening angle: twice the taper angle.
Torch tip hole diameter	0.5 mm
$2H_2 + O_2$ flow	280 mls/min. As indicated by our flow meter, calibrated for H_2 rather than for a mixture.
Effective flame width	0.42 mm
Tip distance from fiber	4 mm
Pulling speed (elongation generated by the two stages)	$<$ 0.5 mm/s
Flame brushing speed	2 mm/s
Initial distance between to two fiber clamps	6 cm

1.2.2 Cleaning and preparing the fiber for pulling

For better cleanliness of the environment, the production rig is placed under a laminar flow system and the rig area is regularly cleaned carefully. Clean gloves, masks, hats and clothes are used, especially when manipulating a nanofiber for transfer into vacuum.

The fiber is cleaned a first time by sweeping a lens paper humidified with a drop of isopropyl alcohol. It is then stripped of its acrylate coating over a few centimeters using standard tools. Careful cleaning of the stripped fiber is then required. Any dust or remnant acrylate would compromise the process. A three-step cleaning, with isopropyl alcohol, then with acetone and finally again with isopropyl alcohol, seems to be efficient here. The two tails of the fibers are then clamped on two linear translation stages, such that the stripped part is held straight between the two clamps. The clamps in their initial positions should be as close as possible to the stripped fiber in order to avoid possible uncontrolled vibrations of the fiber during the tapering process. Objects close to the flame are avoided in order to limit turbulences in the laminar flow, which is set to its minimal intensity during the pulling process.

Once the fiber is ready, the tapering process is started from a computer-controlled interface. The flame is lifted and the motion of the two translation stages is triggered. The tapering process lasts from a few minutes to half an hour depending on the trajectory. It is monitored using cameras with either standard or microscope objectives, and measuring the transmission of a laser source through the fiber as explained below.

Table 1.2: Bill of materials for our nanofiber fabrication setup.

Equipment type	**Company and part number**
Hydrogen/Oxygen generator	Hydrochalumeau Hobby 30
Gas flow controller	Vögtlin red-y smart GSC-A9SA-BB22, range: 20-1000 mls/min
Gas drier (Peltier effect based)	M&C techgroup ECP-1000G
Gas filter	Swagelok SS-6F-MM-7
Laminar flow clean air environment	Air C2, ISO 5 environment
Vibration isolated table and breadboard	Thorlabs, PBG52511 on sorbothane SB12B
2 linear translation stages and controller (for pulling and brushing)	Newport, 2 XMS100 and XPS-Q4
Linear translation stages and controller (for bringing/removing the flame from the fiber)	Thorlabs, Z825B and PT1
2 fiber clamps	Thorlabs, 2 T711/M-250 "V-groove" fiber holders
Fiber cleavers	Thorlabs S90W (quick and versatile cleave), and Fujikura CT-30A (precision cleaver)
Fiber stripper	Thorlabs T06S13 and FTS4 (Jonard)
Temporary fiber connections elements	Thorlabs, BFTU (fiber holder, now obsolete), 30126D1 (ferrule, obsolete), and ADAFC2 (mating sleeve)
UV led (for UV curing glues)	Thorlabs CS2010
Laser source (780nm) and photodetector	Thorlabs S1FC780 and DET100A/M
Cameras, standard or microscope objectives	IDS
Analog signal acquisition device	National Instruments USB-6008
Computer	
Standard single-mode fiber at 850nm	Thorlabs, SM800-5.6-125 (Fibercore)
Lens paper	Thorlabs, MC-5
Isopropyl alcohol	
Acetone	
UV curing glue	Dymax, OP-67-LS

1.2.3 Controlling the pulling stages

The trajectories of the two stages responsible for the pulling and the back-and-forth motion of the brushing are predefined in "pvt" files in which every line defines the positions and velocities of the stages for a given time increment. Those trajectories are computed from the target taper shapes and nanofiber diameters.

Two main algorithms were used in our setup. I wrote the first in python as a draft very close to the algorithm described by Christian Lützler in his master thesis [Lützler12]. This code was used efficiently enough for our first experiments (e.g. for the first fiber that we transfered in vacuum and used for the experiments described in [Gouraud15] and chapter 3). The taper had a constant angle of 1.55 mrad relative to the fiber axis, for 400 nm x 9 mm nanofiber waist.

The pulling process got much more reproducible (the fiber would not break as often before the end of the pulling process) though, once we started to used a more recent code written in matlab by Maxime Joos (intern in LKB at the time) and closely based on Florian Warken's thesis [Warken07] and the code published along with [Hoffman14]. We have had some issues with this more recent code though (the fiber would break when guiding a significant power in vacuum as mentioned below: paragraph 1.2.4) and more work is still required. Here a different taper shape was used: 3 mrad angle from 125 μm diameter to 40 μm, then 5 mrad until 20 μm followed by an exponential decay (with matched slopes at the 20 μm junction). Both source codes are available online for reference [webpage].

1.2.4 Monitoring and characterizing the process

Monitoring the transmission – A relevant way to access real time information during the brushing process is to monitor the transmission of a laser beam through the fiber. This gives information on the total transmission (which is desired close to 100%) but also on the fiber diameter [Orucevic07].

Indeed, part of the tapered transition of the fiber is multi-mode (Figure 1.10), and the input laser can excite modes of higher order than the fundamental HE_{11}. These modes have different propagation constants β. If they can propagate through the whole fiber, and because the length of propagation is varying during the pulling process, their interference leads to a beat-note that can be measured at the fiber output. Experimental evidence of this is shown in Figure 1.14. The laser power detected at the fiber output is plotted as a function of time during the brushing process, oscillations can clearly be identified at different stages of the process. For better visibility of those oscillations, a spectrogram (the spectral amplitudes for small time intervals, as a function of time) is plotted as well.

Now the link between those beat-notes and the fiber diameter comes from the fact that the propagation constants of each mode are a function of the fiber diameter, such that the beat-note frequencies are directly related to the real-time fiber waist diameter. A more specific event is when the fiber waist reaches a cut-off diameter. At this moment, corresponding to a well identified diameter, a precise mode cannot propagate anymore through the whole tapered fiber and the corresponding oscillation simply stops.

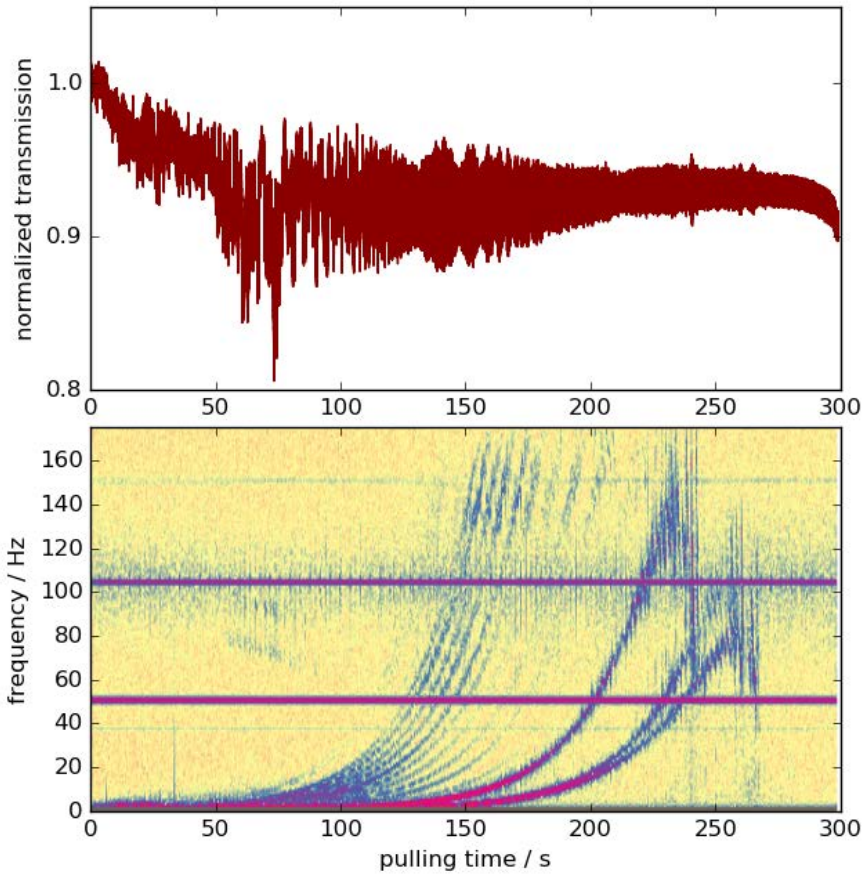

Figure 1.14: Transmission measurement during the pulling process, as well as the corresponding spectrogram. For this pulling, the intermodal oscillations can clearly be seen when zooming on the transmission curve, or on the spectrogram. The two last cutoffs correspond to the HE_{21}-HE_{11} interference and to the $TE_{01}-HE_{11}$ interference. The final decrease in transmission corresponds to diameters for which the nanofiber is too small to guide the input light anymore. The two horizontal lines close to 50 Hz and 100 Hz are due to detection and electric noise and can be ignored here.

Note that these oscillations have better contrast when higher orders modes can indeed be excited. The taper is not perfectly adiabatic, this also corresponds to losses. Figure 1.14 intentionally corresponds to a lossy pulling in order to better show those oscillations, although they have been observed even for very high transmission nanofiber production [Hoffman14].

As a conclusion here, monitoring the transmission of a laser through the fiber during the tapering process is a very simple and useful tool. This allows to get insights on the reproducibility of the process and to easily check that indeed, a nanofiber was produced. In our setup, we usually use a 780 nm laser. After the single-mode cut-off that can be observed on the spectrogram, the produced fiber is already a sub-wavelength optical fiber (at 852 nm) of diameter smaller than 570 nm.

Electron microscopy – Although less flexible (and destructive), scanning electron microscopy (SEM) allows to further characterize the produced fibers. Some SEM images are displayed in Figure 1.15. Before transferring a nanofiber in high vacuum conditions (for cold atom physics experiment, see section 2.1), we typically go through the following procedure: We first predefine all the parameters and the full protocol for the fabrication of the nanofiber. We then fabricate a series of nanofiber using this protocol, and glue them on a specimen stub used for the SEM. We then perform SEM measurements[6] and characterize the fibers. We usually obtain the target fiber diameters with a $\pm 5\%$ variation[7] from one fiber to the other. This gives an idea on the reproducibility of the fabrication process and on the dispersion we can expect on the diameter of a fiber transferred into vacuum.

For the SEM measurements, the fibers are coated with some conductive material (either carbon, gold or platinum). The coating is about 10 nm thick, adding some uncertainty on the measured diameter. Some care had to be taken when focusing the electron beam on the fiber and adjusting its parameters. Since the fiber is thin and suspended in high-vacuum conditions, it can be easily heated and modified (Figure 1.15c) or even broken by the beam.

Testing the nanofibers for high power guidance – One of the constraints for our experiments is that our nanofibers should be able to guide relatively large laser powers (> 10 mW) under vacuum conditions. It is easy enough to send large powers into a nanofiber just after its fabrication in ambient air conditions. In this case, sending up to 1 Watt (at 852 nm) never induced any noticeable damage on our nanofibers (usually tested for 400 nm diameter fibers). However the only way to perform this test under vacuum was to transfer the fiber in our final atom physics setup. Until now the result is the following: for the fibers using the older version of the code defining the stage trajectory[8] we could always use the 10 mW required for a dipole trap (described later in this thesis: chapter 4), and indeed trap atoms in the nanofiber vicinity. For the most recent code[9] this was always a failure: the fiber would break at milliwatt of sub-milliwatt input power. This issue is now under investigation.

[6] This is done with the help and knowledge of Sébastien Charron, using the UPMC's SEM platform.

[7] Note though that the number of SEM characterized fibers is still rather low for deducing very significant error bars.

[8] Constant angle of 1.55 mrad relative to the fiber axis, for a 400 nm x 9 mm nanofiber waist. Two such fibers were tested successfully in winter and spring 2015. A first similar fiber was not tested under dipole trap conditions, although half a milliwatt of 850 nm light was used regularly for 9 months.

[9] The taper had 3 mrad angle from 125 μm diameter to 40 μm, then 5 mrad until 20 μm followed by an exponential decay (with matched slopes at the 20 μm junction). Two fibers were tested (and consequently broken) in April 2015.

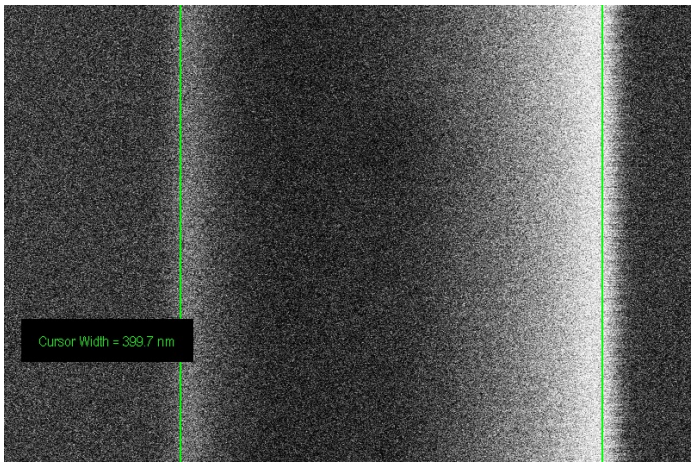

(a) Diameter measurement

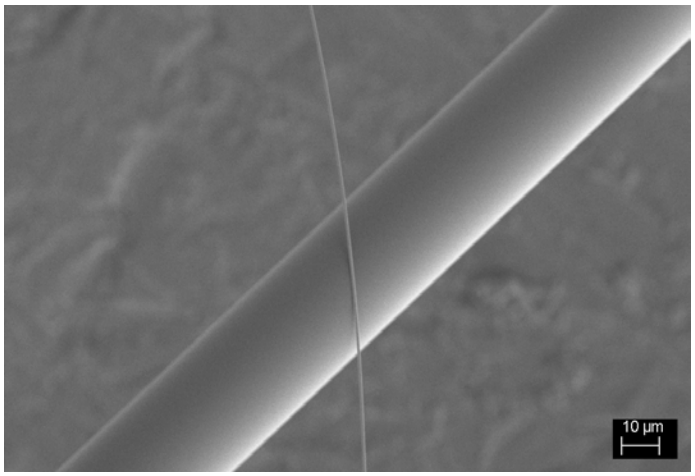

(b) Broken tapered fiber: a thinner part overlaps a thicker part.

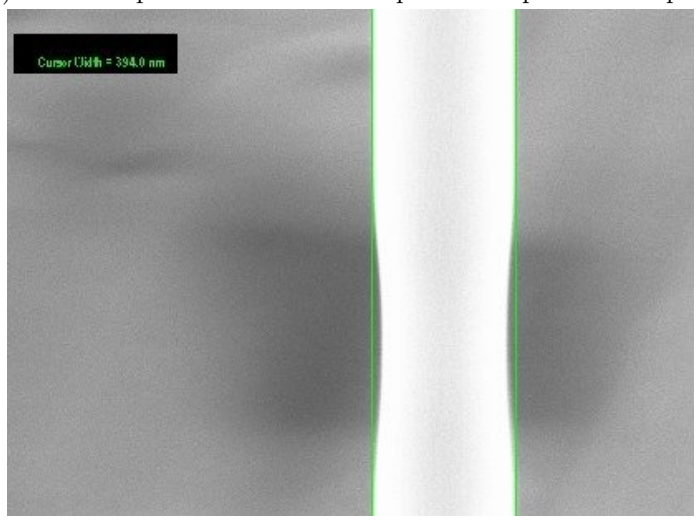

(c) The diameter has been reduced by the electron beam.

Figure 1.15: Scanning electron microscope images obtained with Sébastien Charron using UPMC's SEM platform. The measured fiber diameters usually have the target value with a ±5% accuracy.

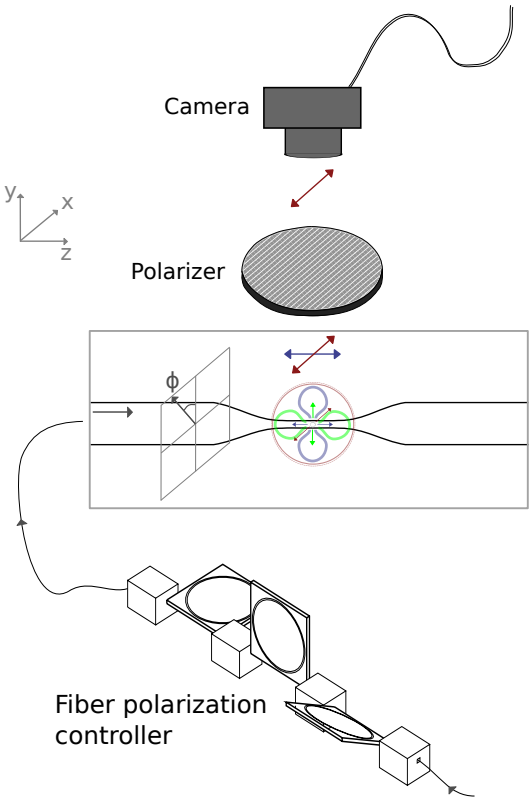

Figure 1.16: Measuring the nanofiber guided polarization. The light scattered by dipole emitters on the nanofiber is collected on a camera on the y-axis. The component oscillating along the fiber axis (z) is filtered out. The collected intensity is minimal (maximal) for $\phi = 0$ ($\phi = \pi/2$): the guided light is quasi-linearly polarized along y-axis (x-axis). Credits: Doris Buu-Sao.

Section summary

We described here the design of a fiber pulling rig used to produce optical nanofibers. The characterized nanofibers match the desired properties. We will soon see that those nanofibers could be inserted and used in a cold atom physics experiment. But beforehand, the next section will focus briefly on the following experimental need: setting up of the polarization of a nanofiber-guided beam.

1.3 Setting the polarization of a nanofiber-guided light beam

Aligning the polarization degree of freedom of a nanofiber guided mode (see subsection 1.1.2) is not a trivial task. Indeed, the commercial fibers used for fabrication of the nanofiber are not polarization maintaining[10]. For a given input in the fiber, the

[10]This mostly because the rotational invariant, non-polarization maintaining fibers are simpler to describe and understand. But pulling nanofibers from highly birefringent fibers -such as PM fibers- would produce nanofiber of interesting characteristics with possible applications in non-linear optics.

polarization state in the nanofiber depends strongly on the birefringence of the whole fiber. This birefringence, sensitive to how the fiber is bent and to its temperature, is compensated using either "bat ears" fiber polarization controllers[11] or wave-plates at the fiber input.

The polarization in the fiber is measured with the method described in [Vetsch12, Goban12] and illustrated in Figure 1.16. The light scattered from imperfections on the nanofiber in a direction orthogonal to the fiber axis (the y-axis) is filtered by a polarizer and collected by a camera. Hundred of micro-watts guided through the nanofiber are necessary in our setup to obtain a significant signal.

The scatterers are supposed to be dipole Rayleigh emitters: the scattered light preserves the polarization and no light is scattered into the direction of a linearly polarized excitation. When filtering out the longitudinal polarization (parallel to the fiber axis z) we can measure the light scattered by the transversal part of the HE_{11} mode. If the guided light is quasi-linearly polarized along the y direction of the camera, the collected intensity is at a minimum. It is at a maximum for light quasi-linearly polarized along x. The major component of the collected intensity is in $\sin^2(\phi)$ where ϕ is the mode orientation angle relative to the camera axis. Finding those extrema easily allows to setup the guided light to quasi-linearly polarized along the y-camera axis or the orthogonal x-axis. Setting an arbitrary polarization state, such at quasi-circularly polarized modes or modes quasi-linearly polarized along another direction would require to monitor the Rayleigh scattering in two different directions.

[11] Thorlabs FPC030

Chapter Conclusion

In this first chapter, we introduced optical nanofibers and focused on the following points:

- The properties of propagation in an optical nanofiber. When the fiber is small enough, only the fundamental HE_{11} propagates with a significant fraction of power in the evanescent field. It has a complex polarization pattern: the polarization is elliptic in general and varies at a subwavelength scale.
- The fabrication of nanofibers. We implemented the flame brushing technique: a standard fiber is pulled while heated by a clean flame with variable effective width. We obtain fiber tapers with high overall transmission. The nanofiber waist is a centimeter long with a 400 nm diameter, optimal for resonant interaction with cesium atoms in the vicinity ($\lambda = 852$ nm).
- Controlling the polarization of nanofiber guided light. Because the birefringence in optical fibers depends on bending and temperature, the polarization state in the nanofiber is *a priori* unknown for a given polarization at the fiber input. It can be measured though via the analysis of the Rayleigh scattered light from the nanofiber waist.

In the next chapter I will report how we introduced nanofibers in a cold atom physics experiment and how we obtained interactions between nanofiber-guided light and the surrounding atoms.

Chapter 2

A nanofiber in a cold atom physics experiment

We began this thesis with the description of the first important tool of our experiment: the optical nanofibers. The second tool, more traditional in our team, are cold atomic ensembles which are prepared with two key ingredients: a gas of the atomic species of interest is isolated in a high vacuum environment - this is the subject of a first section of this chapter -, it is then manipulated with lasers, as presented in a second section. Figure 2.1 is a picture of the lab with all these elements together. It shows the nanofiber production setup, the vacuum system, and part of the laser system. In the last section, I will report a first experimental evidence of those tools working together: the resonant interaction between a nanofiber-guided light beam and cold atoms in its vicinity.

2.1 The vacuum system and the transfer of a nanofiber into vacuum

The central element of the cold-atom-physics experiment is the main vacuum chamber. A set of anti-reflection coated windows provides optical access to its center, enabling light mediated atomic manipulation. The chamber is connected with pipes and valves to the pumping system and to the other components.

The quality of a vacuum system is quantified usually with its residual pressure. Here, the goal is to work in the so-called ultra-high vacuum regime (UHV), where the residual pressure is smaller than 10^{-8} mbar or Torr[1]. This is possible using an ion pump which ionizes and collects the molecules of the residual gas. However this type of pump cannot work with sufficient lifetime at ambient pressure. This is why a first pumping stage is performed using a turbo-molecular pump[2] based on a high speed and

[1] The Torr, named after the inventor of the barometer Evangelista Torriceli, is a commonly used pressure unit in the context of vacuum systems. It is equal to 1/760 of an atmosphere (1,01325 bar), very close to the historical millimeter of mercury. A Torr has the same order of magnitude than a millibar (or the French *hectopascal*), hence the oral habit to quantify a vacuum quality as 10^{-N} without mentioning the units.

[2] HiCube 80 Eco from Pfeiffer Vacuum

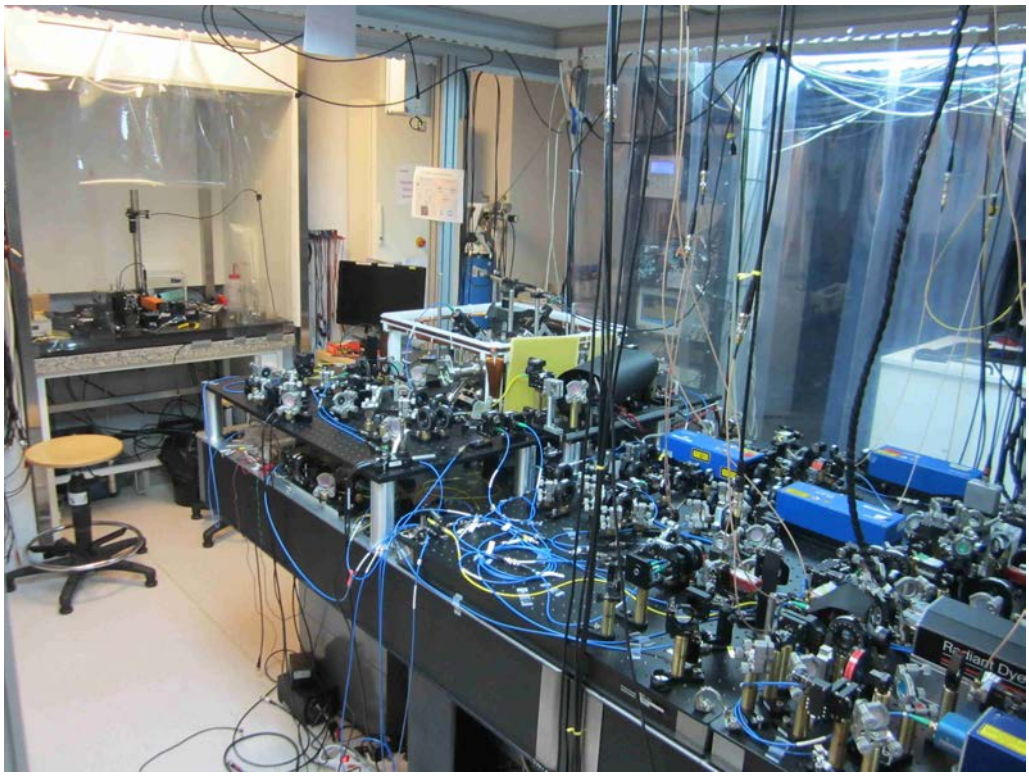

Figure 2.1: General view of the experimental setup. On the left is the nanofiber production rig (section 1.2) under its clean-air laminar flow box. Very close in front of it, in the center of this image, is the main vacuum chamber (section 2.1) surrounded by coils and optical elements. On the right is part of the laser system used for atomic manipulation (section 2.2) and guided to the vacuum chamber with optical fibers (blue and yellow jackets).

oil-free rotor ejecting the molecules from the vacuum system. This first pumping stage allows to reach pressures lower than 10^{-6} mbar. Once this pressure is reached, a valve is closed in order to isolate hermetically the vacuum system and the ion pump is then started.

The main limiting factor of high-vacuum systems is the gas emitted continuously by all the components (*outgassing*). When designing the parts, any trapped air volume (e.g. a screw in a dead-end threaded hole) should be avoided. The total surface exposed to vacuum should be as small as possible and the components cleaned carefully. The standard cleaning procedure is done using ultrasound baths in different solvents: soapy water, normal water, acetone and high-purity isopropyl alcohol[3]. They are then stored in oil-free aluminum foils. Ideally, the components are also *baked*: they are heated in a vacuum environment such that most of the outgassing occurs at a higher rate, diminishing the outgassing rate when going back to room temperature. Some materials, such as stainless steel, are preferred because of their lower outgassing

[3]Most of our parts where supposed to be already UHV clean and were thus cleaned only in isopropyl alcohol.

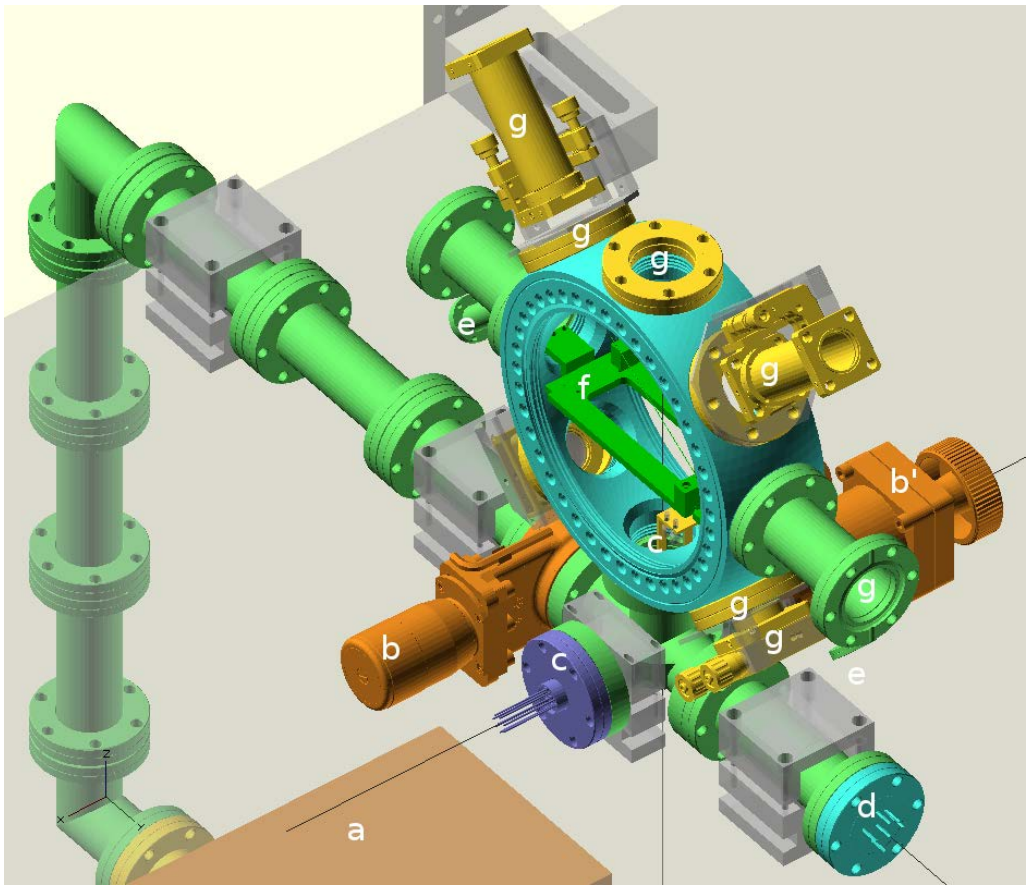

Figure 2.2: Part of the 3D design of the experiment including most of the vacuum components. **a**: ion pump, **b**: valve to ion pump, **b'**: valve to turbopump or nitrogen input, **c**: electrical feedthrough and dispensers connectors and holders, **d**: ion gauge, **e**: fiber outputs, **f**: fiber holder, **g**: some view-ports and some optical elements (collimation packages). Designed with OpenSCAD.

rate, the possibility to clean them efficiently and to bake them at high temperature. They should be used with smooth surface quality to reduce the effective surface area. Other materials might be chosen for magnetic-field-sensitive experiments, or when non-conducting materials are required (e.g. Teflon or ceramics). The standard high-vacuum components are hermetically connected with the so-called CF flanges (ConFlat): a circular copper gasket is squeezed evenly between the "knife edges" of the two CF components.

2.1.1 A "breakable" vacuum system

The whole vacuum setup should be designed properly before assembling. All the necessary tools and components should be gathered and cleaned and all decisions should be made in order to lower the risk of mistake or contamination.

Figure 2.2 shows part of a 3D design of the experiment[4]. The ion pump is rather far from the central chamber and shielded with μ-metal[5] in order the minimize the effects of its strong magnetic field on the experiment. However this distance makes more difficult the efficient pumping of the vacuum system[6]. Here, the whole setup is clamped on a vibration damped optical table. The ion pump is actually under this table. The clamping is also something that should be thought carefully before assembling, especially because the whole vacuum system is rather heavy and uneasy to handle.

This particular setup was designed with the idea that we should be able to transfer a nanofiber in the main chamber easily, and ideally to change the nanofiber on a regular basis. This means that the vacuum has to be "broken" and "rebuilt" efficiently. Because of this, two valves are used. One is separating the main chamber from the ion pump, as close to the chamber as possible, such that a volume including the ion pump can be isolated from the rest, and stay under high-vacuum conditions even when the main chamber is under ambient pressure. The other valve is separating the chamber from a connection used for two different reasons. It is first used as a nitrogen input: when "breaking" the vacuum, a constant and clean nitrogen flow is maintained at this input such that ideally nothing else than nitrogen enters the chamber. It is thus kept as clean as possible, and is more easily re-pumped to high-vacuum conditions. The other use of this connection is for the turbo-pump during the first pumping stage. Once a nanofiber is ready in high-vacuum conditions, this second valve is closed and the ion pump valve re-opened.

In the previous experiment of the group, a chamber made almost only of glass was chosen to avoid issues with magnetic fields (especially eddy currents). Here however, we use a stainless steel chamber for simplicity. The windows are independent components connected with CF flanges and anti-reflection coated on both sides (for 852 nm)[7]. The front large window can be removed to open the chamber and insert a nanofiber in the center.

2.1.2 The cesium dispensers

Figure 2.3 is a picture showing the center of the vacuum system through the front window. In the bottom one can see the two cesium dispensers[8]. They are composed of a cesium chromate (Cs_2CrO_4) mixed with a reducing agent. Heating this mixture to

[4]Because of the complexity of the experiment, the presence of many home-made parts and the need for optimized optical access, I found useful here to make a 3D computer model of the whole setup, including the surrounding parts of the experiment. For this, a very convenient tool was OpenSCAD, a free scripting language and software for 3D designs commonly used in the 3D-printing community. I used it for designing my own parts as well as importing files from manufacturers and arranging them together.

[5]A two-layer shield manufactured by Phynixs according to the design already described in [Giner13b] A.5.

[6]In our setup, we expect a conductance of only a few liters per second between the ion pump and the vacuum chamber. Our ion pump (Vacion Plus 40 Starcell from Agilent Technologies) with nominal speed of 40 L/s will thus not be the limiting factor.

[7]Torr Scientific Ltd.'s BVPZ38VAR-NM (smaller windows) and BVPZ150VAR-NM-45DEG (large windows).

[8]*SAES getters* Cs/NG/3.9/12FT10 alkali metal dispenser, containing 3.9 mg of cesium

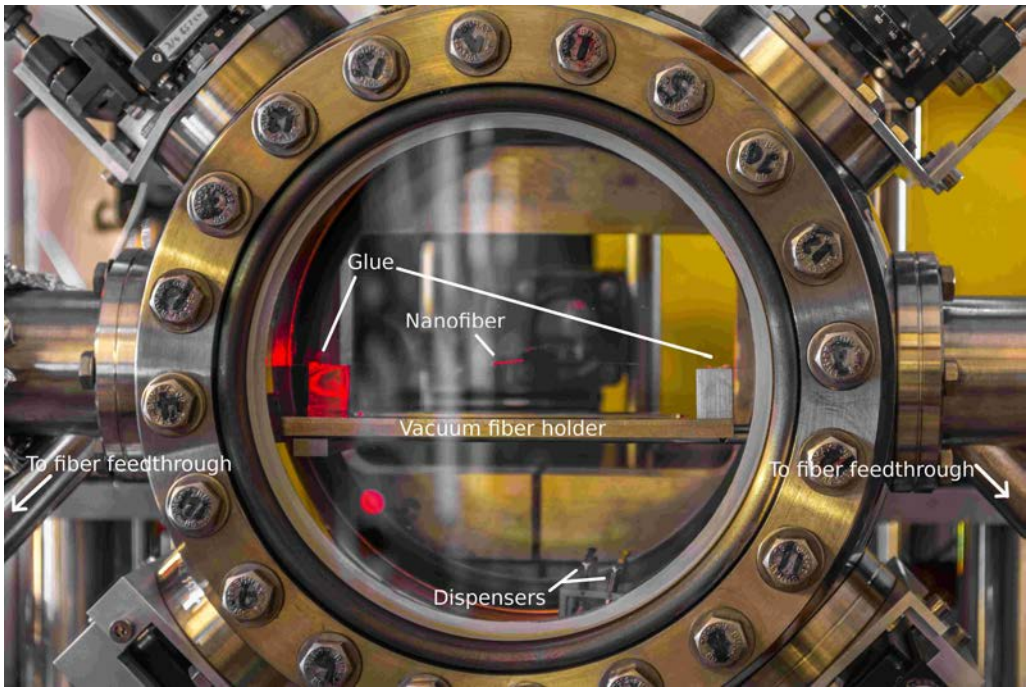

Figure 2.3: An optical nanofiber in the high-vacuum chamber. The nanofiber is scattering the red guided light. Part of this light is also escaping the fiber and illuminating the left part of the chamber. The fiber is glued on its holder and goes outside vacuum through the smaller pipes on both sides. The cesium dispensers can be seen as well at the bottom of this picture.

about 500 °C reduces the chromate and releases cesium atoms in the vacuum chamber. The mixture is packaged with two conductive terminals such that it can be heated using Joule effect when applying an electric current of a few amperes (the total resistance is less than 0.1Ω). A small slit in the package allows the cesium to escape in the vacuum chamber. The flow of released cesium can be conveniently controlled by adjusting the current via the electric connections provided by in-vacuum copper wires and a commercial UHV electrical feedthrough[9]. In our setup, their position close to the large window allows to change the dispensers whenever opening the chamber for a new nanofiber. Their proximity to the center of the chamber means that the cesium can travel directly to the center. A significant part can therefore be captured for the experiment. However, this also means that cold atoms in our traps might have limited lifetime because of the collisions with these hot cesium atoms. The reducing agent of the dispenser (the alloy St101: Zr 84% Al 16%) was chosen for its "getter" properties: it absorbs the different gases produced for a better purity of the released cesium. The dispensers can optionally be baked during the turbopumping step by applying a 2.5 A for 30 min[10]. For a longer lifetime, the dispenser containers are sealed with dry

[9]The dispensers terminal are folded in two with pliers and inserted in Lesker's FTASSC040 set-screw connectors.

[10]The point here is to get rid of some possible humidity or other impurities. The cesium starts to be released at about 4 A.

nitrogen[11].

2.1.3 The vacuum fiber holder

The nanofiber can be seen in the center of Figure 2.3. After the tapered region, on the acrylate coated part, its two tails are glued on the vacuum fiber holder. This holder was designed such that there is optical access for a light beam propagating in free-space along an axis as parallel as possible[12] to the nanofiber. After fabrication, the nanofiber is glued on the holder outside the chamber with UVH compatible ultraviolet curing glue[13]. It is then transfered in the center of the vacuum chamber.

2.1.4 The vacuum fiber feedthroughs

The two tails are fed outside vacuum with a very convenient technique involving Swagelok gas connectors[14]. One of the two metallic rings of the connector is replaced with a home-made Teflon part in which a hole slightly larger than the coated fiber has been drilled. After having passed the fiber through this hole the Teflon is squeezed around the fiber using the Swagelok nut. This system has been described in [Abraham98] and is used in many experiments involving optical fibers and vacuum. In our setup, the Teflon parts have been designed and tested by Kevin Makles (optomechanics team) and fabricated by Arnaud Leclercq (LKB's mechanical workshop). The result is a leak-free system working well enough in UVH conditions. Images and dimensions of the feedthrough are shown in Figure 2.4. Note that the elasticity of Teflon leads to significant fabrication imprecision on the dimensions, although this has never induced leaks in our nanofiber setup. Starting the nut rotation on the thread remains tricky and requires some training in our setup. The nut usually has to be pushed in order to pre-squeeze the Teflon part, which is risky and uneasy (recall there is also an optical fiber that you cannot afford to break). For now, we do this using an adjustable wrench and a fixed pivot point on the table. The next step is to tighten the nut. This is done with a wrench, of about 10 cm length. The nut has to be tightened for a few turns to avoid leaks: a very small torque is needed and the tightening should be stopped when the nut starts to resist against the imposed rotation. Screwing it further would induce optical loss in the fiber.

2.1.5 Transferring a nanofiber into vacuum

Producing a nanofiber and transferring it into vacuum is something that has to be prepared carefully. The full protocol is written beforehand and discussed with the whole team taking part in the task (ideally three persons). A stripped copy of the protocol we have been using is given in Appendix C. I will summarize here the main

[11] Although in my experience, dispensers from outdated box could be used with no issue, even if the boxes were opened and stored without specific care.

[12] Here with an angle of about 15°. Note that due to the stress imposed by the two tapered regions, an uncontrolled angle is added to the nanofiber during the fabrication process. This is visible on Figure 2.3: the whole fiber is not a single straight line.

[13] Dymax OP-67-LS

[14] Lesker F0133X2SWG including 1/8" Swagelok fittings

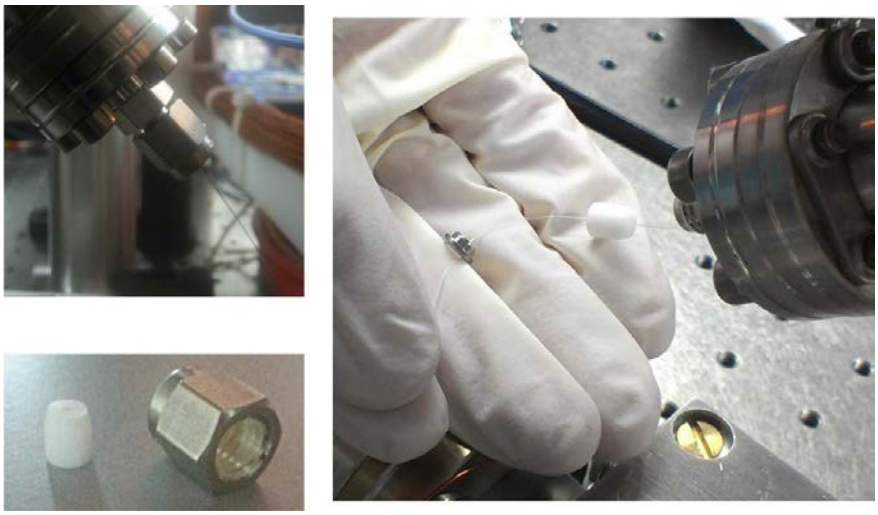

(a) Fiber feedthrough images. Top-left: the whole tightened feedthrough. Bottom left: the Teflon part and the nut. Right: all the feedthrough elements except the nut ready for assembling.

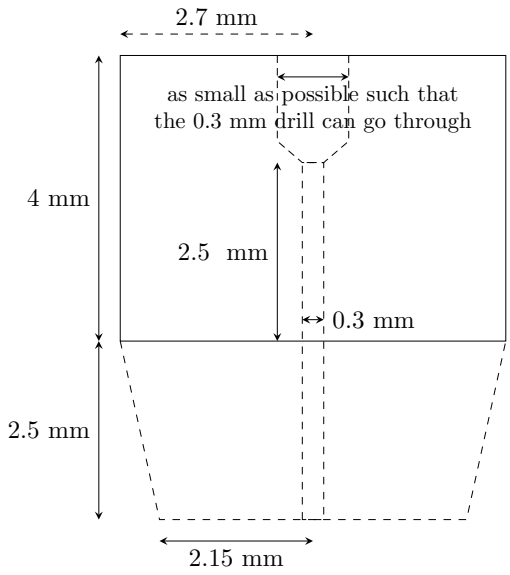

(b) Teflon part dimensions

Figure 2.4: Images and drawings of the vacuum fiber feedthrough.

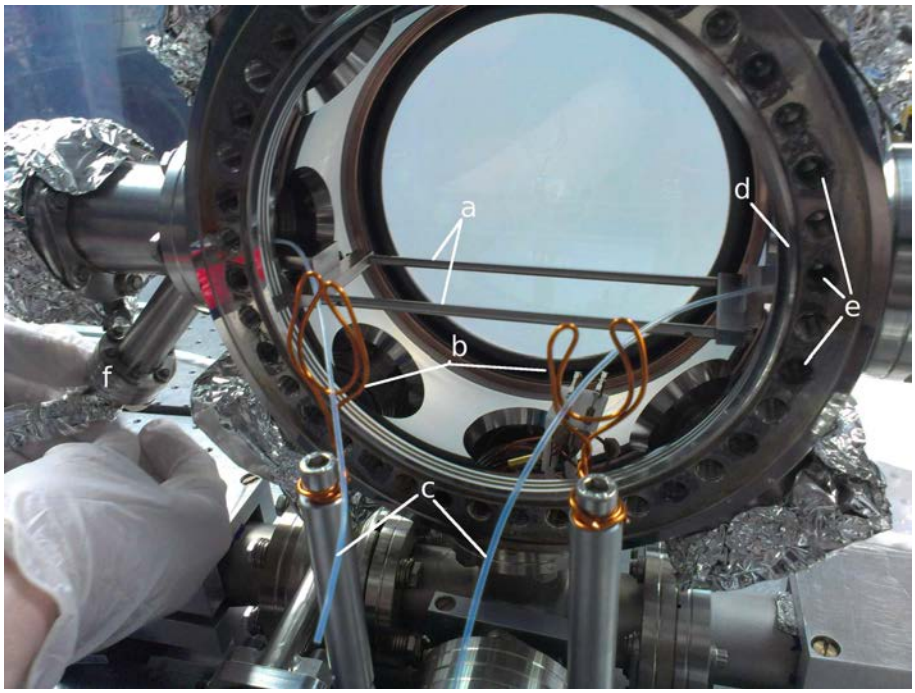

Figure 2.5: The vacuum chamber, ready for fiber installation. The labels correspond to **a**: the rails on which the fiber holder will be clamped; **b**: the fiber guides, i.e. two clean copper wires on which the loose fiber tails will rest away from the grease; **c**: the sheaths, plastic tubes used to guide the fiber tails towards the swagelok outputs; **d**: the front window CF knife-edge; **e**: greasy CF threaded holes; and **f**: the swagelok fiber feedthroughs.

ideas. It has been used in the team repeatedly since 2014 and proved to be efficient and rather fast ($\sim$ half a day) after some training. There are a few tricky points remaining, but the only cause of failure in our group until now (summer 2015) seems to come from the nanofiber fabrication process as mentioned in paragraph 1.2.4[15].

We proceed in the following way. During a first part of the transfer, while someone is making a nanofiber and preparing it[16], one or two persons are "breaking" the vacuum, opening the front large window and preparing the vacuum chamber for reception of the nanofiber (Figure 2.5). Once both the nanofiber and the vacuum are ready, the fiber is actually transferred into the vacuum chamber. The fabrication rig and the vacuum chamber are intentionally in front of each other, both of them under clean-air laminar flows, in order to make this transfer as easy as possible and to avoid that any dust gets deposited on the nanofiber. One of the participants grabs the fiber holder and moves it directly (via a translation) into the vacuum chamber. At the same time, each of the

[15]For a given brushing trajectory of the fabrication stages, the fiber would break when powerful (mW) laser beams are shined through the nanofiber already in high-vacuum conditions. This was never the case for the other tested trajectory.

[16]After fabrication, some tension is added to the nanofiber, it is then glued on the fiber holder and ready for transfer. The transmission through the fiber is monitored continuously, including during all the installation stages and afterwards.

two other persons are responsible for handling each of the two fiber tails: the first tail being connected to the laser input, the other one to a detector (which is moved along with the fiber). At this point, the nanofiber is inside the vacuum chamber but both tails come out from the front window rather than from the two swagelok connectors on the side. Because they should be kept clean (there is grease all around the CF knife-edge of the front window at this point), they rest on two U-shaped copper wires ("fiber guides") in front of the window as can be seen in Figure 2.5. The two loose fiber tails are then passed through two plastic tubes (the "sheaths"[17]) going from the large window to the swagelok connectors. These tubes were placed there prior to the transfer (see Figure 2.5). The fiber can now be pulled through the swagelok connectors, the sheaths pulled away and the fiber feedthrough pre-tightened. It is now time to close the window and start to pump again the vacuum system.

All this is done while keeping as much as possible track of the transmission through the fiber, the main factor of uncertainty being the reproducibility of fiber to fiber connections using bare fiber connectors, or splicing two fibers together.

2.1.6 Detecting leaks

Before using the regular turbopump, and even before tightening the fiber feedthrough, a leak detection system can be used: it consists of a turbopump associated with a mass spectrometer measuring the quantity of helium pumped out from the vacuum system. One can release a small quantity of helium close to the vacuum system to identify the position of the possible leaks[18].

After turbo-pumping for half a day, switching to ion pump, and waiting a few more days, the nanofiber is ready for use in a cold atom physics experiment. The typical residual pressure we obtain is close to 10^{-8} mbar. It can be estimated from the ion pump current, or from the ion gauge placed close to the main chamber.

2.2 Manipulating atoms with lasers

We have seen in the previous section how a vacuum environment was prepared for the atomic species of interest, cesium. In this section, I will give a brief introduction on how atoms can be manipulated with electromagnetic fields. The example I will give is the magneto-optical trap for cesium, which is the essential step to prepare a cold atomic cloud in our experiment. Much more details about atom-field interactions and their applications can easily be found elsewhere (e.g. in Daniel A. Steck's documents [Steck]). I will give more theoretical details for the particular case of electro-magnetically induced transparency (EIT) in the next chapter. Also, recall that the particular MOT setup I will describe is very close to the previous setup of the team, which has been described in much details by former members [Scherman12, Giner13b, Veissier13, Nicolas14].

[17] We use here the inner tube of FT030 optical fiber jackets from Thorlabs.

[18] If there is a leak, some helium will be detected by the leak detection system. In our system, this was useful to detect leaks from damaged seals of glass windows. The fiber feedthrough has always been leak-free thanks to Kevin Makles' successful design

2.2.1 Some general ideas on atom/electro-magnetic field interaction

The properties of an isolated atom are well described by the electro-magnetic interaction between its nucleus and its electrons. The Hamiltonian of the system gives rise to a set of bounded and unbounded eigenstates with well defined wave-functions and energies. The probability amplitudes of an atom in a superposition of these eigenstates oscillate relative to each other at the Bohr frequencies: the energy differences between two levels divided by the universal Planck's constant h. Much of atom physics can then be understood as electromagnetic perturbations of those eigenstates.

There are two main regimes. In the first regime the perturbation is oscillating resonantly with these frequencies. This resonant perturbation will induce variations in the populations of the atomic eigenstates. Most of section 2.3 and chapter 3 will focus on this kind of interaction between atoms and nanofiber guided light.

In the second regime, the perturbation is static or off-resonance. The main result here is a perturbation to both the eigenstates wave-functions and to their energies. The latter is called a level shift and has many different appellations depending on the nature of the perturbation. The *Stark* shifts correspond to perturbations induced by a static electric field while the *Zeeman* shift is the counterpart for a static magnetic field. Oscillating fields lead to the *ac* Stark[19] or Zeeman shifts. When the perturbation field is spatially varying, the atom experiences a spatially dependent energy, or in other words a conservative force. An off-resonance electric field can thus be used as an atomic trap: the so-called optical dipole trap. The last chapter of this thesis will focus on such a trap based on the off-resonance fields propagating in a nanofiber.

A particular example of both regimes is the interaction between an atom and the many unexcited modes of the quantum electro-magnetic field. This coupling is responsible for the instability of the excited states. They decay to lower energy levels and emit photons with a rate often noted Γ: the spontaneous emission rate. It is also associated with a shift of the energy levels, called Lamb shift for a single atom in an infinite space, or more generally the van der Waals or Casimir-Polder shifts in the presence of matter (such as mirrors, dielectric media, or other atoms).

This section will start from a practical and now very common application of these interactions: Doppler cooling of atoms, and magneto-optical trap (MOT). I will give a brief description of the cesium atom structure, and then describe how we implemented a MOT in our nanofiber experiment. Another paragraph will focus on a short description of the laser system we have developed for resonant interaction with cesium.

2.2.2 A magneto-optical trap for cesium

In our experiment, cesium atoms are cooled and gathered around the nanofiber using a magneto-optical trap (MOT) visible in Figure 2.6. The cooling and trapping originates from the radiation pressure from laser beams coming from six orthogonal directions. Because of the Doppler effect, the radiation pressure is velocity dependent. Cooling occurs when the laser beams are red-detuned relative to an atomic transition. The radiation pressure is also position-dependent thanks to a position-dependent magnetic field and the resulting Zeeman shifts. The proper choice of rotating polarizations for

[19] Also called light shifts.

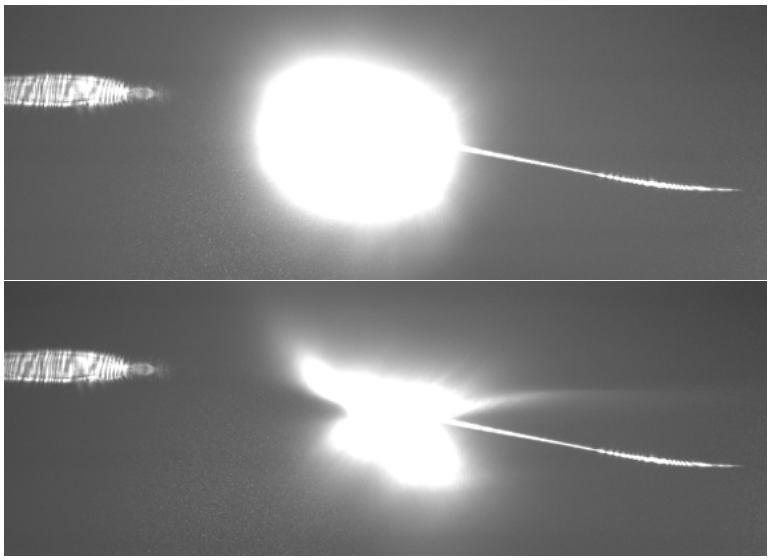

Figure 2.6: Picture of the MOT overlapped with a nanofiber. The continuous atomic scattering from the cooling beams can be imaged directly on a camera and gives an idea of the cloud's shape. In the bottom picture, resonant light (a few microwatts) was sent through the nanofiber, disturbing the cloud and changing its shape.

the laser beams results in a trapping potential.

The magnetic field is produced by a pair of identical coils symmetrically placed on both sides of the vacuum chamber, with currents rotating in opposite directions. This "anti-Helmholtz" configuration leads to a null magnetic field in the center and gradients in all directions. Details about the coils design are given in section B.2. We use rectangular coils, elongated in a direction parallel the fiber, in order to obtain a cigar shaped cloud with larger overlap with the nanofiber. This will be important for our memory experiments (chapter 3).

The spectroscopic structure of the cesium D_2 line [Steck98] is shown in Figure 2.7. In our experiment, only this line is used for resonant or close to resonance interaction. The two $6S_{1/2}$ states are long lived, while the excited states decay via spontaneous emission at the rate $\Gamma/2\pi = 5.23$ MHz. Another resonance (the D_1 line) occurs at 894.6 nm.

Our MOT is implemented using beams 10 MHz red-detuned from the cyclic $\{6S_{1/2},F=4\} \rightarrow \{6P_{3/2},F=5\}$ transition ($\sim$ 25 mW in each beam of $\sim$ 1 inch diameter). Four additional beams on the $\{6P_{3/2},F=3\} \rightarrow \{6P_{3/2},F=4\}$ transition are used as repumpers: any atom accidentally falling in the $F=3$ ground state will be rapidly pumped back in the trapped $F=4$ state ($\sim$ 3 mW in each beam of $\sim$ 1 inch diameter).

Instead of using 6 independent cooling beams, 3 beams are generated (2 of them are mixed with the repumping beams), collimated through the chamber and retro-reflected at the opposite side of the vacuum chamber (Figure 2.8). The collimator packages use convex lenses with 76.6 mm focal length. They are mounted on a Thorlabs orientable "cage system" together with a quarter waveplate aligned to produce the

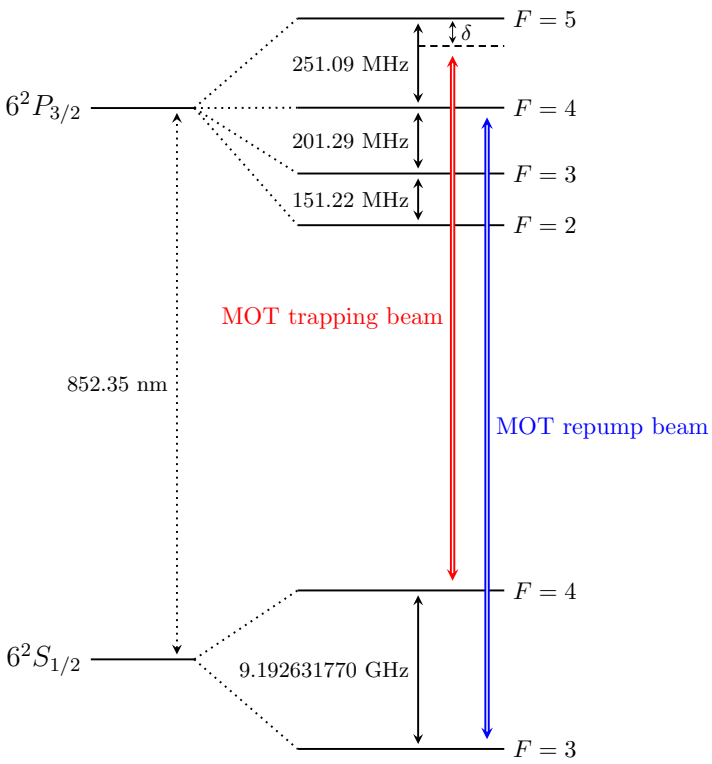

Figure 2.7: The D_2 line spectroscopic structure of cesium atoms, and the transitions used for the MOT implementation. The trapping beams are red-detuned by 10 MHz relative to $\{6S_{1/2}, F = 4\} \rightarrow \{6P_{3/2}, F = 5\}$ transition.

proper circular polarization. The retro-reflection package are composed of a mirror and another quarter waveplate as required to preserve the polarization relatively to the propagation direction.

2.2.3 Laser system

The laser beams[20] on the D_2 line are produced with two different kind of lasers: a set of extended cavity diode lasers ($\sim$ 50 mW each) and a Ti:sapphire laser ($\sim$ 2 W). Each laser output is followed by an optical isolator and the different beams are divided, prepared and handled with a series of techniques summarized below and illustrated in Figure 2.9. All the challenge here is to obtain all the required beams with enough power, frequency tunability, and long-term stability (power is costly and every optical element induces losses that might be highly sensitive to alignment, focusing or polarization).

Saturated absorption spectroscopy – Spectroscopic measurements of a room temperature cesium cloud (contained in a glass cell) allows to measure and control the

[20] Although I mentioned only two particular transitions used for the MOT until now, we will see that many other configurations of beams on the D_2 line are used throughout this thesis.

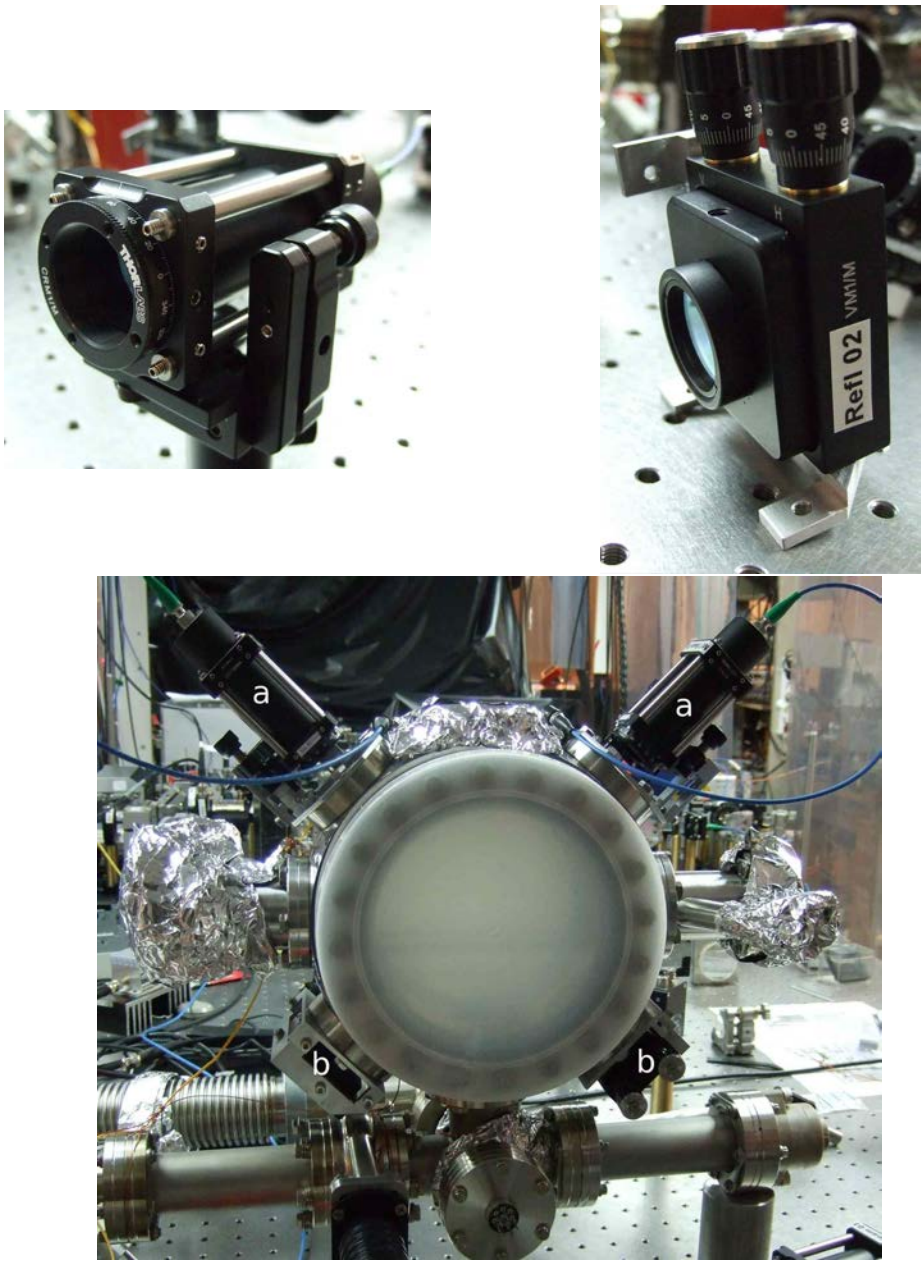

Figure 2.8: Collimation (top-left and bottom **a**) and retro-reflection packages (top-right and bottom **b**) for the MOT beams. The collimation package is composed of a fiber connector, a lens and a quarter waveplate. The retro-reflection package is composed of a quarter waveplate and a mirror. Both are on orientable mounts.

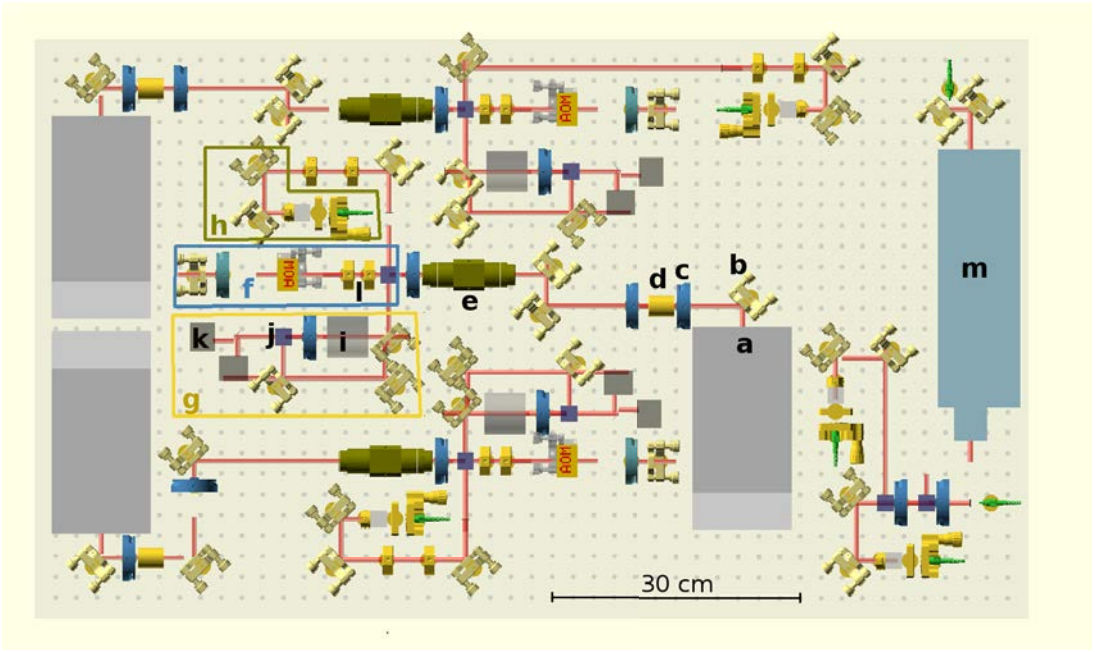

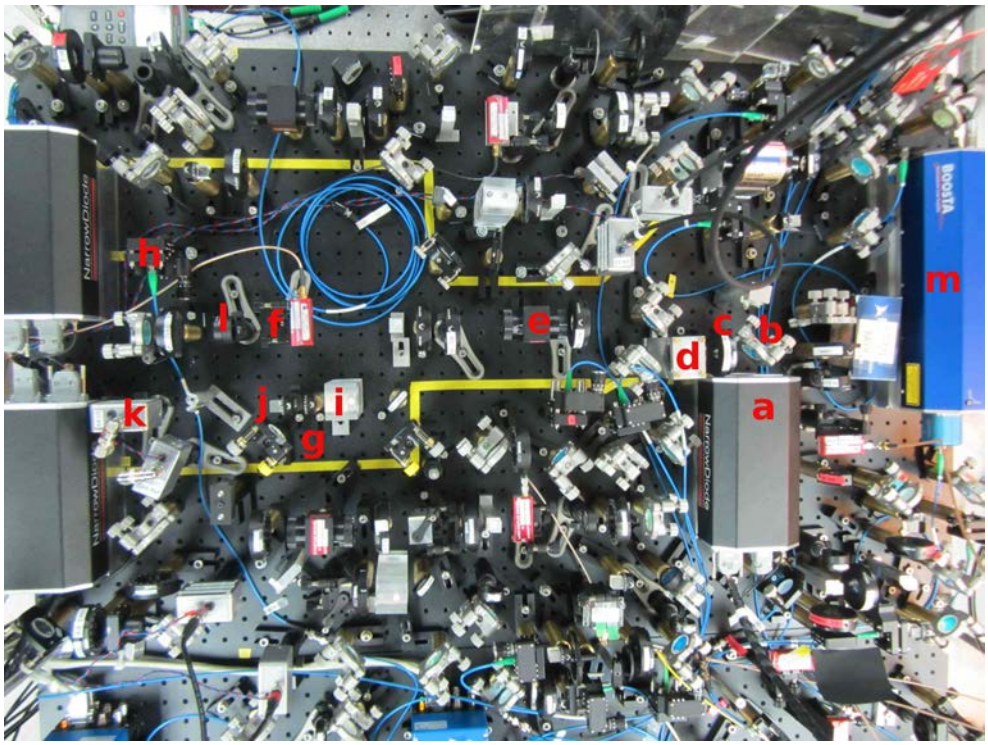

Figure 2.9: Images of the optical table arrangement for 3 laser diodes and a tapered amplifier. On top are the initial 3D drawings, very useful for a compact design. Below is a photo of the implementation, more optical paths have been finally added. The annotations corresponds to: **a**. extended cavity laser diode, **b**. mirror mount, **c**. waveplate mount, **d**. prism pair, **e**. optical isolator, **f**. double pass AOM, **g**. saturated absorption setup, **h**. optical fiber coupling setup, **i**. room temperature cesium cell, **j**. polarizing beam splitter cube, **k**. detector, **l**. lenses, **m**. tapered amplifier.

laser beam frequency. The hyperfine structure of the excited state (the states with different F value) is resolved using the common saturated absorption technique[21].

The laser frequency is then locked with frequency modulation (of the beam used for the spectroscopy) and feedback on the laser. The modulation can be produced by directly modulating the laser. We typically modulate the current of our laser diodes. However this modulation will be present on all the beams derived from this laser. On our Ti:sapphire laser, the modulation is induced by a double-pass AOM (see below) placed on the spectroscopic beam path before the saturated absorption setup (all the other beams derived from this laser are modulation free).

The locked-laser linewidths using these techniques are typically a few MHz with our laser diodes and tens of kHz with the Ti:sapphire laser. The laser diodes are broadened by the use of a high modulation amplitude. The low visibility of the peaks chosen in the saturated absorption signal made this amplitude necessary for locking so far. The laser used for our MOT cooling beams for example is locked on the $F = 4 \rightarrow F' = \{3,5\}$ crossover, very close to the $F = 4 \rightarrow F' = 4$ peak. It is largely broadened to a 5 MHz width, measured with 10 kHz resolution by spectral analysis of the interference with a Ti:sapphire laser.

Phase locking – Another technique used for tuning and controlling a laser frequency is the so-called phase locking technique. The beat-note obtained when overlapping a reference laser (already locked with the technique described above) and the laser of interest is measured and locked to the desired offset. The beat-note, possibly after performing a division of the beat-note frequency, is compared to the signal generated by a stable electronic oscillator.

This technique is especially useful when considering atomic Raman resonances with two lasers, such as for our EIT experiments described in chapter 3. In this case, the frequency difference between the lasers is an important parameter given directly by the beat-note frequency. Using a phase locking system, the width of the beat-note can get much smaller (at the Hertz level) than the two individual lasers linewidths.

The technique is also very handy for changing dynamically the frequency of a laser beam (by changing the frequency of the reference electronic oscillator), without significant change in e.g. the beam power. We used both a home-made and a commercial[22] phase-locking system, both compatible (including the optical detector) with the high frequency required for addressing the ground state hyperfine splitting of cesium (9.2 GHz). An example of the beatnote spectrum obtained when using the commercial

[21] Doppler broadening at room temperature would prevent to resolve these different states with a simple probing scheme. Instead, in addition to the relatively weak probe beam, a counter-propagating and relatively intense beam is sent through the cell (for cesium the saturation intensity is a few mW/cm^2). Although the two beams have the same frequency, they do not address the same atoms because of the velocity dependent Doppler shift. The probe beam is thus absorbed in general, if the laser frequency is already less than a Doppler width away from resonance. However for specific velocities and laser frequencies, both beams address the same atoms. For example when the laser is at resonance, both beams address the atoms whose velocity is perpendicular to the propagation axis. Absorption of the probe beam is thus canceled by the saturation induced by the counter-propagating beam. This induces a peak when scanning the laser frequency whose width can be close the natural linewidth Γ.

[22] Vescent photonics D2-135.

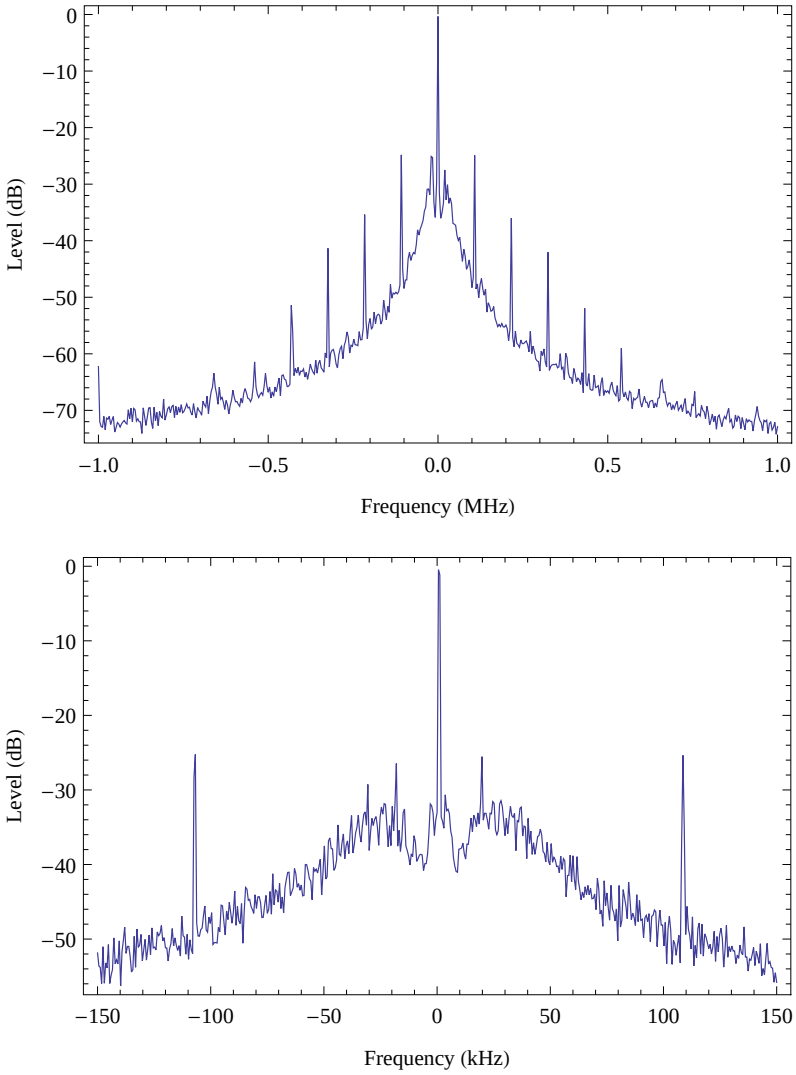

Figure 2.10: Locked beatnote of a laser diode and a Ti:sapphire observed on a spectrum analyzer. The D2-135 electronics frequency-divides by two the signal before analysis. The graphs shows the result for different plotting range and a 300 Hz resolution. They are both centered on the beatnote carrier frequency, here 4420.8 MHz.

system is displayed in Figure 2.10.

Acousto-optic modulators (AOM) – Another tool commonly used is the acousto-optic modulator. Both the optical beam and an acoustic wave propagate through a medium in approximatively orthogonal directions. The acoustic wave induces Bragg diffraction in well-defined directions[23], as well as a frequency shift of the beam corre-

[23]More than 80% of the input power can typically be obtained in the first order of diffraction with fine alignment of the angle of incidence and of the beam size.

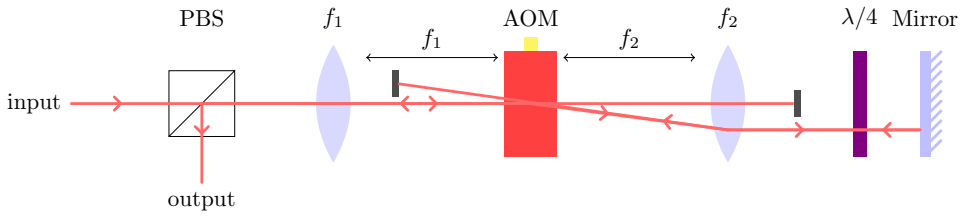

Figure 2.11: Double-pass AOM. Different lenses arrangement can be used. f_1 can be removed for example: the beam will be collimated in the AOM and focused by a lens f_2 on the mirror (which should be at a distance f_2 from the lens). Focusing in the center of the AOM as proposed in the drawing allows faster switching but can be an issue when dealing with high input powers.

sponding to a integer multiple of the acoustic-wave frequency.

We use AOMs for modulating both the laser beam intensity and frequency. Both modulations can be obtained by modulating the input electronic signal generating the acoustic wave. The two most common applications in our setup are switching on/off a laser beam at relatively high speed (tens of nanoseconds, or even faster for beams strongly focused in the AOM), and shifting the beam frequency from the locking spectroscopic line.

We generally use AOMs in a double-pass setup. After passing through the AOM a first time, the beam is retro-reflected and experiences a second diffraction and frequency shift. With an ingenious use of polarization optics and lenses (Figure 2.11), the output beam propagation axis is independent from the AOM driving frequency. This setup thus allows dynamic tuning of the laser beam frequency with relatively small change on the beam power and alignment. Using a 110 MHz centered AOM (AA optics MT110-B50A1-IR), we achieve less than 50% power variations when tuning the output over a 100 MHz range.

Tapered amplifier – In order to obtain the desired power for the MOT trapping beams from one of the laser diodes, we use a commercial tapered amplifier (Toptica's BoosTA) injected with 15 mW and giving slightly more than 400 mW after coupling into a single-mode fiber. The timing for the trapping beams is done with a double-pass AOM after amplification.

Optical fibers – Most of the laser beams are coupled into single-mode optical fibers. This allows to route them to different places in the lab, including towards the vacuum system. It also allows to mix them using fibered beam splitters and to decouple the alignment of different parts of the optical system.

The coupling is obtained by focusing the beams into the core of the fibers, with precise alignment of the propagation axis using a pair of 45° incidence mirrors mounted on kinematic mirror mounts. Single-mode fibers are also responsible for defining a stable circularly symmetric mode function. The rather unclean output from the laser diodes is filtered by the fibers, its shape is adapted with prism pairs and cylindrical lenses for optimal coupling efficiency in the fibers. The polarization stability is harder

to reach when using optical fiber. We commonly use polarization maintaining fibers[24] for this purpose, although this requires a very careful alignment of polarization at the fiber input[25]. For fiber coupling and routing of the beams, we use fibers sold with connectors at both outputs. This allows to easily connect two fibers, although connecting and disconnecting the many fibers might be the most serious source of irreproducibility in our setup (the connectors can easily get scratched or dirty).

Section summary

In the first part of this chapter, we described most of the experimental setup and tools that will be used in the rest of this thesis. The nanofibers produced in the first chapter are now suspended at the core of a cold atom setup. This involves a high-vacuum system, and lasers for cooling and trapping cesium atoms.

In the next section, we present the resonant interaction of a nanofiber guided light beam, and cold cesium atoms in the fiber vicinity.

[24] usually provided by Oz Optics Ltd.

[25] This is done by measuring the polarization fluctuations at the output of the fiber.

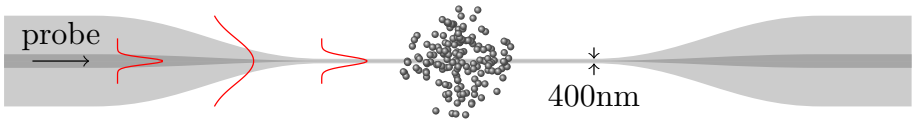

Figure 2.12: Illustration of a cold cesium cloud overlapped with an optical nanofiber. A signal beam can be coupled from a standard fiber to the nanofiber via the tapered region, and interact with the atomic cloud.

2.3 First guided-light/atom cloud interaction evidence

After having detailed how a cold atom cloud was prepared around a nanofiber, I will now describe the first observations and measurements obtained when overlapping a nanofiber and a cold cesium cloud released from a magneto-optical trap.

The results here were obtained with the first nanofiber successfully placed in our vacuum chamber. This was done in March 2014, soon followed by the overlap of a cold atomic cloud with the nanofiber, and by measurements of absorption of resonant light propagating through the fiber and cesium atoms. These first experiments led to the observation of electromagnetically induced transparency and a memory for light in May 2014. After studying different parameters of this setup the detailed results were published in 2015 [Gouraud15].

The nanofiber used here has a diameter of approximately 400 nm over a length of 0.9 cm and was made from Thorlabs SM800-5.6-125 fiber. The symmetric tapered regions have a constant angle shape with 3.1 mrad opening angle. The tapered regions and the nanofiber are 9 cm long overall and thus fit into the vacuum chamber. 11.5% losses for light guided through the fiber was induced by fabrication of the nanofiber and 1.8% more losses were recorded during the transfer into vacuum (they occurred when over-tightening one of the swagelok fiber feedthrough).

2.3.1 Overlapping the MOT and the nanofiber

Atoms in the magneto-optical trap (MOT) can be overlapped with the nanofiber in two different ways. The first (and easiest in a first step) possibility is to use 3 pairs of bias coils in the three orthogonal directions to modify the magnetic field gradient of the MOT, in particular the position where the field cancels. The other possibility is to misalign the MOT laser beams. Both of the methods allow to displace the MOT, though the second method will be preferred since it offers better flexibility on magnetic field manipulation or cancellation for further experiments. The MOT overlap with the fiber is first established while monitoring with cameras in 3 different directions. It is then further optimized by monitoring the absorption of a laser beam through the fiber as described in the next paragraph and illustrated in Figure 2.12. Note that the MOT cloud is typically a few millimeters long, thus a little shorter here than the nanofiber waist.

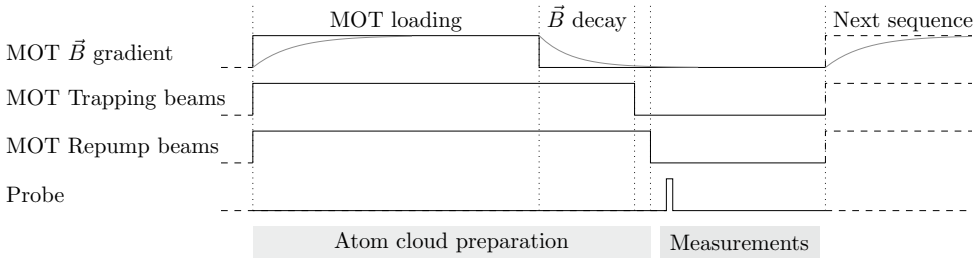

Figure 2.13: Typical timing sequence for different measurements on atoms released from the magneto-optical trap. The MOT reloading time is a few tens of milliseconds : the full loading time would be a few seconds, but since the sequence is repeated in cycle most atoms stay cold and in the trapping region during the release time. The trapping beams keep cooling and trapping the atoms while the $\vec{B}$ field gradient decays (a few milliseconds). Switching off the repump beam hundreds of microseconds after the trapping beams ensures the pumping of all atoms in the $\{6S_{1/2},F=4\}$ hyperfine ground state before the measurements interval. It may be switched off before the trapping beams for experiments with atoms initially in the $\{6S_{1/2},F=3\}$ state. However the transfer to this state will be inefficient because the trapping beams are tuned on a cyclic transition ($\{6S_{1/2},F=4\} \rightarrow \{6S_{1/2},F'=5\}$).

2.3.2 Absorption measurements

Absorption measurement are done using the timing scheme depicted in Figure 2.13, all the experiment being synchronized using an FPGA board as described in Appendix A. After loading the MOT, the atoms are released by shutting off the magnetic field gradient and the MOT laser beams. After a few more milliseconds a probe laser pulse tuned close to an atomic resonance of typically 10 microseconds duration is sent through the fiber. The transmitted light amplitude is then measured on a sensitive photodiode and compared to the transmitted amplitude when no cold atoms are present (this is usually done by continuously shutting off the MOT laser beams).

The photodiode used is an avalanche photodiode (Pacific Silicon Sensor AD-500-9-TO52) with home-made electronics, including polarization at 180 V and amplification. The sensitivity is ~ 0.36 V/nW with ~ 0.5 MHz bandwidth.

This process is repeated in a cycle, and the signal observed on an oscilloscope. Part of the noise observed when the probe pulse is absorbed is due to the current modulation used to lock our probe laser: this modulation induces a frequency modulation and thus a modulation of the absorbed peak amplitude.

This modulation easily allows fine tuning of the laser beam frequency f to the central maximally absorbed frequency f_0 by synchronizing the probe and the modulation before observing the absorbed pulse signal. If the beam frequency is away from f_0, the signal is modulated at the same frequency than the laser (maximum transmission when f is farther from f_0), while the frequency is doubled when the laser is modulated across the central frequency (one maximum in transmission for each extremum of f : $f_1 < f_0$, and $f_2 > f_0$). Detecting this frequency doubling in saturated absorption spectroscopy is the basis for the laser frequency control loop.

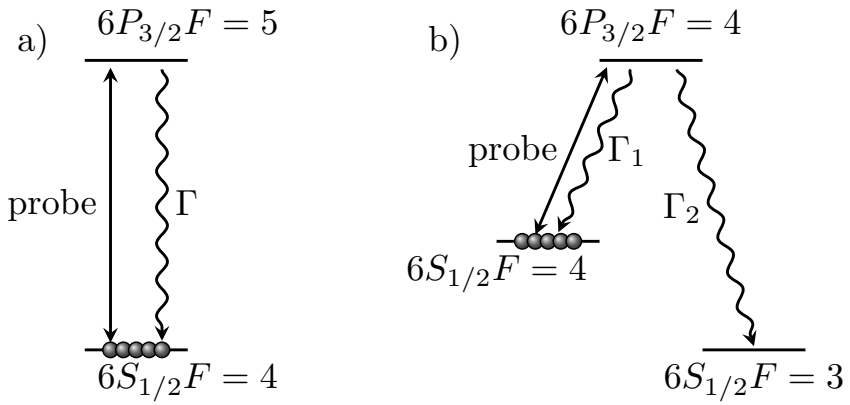

Figure 2.14: Energy level diagrams for probing the atomic cloud. a) Cycling transition : atoms excited in the upper state can only decay in the initial state. Note that atoms in the MOT are prepared in this initial $\{6S_{1/2},F = 4\}$ state. b) Here, atoms excited in the upper state can decay in both hyperfine level ground states.

Overlapping the MOT with the fiber and probing the cycling (see Figure 2.14 a) $\{6S_{1/2},F = 4\} \rightarrow \{6P_{3/2},F = 5\}$ transition of cesium D_2 line led to optical depths (OD) of typically of few units (OD is defined as $-\ln(\frac{P_{\text{abs}}}{P_{\text{ref}}})$ when P_{abs} and P_{ref} are the measured amplitudes of the absorbed and reference pulses). Values up to 8 for the optical depth were observed in this system, though proper probe power should be used, as explained in the next paragraph.

For all the measurements presented in this chapter, the magnetic field (after the MOT gradient has decayed) is canceled using 3 pairs of bias coils and Zeeman spectroscopy (section B.1).

2.3.2.1 Low-power saturation and pumping effects

An interesting observation is that the saturation power is much lower than in analog experiments where the probe pulse propagates in free space. Thus very low powers and a high sensitivity of the detector are needed to measure large absorptions, and even lower powers are needed the reach the linear regime.

In this section, we will explain and report data related to this saturation effect. We will also discuss some experimental parameters of our system with the insights from this first set of data. We will show that the number of atoms N involved in the interaction is low, with however a significant optical depth OD, an important parameter for the EIT-based memories described in chapter 3. The optical depth per atom can get large in nanoscale waveguides. Reaching ever higher values would make possible non-linear optics phenomena involving a few photons only, an exciting challenge of nowadays quantum optics [Chang14]. When targeting this regime, the usual scattering theory has to be adapted to take into account a modified spontaneous emission: the emission rate is larger and a significant part of the scattered light couples in the guided mode of interest. The last important parameter we will discuss is the atomic density, lower in the nanofiber vicinity.

Measured saturation curves are displayed on Figure 2.15 (a). Measurements for a free-space beam are shown for comparison in Figure 2.15 (b). The optical path used is the same as described later in subsubsection 3.2.1.1 for the EIT control beam. Transmission of a guided probe pulse as a function of its detuning is also given in Figure 2.16 for reference.

For an atomic cloud supposed uniform in the transverse direction, and for intensities far below saturation, the OD is independent of the probe beam size, as explicited below in Eq. (2.3.2). This is not true anymore when focusing the probe beams leads to intensities close to the saturation intensity of the atomic transition. This is what happens with our nanofiber guided probe beam which is highly focused over the whole length of the fiber. Note that even in the linear regime, the OD must be smaller for a guided beam since part of the light is inside the fiber core and cannot interact with the atoms.

The saturation-curve is fitted accordingly to the following empirical nonlinear model, which has been shown to be adapted to the nanofiber case with $k = 1$ [Jones14]:

$$T = e^{-\frac{d_0}{(1+P_{\text{in}}/P_{\text{sat}})^k}},$$

where P_{in} is the input power, T is the transmission and d_0 is the unsaturated optical depth. This fit yields a saturation power $P_{\text{sat}} = 1.3 \pm 0.2$ nW and an absorbed power in the saturated regime $P_{\text{absorbed}} = d_0 P_{\text{sat}} = 8 \pm 2$ nW.

Atom number estimation – Let us suppose that the number of atoms is a defined quantity. It can be estimated from P_{absorbed} as explained here. When the transition is saturated for all atoms the absorbed power is given by:

$$P_{\text{absorbed}} = P_{\text{in}}(1 - T) = \hbar\omega R_{sc} N = \frac{1}{2}\hbar\omega N\Gamma, \tag{2.3.1}$$

where R_{sc} is the atomic scattering rate. N can thus be inferred as $N = P_{\text{absorbed}}/p = 2000 \pm 500$ atoms, with $p = 3.8$ pW the nominal power radiated by a saturated single Cs atom.

Note however that this number is not well defined in the experiment we are considering here. As the probe power increases, more atoms are interfaced farther in the evanescent field. Since the atomic cloud is much larger than the probe, there are always more saturated atoms for larger probe powers. This kind of estimations however, will make more sense in chapter 4 with trapped atoms.

Even lower powers have to be used when probing a non-cyclic transition (measurements in Figure 2.15 (c)). In the $\{6S_{1/2}, F = 4\} \rightarrow \{6P_{3/2}, F = 4\}$ transition for example - which we will use in the EIT scheme - atoms in the excited state have two decay paths of similar probability (to the two hyperfine ground states of cesium: $6S_{1/2}F = 3$ and $F = 4$). Atoms pumped in the $\{6S_{1/2}, F = 3\}$ state are not addressed anymore by the probe pulse. An effective saturation is observed when the number of absorbed photons per pulse gets close to the number of atoms involved. A rough estimation from Figure 2.15 (c) gives the same order of magnitude for N (with a 5 μs pulse and a saturation power on the order of 0.1 nW).

$$N \sim \frac{\text{Effective Saturation Power} \times \text{Pulse duration}}{h\nu} \sim 2000.$$

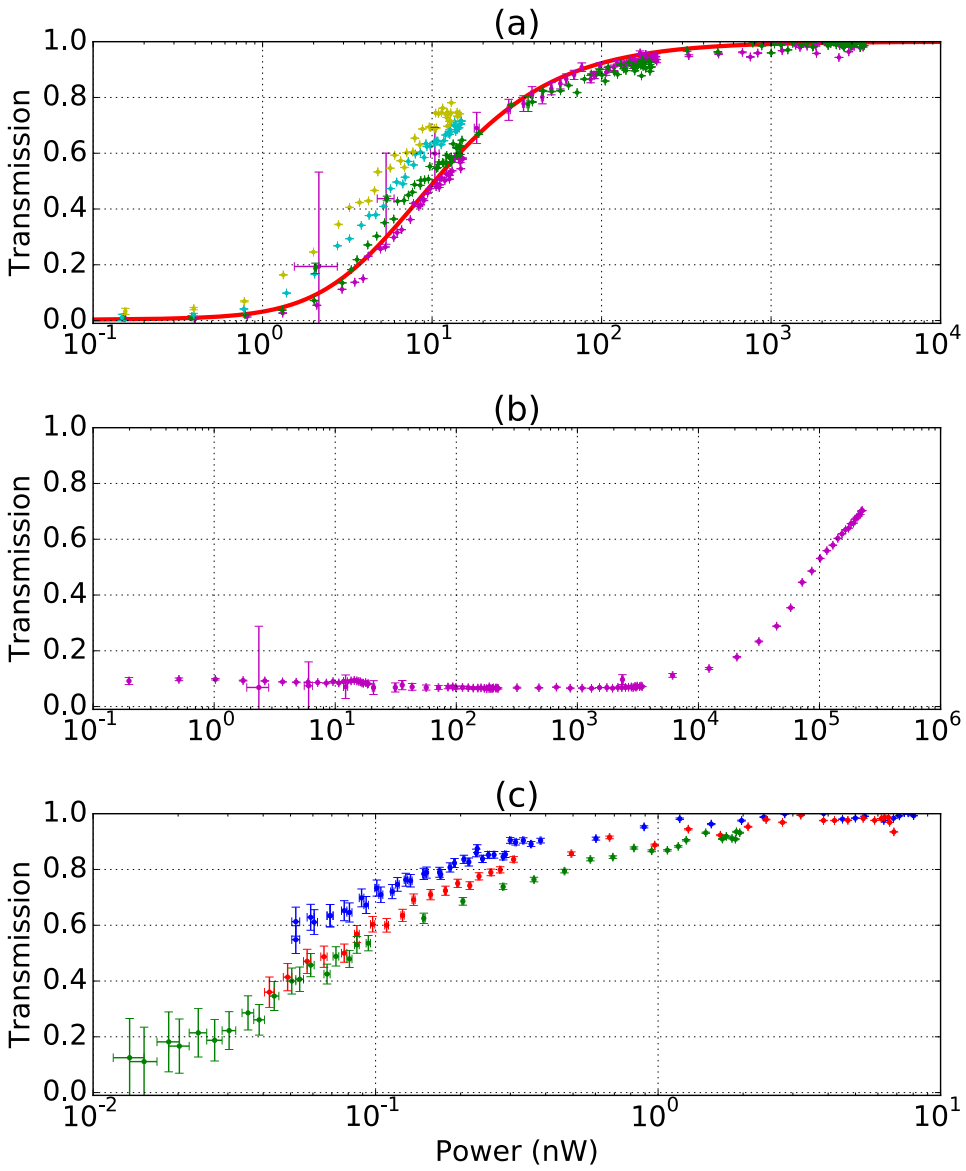

Figure 2.15: Absorption of a probe through a cold cesium cloud. (a) Probe on $\{6S_{1/2},F=4\} \rightarrow \{6P_{3/2},F=5\}$ cyclic transition guided by the nanofiber. Different colors reflects shot to shot fluctuations of optical depth over an hour. The solid red curve is a fit described in the text. (b) Free-space probe (optical path described in subsubsection 3.2.1.1) on $\{6S_{1/2},F=4\} \rightarrow \{6P_{3/2},F=5\}$ cyclic transition. (c) Guided probe on $\{6S_{1/2},F=4\} \rightarrow \{6P_{3/2},F=4\}$ "pumping" transition. For this figure, the pulse durations are $10\mu s$ (blue), $5\mu s$ (red) or $1\mu s$ (green). Error bars for all figures corresponds to the lower signal/noise ratio at low powers. Points for higher powers (> 10 nW) are measured with an attenuator in front of the detector.

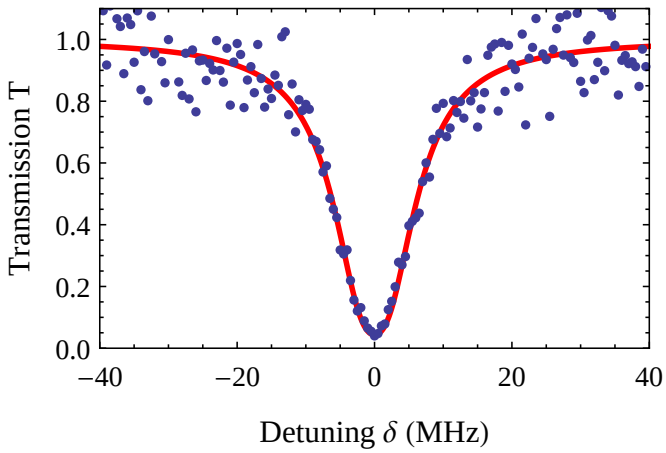

Figure 2.16: Transmission profile for a signal pulse at the single-photon level as a function of the detuning δ from the $\{6S_{1/2},F=4\} \rightarrow \{6P_{3/2},F=4\}$ transition. Here the resonant optical depth is 3 ± 0.4 and the measured Lorentzian width is 6.8 ± 0.5 MHz, 30% larger than the natural linewidth in free space (5.2 MHz).

A few equations for a uniform cloud – After these estimations, we now consider in more detail the cesium properties and the atomic scattering theory in the linear and saturated regimes. We start with a very simple model here, completely neglecting for example the modified spontaneous emission close to a nanofiber, and the power scattered back into the guided mode.

For the $\{6S_{1/2},F=4\} \rightarrow \{6P_{3/2},F=5\}$ transition, the saturation intensity I_{sat} is somewhere between 11 pW/μm^2 and 27 pW/μm^2 depending on the Zeeman sublevels populations and the local polarization. The lower value is valid for atoms polarized in extreme m_F Zeeman sublevels while the higher value is for unpolarized atoms excited by light with isotropic polarization [Steck98].

The steady state photon scattering rate per atom is given by the following equation:[26]

$$R_{sc} = \frac{\Gamma}{2} \frac{I_E/I_{sat}}{1+4(\Delta/\Gamma)^2 + I_E/I_{sat}}.$$

The ratio I_E/I_{sat} can be expressed as a function of the Rabi frequency and the spontaneous emission rate:

$$\frac{I_E}{I_{sat}} = 2\left(\frac{\Omega}{\Gamma}\right)^2.$$

The optical depth for a single atom located in $\vec{r}$ in the linear regime ($I_E \ll I_{sat}$) is therefore:

$$\mathrm{OD}_{at} = -\ln\left(1 - \frac{\Gamma\hbar\omega}{2I_{sat}}\frac{I_E(\vec{r})}{P}\right).$$

[26] Recall that the electromagnetic intensity $\frac{1}{2}\vec{e}\times\vec{h}^*$ is different from the electric field intensity $I_E = \frac{1}{2}c\epsilon_0|\vec{e}|^2$. I_E is defined twice larger here than in subsection 1.1.1, in order to match the definitions used in [Steck98].

The full optical depth can be obtained from the integration of:

$$\frac{dP(z)}{dz} = \hbar\omega \iint dxdyR_{sc}(x,y,z)d(x,y,z),$$

with $d(x,y,z)$ the atomic density, which can usually be supposed uniform in a large MOT. The resonant optical depth in the linear regime for a *uniform cloud* is then:

$$\mathrm{OD} = \eta\frac{\hbar\omega\Gamma}{2I_{sat}}dL = \eta\sigma dL, \tag{2.3.2}$$

where L is the overlapping length of the atomic cloud and the nanofiber, σ is the resonant scattering cross section, and η quantifies the electric intensity located outside the nanofiber in the evanescent field.

$$\eta = \frac{\iint_{r>\rho} I_E}{P}.$$

It is clear here that the OD is independent of the beam focusing in the linear regime. But, as mentioned above, it is intrinsically smaller for a nanofiber guided beam than for a freespace beam because of the presence of η in the equations.

If A is the area around the nanofiber where a ratio $r > 0.9$ of the light is absorbed, an effective number of atoms can be evaluated as:

$$N = dAL = \frac{2\mathrm{OD}I_{sat}A}{\eta\hbar\omega\Gamma} = \frac{\mathrm{OD}}{\eta}\frac{A}{\sigma}. \tag{2.3.3}$$

For a nanofiber of radius $\rho = 200$ nm, the region going from the fiber surface to a distance $4\rho = 800$ nm away from the surface leads to $r = 98.8\%$ (r = 66.8% for a distance of 200 nm). Therefore, with the measured OD = 6 and an average 18 pW/μm^2 saturation intensity, one finds $N \sim 120$ atoms using Eq. (2.3.3), more than an order of magnitude lower than the previous estimations. If L=5 mm this corresponds to a density of 0.008 μm^{-3}, a weak value relatively to typical cesium MOT densities (0.1 μm^{-3}). As we will see below this can be explained by a lower atomic density close to the nanofiber. The OD per atom is 0.06 using this value, or 0.003 for 2000 atoms.

Modified atomic density close to a nanofiber – To explain our experimental numbers, we must consider that the density is modified close to the fiber because of surface interactions. Consequently, the cloud is *not uniform*. There are indeed less atoms in the fiber vicinity because of Van der Waals (VdW) interactions and the force exerted by the probe beam itself [Sagué07]. The latter depends on power, detuning and atomic position. It is of course negligible for smaller powers, far from saturation. The remaining modification of the atomic density due to VdW forces is compatible with our data as we will see below. It can be taken into account with the expression provided in [Le Kien09]:

$$d(r) = \frac{d(r=\infty)}{k_BT}\int_1^\infty e^{-E/k_BT}\frac{\sqrt{E}}{\sqrt{E-U_{VdW}(r)}}dE. \tag{2.3.4}$$

The atomic density integrated from Eq. (2.3.4) is plotted in Figure 2.17. It corresponds to $N = 1430$ atoms in the $\rho < r < 4\rho$ interval for $d(r=\infty) = 0.1$ μm^{-3}.

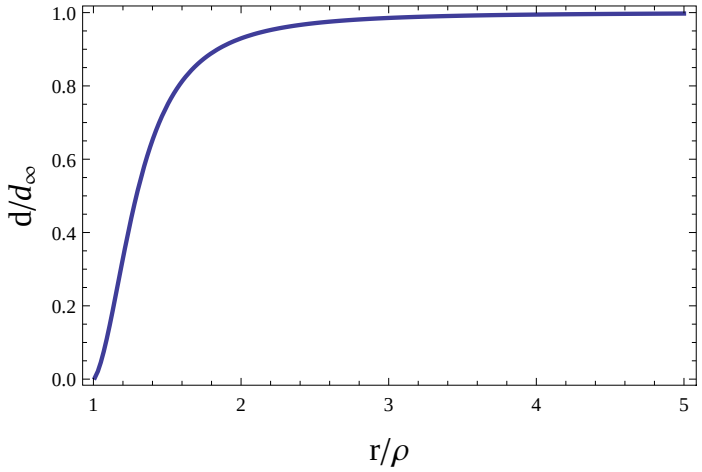

Figure 2.17: The atomic density close to the nanofiber surface. This result is obtained from Eq. (2.3.4) with $T = 200$ μK, $U_{VdW}(r) = -\frac{C_g}{(r-\rho)^3}$, and $C_g = 1.56$ kHz.μm^3. The order of magnitude chosen for the temperature was later confirmed by time of flight measurements.

Modified spontaneous emission theory – If we consider the electric field intensity of fiber guided modes, the maximal OD for an atom is obtained if the atom is at the fiber surface: $\mathrm{OD}_{at}(r = \rho) = 1.16$ for a quasi-circularly-polarized mode. However, for such a high absorption, the formula for R_{sc} cannot be valid anymore: a modification of the regular scattering theory must be considered as detailed below. For a quasi-linearly-polarized beam, an atom at the position of maximum electric intensity would scatter more power than the input power using this formula. For atoms farther from the fiber surface, the absorption is smaller: $\mathrm{OD}_{at}(r = 2\rho) = 0.12$ and $\mathrm{OD}_{at}(r = 5\rho) = 0.0016$.

Because of the presence of a nanofiber, the total spontaneous emission rate is actually $\Gamma_{\mathrm{tot}} = \Gamma' + \Gamma_{\mathrm{m}}$ where Γ_{m} is the emission rate in the probing mode, and Γ' is the emission rate in all other accessible modes of the electromagnetic field. These other modes include guided modes: the backward propagating mode and the orthogonally quasi-polarized modes. The power scattered in other modes (the absorbed power) by a single two-level atom is then[27]:

$$P_{sc} = \hbar\omega\frac{\Gamma'}{2}\frac{I_E/I_{sat}}{1+4(\Delta/\Gamma_{\mathrm{tot}})^2+I_E/I_{sat}} = \hbar\omega\frac{\Gamma'}{2}\frac{2\left(\frac{\Omega}{\Gamma_{\mathrm{tot}}}\right)^2}{1+4(\Delta/\Gamma_{\mathrm{tot}})^2+2\left(\frac{\Omega}{\Gamma_{\mathrm{tot}}}\right)^2}.$$

This expression is simply $\hbar\omega\Gamma'$ multiplied by the steady state population ρ_{ee} obtained from the following optical Bloch equations (more on OBEs in section 3.1, and in the

[27]Here I consider that the absorbed power is given by the power scattered in all the modes different from the probing mode. Experimentally, this means that light in the forward propagating mode with polarization orthogonal to the (forward propagating) probing mode is filtered out before measurement. This can be done via polarization filtering at the fiber output. Such as for our experiments in the next chapter.

atom-waveguide coupling context in e.g. [Le Kien14b, Goban15, Chang07]):

$$\dot{\tilde{\rho}}_{ee} = +\frac{i}{2}\Omega(\tilde{\rho}_{eg} - \tilde{\rho}_{ge}) - \Gamma_{\text{tot}}\tilde{\rho}_{ee}$$
$$\dot{\tilde{\rho}}_{ge} = -i\Delta\tilde{\rho}_{ge} - \frac{i}{2}\Omega(2\tilde{\rho}_{ee} - 1) - \frac{\Gamma_{\text{tot}}}{2}\tilde{\rho}_{ge}.$$

Depending on atomic position, the absorbed power thus varies accordingly to the increase of the saturation intensity $I_{sat} \propto \Gamma_{\text{tot}}^2$ and of Γ'. The different scattering rates can be computed given the proper set of electromagnetic-field mode functions [Klimov04, Le Kien05, Le Kien14a].

Note that the contribution to Γ is in general different for the two quasi-linear polarizations because of the different electric field amplitudes at the atomic position, but also different for the forward and backward propagating modes because of the different polarization of those two modes. If the forward mode is supposed perfectly σ_+ polarized at the atomic position, and the backward mode σ_- polarized, reflection in the backward mode will be forbidden in a $F = 0 \to F' = 1$ transition. Others values for the local polarization and F can be treated similarly than in subsection 3.1.3.

Chapter Conclusion

In this chapter, we addressed the following experimental steps:

- Embedding a nanofiber into a high-vacuum system.

  Our main vacuum chamber is located very close to the fabrication rig for easier nanofiber transfer. It can easily be opened for nanofiber insertion. The nanofiber is glued inside the chamber and the two tails are fed outside vacuum with Teflon feedthrough.

- Preparing a cold cesium cloud overlapped with the nanofiber.

  A MOT is prepared around the fiber with laser cooling and pumping beams in addition to a spatially dependent magnetic field. More lasers, all locked on an external atomic reference, are setup for atomic manipulation.

- Studying absorption of resonant nanofiber-guided light by the surrounding atoms.

  One of the first consequences of using nanofiber-guided light is the possibility for non-linear optical phenomena at very low power levels. In particular, saturation data were presented, and a significant optical depth can be obtained with a small number of atoms. We also argued that, compared to usual light-matter interaction experiments in atomic clouds, more complex theoretical models have to be used. This includes a non-uniform atomic density, as well as a modified and position dependent spontaneous emission close to the nanofiber surface.

The next chapter will first introduce electromagnetically-induced transparency (EIT). We will then report the observation of EIT and slow light for light tightly confined in an optical nanofiber, as well as the demonstration of an atomic memory for this guided light at the single-photon level.

Chapter 3

An EIT-based memory for nanofiber guided light

Until here, we have seen how our experimental setup was prepared. We now have an optical nanofiber in a high-vacuum system. Light tightly confined in this nanofiber is interacting via its evanescent field with cold atoms surrounding the fiber, with very low saturation power as described in the previous chapter.

Now, the question is the following: Can we use this system in quantum optics related experiments? And more precisely, in the group's perspective, can we observe electromagnetically induced transparency (EIT) - a phenomenon closely related to e.g. quantum memories or single-photon generation in atomic ensembles - in this system?

The chapter will first give a theoretical introduction to EIT and its application to optical memories. This theoretical part will also focus on a few important points, such as the effect of polarization of light and atoms in EIT. The second part will report on the observation of EIT and on the realization of a memory for nanofiber-guided light at the single-photon level.

3.1 Theoretical basis for a Λ-type 3-level atom

In this section, I will present some theoretical tools for understanding the main concepts used in our experiment. They are all related to EIT, a quantum interference effect occurring in 3-level atomic systems. These tools will be introduced starting from the most simple model and aiming towards the most realistic. The realism will focus on only a few points though, and the more complete and realistic considerations will be found in recent publications from the international community. There is much bibliography to be found on EIT and quantum optics in atomic ensembles (see e.g. [Fleischhauer05, Hammerer10] for reviews). A few theoretical publications have considered EIT in nanofibers, something I will not discuss specifically in this section [Patnaik02, Le Kien09, Le Kien15].

In the first step we will consider the Schrödinger equation formalism for a 3-level atomic system, introducing the dark-state concept. The study of propagation of a probe pulse through an atomic ensemble will then require the use of the optical Bloch equations (OBEs) including decoherence. In order to study the effect of light polariza-

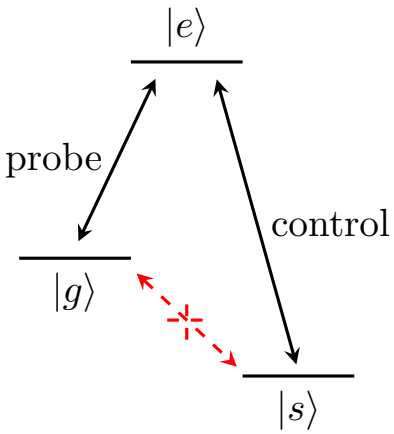

Figure 3.1: Level diagram for a Λ-type 3-level atom in an EIT configuration including a probe and a control field.

tion, the OBEs approach will be extended in the third part to a Zeeman degenerate atom. In the fourth part we will consider dynamic EIT, where modulations of a control beam allow to modify the propagation properties. The final part will briefly mention the quantization of the probe field with the dark-state-polariton formalism and the application for memories storing the quantum state of light as collective atomic excitations.

3.1.1 Schrödinger equation and dark state

We start this paragraph with the most simple model for EIT: we consider a 3-level atom in the Λ configuration. As depicted in Figure 3.1, two ground states $|g\rangle$ and $|s\rangle$ are optically coupled to an excited $|e\rangle$ state. The direct transition between $|g\rangle$ and $|s\rangle$ is electric-dipole forbidden. The optical transition from $|g\rangle$ to $|e\rangle$ is excited by the *probe* or *signal* field and the $|s\rangle$ to $|e\rangle$ is excited by the *control* field.

The energies for states $|g\rangle$, $|s\rangle$ and $|e\rangle$ are $-\hbar\omega_{eg}$, $-\hbar\omega_{es}$ and 0 respectively. ω_p and ω_c are the probe and the control field frequencies, supposed resonant in this paragraph ($\omega_p = \omega_{eg}$ and $\omega_c = \omega_{es}$).

With these notations, the Hamiltonian H for this system can be written as:

$$H = H_0 + H_1,$$

with

$$H_0 = -\hbar\omega_{eg}|g\rangle\langle g| - \hbar\omega_{es}|s\rangle\langle s|,$$

and

$$H_1 = \frac{\hbar}{2}\left(\Omega_p e^{-i\omega_p t}|e\rangle\langle g| + \Omega_c e^{-i\omega_c t}|e\rangle\langle s|\right) + \text{H.c.}, \tag{3.1.1}$$

where H_0 is the unperturbed Hamiltonian and H_1 is the electric field perturbation in the dipole and rotating-wave approximations, taking only into account the resonant terms. $\Omega_p = -\frac{\langle e|\vec{d}|g\rangle.\overrightarrow{E_{0p}}}{\hbar}$ and $\Omega_c = -\frac{\langle e|\vec{d}|s\rangle.\overrightarrow{E_{0c}}}{\hbar}$ are the Rabi frequencies for the two

optical transitions, which are directly proportional to the corresponding electric field amplitudes ($\overrightarrow{E_{0p}}$ and $\overrightarrow{E_{0c}}$) and chosen real in this paragraph.

Now we consider the following superposition of the two ground states:

$$|D\rangle = \cos(\theta)e^{i\omega_{eg}t}|g\rangle - \sin(\theta)e^{i\omega_{es}t}|s\rangle,$$

with

$$\cos(\theta) = \frac{\Omega_c}{\sqrt{\Omega_p^2 + \Omega_c^2}},$$

and

$$\sin(\theta) = \frac{\Omega_p}{\sqrt{\Omega_p^2 + \Omega_c^2}}.$$

The action of H_1 on this state is $H_1|D\rangle = 0$. This state is thus not coupled to the excited state via the perturbation Hamiltonian. It cannot scatter light via the two optical transitions and is thus called a *dark state*.

Similarly, writing the atomic state $|\psi(t)\rangle = c_g(t)e^{i\omega_{eg}t}|g\rangle + c_s(t)e^{i\omega_{es}t}|s\rangle + c_e(t)|e\rangle$ in the interaction picture leads to a simplified Schrödinger equation:

$$\begin{cases} \dot{c_g} &= -\frac{i}{2}\Omega_p c_e \\ \dot{c_s} &= -\frac{i}{2}\Omega_c c_e \\ \dot{c_e} &= -\frac{i}{2}(\Omega_p c_g + \Omega_c c_s). \end{cases}$$

And searching a time-independent solution state gives $c_e = 0$ and $c_s = -\frac{\Omega_p}{\Omega_c}c_g$, which corresponds to the same dark state.

Some applications of the Λ configuration – Note that in this stable superposition of the two ground states, the relative populations are directly linked to the ratio between the two light field amplitudes. An immediate application is the so-called *coherent population trapping* (CPT). When both the probe and control beams are continuous, the atom in any initial state will be optically pumped in the dark state.

Adiabatic variations of the electric field amplitudes Ω_p and Ω_c can also be used for coherent atomic state manipulation. Consider an atom initially pumped in $|g\rangle$ by a continuous control field. There is no probe field yet, this atom is actually initially in the dark state. Now if a probe pulse comes in, the atom can adiabatically follow the dark state and will not scatter any light. This is called *electro-magnetically induced transparency* : the probe is not absorbed when a control beam is present. We will show in the next paragraph that EIT is associated as well with a slow propagation of the probe (*slow light*). Similarly, with the same initial conditions, if a continuous probe beam is turned on, then the control beam turned off, the atom will be transfered from $|g\rangle$ to $|s\rangle$. This is the technique known as *stimulated Raman adiabatic passage* (STIRAP).

Another common application is a *quantum memory for light*, which will be described in more details later. As shown in Figure 3.2, the probe pulse enters the

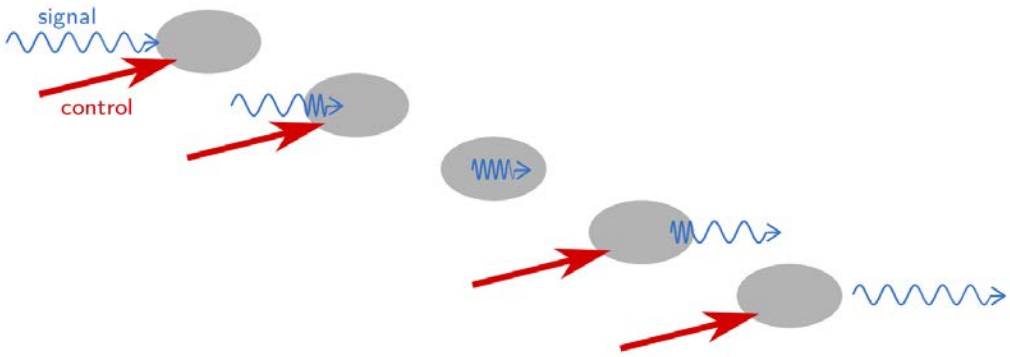

Figure 3.2: Illustration of the EIT-based memory protocol. In the presence of a control field, the incoming pulse is spatially compressed inside the medium due to the reduction in the group velocity. When the control laser is switched off, the pulse is stored as a collective state of the atomic ensemble. Then, by switching on again the control laser the pulse can propagate again and be retrieved at the cloud's output.

atomic cloud in EIT conditions. While it is slowly propagating through the cloud, the control beam Rabi frequency is ramped down to zero (by ramping down the beam power). At this point the quantum information initially carried by the probe is stored as a quantum superposition involving all the atoms taking part in the process. This information can be retrieved by ramping back up the control beam Rabi frequency: the atomic excitation is mapped back to a slowly propagating probe which can exit the atomic cloud.

3.1.2 Optical Bloch equations

A more detailed study of the propagation of a light pulse in EIT conditions is made possible by deriving the frequency dependence of the linear dielectric susceptibility for a collection of non-interacting atoms. This can be done by writing down the *optical Bloch equations* (OBEs) for the atomic system. The OBEs are simply the Schrödinger equation for the density matrix ρ, taking into account decoherence via spontaneous emission. We will use here the notations defined in Figure 3.3.

OBE – The time-evolution of the density matrix is given by:

$$\dot{\rho} = -\frac{i}{\hbar}[H,\rho] - \sum_i \frac{\Gamma_i}{2}(\sigma_i^\dagger \sigma_i \rho - 2\sigma_i \rho \sigma_i^\dagger + \rho \sigma_i^\dagger \sigma_i), \tag{3.1.2}$$

where the sum is over the possible spontaneous emission channels and σ_i are the corresponding lowering operators ($|g\rangle\langle e|$ and $|s\rangle\langle e|$).

Writing the equation in a frame rotating at the optical field frequencies, more practical than the interaction frame here, leads to simplified equations. This is done

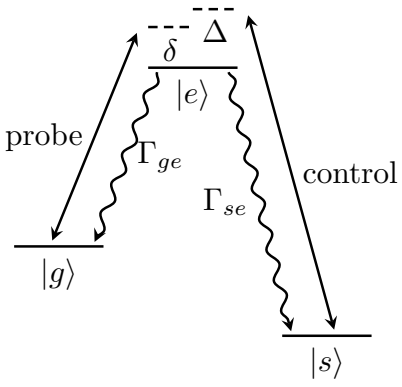

Figure 3.3: Level diagram with spontaneous emission and detuned fields.

with the following definitions:

$$\begin{cases} \tilde{\rho} &= U^\dagger \rho U \\ U &= e^{-iFt/\hbar} \\ F &= -\hbar\omega_p |g\rangle\langle g| - \hbar\omega_c |s\rangle\langle s| \\ \Gamma &= \Gamma_{ge} + \Gamma_{se}, \end{cases} \tag{3.1.3}$$

and results in the following OBEs for the Λ-type atom:

$$\begin{cases} \dot{\tilde{\rho}}_{gg} &= -\frac{i}{2}\Omega_p(\tilde{\rho}_{eg} - \tilde{\rho}_{ge}) + \Gamma_{ge}\tilde{\rho}_{ee} \\ \dot{\tilde{\rho}}_{ss} &= -\frac{i}{2}\Omega_c(\tilde{\rho}_{es} - \tilde{\rho}_{se}) + \Gamma_{se}\tilde{\rho}_{ee} \\ \dot{\tilde{\rho}}_{ee} &= +\frac{i}{2}\Omega_p(\tilde{\rho}_{eg} - \tilde{\rho}_{ge}) + \frac{i}{2}\Omega_c(\tilde{\rho}_{es} - \tilde{\rho}_{se}) - \Gamma\tilde{\rho}_{ee} \\ \dot{\tilde{\rho}}_{ge} &= -i\delta\tilde{\rho}_{ge} - \frac{i}{2}\Omega_p(\tilde{\rho}_{ee} - \tilde{\rho}_{gg}) + \frac{i}{2}\Omega_c\tilde{\rho}_{gs} - \frac{\Gamma}{2}\tilde{\rho}_{ge} \\ \dot{\tilde{\rho}}_{se} &= -i\Delta\tilde{\rho}_{se} - \frac{i}{2}\Omega_c(\tilde{\rho}_{ee} - \tilde{\rho}_{ss}) + \frac{i}{2}\Omega_p\tilde{\rho}_{sg} - \frac{\Gamma}{2}\tilde{\rho}_{se} \\ \dot{\tilde{\rho}}_{gs} &= -i(\delta - \Delta)\tilde{\rho}_{gs} - \frac{i}{2}(\Omega_p\tilde{\rho}_{es} - \Omega_c\tilde{\rho}_{ge}). \end{cases}$$

Steady state in the weak probe limit – We now look for a steady state solution in the weak probe limit. At the zeroth order in Ω_p only the $|g\rangle$ state is populated:

$$\tilde{\rho}^{(0)} = |g\rangle\langle g|.$$

Then at the first order in Ω_p:

$$\begin{cases} \tilde{\rho}_{ee} = 0 \\ \tilde{\rho}_{se} = 0 \\ \tilde{\rho}_{ss} = 0 \\ (i\delta + \dfrac{\Gamma}{2})\tilde{\rho}_{ge} = \dfrac{i}{2}\Omega_p + \dfrac{i}{2}\Omega_c\tilde{\rho}_{gs} \\ (\delta - \Delta)\tilde{\rho}_{gs} = \dfrac{1}{2}\Omega_c\tilde{\rho}_{ge}. \end{cases}$$

Then, noting with tildes the variables homogeneous to frequencies normalized to Γ:

$$\begin{cases} \tilde{\rho}_{ge} &= \dfrac{\tilde{\delta} - \tilde{\Delta}}{2(\tilde{\delta} - \tilde{\Delta})(\tilde{\delta} - \frac{i}{2}) - \frac{1}{2}\tilde{\Omega}_c^2}\tilde{\Omega}_p \\ \tilde{\rho}_{gs} &= -\dfrac{\frac{1}{2}\tilde{\Omega}_c}{2(\tilde{\delta} - \tilde{\Delta})(\tilde{\delta} - \frac{i}{2}) - \frac{1}{2}\tilde{\Omega}_c^2}\tilde{\Omega}_p. \end{cases} \tag{3.1.4}$$

Linear susceptibility and propagation – The atomic electric dipole is given by:

$$Tr(\rho\vec{d}) = 2\Re(\rho_{eg})\vec{d}_{eg} + 2\Re(\rho_{es})\vec{d}_{es} = 2\Re(\tilde{\rho}_{eg}e^{-i\omega_p t})\vec{d}_{eg} + 2\Re(\tilde{\rho}_{es}e^{-i\omega_c t})\vec{d}_{es},$$

such that $2\rho_{eg}\vec{d}_{eg}$ and $2\rho_{es}\vec{d}_{es}$ are the complex dipole components oscillating at ω_p and ω_c frequencies respectively, while $\tilde{\vec{D}} = 2\tilde{\rho}_{eg}\vec{d}_{eg} + 2\tilde{\rho}_{es}\vec{d}_{es} = 2\rho_{eg}e^{i\omega_p t}\vec{d}_{eg} + 2\rho_{es}e^{i\omega_c t}\vec{d}_{es}$ is the slowly-varying dipole envelope[1].

For an atomic cloud, the dipole moment per unit volume can be derived recalling equations (3.1.4):

$$\vec{P} = n\tilde{\vec{D}} = 2n\tilde{\rho}_{eg}\vec{d}_{eg} = \epsilon_0\chi_{EIT}\vec{E}_{0p},$$

where n is the atomic density. The linear susceptibility is thus:

$$\chi_{EIT} = \frac{2nd_{eg}^2}{\epsilon_0\hbar\Gamma}\frac{\tilde{\delta} - \tilde{\Delta}}{\frac{1}{2}\tilde{\Omega}_c^2 - 2(\tilde{\delta} - \tilde{\Delta})(\tilde{\delta} + \frac{i}{2})} = \frac{2nd_{eg}^2}{\epsilon_0\hbar\Gamma}\frac{\frac{\tilde{\Omega}_c^2}{2(\tilde{\delta}-\tilde{\Delta})} - 2\tilde{\delta} + i}{\left(\frac{\tilde{\Omega}_c^2}{2(\tilde{\delta}-\tilde{\Delta})} - 2\tilde{\delta}\right)^2 + 1}.$$

This result is plotted in Figure 3.4 and Figure 3.5. Recall from Maxwell equations in dielectrics that the refractive index is $1 + \frac{1}{2}\chi_{EIT}$. The field complex amplitude after propagation over a distance z elvolved as

$$E(z) = E(z = 0)e^{i(1+\frac{Re(\chi)}{2})kz}e^{-\frac{Im(\chi)}{2}kz}. \tag{3.1.5}$$

The imaginary part is thus linked to absorption, and the real part to dispersion of the propagating field. On the absorption curve, the control beam opens a transparency window: there is no absorption on two-photon resonance $\delta = \Delta$. On the dispersion curve, we can see that the refractive index is 1 on resonance. There is thus perfect index matching with vacuum and an incoming light pulse can propagate through the medium without experiencing any reflection. Although, unlike in vacuum, Re(χ) has a

[1] Be careful, it is $\tilde{\rho}_{eg}$ here, not $\tilde{\rho}_{ge}$.

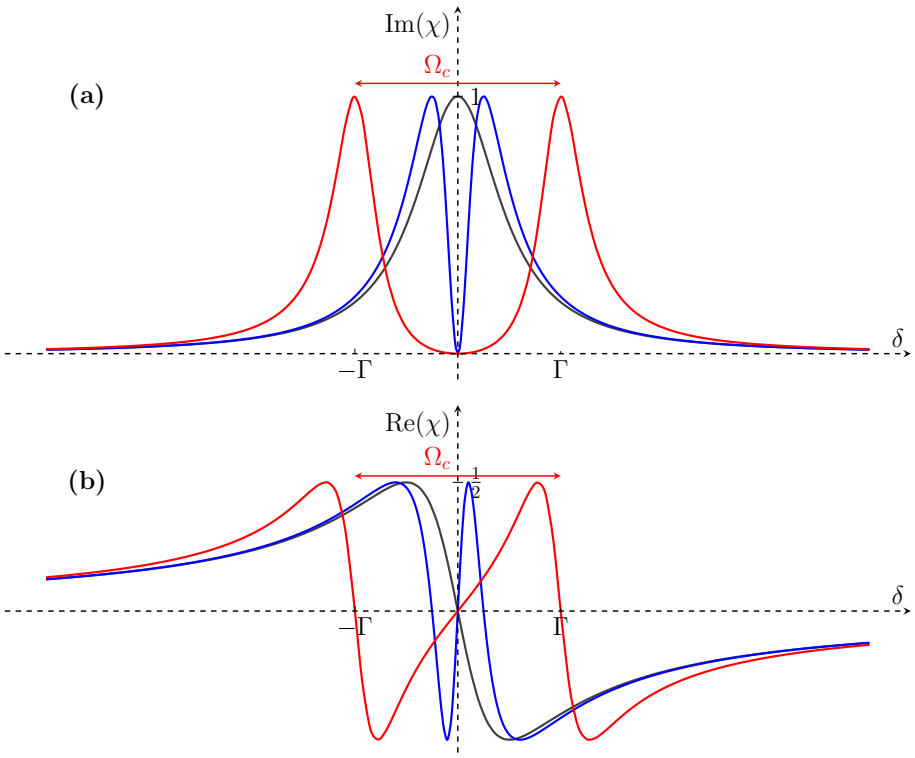

Figure 3.4: Imaginary (a) and real (b) parts of the EIT atomic susceptibility χ_{EIT}, in units of $\frac{2nd_{eg}^2}{\epsilon_0\hbar\Gamma}$. The different curves correspond to different control beam Rabi frequencies, all for $\Delta = 0$. Gray: $\Omega_c = 0$, Blue: $\Omega_c = \frac{1}{2}\Gamma$ and, Red: $\Omega_c = 2\Gamma$. The separation between the two absorption peaks is Ω_c.

non zero slope on two-photon resonance, which can be made very steep for low control beam power or high atomic densities. This slope is responsible for a group velocity which can be much smaller than c, this is the *slow-light* effect.

Note here the presence of the atomic density n in the susceptibility. With an increase of n, the group velocity will decrease directly as $\frac{1}{n}$. Now, looking at the full propagation equation (3.1.5) across a cloud of length L, the delay induced by the slow light effect scales as nL. Thus, a very important parameter in slow light experiments is the two-level atom resonant optical depth OD, directly proportional to nL (Eq. (2.3.2)). OD should in principle be as large as possible. However, as we will see below, there will always be residual absorption in experiments ($Im(\chi)$ not perfectly zero) which will set a limit on the highest acceptable OD[2].

In the so-called *Raman* configuration (Figure 3.5), i.e. when $\Delta \neq 0$, an optimal value of $|\delta|$ slightly detuned from exact two-photon resonance can be found for slow-light protocols. Indeed, if $|\delta|$ is chosen slightly larger, the absorption remains small while dispersion is improved, leading to smaller group velocities [Parigi15].

[2]Any residual absorption always lead to 100% absorption for large OD.

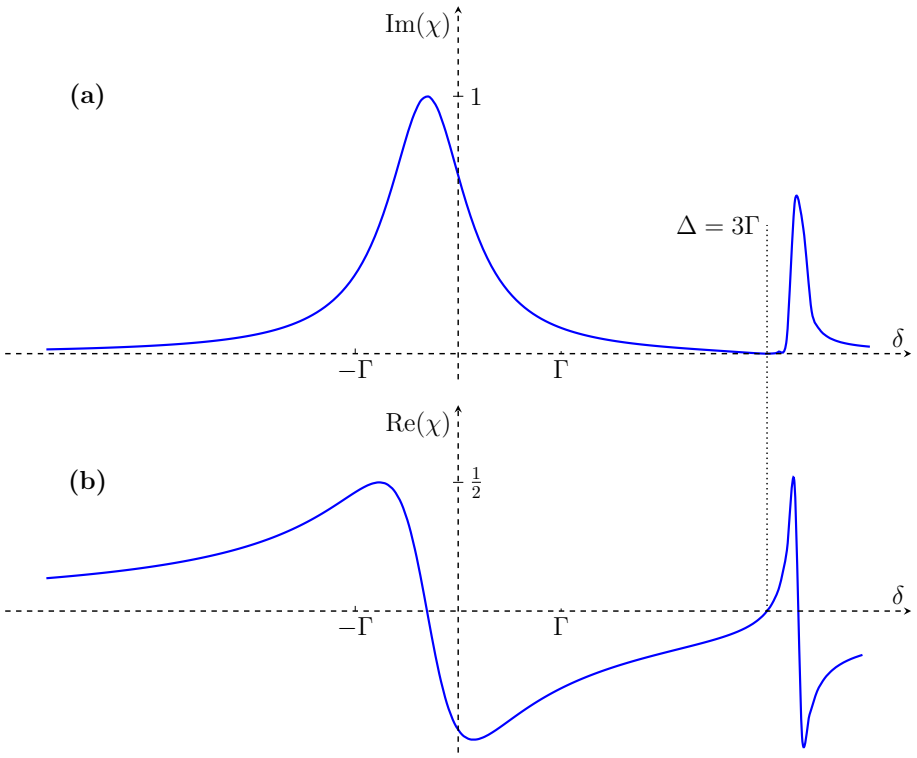

Figure 3.5: Imaginary (a) and real (b) parts of the EIT atomic susceptibility χ_{EIT}, in units of $\frac{2nd_{eg}^2}{\epsilon_0\hbar\Gamma}$ for the Raman configuration. Here $\Omega_c = 2\Gamma$ and $\Delta = 3\Gamma$. In slow light and memory protocols, $|\delta|$ is optimal for a value slightly higher than the exact 2-photon resonance ($\delta = \Delta$), on the right of the dotted line. For such a value, the group velocity is lower (larger derivative in curve (b)) with still very small absorption (curve (a) is almost zero).

Adding decoherence in the OBEs – Until now, the only decoherence mechanism considered was spontaneous emission. Other mechanisms such as dephasing due to collisions or the effect of transit time broadening can be taken into account by adding phenomenogical decay terms in the optical Bloch equations. Dephasing rates $\gamma_{g_{deph}}$, $\gamma_{s_{deph}}$ and $\gamma_{e_{deph}}$ can be added in Eq. (3.1.2) ([Fleischhauer05]) in association with operators $\sigma_i = |g\rangle\langle g|$, $|s\rangle\langle s|$ and $|e\rangle\langle e|$. Noting $\Gamma' = \Gamma + \gamma_{g_{deph}} + \gamma_{e_{deph}}$ and $\gamma_{gs} = \gamma_{g_{deph}} + \gamma_{s_{deph}}$, one finds:

$$\chi_{EIT} = \frac{2nd_{ge}^2}{\epsilon_0\hbar\Gamma'} \frac{\delta' - \Delta' + \frac{i}{2}\gamma'_{gs}}{\frac{1}{2}\Omega_c'^2 - 2(\delta' - \Delta' + \frac{i}{2}\gamma'_{gs})(\delta' + \frac{i}{2})}, \tag{3.1.6}$$

where all frequencies are now in Γ' units, which is the broadened two-level linewidth on $|g\rangle$ to $|e\rangle$ transition.

As Figure 3.6 shows, ground state decoherence results in imperfect transparency and smaller dispersion. It can be a strong experimental limiting factor. For a strong slow-light effect for example, a small control Rabi frequency is required as well as a large two-level optical depth, absorption will be strong though if the Rabi frequency

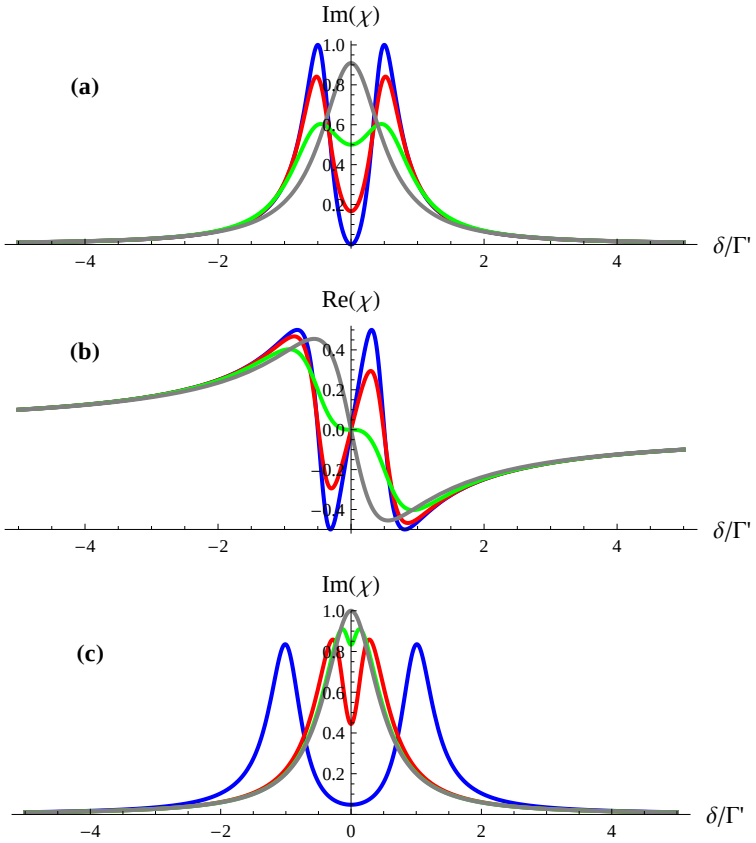

Figure 3.6: Imaginary (a),(c) and real (b) parts of the EIT atomic susceptibility with finite ground-state decoherence. For (a) and (b), $\Omega_c = \Gamma'$. The different curves correspond to different ground-state decoherence rates. Blue: $\gamma_{gs} = 0$, Red: $\gamma_{gs} = 0.2\Gamma'$, Green: $\gamma_{gs} = \Gamma'$, Gray: $\gamma_{gs} = 10\Gamma'$. In (c), $\gamma_{gs} = 0.2\Gamma'$. The different curves correspond to different control beam Rabi frequencies. Blue: $\Omega_c = 2\Gamma'$, Red: $\Omega_c = \frac{1}{2}\Gamma'$, Green: $\Omega_c = 0.2\Gamma'$, Gray: $\Omega_c = 0$. For all these plots, $\Delta = 0$.

is smaller than the dephasing rate.

Consequences of the finite atomic transit time in the probing volume can be added in a very similar manner [Arimondo96]. The lasers linewidth can be taken into account as well: [Fleischhauer05, Agarwal78, Boller91]. Note that due to the role of $\delta - \Delta$ in the susceptibility, EIT can be preserved with relatively large laser linewidth as soon as they are phase locked (paragraph 2.2.3). Similarly, the effect of Doppler broadening can be canceled if the two beams are co-propagating.

As a conclusion for this paragraph, we have derived here the susceptibility of an ideal Λ-type atomic medium. This allows to study the properties of propagation in EIT. We also mentioned a few limitations of EIT. They will be completed in the next paragraph by considering a more realistic atom involving more than 3 levels in the Λ configuration.

3.1.3 Polarization of the fields and atomic angular momentum in EIT

The previous two paragraphs presented the basics of EIT and discussed some experimental limitations of this phenomenon. In this paragraph, I will address another specific experimental issue : Λ-type atoms as simple as considered previously do not correspond to real atoms used in experimental realizations. We will consider here an atom consisting of 3 different hyperfine levels and include into the optical Bloch equations all the possible Zeeman sublevels. This will allow to study the effect of atomic angular momentum, for atoms prepared or not in a given Zeeman level or superposition, as well as the effect of light polarization - for any polarization, including the elliptic polarization of nanofiber-guided light.

In the following, each of the 3 levels considered has a total angular momentum F_g, F_s and F_e. The corresponding Zeeman levels are noted $|i,\mu\rangle$ with $i \in \{g,s,e\}$ and $-F_i \leq \mu \leq F_i$.

The proper tool for describing the polarization of a light beam when studying its interaction with an atom with a Zeeman structure is the so-called *spherical basis* (the reader can refer to [Steck] chap. 7: Atomic Angular-Momentum Structure). What matters is the local electric field polarization, independently of the propagation axis. We thus express the electric fields for the probe and control beams and their normalized polarization vectors $\vec{\epsilon^p}$ and $\vec{\epsilon^c}$ in the following way:

$$\begin{aligned}
\vec{u}_{\pm 1} &= \mp\frac{1}{\sqrt{2}}(\vec{x} \pm i\vec{y}) \\
\vec{u}_0 &= \vec{z} \\
\vec{E_p} &= E_{p0}\frac{e^{-i\omega_p t}}{2}\sum_{q=-1,0,1}\epsilon_q^p\vec{u}_q^* + c.c. = E_{p0}\frac{e^{-i\omega_p t}}{2}\vec{\epsilon^p} + c.c. \\
\vec{E_c} &= E_{c0}\frac{e^{-i\omega_c t}}{2}\sum_{q=-1,0,1}\epsilon_q^c\vec{u}_q^* + c.c. = E_{c0}\frac{e^{-i\omega_c t}}{2}\vec{\epsilon^c} + c.c..
\end{aligned}$$

We chose here $\vec{z}$ as the quantization axis. If the field is oscillating along $\vec{u}_0 = \vec{z}$, it will be traditionally noted as π polarized. If it is rotating around the z-axis, it will be noted σ_+ or σ_-, which correspond respectively to polarization vectors $\vec{u}_{+1}$ and $\vec{u}_{-1}$. An electric field polarized along $\vec{u}_q$ couples a $|g\rangle$ state with angular quantum number m to a $|e\rangle$ state with $m' = m + q$. We now give a few examples considering a propagating plane wave in vacuum. If the wave is propagating along z-axis the polarization is $\sigma_\pm$ if circularly polarized or a combination of σ_+ and σ_- in general. Because the field is transverse, there can be no π component. If the wave is propagating along an orthogonal axis, say the x-axis, it will be π-polarized if polarized along $\vec{z}$, and a balanced combination of σ_+ and σ_- if polarized along $\vec{y}$. Otherwise it has components on the three vectors of the spherical basis.

Now that we have a proper description of polarization for atoms and electric fields, the Hamiltonian can be written as:

$$H = H_0 + H_1,$$

$$\text{with} \qquad H_0 = -\hbar\omega_{eg}\sum_{\mu}|g,\mu\rangle\langle g,\mu| - \hbar\omega_{es}\sum_{\mu}|s,\mu\rangle\langle s,\mu|,$$

$$\text{and} \qquad H_1 = +\frac{\hbar}{2}\Omega_p e^{-i\omega_p t}\sum_{\mu}\sum_{q=-1,0,1} P_{\mu,\mu+q}\epsilon^{p}_{-q}|e,\mu+q\rangle\langle g,\mu| + h.c.$$
$$+\frac{\hbar}{2}\Omega_c e^{-i\omega_c t}\sum_{\mu}\sum_{q=-1,0,1} C_{\mu,\mu+q}\epsilon^{c}_{-q}|e,\mu+q\rangle\langle s,\mu| + h.c..$$

where the Rabi frequencies and Clebsch-Gordan coefficients are defined in the following equations using the Wigner-Eckart theorem:

$$P_{\mu,\mu+q} = \langle F_g,\mu|F_e,\mu+q;1,-q\rangle$$
$$C_{\mu,\mu+q} = \langle F_s,\mu|F_e,\mu+q;1,-q\rangle$$
$$\Omega_p = -\frac{\langle F_g||\vec{d}||F_e\rangle E_{p0}}{\hbar}$$
$$\Omega_c = -\frac{\langle F_s||\vec{d}||F_e\rangle E_{c0}}{\hbar}.$$

Using a rotating frame defined by Eq. (3.1.3) and:

$$F = -\hbar\omega_p\sum_{\mu}|g,\mu\rangle\langle g,\mu| - \hbar\omega_c\sum_{\mu}|s,\mu\rangle\langle s,\mu|,$$

one finds the following OBEs (considering only spontaneous emission as a decoherence mechanism):

$$
\begin{aligned}
\rho_{i,\mu}^{j,\nu} &= \langle i,\mu|\,\tilde{\rho}\,|i,\nu\rangle \\
\dot{\rho}_{g,\mu}^{g,\nu} &= -\frac{i}{2}\Omega_p \sum_q (P_{\mu,\mu+q}\epsilon_{-q}^{p*}\rho_{e,\mu+q}^{g,\nu} - P_{\nu,\nu+q}\epsilon_{-q}^{p}\rho_{g,\mu}^{e,\nu+q}) \\
&\quad + \delta_\mu^\nu \Gamma_{ge}\frac{2F_e+1}{2F_g+1}\sum_q P_{\mu,\mu+q}^2 \rho_{e,\mu+q}^{e,\mu+q} \\
\dot{\rho}_{s,\mu}^{s,\nu} &= -\frac{i}{2}\Omega_c \sum_q (C_{\mu,\mu+q}\epsilon_{-q}^{c*}\rho_{e,\mu+q}^{s,\nu} - C_{\nu,\nu+q}\epsilon_{-q}^{c}\rho_{s,\mu}^{e,\nu+q}) \\
&\quad + \delta_\mu^\nu \Gamma_{se}\frac{2F_e+1}{2F_s+1}\sum_q P_{\mu,\mu+q}^2 \rho_{e,\mu+q}^{e,\mu+q} \\
\dot{\rho}_{e,\mu}^{e,\nu} &= -\frac{i}{2}\Omega_p \sum_q (P_{\mu-q,\mu}\epsilon_{-q}^{p}\rho_{g,\mu-q}^{e,\nu} - P_{\nu-q,\nu}\epsilon_{-q}^{p*}\rho_{e,\mu}^{g,\nu-q}) \\
&\quad - \frac{i}{2}\Omega_c \sum_q (C_{\mu-q,\mu}\epsilon_{-q}^{c}\rho_{s,\mu-q}^{e,\nu} - C_{\nu-q,\nu}\epsilon_{-q}^{c*}\rho_{e,\mu}^{s,\nu-q}) - \Gamma\rho_{e,\mu}^{e,\nu} \\
\dot{\rho}_{g,\mu}^{e,\nu} &= -(i\delta + \frac{\Gamma}{2})\rho_{g,\mu}^{e,\nu} + \frac{i}{2}\Omega_c \sum_q C_{\nu-q,\nu}\epsilon_{-q}^{c*}\rho_{g,\mu}^{s,\nu-q} \qquad (3.1.7) \\
&\quad - \frac{i}{2}\Omega_p \sum_q (P_{\mu,\mu+q}\epsilon_{-q}^{p*}\rho_{e,\mu+q}^{e,\nu} - P_{\nu-q,\nu}\epsilon_{-q}^{p*}\rho_{g,\mu}^{g,\nu-q}) \\
\dot{\rho}_{s,\mu}^{e,\nu} &= -(i\Delta + \frac{\Gamma}{2})\rho_{s,\mu}^{e,\nu} + \frac{i}{2}\Omega_p \sum_q P_{\nu-q,\nu}\epsilon_{-q}^{p*}\rho_{s,\mu}^{g,\nu-q} \\
&\quad - \frac{i}{2}\Omega_c \sum_q (C_{\mu,\mu+q}\epsilon_{-q}^{c*}\rho_{e,\mu+q}^{e,\nu} - C_{\nu-q,\nu}\epsilon_{-q}^{c*}\rho_{s,\mu}^{s,\nu-q}) \\
\dot{\rho}_{g,\mu}^{s,\nu} &= -i(\delta-\Delta)\rho_{g,\mu}^{s,\nu} - \frac{i}{2}\Omega_p \sum_q P_{\mu,\mu+q}\epsilon_{-q}^{p*}\rho_{e,\mu+q}^{s,\nu} \qquad (3.1.8) \\
&\quad + \frac{i}{2}\Omega_c \sum_q C_{\nu,\nu+q}\epsilon_{-q}^{c}\rho_{g,\mu}^{e,\nu+q}.
\end{aligned}
$$

Supposing that at zeroth order in Ω_p only the $|g,\mu\rangle$ states are populated ($\rho_{i,\mu}^{j,\nu(0)} \propto \delta_i^g \delta_j^g$), one finds at first order in Ω_p, using Eq. (3.1.7) and Eq. (3.1.8):

$$
\begin{aligned}
(-\delta + i\frac{\Gamma}{2})\rho_{g,\mu}^{e,\nu} &= -\frac{1}{2}\Omega_p \sum_q P_{\nu-q,\nu}\epsilon_{-q}^{p*}\rho_{g,\mu}^{g,\nu-q(0)} \\
&\quad - \frac{\Omega_c^2}{4(\delta-\Delta)}\sum_{qq'} C_{\nu-q,\nu}C_{\nu-q,\nu-q+q'}\epsilon_{-q}^{c*}\epsilon_{-q'}^{c}\rho_{g,\mu}^{e,\nu-q+q'},
\end{aligned}
$$

or written in another form:

$$
M_\nu^0 A_\nu + M_\nu^{+1} A_{\nu+1} + M_\nu^{-1} A_{\nu-1} + M_\nu^{+2} A_{\nu+2} + M_\nu^{-2} A_{\nu-2} = B_\nu, \qquad (3.1.9)
$$

with the following definitions:

$$\begin{cases} A_\nu & = \rho_{g,\mu}^{e,\nu} \\ B_\nu & = -\frac{1}{2}\Omega_p \sum_q P_{\nu-q,\nu}\epsilon_{-q}^{p*}\rho_{g,\mu}^{g,\nu-q(0)} \\ J & = -\delta + i\frac{\Gamma}{2} \\ c & = \frac{\Omega_c^2}{4(\delta-\Delta)} \\ M_\nu^0 & = J + c(C_{\nu+1,\nu}^2|\epsilon_1^c|^2 + C_{\nu,\nu}^2|\epsilon_0^c|^2 + C_{\nu-1,\nu}^2|\epsilon_{-1}^c|^2) \\ M_\nu^{+1} & = c(C_{\nu+1,\nu}C_{\nu+1,\nu+1}\epsilon_1^{c*}\epsilon_0^c + C_{\nu,\nu}C_{\nu,\nu+1}\epsilon_0^{c*}\epsilon_{-1}^c) \\ M_\nu^{-1} & = c(C_{\nu,\nu}C_{\nu,\nu-1}\epsilon_0^{c*}\epsilon_1^c + C_{\nu-1,\nu}C_{\nu-1,\nu-1}\epsilon_{-1}^{c*}\epsilon_0^c) \\ M_\nu^{+2} & = cC_{\nu+1,\nu}C_{\nu+1,\nu+2}\epsilon_1^{c*}\epsilon_{-1}^c \\ M_\nu^{-2} & = cC_{\nu-1,\nu}C_{\nu-1,\nu-2}\epsilon_{-1}^{c*}\epsilon_1^c. \end{cases}$$

Our initial problem, involving a Hilbert space of dimension $(2F_g+1)(2F_e+1)(2F_s+1)$, is already drastically reduced to Eq. (3.1.9): a linear system of $2F_g+1$ equations. A is the vector of the $\rho_{g,\mu}^{e,\nu}$ coherences, which are essential for deriving the atomic susceptibility. B is directly linked to the probe polarization and to the initial atomic polarization in the $|g\rangle$ states. And the M coefficients correspond to the properties of the control beam (two-photon detuning, Rabi frequency and polarization). These equations can be inversed for every μ such that $-F_g \leq \mu \leq F_g$. Then, expressing the slowly-varying polarization of an ensemble of atoms under the presence of the control and weak probe fields $\tilde{\vec{P}} = 2n\langle F_g||\vec{d}||F_e\rangle \sum_{\mu q} P_{\mu,\mu-q}\rho_{e,\mu-q}^{g,\mu}\vec{u}_q^*$, one finds the linear electric susceptibility of the medium.

There are a few cases for which the result can be anticipated easily. Namely, when the quantification axis can be chosen such that the control-beam polarization vector is exactly one, and only one, of the three vectors of the spherical basis. The polarization of the control beam must be either π ($\mathcal{C}=0$), i.e. linearly polarized along z, or $\sigma_\pm$ ($\mathcal{C}=\pm1$), i.e. circularly polarized rotating around z. This results in $M_\nu^{\pm1} = M_\nu^{\pm2} = 0$ and Eq. (3.1.9) can be inversed easily: $\rho_{g,\mu}^{e,\nu} = B_{\nu,(\mu)}/M_\nu^0$. For an unpolarized atom[3], the resulting (normalized) susceptibility is[4]:

$$\vec{\mathcal{X}} = \vec{\chi}/\frac{2n\langle F_g||\vec{d}||F_e\rangle^2}{3\epsilon_0\hbar\Gamma} = \frac{3}{2(2F_g+1)}\sum_q\sum_\mu\left(\frac{P_{\mu,\mu-q}^2}{-\tilde{\delta}-\frac{i}{2}+\frac{\tilde{\Omega}_c^2}{4(\tilde{\delta}-\tilde{\Delta})}C_{\mu-q-\mathcal{C},\mu-q}^2}\right)\epsilon_q^p\vec{u}_q^*.$$

It is simply the sum of the EIT susceptibilities for each possible transition from $|g\rangle$ to $|e\rangle$ (i.e. whenever $P_{\mu,\mu-q}\neq0$), reducing to a simple 2-level atom Lorentzian when $C_{\mu-q-\mathcal{C},\mu-q}=0$. A drawing showing all the degenerate levels allows to identify a subset of independent ideal 3-level Λ-type systems. Examples are depicted on Figure 3.7 that will be commented in detail in a dedicated subsection below. An additional subset

[3] The initial populations in $|g\rangle$ are thus equal. If they are not, the different terms in the susceptibility are simply weighted by the populations of the different $|g,\mu\rangle$ states.

[4] $\sum_\mu P_{\mu,\mu-q}^2 = \frac{2F_g+1}{3}$, allowing for a simplification of the susceptibility to 2-level like when $\Omega_c=0$.

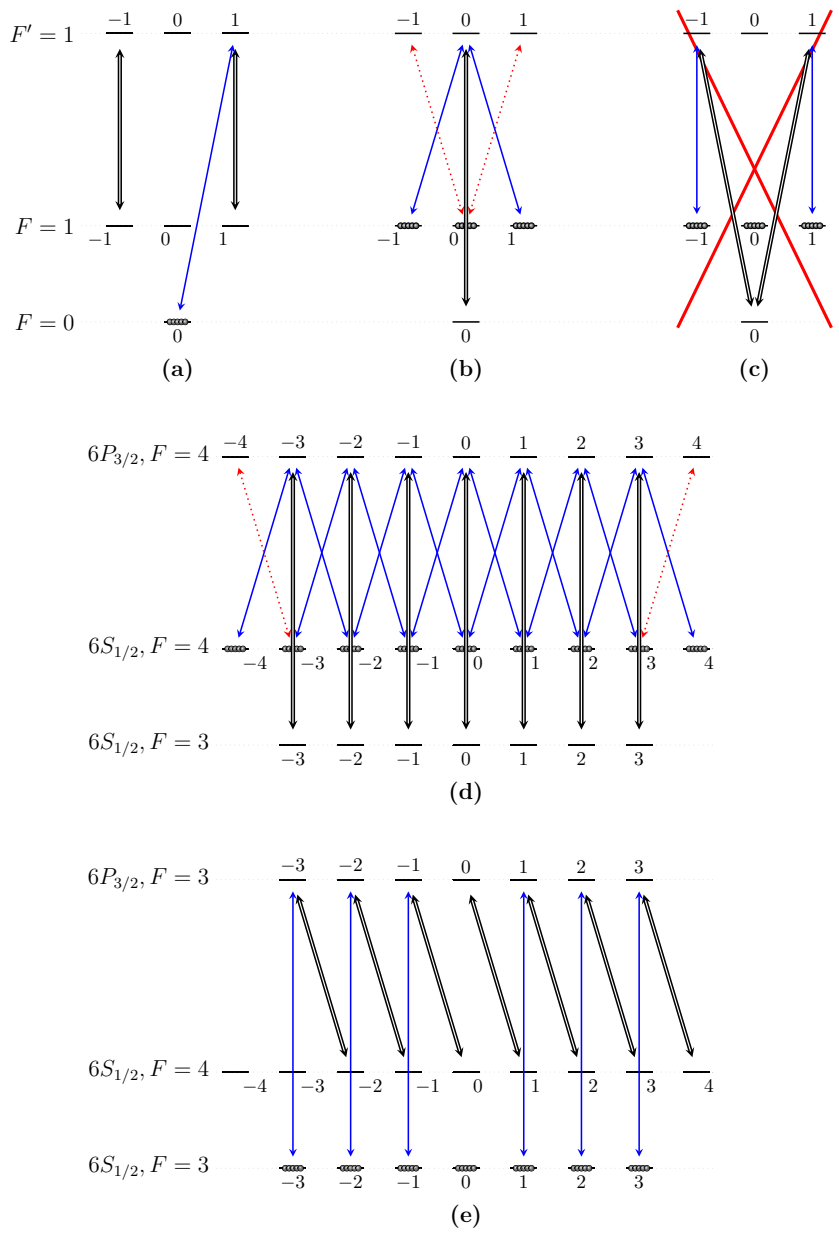

Figure 3.7: Level diagrams for different EIT configurations with Zeeman degenerate atoms. This figure is commented in detail in a paragraph below (paragraph 3.1.3). The control field is represented with double-arrows, while the probe is represented with single arrows, either blue when the transition is part of a Λ EIT system or red and dotted when it leads to absorption. The circles denote the initially populated states $|g,\mu\rangle$. (a) shows an ideal configuration for a simple atom. In (b) and (c), the probe and control beams are linearly polarized and orthogonal. The quantization axis is intentionally ill-chosen in (c). (d) is the configuration for cesium traditionally used in our team. (e) is a configuration for cesium compatible with perfect EIT.

(red and dotted arrows) can as well be identified for some configurations: it consists of 2-level systems for which $|g\rangle$ and $|e\rangle$ are coupled by the probe beam, but $|e\rangle$ cannot be coupled to any of the $|s\rangle$ states by the control beam. If some atoms are populated in the $|g\rangle$ state of a 2-level subset, they will absorb the probe and the EIT cannot be perfect. This unwanted residual absorption scales as $1 - e^{-\mathcal{X}\mathrm{OD}}$ where OD is the on-resonance optical depth when $\Omega_c = 0$, and will thus be significant in the large OD systems necessary for efficient memories. This is solved by choosing the proper light polarizations and hyperfine levels when possible or by pumping the atoms in well chosen Zeeman levels.

However, in general, when the control is not exactly π or $\sigma_\pm$, such a drawing is not sufficient to give any conclusion. When the control beam is a superposition of two or three components of the spherical basis, coherences can be built in the density matrix over more than two ground state levels, and if there is a dark state, it will have a rather complex expression. In this case, Eq. (3.1.9) has to be inversed. Note that, in this discussion, it is the polarization of the control that must have a simple expression, not the polarization of the probe. The difference between probe and control lies in the fact that the probe is treated perturbatively while the control is not.

We will now comment the configurations of Figure 3.7 and give examples of the obtained susceptibilities, derived with computer-aided inversion of the equations (Eq. (3.1.9)) when necessary[5]. This includes results of experimental interest for the cesium atom.

Detailed comments on Figure 3.7 –

- Diagram (a) shows one of the simplest configurations. The only populated $|g\rangle$ state ($|F = 0, m_f = 0\rangle$[6]) is involved in a Λ system with $|e\rangle = |F' = 1,1\rangle$ and $|s\rangle = |F = 1,1\rangle$. Ideal EIT will be obtained in this configuration.

- Diagrams (b) and (c) correspond to the same physical situation where the probe and control beam are linearly polarized and orthogonal. However, the quantization axis was intentionally ill chosen in (c). We can see in (b) that there will be residual absorption in this configuration (red, dotted arrows). In (c), it seems that the two states addressed by the probe are both involved in Λ systems. However, there are in fact two independent systems that are not shown straightforwardly by this drawing. The single $|s\rangle = |F = 0,0\rangle$ indeed couples to a single excited state $|e_\Lambda\rangle$, superposition of $|F' = 1, -1\rangle$ and $|F' = 1,1\rangle$, which itself couples to a single $|g_\Lambda\rangle$ state superposition of $|F = 1, -1\rangle$ and $|F = 1,1\rangle$, forming a Λ system as it appears on the drawing. The two states orthogonal to $|e_\Lambda\rangle$ and $|g_\Lambda\rangle$ in the respective $\{|F' = 1, -1\rangle, |F' = 1,1\rangle\}$ and $\{|F = 1, -1\rangle, |F = 1,1\rangle\}$ subspaces form a 2-level system leading to residual absorption.

- Diagram (d) corresponds to the situation commonly used in our group, using unpolarized cesium atoms initially pumped in $\{6S_{1/2}, F = 4\}$, and orthogonal linearly-polarized fields. It is clear here that imperfect EIT is expected: there

[5] See the Mathematica code EITzeeman-inversion.nb available online [webpage].

[6] From now on, such a state will be noted $|F = 0,0\rangle$ or even $|g,0\rangle$, with adapted notations for $|e\rangle$-type and $|s\rangle$-type states and to all possible values of m_f.

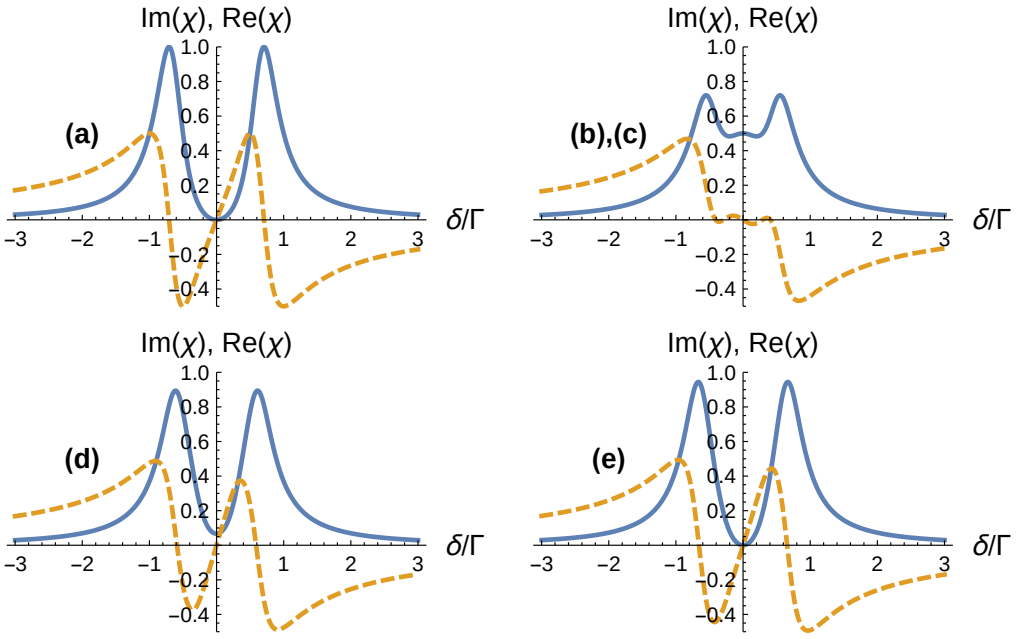

Figure 3.8: Atomic susceptibilities for the configurations of Figure 3.7 in units of $\frac{2n\langle F_g||\vec{d}||F_e\rangle^2}{3\epsilon_0\hbar\Gamma}$. Solid line: Imaginary part, Dashed line: Real part. Here $\Omega_c = 2\Gamma$ and $\Delta = 0$.

will be absorption from the $|F = 4, \pm 3\rangle$ states, although this is a decent choice of polarizations for such a combination of states. Note that this drawing corresponds to experiments where the probe and control fields are propagating in free space, but also approximately to the configuration used in the next, experimental, section (section 3.2) involving a nanofiber-guided probe. Indeed, the nanofiber-guided probe is chosen quasi-linearly polarized orthogonally to the control field linear polarization. At the maximum of intensity of the quasi-linearly polarized HE_{11} mode, the local polarization is elliptic. It is expressed as a superposition of σ_+ and σ_- if the quantization axis is chosen along the control polarization axis. Thus, at this maximum of intensity the diagram (d) is indeed pertinent.

- Diagram (e) corresponds to the only possible choice of hyperfine levels for perfect EIT when using unpolarized cesium and the D_2 spectroscopic line. With this choice of hyperfine levels, whatever the polarization of the fields, the control beam addresses all the possible excited states and there is no residual absorption. A particular choice of polarization is shown here. Experimentally, orthogonal polarizations will be preferred for easier filtering of the control beam out from the detection path (see paragraph 3.2.1.4).

Examples of susceptibility – Figure 3.8 shows plots of the susceptibilities obtained for the different configurations considered above. This results in more complex absorption profiles than for the ideal Λ-type atom.

For the configuration (d), for example, the susceptibility is proportional to:

$$\frac{1}{6}\left(\frac{1/2}{\frac{\tilde{\Omega}_c^2}{9\tilde{\delta}}-\tilde{\delta}-\frac{i}{2}}+\frac{19/20}{\frac{5\tilde{\Omega}_c^2}{48\tilde{\delta}}-\tilde{\delta}-\frac{i}{2}}+\frac{4/5}{\frac{\tilde{\Omega}_c^2}{12\tilde{\delta}}-\tilde{\delta}-\frac{i}{2}}+\frac{11/20}{\frac{7\tilde{\Omega}_c^2}{144\tilde{\delta}}-\tilde{\delta}-\frac{i}{2}}+\frac{1/5}{-\tilde{\delta}-\frac{i}{2}}\right).$$

Each term corresponds to a particular subset of atomic levels. The last term is brought by the two 2-level subset $\{|g,\pm 3\rangle, |e,\pm 4\rangle\}$. The other terms correspond from left to right to the following Λ subsets:

$\{|g,\pm 1\rangle, |e,0\rangle, |s,0\rangle\}$,

$\{|g,0\rangle, |e,\pm 1\rangle, |s,\pm 1\rangle\}$ and $\{|g,\pm 2\rangle, |e,\pm 1\rangle, |s,\pm 1\rangle\}$,

$\{|g,\pm 1\rangle, |e\pm 2\rangle, |s\pm 2\rangle\}$ and $\{|g\pm 3\rangle, |e\pm 2\rangle\, |s\pm 2\rangle\}$,

$\{|g,\pm 2\rangle, |e,\pm 3\rangle, |s,\pm 3\rangle\}$ and $\{|g,\pm 4\rangle, |e,\pm 3\rangle, |s,\pm 3\rangle\}$.

The residual on resonance optical depth is OD/15, leading for example to a limited transmission of 37% when OD=15. This value is comparable to the 45% transmission recorded in the freespace experiment for the same OD [Nicolas14]. The lower absorption recorded in the experiment may be explained by the day-to-day optimization of the transparency, which could have led to a partial optical pumping of the atoms (via an asymmetric alignment of the MOT beams for instance) into a more favorable balance of Zeeman-sublevel populations.

As a conclusion for this section, we have extended the OBEs formalism of EIT to Zeeman degenerate atoms. Proper choices of hyperfine levels, polarizations of light, and possibly pumping in a given Zeeman sublevel are required to obtain perfect EIT in experiments. For complex configurations, i.e. when the control beam has a polarization with different component of the spherical basis, the resulting susceptibility can be computed numerically. More generally, the OBE formalism can be extended to more complex atomic systems as soon as one can handle, possibly with the help of computers, the ever larger Hilbert spaces involved. An important step for experiments is to take into consideration not only one hyperfine excited, but also the other possible excited states of the D_2 line of cesium (see for example [Sheremet10, Mishina11]).

3.1.4 Dynamic EIT and the classical dark-state polariton

It this section, we consider again the ideal Λ-type atomic medium and address the consequence of adiabatic variations of the control beam Rabi frequency [Fleischhauer00, Raczyński13]. The immediate consequence will be the application of this dynamic EIT as a reversible memory for light.

We have to go back here to the OBEs in the weak probe limit, but without supposing the steady state regime. Note that although we will consider variations of the control beam Rabi frequency, we will neglect the effects of the control beam propagation supposed much faster than the probe (which is experiencing slow light effect). The control beam Rabi frequency is thus supposed uniform in the atomic medium.

Before considering the OBEs again, let us have a closer look at Maxwell equations. Considering plane waves and scalar fields, the probe's electric field propagates with the following wave equation:

$$\frac{\partial^2 E_p(z,t)}{\partial z^2} - \frac{\partial^2 E_p(z,t)}{c^2 \partial t^2} = \mu_0 \frac{\partial^2 P(z,t)}{\partial t^2}.$$

Defining slowly-varying complex amplitudes,

$$\begin{aligned}
E_p(z,t) &= \varepsilon_p(z,t)\frac{e^{i\omega_p(\frac{z}{c}-t)}}{2} + c.c. = E_{0p}(z,t)\frac{e^{-i\omega_p t}}{2} + c.c. \\
P(z,t) &= p(z,t)\frac{e^{i\omega_p(\frac{z}{c}-t)}}{2} + c.c. \\
\Omega_p(z,t) &= \Omega_p\frac{e^{i\omega_p\frac{z}{c}}}{2} + c.c. \\
\rho_{eg}(z,t) &= \varrho_{eg}\frac{e^{i\omega_p(\frac{z}{c}-t)}}{2} + c.c.,
\end{aligned}$$

and using the slowly-varying-envelope approximation [Raczyński13] leads to:

$$(\frac{\partial}{\partial t} + c\frac{\partial}{\partial z})\varepsilon_p(z,t) = \frac{i\omega_p}{2\epsilon_0}p(z,t),$$

or, in terms of Rabi frequency and atomic coherence:

$$(\frac{\partial}{\partial t} + c\frac{\partial}{\partial z})\Omega_p(z,t) = -\frac{i\omega_p n d_{ge}^2}{\hbar\epsilon_0}\varrho_{eg}(z,t).$$

This equation and the relevant OBEs are the Maxwell-Bloch equations for EIT. We consider the weak probe and $\delta = \Delta = 0$ limit, which results in:

$$\begin{cases}
(\frac{\partial}{\partial t} + c\frac{\partial}{\partial z})\Omega_p(z,t) & = -i\kappa^2\varrho_{eg}(z,t) \\
\dot{\varrho}_{eg} & = -\frac{i}{2}\Omega_p - \frac{i}{2}\Omega_c\varrho_{sg} - \frac{\Gamma}{2}\varrho_{eg} \\
\dot{\varrho}_{sg} & = -\frac{i}{2}\Omega_c\varrho_{eg}.
\end{cases}$$

In the adiabatic conditions (slow variations of Ω_c as discussed in [Fleischhauer00]), these equations lead to

$$\varrho_{sg} = -\frac{\Omega_p}{\Omega_c},$$

and finally

$$(\frac{\partial}{\partial t} + c\frac{\partial}{\partial z})\Omega_p(z,t) = -2\frac{\kappa^2}{\Omega_c}\frac{\partial}{\partial t}\frac{\Omega_p(z,t)}{\Omega_c(t)}.$$

This wave equation has a simple expression if we introduce the so-called *dark-state polariton* defined as:

$$\begin{cases}
\Psi(z,t) & = \cos(\gamma)\Omega_p(z,t) - \sqrt{2}\kappa\sin(\gamma)\varrho_{sg}(z,t) \\
\cos(\gamma) & = \frac{\Omega_c}{\sqrt{\Omega_c^2 + 2\kappa^2}} \\
\sin(\gamma) & = \frac{\sqrt{2}\kappa}{\sqrt{\Omega_c^2 + 2\kappa^2}}.
\end{cases}$$

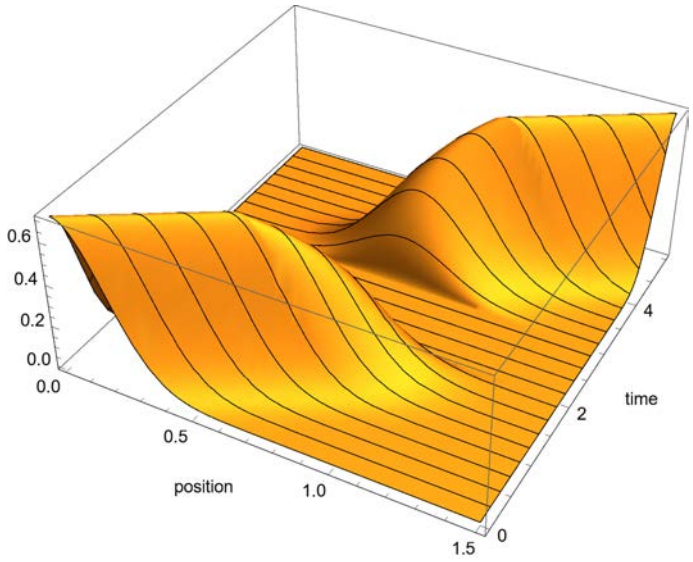

Figure 3.9: Electric field component of a Gaussian pulse during the memory protocol. As the control beam power is ramped down (from $t = 1$ to $t = 2$), the velocity and the field amplitude are reduced to zero. The stored pulse is retrieved by turning back on the control beam (from $t = 4$ to $t = 5$).

The wave equation is then

$$\Big(\frac{\partial}{\partial t} + c\cos^2(\gamma)\frac{\partial}{\partial z}\Big)\Psi(z,t) = 0,$$

and the solution can be written as:

$$\Psi(z,t) = \Psi\Big(z - c\int_0^t \cos^2(\gamma(t'))dt',\ t = 0\Big).$$

This describes simple propagation of a pulse with a group velocity $v_g = c\cos^2(\gamma) = c\frac{\Omega_c^2}{\Omega_c^2+2\kappa^2}$. If γ is changed, the shape is preserved while the velocity changes, as well as the light ($\Omega_p = \cos(\gamma)\Psi$) and matter ($\varrho_{sg} = -\frac{1}{\sqrt{2}\kappa}\sin(\gamma)\Psi$) components of the polariton.

Let's consider now the *memory protocol* illustrated in Figure 3.2 and Figure 3.9: the control beam is ramped down to zero while a probe pulse is propagating in EIT conditions. The velocity of the polariton is as well ramped down to zero, and the polariton is made only of its matter component. The pulse is thus stored as an atomic excitation which can be retrieved by turning back on the control beam.

Since the pulse shape is preserved while ramping down the control beam, but its velocity decreases, its spectral width decreases accordingly and it conveniently always fits in the transparency window[7]. Also, note that the storage time will be limited by the lifetime of the atomic coherence ρ_{gs}.

We already mentioned that a large 2-level optical depth is important for slow-light experiments. This parameter is even more important in the memory protocol. Indeed,

[7]The spectral width of a pulse of spatial length l propagating at speed v_g is proportional to v_g/l. So if l is conserved, the spectral width decreases proportionally to v_g.

for the storage to be efficient, the input pulse must fit into the atomic medium. This means that the pulse length, when propagating in the cloud, must be smaller than the cloud length. This is made possible by the spatial compression of the pulse inherent to its slower velocity when propagating in EIT conditions. It is optimized with large slow-light delays, obtained as we already said with both larger atomic densities and longer clouds, i.e. large OD. Also, note that the temporal length of the input pulse, which should be as short as possible according to our present discussion, is constrained by the spectral response of the medium: i.e. the spectral width of the susceptibility.

As a conclusion here, we have introduced the classical dark-state polariton picture to account for dynamic variations of the control beam power during EIT. The application is a memory for light in high optical depth media. The next step will be the quantization of the electro-magnetic field, in order the show how quantum information can be preserved in this memory process.

3.1.5 The quantum dark-state polariton

I mentioned the field of quantum optics a few times already, but never wrote anything specific about the quantum state of light - its object of study. This paragraph will briefly mention how the slowly propagating probe field of EIT can be quantized. The result is a description in terms of the so-called *dark-state polariton*, a quantum bosonic field involving both a light field component and a matter component consisting of atomic dark-states. Its application is the use of EIT systems as memories for light that preserve the quantum information carried by such light. Different kind of quantum optics protocols can as well be implemented with very similar physics [Duan01, Hammerer10].

In this section, I will naively follow the original article introducing dark-state polaritons [Fleischhauer00]. This is rather straightforward with the notions and derivations introduced previously. We first introduce the quantized electric field slowly-varying amplitude, as well as slowly-varying atomic operators averaged over a small volume containing $N_z \gg 1$ atoms:

$$\hat{E}(z,t) = \frac{i}{2}\sqrt{\frac{2\epsilon_0 V}{\hbar\omega_p}}\hat{\varepsilon}_p(z,t) = \sum_k \hat{a}_k(t)e^{ikz}e^{-i\omega_p(\frac{z}{c}-t)}$$

$$\hat{\sigma}_{\alpha\beta}(z,t) = \frac{1}{N_z}\sum_{j=1}^{N_z} |\alpha_j\rangle\langle\beta_j| e^{-i\omega_{\alpha\beta}t},$$

where V is the quantization volume. The interaction Hamiltonian is now:

$$H_1 = \frac{\hbar N}{2}\int \frac{dz}{L}\Big(g\sum_k a_k e^{ikz}\hat{\sigma}_{ge}(z,t) + \Omega_c\hat{\sigma}_{se}(z,t)\Big) + H.c.,$$

with $g = -d_{ge}\sqrt{\frac{2\omega_p}{\hbar\epsilon_0 V}}$.

The equations of motion are very similar to the classical equations. The electric field evolution is governed by:

$$(\frac{\partial}{\partial t} + c\frac{\partial}{\partial z})\hat{E}(z,t) = -\frac{i}{2}gN\hat{\sigma}_{ge}.$$

The expression of the dark-state polariton is now

$$\begin{cases} \hat{\Psi}(z,t) & = \cos(\gamma)\hat{E}(z,t) - \sin(\gamma)\sqrt{N}\hat{\sigma}_{gs}(z,t) \\ \cos(\gamma) & = \dfrac{\Omega_c}{\sqrt{\Omega_c^2 + g^2 N}} \\ \sin(\gamma) & = \dfrac{g\sqrt{N}}{\sqrt{\Omega_c^2 + g^2 N}}, \end{cases}$$

and its propagation described by

$$\Big(\frac{\partial}{\partial t} + c\cos^2(\gamma)\frac{\partial}{\partial z}\Big)\hat{\Psi}(z,t) = 0.$$

Let us now consider the Fourier transform:

$$\hat{\Psi}(z,t) = \sum_k \hat{\Psi}_k(t)e^{ikz}.$$

One can define Fock states as

$$|D_k^n\rangle = (\hat{\Psi}_k^\dagger)^n\,|0\rangle\,|g_1,g_2,...g_N\rangle\,,$$

where $|0\rangle$ is the electromagnetic vacuum and $|g_1,g_2,...g_N\rangle$ indicates that all atoms are in $|g\rangle$ state.

These states are dark states, with the same meaning than in subsection 3.1.1 where we considered a single atom. Indeed, there is no excited atomic component $|e\rangle$, and the states verify:

$$H_1\,|D_k^n\rangle = 0.$$

Note also that, still in the weak-probe regime[8], the operators $\hat{\Psi}_k$ have bosonic commutation rules $[\hat{\Psi}_k,\hat{\Psi}_{k'}^\dagger] = \delta_{k,k'}$.

We thus have a description of propagation in EIT in terms of quantum bosonic quasi-particles. They are very similar to photons, but have richer properties which can be controlled with a classical tool: the control beam.

In particular, one can store and retrieve the quantum state of an input light pulse. The state is stored as a collective quantum superposition of atomic excitations. A single photon for instance, will be mapped to a superposition involving all the states for which a single atom is transferred into $|s\rangle$. This collective excitation can be written as:

$$|S\rangle = \frac{1}{\sqrt{N}}\sum_{i=1}^{N} f_i\,|g_1,g_2,...,g_{i-1},s_i,g_{i+1},...,g_N\rangle\,,$$

where f_i is related to the stored wavepacket shape. In the experimental implementations, different mechanisms will always induce a time evolution of this collective state. Those mechanisms will be responsible for a loss of the stored information as detailed in subsection 3.2.5.

[8]More precisely by considering that the density of photons is much smaller than the density of atoms.

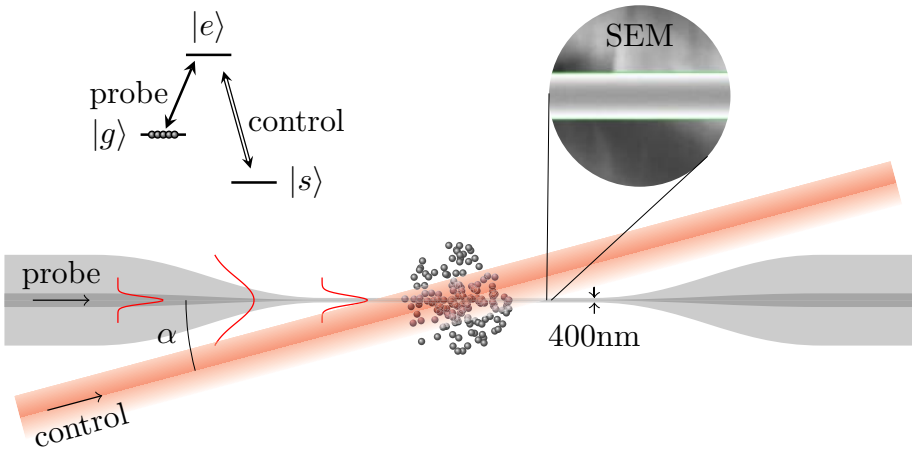

Figure 3.10: Illustration of the EIT scheme, for a nanofiber-guided probe and a control beam propagating in free space. The angle α is around 13°.

Section summary

In this theoretical section, we first introduced the phenomenon of *electromagnetically induced transparency* in an ideal Λ-type 3-level atom.

With the help of the *optical Bloch equations*, we then considered the *slow light* effect and we discussed some technical considerations required for experimental implementations of EIT. In particular, we derived the EIT susceptibility for atoms of arbitrary angular momentum, excited by probe and control fields of *arbitrary polarization*. We introduced as well the *dark-state polariton* formalism. Dynamic EIT in atomic ensembles can serve as a platform for *quantum memories* for light in *high optical depth* media.

The following section will go back to the experimental setup described previously. It will report how EIT and a memory for light at the single-photon level was implemented in our cold atom/nanofiber interface.

3.2 Experimental evidence of EIT for a nanofiber guided probe

In the previous chapters, we discussed the different elements of our experimental setup enabling to study the interaction between laser beams tightly confined in an optical nanofiber and a cold cesium cloud. The cesium atoms are loaded in a magneto-optical trap and released. The experiment is then started while the cloud is in free-fall around the fiber.

The optical depths obtained, a few units as shown in chapter 2, are high enough to consider studying EIT-based memory experiments introduced in the previous section (section 3.1). In addition to the probe beam, a second beam with relatively high power is shone on the atomic cloud, giving control on the probe propagation. This configuration is illustrated in Figure 3.10.

A memory for the guided light is obtained by switching off the control beam when

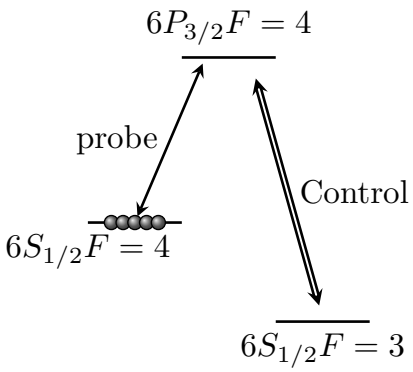

Figure 3.11: Energy level diagram used for the EIT experiment.

the probe pulse is propagating through the atomic cloud. The light pulse is then stored as a coherent superposition of the different possible atomic states. Turning back on the control beam allows to read the light pulse, and the information it may contain, from the memory.

The experiments presented here were proposed theoretically more than ten years ago [Patnaik02]. Similar experimental results were obtained simultaneously than ours in Vienna [Sayrin15]. Our work is reported in [Gouraud15].

The section in organized in the following way. In a first subsection, details are given on the experimental parameters required to observe EIT. In the following subsection, observation of EIT and slow light is reported. Data for the memory experiment is then analyzed. Finally, the lifetime of the memory is studied together with the observation of collapses and revivals of the collective atomic excitation in controlled magnetic fields.

3.2.1 Some experimental parameters

Figure 3.11 shows the atomic level diagram used for the EIT experiments. Atoms are prepared in the Zeeman degenerate state $|g\rangle = \{6S_{1/2},F = 4\}$. The excited state is $|e\rangle = \{6P_{3/2},F = 4\}$ in the D_2 line, while the third state of EIT is the other hyperfine ground state of cesium $|s\rangle = \{6S_{1/2},F = 3\}$.

Different other experimental parameters important for the experiment will be discussed below.

3.2.1.1 The control beam path

For extended coherence time with moving atoms, the control beam should preferably be co-propagating with the probe beam (subsection 3.2.5). Yet, this is unpractical for measurements where the probe beam (possibly with powers corresponding to less than a single photon per pulse) should be detected independently from the control beam. A relatively small angle can be used as a separation and chosen as a compromise between coherence time and spatial modes distinction. A good compromise for cesium released from a MOT is usually a few degrees [Veissier13]. For technical reasons, in our nanofiber experiment, the lowest possible value was $\alpha \sim 13°$ and was thus chosen for the control beam path.

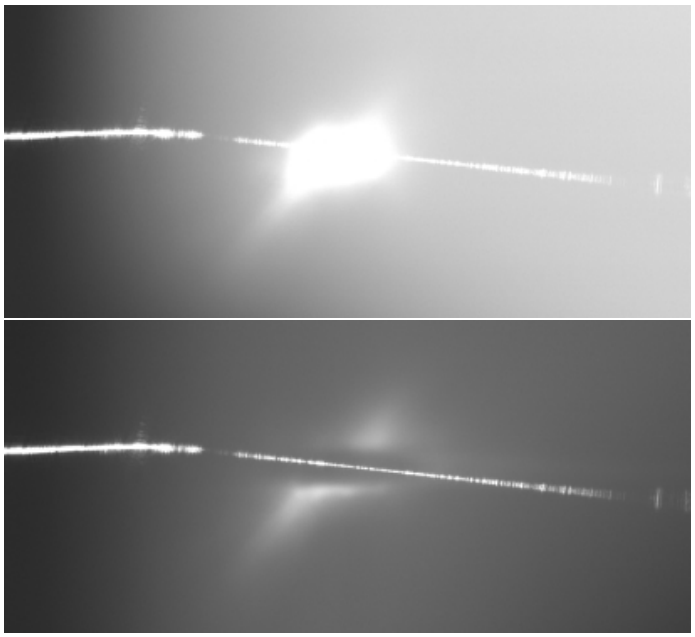

Figure 3.12: Pictures of the MOT when aligning the control beam. In the top picture, no light is shone through the control beam path. In the bottom picture, resonant light (a fraction of milliwatt) was sent through the control beam path, pushing the atoms away and showing the beam position relative to the cloud and to the fiber.

Interestingly, choosing a small angle is less important when the probe typical spatial extension is the wavelength λ, which is the case in the nanofiber experiment. Indeed, as detailed in subsection 3.2.5, loss of coherence by motional dephasing appears when atoms travel over a distance $\lambda/(4\pi \sin(\alpha/2))$, always comparable to or larger than λ. Minimizing α is consequently not so important here: after traveling over this distance, atoms will be lost from the probing region anyway.

Using a co-propagating fiber-guided control beam is actually possible and is the choice made in [Sayrin15]. Here the control beam is guided and focused by the nanofiber, thus less power is required than for a free-space propagating control beam. This means that less filtering (see subsubsection 3.2.1.4) is required, making this scheme experimentally compatible as well with single photons in the probe beam. It also means that such a control beam might be able to trigger transparency with only a few control photons. In the latter experiment ([Sayrin15]) as well as in our future experiments (chapter 4), the atoms are trapped in potential wells of sub-wavelength dimensions, the above-mentioned concerns about atomic motion do not hold. They are replaced by considerations on lifetime and coherence in dipole traps (which include phenomena related to atomic motion).

The control beam is chosen collimated and relatively large - the waist size is $w_0 = 400\ \mu$m - in order to shine the whole part of the cloud overlapping the nanofiber. The overlap between the beam and the nanofiber is ~ 3.5 mm long. This is actually a bit smaller than the ideal size in our experiment. However the beam size must stay compatible with the available laser power.

The beam is first aligned with the method illustrated in Figure 3.12. The MOT is left continuously on and imaged with cameras in different directions. The atomic cloud is visible because it continuously scatters the light from the cooling beams. A laser resonant with the $\{6S_{1/2},F=4\} \rightarrow \{6P_{3/2},F=5\}$ transition is coupled into the control beam path. The first element of this path is indeed an optical fiber which may easily be connected to different lasers. A fraction of a milliwatt of such a beam resonant with the MOT cooling transition is enough to make a hole in the cloud. The beam is then aligned until the hole covers the region where the atomic cloud and the nanofiber overlap.

Optionally, we can proceed to a second alignment method. Light is sent through nanofiber already in EIT conditions and the transmitted power monitored with a sensitive detector as in section 2.3. Because of the very low power required to avoid saturation, the signal-to-noise ratio can be unpractical during this alignment step. If the signal is large enough though, the control beam path can then be further optimized for both a high transparency and a low coupling of the control beam into the nanofiber[9].

3.2.1.2 Canceling the magnetic field

Another important parameter that can lead to decoherence is the residual magnetic field (subsection 3.2.5). This is because the atomic states used for EIT are Zeeman degenerate, and all the involved sub-levels have different sensitivities to the magnetic field. The magnetic field gradient used for the magneto-optical trap must be shut off (section B.2), but also the environing magnetic field (including the Earth field) which is canceled using 3 pairs of bias coils. The magnetic field is measured by performing the Zeeman level spectroscopy as described in section B.1. After cancellation, the residual field shows variations of $\sim$ 20 mG magnitude. This result is mainly limited by the slow decay of eddy currents in our setup.

3.2.1.3 Polarizations

With the level scheme chosen (Figure 3.11), the polarizations of the probe and the control should preferably be linear and orthogonal (even though some residual absorption will remain). As discussed before (paragraph 3.1.3), this choice can be made compatible with a nanofiber-guided probe. The control beam polarization is first set linear and horizontal. We chose here the control beam polarization axis as the quantization axis, the control beam is thus π-polarized. Then, using the technique described in section 1.3, the probe is set quasi-linearly polarized vertically. The local polarization at the maximum of intensity is thus a combination of σ_+ and σ_-, rather similar to the polarization of a vertically-polarized free-space-propagating probe.

This choice of polarization is also useful for easier filtering as we will see below and will be justified as well with the experimental results.

3.2.1.4 Working at the single-photon level

We already mentioned that the interaction between a nanofiber guided probe and the atoms surrounding the fiber exhibits low power saturation. In order to avoid

[9]This leads to an undesired background noise at detection that will be further discussed below.

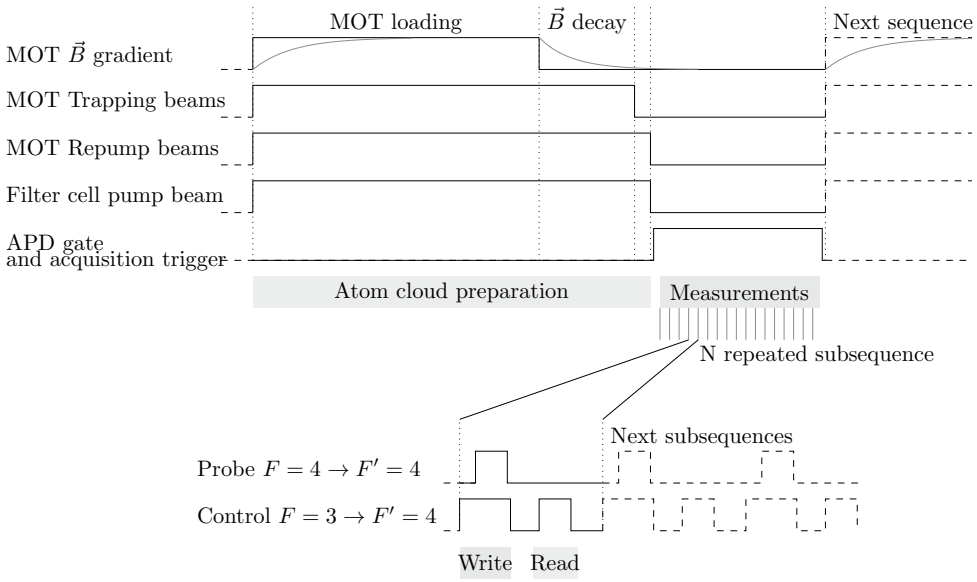

Figure 3.13: Typical experimental sequence when working in the photon-counting regime for EIT and memory experiments. Once the atoms are in free expansion around the nanofiber and the magnetic field has decayed, starts the measurement interval (1 ms). During this interval many repetitions of the same protocol (typically 1 μs for each subsequence) are repeated. Data from all those repetitions, possibly over many MOT cycles, are gathered together to build statistics.

any saturation effect, we thus work at very low power of the probe beam and use photon-counting devices as detectors[10]. The experiments are repeated many times and the results processed by statistical analysis, typically building histograms from photo-detection events.

Building statistics – The typical timing sequence is shown in Figure 3.13. The MOT is loaded (40 ms), released and the magnetic field is left decaying for a few milliseconds (4.4 ms). Then starts the 1 ms measurement measurement interval. This measurement interval is typically splitted into a thousand repetitions of a 1 μs long experiment. This can consist of sending a probe pulse for measurement of its absorption, or e.g. of a full memory protocol with read and write steps.

The photon counting module output is made of individual electric pulses sent for each photo-detection event. The arrival times are recorded using an FPGA based device (Appendix A), and transferred to a computer for analysis.

The most simple result is the probability of detection in the experiment interval. It can be compared for different experimental configurations in order to compute a physically meaningful result. For example, absorption will be defined as the detection probability of a probe pulse when atoms are present divided by the detection probability when no atoms are loaded in the MOT (background noise can be measured and

[10]SPCM-AQR-14-FC, also referred to as avalanche photodiode - or APD - in the text.

substracted accordingly).

Another typical result is the histogram of photo-detection arrival times: the probability for a detection to occur as a function of time during a repetition of the experiment, i.e. a single subsequence in Figure 3.13. This histogram actually gives the shape of the weak coherent light pulses involved in the experiment (see subsection 3.2.4 for examples).

Filtering – Another reason for using very low power probes, is our goal to show that our experiments are compatible - in terms of noise level - with single photons. Such single photons could be stored or processed in quantum information protocols.

Working at those very low powers requires to get rid of the contamination from the control beam in the detection path. Indeed, part of the control beam couples from free-space into the guided mode with about 10^{-8} efficiency. For this purpose, we use polarization filtering at the fiber output, taking advantage of the experimental fact that the control couples into the nanofiber with a quasilinear vertical polarization, thus orthogonal to the signal polarization.

Additional filtering based on the different frequencies of the probe and control beams is performed. Because of the very small frequency difference between the beams, i.e. 9.2 GHz, this could be hard to implement. However, since we use a resonant control beam in our experiments, it can be conveniently filtered out with a cesium vapor pumped in $|s\rangle = \{6S_{1/2},F = 3\}$. We use here a glass cell filled with cesium pumped by a laser beam[11] on the $\{6S_{1/2},F = 4\} \rightarrow \{6P_{3/2},F = 4\}$ transition. The pump beam is shut off during the measurement interval as shown in Figure 3.13 such that the scattered pumping light is not detected. The ground state coherence time in the filter cell must be longer than the measurements interval. This is made possible by using a cell coated with paraffin on the internal surface.

The *queusot*[12] is heated to about 37°C in order to increase the vapor density and thus the optical depth and the filtering efficiency. However, heating the cell also decreases the coherence time. The temperature was thus chosen as a compromise between the filtering efficiency and a coherence time larger than the millisecond scale. The filter cell is mounted on a small optical breadboard on which the signal to be filtered travels in free space from a fiber to another one, the polarization filter being mounted on the same breadboard.

With these two cascaded methods of filtering, the remaining light at the detection stage is overall about 10^{14} times smaller than the initial control power.

3.2.2 Transparency

We now present the experimental data. Figure 3.14 provides the absorption of the guided probe as a function of its detuning for different powers of the control beam. The regular Lorentzian absorption profile when no control beam is applied is given

[11] >10 mW, ∼1 inch wide, passing two times through the cell.

[12] This French word refers to the small tube used to fill the cell. Cesium is condensed in the queusot which is heated in order to increase the pressure in the cell. The other surfaces are heated to a higher temperature, close to 50°C, in order to avoid any undesired condensation. The surfaces used for the optical paths cannot be directly in contact with heating elements though, and are harder to heat. Care is required when heating in order not to damaged the paraffin.

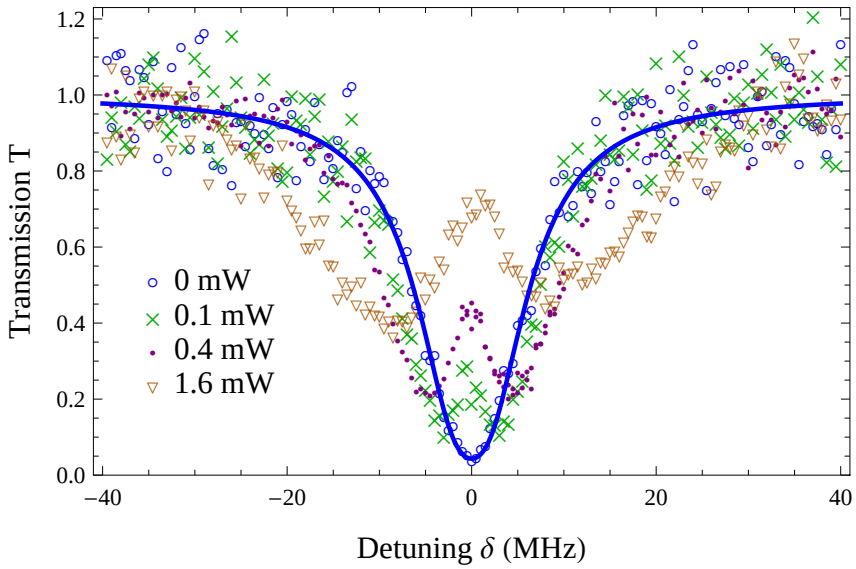

Figure 3.14: Transmission of a weak nanofiber guided probe as a function of its detuning δ from resonance. The data is given here in EIT conditions for different powers of the control beam. The blue curve and data points show the usual Lorentzian absorption when no control beam is present.

for reference. In the results shown here, the control beam is always resonant with the $|s\rangle \rightarrow |e\rangle$ transition.

The general behavior of EIT is observed. The control beam opens a transparency window centered on the two-photon resonance. For a larger control beam power, the on-resonance transparency gets larger as well as the window width.

However, this experimental data cannot be fitted with simple models of EIT. Both a model of a Λ-type 3-levels atom including ground state decoherence (Eq. (3.1.6)), or a model including Zeeman degeneracy (with no ground state decoherence, subsection 3.1.3) fail to fit the experimental data. A full model should include the complexity of the guided light polarization and its evanescent nature, as done in [Le Kien09], but also, importantly, the complex level structure of atomic Cs, including Zeeman levels and other excited levels of the $6P_{3/2}$ manifold, as testified by the damping and asymmetries of the resonances [Giner13a].

3.2.3 Slow light

After having observed transparency, we measure the delay, i.e. the slow-light effect, resulting from pulse propagation under EIT condition. As a signal, we use weak laser pulses at the single-photon level. Results are displayed in Figure 3.15, showing the photo-detection probability as a function of time on two-photon resonance, again for different powers of the control beam.

The reference curve, when there are no control beam nor atoms around the fiber, has the shape of the input pulse for this set of data. Because the pulses are rather short (hundreds of nanoseconds), their high-frequency components are not negligible

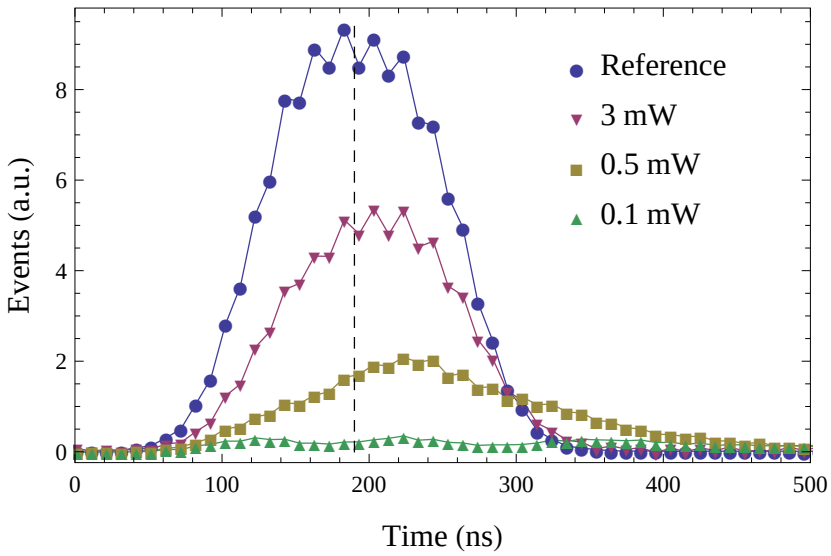

Figure 3.15: Detection event probability as a function of time, for a nanofiber guided probe and different powers of the control beam. The reference curve corresponds to a pulse propagating in the nanofiber when no atoms nor control beam are present. The dashed line gives the mean arrival time of this reference pulse. The other curves are for EIT conditions.

compared to the atomic natural linewidth, and propagation in the medium will result in a complex frequency filtering. Here the pulse is shaped as a Gaussian pulse, rather than as a simple square pulse, in order to minimize the role of high-frequency components which would not interact with the atomic medium.

When atoms and a control beam are added, some transparency is observed as described above, but a delay of the pulse can be observed as well. This is the slow light effect.

The delay can be defined quantitatively as the mean photo-detection time after substraction of the background noise. Measured when no probe pulse is sent, but however with a control beam continuously on, this noise includes contamination from the control beam as well as the different other noises occurring in the detection process usually very close to the expected dark noise of the detection device. With this definition, the delays for the plotted curve are about 20 ns for a 3 mW control beam and 60 ns for a 0.5 mW control beam. A 60 ns delay corresponds approximately to a reduction of the group velocity by a factor 3000 compared to propagation in the optical nanofiber. Also, note that the shape of the pulses are changed at the fiber output, because of the frequency filtering mentioned above and in contrast to what is expected from the theory of an ideal dark state polariton.

3.2.4 Implementation of the memory protocol

The next step is the realization of dynamic EIT and of the memory protocol for the guided light. A probe pulse is sent through the nanofiber in EIT conditions, and while

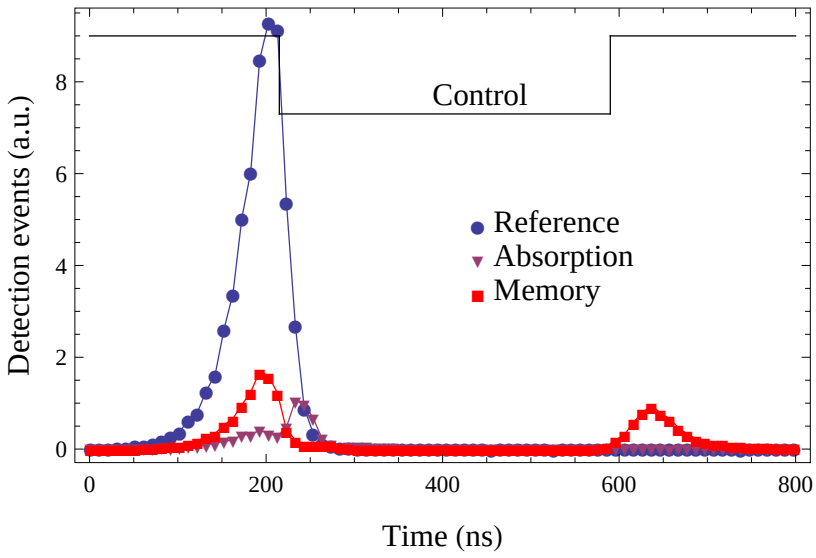

Figure 3.16: Detection histograms for the memory protocol. The *reference* gives the shape and amplitude of the input pulse, no atoms are present. For the *absorption* curve, atoms are present but there is no control beam. The *memory* curve corresponds to the data when the memory protocol is implemented. Part of the input pulse leaks out of the memory at storage time (around 200 ns). $10 \pm 0.5\%$ of it is retrieved after a chosen delay (here starting from t = 600 ns). The black line indicates when the control beam (0.3 mW) is turned off and on for the successive storage and retrieval steps. The mean photon number per pulse in the reference is equal to 0.6 ± 0.1.

it is slowly propagating, the control beam is turned off. At this point, the input pulse is stored as a collective excitation in the atomic medium, and can be retrieved later on demand.

Figure 3.16 displays the measured histograms for the memory protocol with red squares. The first pulse in this curve (at time t=200 ns) is due to leakage during storage : part of the input pulse doesn't fit into the atomic medium and reaches the detector at the same time than a reference pulse (obtained with no atoms, and displayed here with blue dots). However, when the control beam is turned back on after a chosen storage time, part of the pulse - up to 10% in our experiment - is retrieved. This demonstrates an EIT based memory for a light beam propagating in a nanoscale device, and interacting with an atomic medium via its evanescent field.

The mean photon per pulse in this realization is equal to 0.6 ± 0.1 after corrections for the losses in the detection path and the limited detection efficiency (about 8% of the light leaving the nanofiber is detected). Yet, the contamination from the control pulse is hardly visible on the curve. This implementation of a memory for light is thus compatible for realizing a quantum memory for single photons. The signal-to-noise ratio in the retrieved pulse is about 13 corresponding to a single-photon SNR equal to 22. It can rather easily be further improved in our setup with some work on the filtering system.

The mentioned value of 10% overall storage and retrieval efficiency of the memory

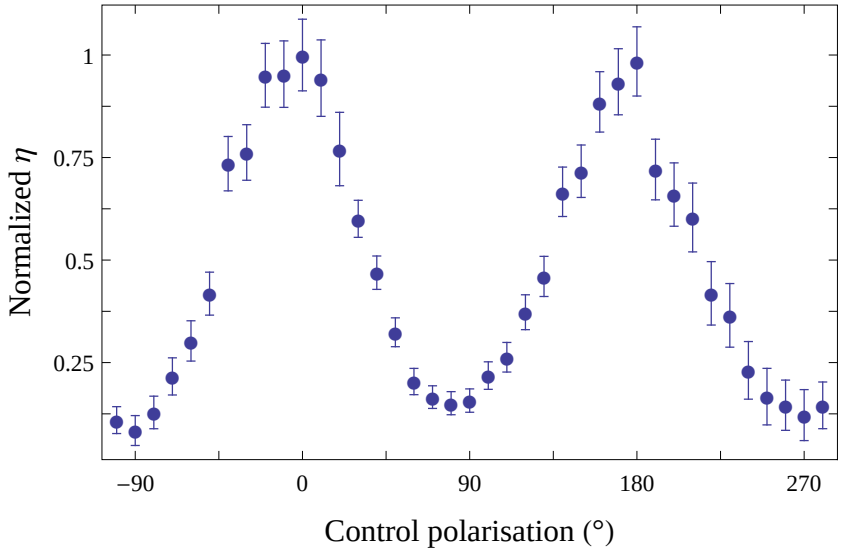

Figure 3.17: Normalized memory efficiency as a function of the control-beam linear polarization angle. 0° is for a polarization orthogonal to the quasi-linearly polarized mode of the guided beam.

is obtained after optimizing all the accessible parameters. Some of the parameters were already discussed, a few others will be mentioned here. All the properties of the control beam are very important. The control beam power for example, is chosen as a compromise between good transparency (higher powers) in order to avoid any residual absorption, and good slow-light effect (lower powers) such that the pulse is spatially compressed during propagation and can fit into the atomic sample. The time when the control beam is shut off for storage is tweaked precisely, and the shape and length of the input pulse are adjusted [Novikova07].

We mentioned already that the control-beam polarization should be linear and orthogonal to the polarization axis of the nanofiber-guided probe. Because of the unusual nature of polarization of the nanofiber-guided light, this is checked experimentally and plotted in Figure 3.17. It is clear from this curve, which gives the memory efficiency as a function of the angle between control-beam linear polarization axis and the guided-probe polarization axis, that this polarization is optimal for the chosen parameters.

Note that in principle, the memory efficiency can also be improved a little by using a control beam tuned away from the $|s\rangle \rightarrow |e\rangle$ resonance therefore limiting residual absorption from the atomic sample. However this effect was not clearly observed in our setup, possibly because of the limited optical depth of the atomic medium on the $|g\rangle \rightarrow |e\rangle$ resonance.

One of the main parameters remaining for further improvement of the memory efficiency is this optical depth, which should be as high as possible, at least in ideal EIT systems. This can be done in principle by scaling up the setup for a larger atomic cloud and a longer fiber, although the chosen direction for future experiments in the team is to increase the effective atomic density close to the fiber surface as described in chapter 4. Another important possibility would be the choice of a different atomic

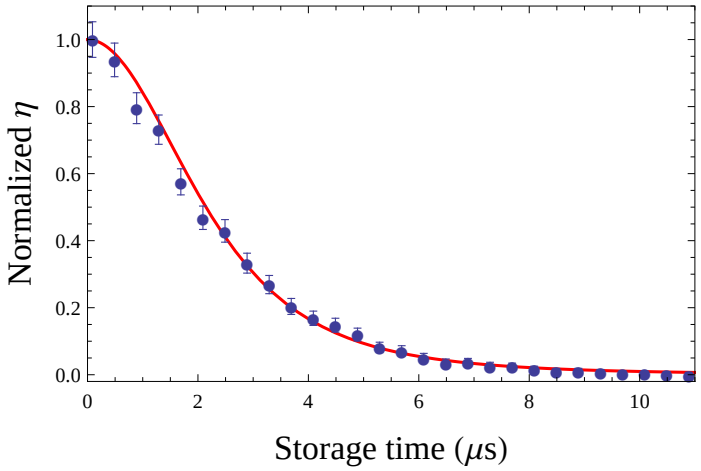

Figure 3.18: Memory efficiency as a function of the storage duration. The efficiency is normalized to its value at $t = 0$. The red curve is a fit using a theoretical result from [Jenkins12] as commented in the text.

configuration compatible with perfect EIT, using different hyperfine levels of cesium, or polarizing the atoms via optical pumping (subsection 3.1.3).

We have presented here the demonstration of a memory for a nanofiber guided laser beam, discussing the important parameters for such an experiment. The next section will study the lifetime of the memory, also giving more insight of the physical process underlying the storage protocol and the specificities of the nanofiber-based light-matter interface.

3.2.5 Memory lifetime and controlled revivals

In this section, we investigate the lifetime of the memory. Figure 3.18 is a plot of the memory efficiency as function of the storage duration. The finite lifetime observed here, a few microseconds, is linked to the time evolution of the collective state which plays a central role in ensemble-based memories. In the theoretical considerations of section 3.1, we supposed that this state was a steady state. In the experimental implementations however, different mechanisms always induce a time evolution. Those mechanisms might be responsible for a loss of the stored information. Ideally the time scales of those mechanisms are much larger than the storage/retrieval time scales. They define the lifetime of the memory.

Loss of atoms – A first straightforward mechanism reducing the retrieval efficiency is the loss of atoms. Because of their finite temperature, the atoms might fly away from the probing region, or lose their coherence in a collision with, for example, the nanofiber surface. By denoting $v = \sqrt{k_B T/m}$ the thermal velocity of an atom of mass m at a temperature T, the transit time can be estimated by $\tau_1 = 2\rho/v$, with ρ the fiber radius. For a 200 μK temperature, this expression provides $\tau_1 = 3.6$ μs. Loss will thus occur at this time scale because of the atomic motion in transverse directions.

Dephasing of the collective excitation – There are two other important decay mechanisms in our experiment. They are both responsible for a dephasing in the stored collective excitation.

In the ideal case, the collective excitation just after storage is the following superposition:

$$|S(0)\rangle = \frac{1}{\sqrt{N}} \sum_{j=1}^{N} e^{i\phi_i(0)} |g_1,g_2,...,g_{j-1},s_j,g_{j+1},...,g_N\rangle .$$

Independent time evolution of phase factors ϕ_i may occur during storage:

$$|S(t)\rangle = \frac{1}{\sqrt{N}} \sum_{j=1}^{N} e^{i\phi_i(t)} |g_1,g_2,...,g_{j-1},s_j,g_{j+1},...,g_N\rangle .$$

And the efficiency after retrieval will scale as:

$$\eta(t) = |\langle S(0)|S(t)\rangle|^2 = \left| \frac{1}{N} \sum_{j=1}^{N} e^{i(\phi_j(t)-\phi_j(0))} \right|^2 . \tag{3.2.1}$$

A first dephasing process also involves the atomic motion, but in the optical axis direction [Carvalho04, Zhao09, Peters12]. It is usually called motional dephasing. The phase acquired in a two-photon transition depends on the atomic position, and results in a phase change between the storage and retrieval times $\Delta\phi = \Delta\vec{k}.(\vec{r}_s - \vec{r}_r) = \Delta\vec{k}.\vec{v}_j t$ where $\vec{r}_s$ and $\vec{r}_r$ are the initial and final positions of the jth atom, and $\Delta\vec{k}$ is the wave-vector mismatch of the control and guided probe[13]. In a thermal gas, the velocities follow a Gaussian distribution and a sum over the atomic velocities can be carried out [Nicolas14, Choi11]. The efficiency is then:

$$\eta(t) \propto \left| \int d^3\vec{v} e^{-\frac{m|\vec{v}|^2}{2k_B T}} e^{i\Delta\vec{k}.\vec{v}t} \right|^2 \propto e^{-t^2/\tau_2^2}.$$

The lifetime is τ_2 with $1/\tau_2 = (4\pi/\lambda)\sin(\alpha/2)v$. With $\alpha \sim 13°$, one finds $\tau_2 = 5.3$ μs.

The second dephasing mechanism is caused by the residual magnetic field that results in an atom-dependent Larmor precession. The different Zeeman shifts (Figure B.1) contribute to oscillations at different frequencies. In a constant magnetic field gradient for example, an atom in state $\{F,m_F\}$ and at position z will acquire a phase $\hbar(\phi_j(t) - \phi_j(0)) = \mu_B g_F m_F \frac{dB}{dz} zt = \hbar\kappa zt$ (μ_B is the Bohr magneton and g_F the Landé factor of the hyperfine state F). Assuming a Gaussian distribution of atomic density one finds:

$$\eta(t) \propto \left| \int d^3\vec{v} e^{-\frac{4z^2}{L^2}} e^{i\kappa zt} \right|^2 \propto e^{-t^2/\tau_3^2}.$$

[13] This phase term is derived from the usual propagation of electromagnetic fields in $e^{i(\vec{k}.\vec{r}-\omega t)}$. The minus sign in $\Delta\vec{k} = \vec{k}_{probe} - \vec{k}_{control}$, comes from the interaction Hamiltonian in the rotating wave approximation (Eq. (3.1.1)). In the atomic transfer from $|g\rangle$ to $|s\rangle$ via $|e\rangle$, the probe amplitude is associated with the raising operator $|e\rangle\langle g|$ while the *conjugate* of the control amplitude is associated with a lowering operator $|s\rangle\langle e|$.

with $\tau_3 = 2\sqrt{2}/\kappa L$. The Zeeman inhomogeneous broadening measured with the method described in section B.1 is 100 kHz and the associated lifetime can be estimated to $\tau_3 \sim 10$ μs.

The combination of the loss of the atoms on one hand and the dephasing of the collective state on the other gives a decay of the efficiency of the form [Jenkins12]:

$$\exp\left(\frac{-(t/\tau_D)^2}{1+(t/\tau_T)^2}\right)/(1+(t/\tau_T)^2)^2,$$

with $\tau_T = \tau_1$ and $1/\tau_D^2 = 1/\tau_2^2 + 1/\tau_3^2$.

The fit in Figure 3.18 yields $\tau_D = 5.5 \pm 1$ μs and $\tau_T = 3.7 \pm 0.2$ μs. These values are in agreement with the evaluated time scales and thereby confirm that the decoherence mechanisms are identified.

Collapses and revivals – The dephasing mechanism described above can sometimes evolve into complete or partial rephasing.

A simple situation where such a phenomenon happens is when one applies a constant and homogeneous magnetic field on the atomic sample. Because of the different Zeeman sublevels, the phases ϕ_j rotate at multiples of the Larmor frequency and revivals occur when the terms are again in phase.

We implemented this situation by applying a magnetic field parallel to the fiber axis. The field is calibrated by measuring the Zeeman shifts (again with the technique described in section B.1). Results are plotted in Figure 3.19. Revivals are observed as expected at multiples of the half Larmor period [Jenkins06, Matsukevich06], equal to 3.5 μs for 0.4 G and 2.35 μs for 0.6 G.

In the previous paragraph, what mattered was the finite number of Zeeman levels. In principle a similar rephasing is also possible because of the finite number of atoms. In Eq. (3.2.1), the sum over j would usually be replaced by an integral for large N. This approximation breaks down for a small number of atoms. Let us suppose that each atom has a well defined velocity, and thus a corresponding phase oscillation rate. After specific time intervals rephasing will occur. However, the rephasing time will depend on the initial atomic velocities, which will be different for each realization of the experiment. After averaging over many repetitions, the theoretical curve leads to a constant but non-null efficiency after large storage time (Figure 3.20). The height of this plateau decreases as $1/N$ and is thus negligible for large N. This plateau was not clearly observed in our experiment. However it might be observed in similar experiments involving highly confined light such that a few atoms (or analog quantum oscillators) are enough to generate a high optical depth.

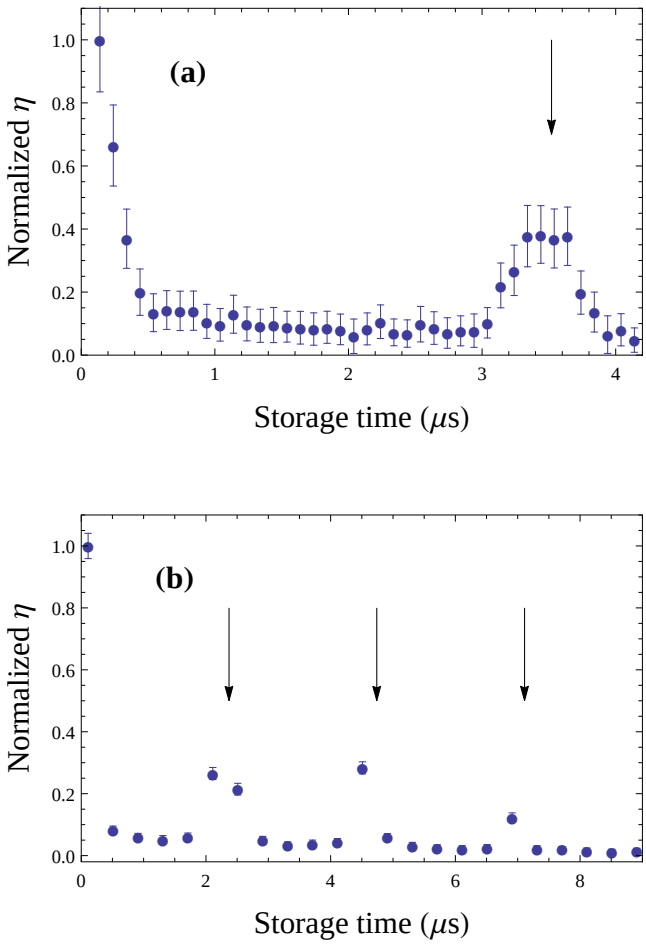

Figure 3.19: Memory efficiency as a function of the storage duration. Here, a constant magnetic field of 0.4 G (a) and 0.6 G (b) is applied parallel to the nanofiber axis. The arrows indicate the theoretical positions of revival calculated from the calibrated field.

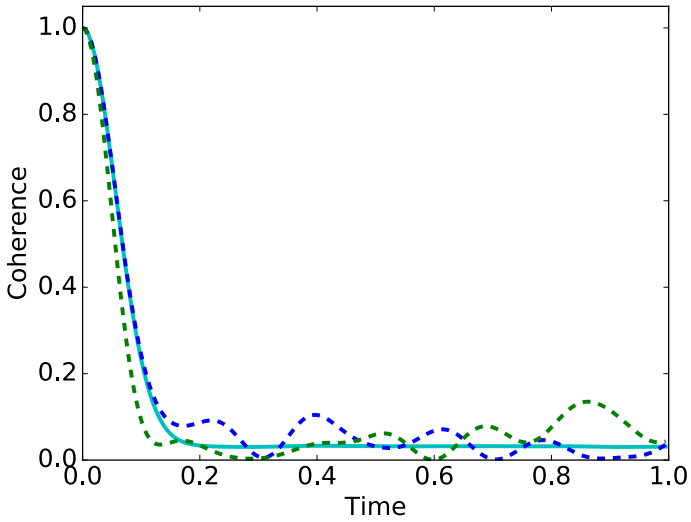

Figure 3.20: Partial rephasing for N=32 atoms. The curves are obtained by summing N oscillating amplitudes with random frequencies. The dashed lines correspond to a single atomic sample, while the solid line is averaged after 1024 repetitions of the experiment. A plateau with a non-vanishing value appears for large storage time, its height scales as $1/N$.

Chapter Conclusion

The key results of the present work were presented in this chapter.

In a first section, we gave a theoretical introduction on the quantum interference responsible for the EIT phenomenon. We addressed a few more advanced aspects of EIT, including the role of the polarization of light and of the atomic angular momentum, as well as the description of propagation in terms of dark-state polaritons. We also introduced the possibilities of EIT in atomic ensembles as a platform for quantum memories.

In the second and central section of the chapter, we reported the experimental demonstration of a memory for the tightly focused light propagating in an optical nanofiber. We summarize below the fundamental ingredients of this achievement:

- A light/matter *interface* mediated by evanescent fields:
  1. An *optical nanofiber*. The light beam of interest (λ=852 nm) is guided by a nanofiber of 400 nm diameter. It is:
     - sub-wavelength *focused*,
     - adiabatically coupled to standard optical fiber which can be connected to a larger *network*,
     - in large part in the form of an evanescent field accessible from *outside* the fiber.
  2. A cold *atomic cloud* overlapped with the nanofiber: the nanofiber is inserted in a high-vacuum system where cesium atoms are released from a magneto-optical trap. Magnetic fields are precisely measured and made smaller than 20 mG.
- A carefully handled *control beam*:
  - Propagation in *free-space*, with a small (13°) angle relative to the nanofiber.
  - A proper choice of *polarization*, linear and orthogonal to the quasi-linearly polarized guided mode.
  - Optimization of the beam *power* and *timing*.
  - *Filtering* out the control contamination in the detection path in order to reach the single-photon level.

The key quantitative characteristics of the memory are:

- a 10% storage-and-retrieval *efficiency*,
- a few microsecond scale *storage time*, limited by atomic motion in the fiber vicinity and residual magnetic fields,
- the possibility to operate at the *single-photon level* with a signal-to-noise ratio larger than 20.

The next chapter will focus on more manipulations of the cesium atoms using light guided by the nanofiber and will show how atoms can be trapped in the vicinity, enabling a larger OD and trapping time.

Chapter 4

A nanofiber-trapped ensemble of atoms

Until now, we have studied atomic clouds in free expansion around a nanofiber. While the cold atoms were flying in the nanofiber vicinity, they interacted with the light guided by the nanofiber. Such an interaction allowed us to store and retrieve part of the information contained in a guided light pulse as detailed in the previous chapter. However this first demonstration was plagued by two limiting factors. First, the atomic density was reduced close to the surface, thus limiting the optical depth. Also, the very short transit time of the atoms in the small probing evanescent region was a strong limiting factor for our experiments.

In this chapter, we implement a trapping scheme based on far-detuned interaction with guided beams. This scheme results in individual trapping sites in the nanofiber vicinity where atoms can stay for longer time scales. The idea, proposed originally in [Le Kien04] and already experimentally implemented with two different variations [Vetsch10, Goban12] also leads to much higher optical depths.

The first section will introduce the theoretical ideas on which the nanofiber dipole trap is based. As we will see, the complex polarization pattern of nanofiber guided evanescent waves has to be considered carefully and the consequence on dipole traps has been studied thoroughly in the past years [Lacroûte12, Ding12, Le Kien13b, Le Kien13a, Reitz13]. The second section will give the first results we obtained in our lab with such a trap and the different experimental characterizations we performed up to now.

4.1 A two-color dipole trap in the evanescent field of a nanofiber

4.1.1 Basic ideas of two-color trapping

The optical dipole force – In the simplest model of a two-level atom (notations defined in Figure 4.1) interacting with a far off-resonance field ($\Delta \gg \Gamma$), the main result of the interaction is a shift of the atomic levels. At the first order of approximation the ground-state shift is[1]:

$$\delta E_g = \frac{\hbar\Omega^2}{4\Delta} \propto \frac{\Gamma}{\Delta} I,$$

[1] The shift is opposite for the only excited state coupled to the ground state, and null for the other two excited states. The coupled excited state will be a superposition of the different states of the $\{|1,m_L\rangle\}$ basis if the polarization is not a "pure" π, or $\sigma_\pm$ polarization.

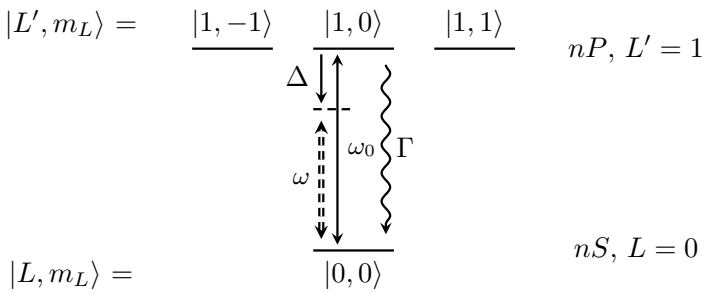

Figure 4.1: Level diagram for an atom with a single valence electron, no electronic spin nor nuclear spin, in the two-level approximation. The atom is driven by an oscillating field of frequency ω, detuned from resonance. This idealized atom is a rough description of an alkali atom when the detuning relative to the D-line is large compared to the fine-structure ($|\Delta| \gg \Delta'_{fs}$, see Figure 4.3), but small enough to neglect other atomic transitions.

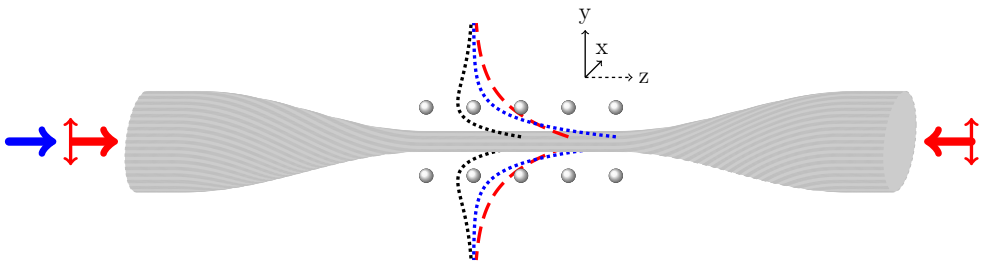

Figure 4.2: Two-color trapping scheme. An attractive red-detuned beam (dashed) and a shorter-range repulsive blue-detuned beam (dotted) are combined, resulting in a potential minimum in the fiber vicinity (solid line). An array is obtained by forming a standing wave with the red-detuned beams. The trapping sites are located in the yOz plane thanks to the use of red-detuned light quasi-polarized along y.

where Ω is the Rabi frequency and I the electric field intensity.

Since the shift is proportional to the electric field intensity, if the intensity is spatially varying, the atom experiences a spatially dependent energy, or equivalently a conservative potential $V(r) = \delta E_g(r) \propto \frac{\Gamma}{\Delta} I(r)$. This potential is responsible for the so-called optical dipole force $\vec{f} = -\vec{\nabla} V(r)$.

For an atom in the ground state, the potential is negative for a red-detuned beam (detuned to lower frequencies: $\Delta < 0$), it is thus attracted to areas with larger field intensity. In contrast, the ground-state shift is positive for a blue-detuned beam: the atom is repelled from areas of large field intensities.

The optical dipole force can obviously be used to create conservative traps. A focused red-detuned Gaussian beam for example can be used as a microscopic optical tweezer [Schlosser01]. If the beam is focused to a 1 μm^2 area, and detuned 100 nm from cesium D_2-line resonance, the resulting trapping depth is about 0.25 mK/mW, or 4 MHz/mW.

Another important parameter is the scattering rate, which generally leads to heating. It is proportional to I/Δ^2. Because the trap depth is in I/Δ, larger detunings with large intensities are preferable for a trap with constant trapping depth but smaller scattering rate.

Nanofiber-based two-color trapping – Because of the tight confinement of nanofiber-guided modes, the dipole force exerted by guided light can be significant, even with relatively low guided power. The basic idea for trapping atoms in a nanofiber vicinity is to use a two-color dipole trap (Figure 4.2). A red-detuned guided beam is used to attract the atoms to the surface, while a blue-detuned beam, naturally of shorter range because of its smaller wavelength, keeps the atoms away from the surface. The combination of these two colors, with proper power adjustment, creates a well of potential located at a few hundred nanometers from the surface which confines atoms in the radial direction. Confinement in the fiber-axis direction can be obtained with a standing wave similarly to more common optical lattices. Finally, the trapping geometry when rotating around the fiber axis will depend on the guided-mode symmetry. For quasi-circularly polarized guided modes, the rotational invariance lets the atom rotate around the fiber. But for a quasi-linearly polarized mode along y (the fiber axis is z as in Figure 4.2), the electric-field intensity is larger on y-axis than on the orthogonal x-axis (subsection 1.1.2). Using such a mode allows to confine atoms in the yOz plane.

The combination of these confining strategies leads to trapping sites of sub-wavelength size in all directions. At most one atom can be loaded per site due to the collisional blockade effect during the loading stage, which will be described later.

4.1.2 Dynamical (*ac*) Stark shifts for a real alkali atom

Real atoms have a complex multi-level structure. A full description should consider the atomic angular momentum structure as well as the fine and hyperfine interactions. The *ac* Stark shifts responsible for the dipole force will in general depend on the specific atomic level considered and on the specific electric field polarization. A different level of approximation will be relevant depending on the value of the detuning as shown in Figure 4.3. For an alkali atom in the ground state and a linearly-polarized free-space-propagating beam, the expression of the (far detuned) susceptibility can be reduced to a uniform scalar field. But for a nanofiber-guided beam, the polarization is elliptic, and varies at a sub-wavelength scale. A more careful description of the trap is thus necessary for a thorough understanding.

Because of the complexity of the problem in the general case, the atomic susceptibilities have been computed in different contexts and with different techniques, approximations and conventions. Fam Le Kien and co-workers recently reviewed the problem of computing atomic susceptibilities and presented a comprehensive formalism applied to the cesium atom ground state and D_2 line excited state [Le Kien13b]. A short introduction (in French) to a simplified description of the dipole force for alkali atoms can be found in recent Jean Dalibard's notes [Dalibard13]. Similar results are described in a review of optical dipole traps ([Grimm00] II.B.). I will summarize the main results here following [Dalibard13], before discussing the more general expression from [Le Kien13b].

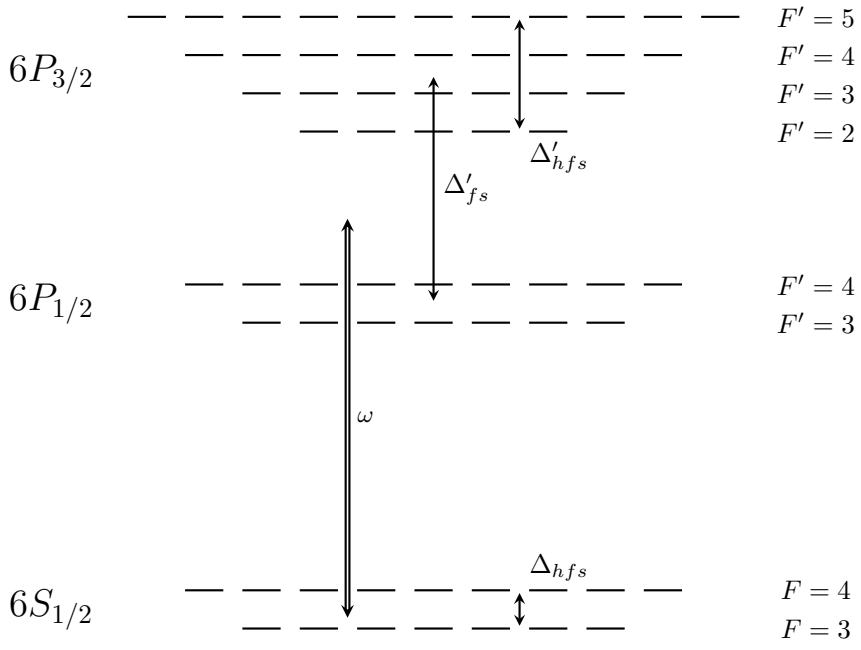

(a)

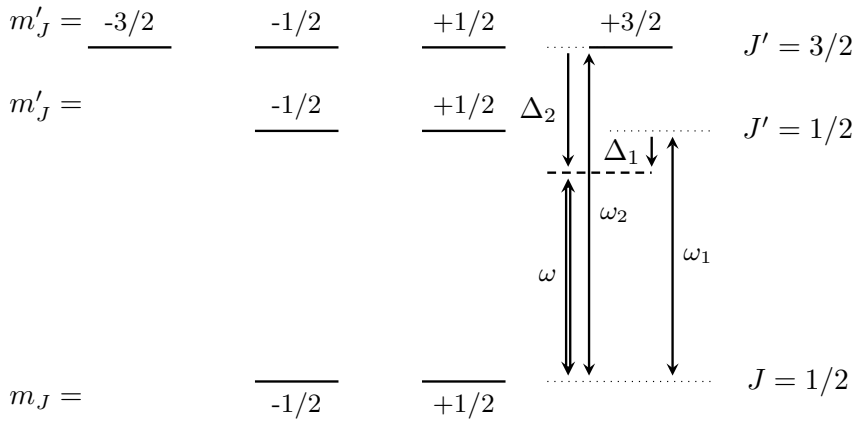

(b)

Figure 4.3: Level diagram for the D-line of an alkali atom subject to a field of frequency ω. (a) Full structure for nuclear spin I=7/2 (cesium). (b) Reduced scheme for intermediate detunings ($|\Delta_{1,2}| \sim \Delta'_{fs} \gg \Delta_{hfs}, \Delta'_{hfs}$). For a larger detuning ($|\Delta_{1,2}| \gg \Delta'_{fs}$) the diagram reduces as depicted in Figure 4.1.

Simplified description with fine-splitting structure – We consider here a typical alkali atom with a principal quantum number n, a ground state nS and fine-splitted excited states $nP_{1/2}$ and $nP_{3/2}$ with the notations defined in Figure 4.3b for the case of cesium. The atom interacts with an electric field of frequency ω and Rabi frequency Ω. The two transitions $nS \leftrightarrow nP_{1/2}$ and $nS \leftrightarrow nP_{3/2}$ with respective resonance frequencies ω_1 and ω_2 correspond to the D_1 and D_2 spectroscopic lines. The angular momentum structure is denoted with the quantum numbers $\{L,m_L\}$ (characterizing the electronic *orbital* angular momentum and its projection along the quantization axis), $\{J,m_J\}$ (for the *total electronic* angular momentum and its projection), or $\{F,m_F\}$ (for the *total atomic* angular momentum and its projection). We stay in the rotating wave approximation (RWA) for simplicity, although it is invalid for the large detunings considered here[2]. We also work in the adiabatic approximation supposing the atomic motion much slower than its internal dynamics.

For a linearly polarized electric field, the light shift in the ground state nS is independent of the projection of the total angular momentum m_z along a quantization axis. In the ground state manifold the shift reduces to its scalar part $\Delta E = \langle m|\, \hat{V}_{\text{eff}}\, |m\rangle$ with the effective interaction Hamiltonian[3] $\hat{V}_{\text{eff}}$:

$$\hat{V}_{\text{eff}} = \frac{\hbar\Omega^2}{4\Delta}\hat{1} \qquad \text{and} \qquad \frac{1}{\Delta} = \frac{1}{3}\left(\frac{1}{\Delta_1} + \frac{2}{\Delta_2}\right). \tag{4.1.1}$$

For large detunings compared to the fine splitting $\omega_2 - \omega_1$, the result is the two-level atom shift $\hbar\Omega^2/4\Delta$. It is modified however for intermediate detunings, and even suppressed for $\Delta_2 = -2\Delta_1$.

For a more general polarization of the electric field, different angular-momentum levels of the ground state degeneracy will be shifted differently, in a similar way than when a static magnetic field is applied. We express the field as:

$$\vec{E} = E(\vec{r})\frac{e^{-i\omega t}}{2}\vec{\epsilon} + c.c..$$

We also define a vector Rabi frequency $\vec{\Omega}$ as:

$$\hbar\vec{\Omega} = -\langle nS\|\vec{d}\|nP\rangle E(\vec{r})\vec{\epsilon}.$$

The light shift is then expressed in the ground state manifold as the sum of a scalar and a vector component:

$$\hat{V}_{\text{eff}} = \frac{\hbar|\vec{\Omega}|^2}{4\Delta}\hat{1} + \vec{B}.\hat{\vec{J}},$$

where the effective magnetic field is defined as:

$$\vec{B} = \frac{i}{6}\left(\frac{1}{\Delta_2} - \frac{1}{\Delta_1}\right)\vec{\Omega}\times\vec{\Omega}^*.$$

[2] Outside the RWA, the inverse detuning $1/\Delta = 1/(\omega - \omega_0)$ for a two-level atom should be replaced by $\frac{1}{\Delta} = \frac{1}{\omega-\omega_0} - \frac{1}{\omega+\omega_0}$. A more general expression is given in [Le Kien13b] as mentioned in the next paragraph.

[3] In general the effective interaction Hamiltonian should be diagonalized to obtain the eigenenergies. Here, it is already diagonal.

For a π polarization (linear along the quantization axis), $\vec{B} = 0$ and the previous result is recovered. For a circular or elliptic polarization rotating in a plane perpendicular to the quantization axis, the effective magnetic field is simply parallel to this axis.

This effective magnetic field splits the angular-momentum sublevels similarly to the Zeeman effect: for a quantization axis chosen along the effective magnetic field direction, the shift experienced by atomic state $|m_J\rangle$ is

$$V_{m_J} = \frac{\hbar|\vec{\Omega}|^2}{4\Delta} + \hbar m_J B,$$

and if the polarization is exactly π ($\zeta = 0$) or $\sigma_\pm$ ($\zeta = \pm 1$) the shift is

$$V_{m_J} = \frac{\hbar|\vec{\Omega}|^2}{4}\left(\frac{1 - 2\zeta m_J}{3\Delta_1} + \frac{2 + 2\zeta m_J}{3\Delta_2}\right).$$

Again, for large detunings compared to the fine splitting, the two-level atom result is recovered. However, the differential shifts in the ground state manifold can be significant for intermediate detunings, and larger than the scalar shift which still vanishes for $\Delta_2 = -2\Delta_1$.

Taking into account the hyperfine structure leads to the following result for the hyperfine ground state with $F = I \pm 1/2$:

$$\hat{V}_{\text{eff}} = \frac{\hbar|\vec{\Omega}|^2}{4\Delta}\hat{1} + \vec{B'}.\hat{\vec{F}},$$

where the effective magnetic field is now defined as:

$$\vec{B'} = \frac{\pm\vec{B}}{2I+1}.$$

Let's now put in a few numbers for cesium, and wavelengths that have been used for trapping cesium close to a nanofiber. The D_1 and D_2 resonance wavelengths are 894 nm and 852 nm, the fine splitting is thus about 40 nm and the hyperfine splitting is 0.02 nm for the ground state and lower for the excited states. In the first demonstration of a nanofiber mediated dipole trap [Vetsch10], the wavelengths were 780 nm and 1064 nm, the state-insensitive trap built later [Goban12] used 686 nm and 937 nm wavelengths[4]. In both case, the detunings, although much larger than the hyperfine splitting, are not much larger than the fine splitting. The level diagram of Figure 4.3b is thus relevant and the effect of the effective magnetic field will be significant. The differential shifts in a Zeeman manifold for σ-polarized light of 937 nm wavelength for example, is about half of the trap depth.

As a conclusion for this paragraph, we now have a simple description for the polarization dependent *ac*-Stark shifts in the ground-state manifold of alkali atoms. This expression still relies on a number of approximations though (only the D-line was considered, we worked in the RWA framework), and is not valid for excited states. In the coming paragraph we present a more general theory valid for excited states and leading to quantitatively meaningful results.

[4]Those are the magic wavelengths described later in this section.

General dynamical-Stark-shift theory – In the general case [Steck, Le Kien13b], the Stark shift is obtained from perturbation theory. The first order shift for a non-degenerate level $|i\rangle$ is $\langle i|\, H_1\, |i\rangle$ where $H_1 = -\vec{d}.\vec{E}$ is the perturbing Hamiltonian. Since the dipole operator only couples states of opposite parity, this term reduces to zero except for the exceptions (hydrogen, molecules) with two degenerate states of opposite parity. The first significant term is thus obtained with second order perturbation theory, and the result is quadratic in H_1. It can be expressed as the contraction of a rank-2 susceptibility tensor built from the dipole operator and a tensor built quadratically with the electric field vector. The shift for state $|i\rangle$ is[5]:

$$\Delta E_{|i\rangle} = -\alpha_{\mu\nu,|i\rangle}\epsilon^*_\mu\epsilon_\nu\,|E|^2\,,$$

where μ and ν are Cartesian coordinates (x,y or z).

In the context of atoms with angular momentum degeneracy (see [Steck] ch. 7), a rank-2 tensor is more conveniently expressed as a sum of irreducible (considering their transformation under rotation) tensors of ranks 0, 1 and 2. And the shift is finally expressed with three corresponding susceptibilities, namely the scalar, vector and tensor susceptibilities (denoted S,V, and T). The effective Stark shift Hamiltonian is given for a particular fine level $|nJ\rangle$ by [Le Kien13b]:

$$V_{\text{eff}} = -\frac{1}{4}\,|E|^2\left(\alpha^S_{nJ} - i\alpha^V_{nJ}\frac{(\vec{\epsilon}^*\times\vec{\epsilon}).\hat{\vec{J}}}{2J} + \alpha^T_{nJ}\frac{3[(\vec{\epsilon}^*.\hat{\vec{J}})(\vec{\epsilon}.\hat{\vec{J}}) + (\vec{\epsilon}.\hat{\vec{J}})(\vec{\epsilon}^*.\hat{\vec{J}})] - 2\hat{\vec{J}}^2}{2J(2J-1)}\right).$$

The susceptibilities α^a_{nJ} are elaborate sums, with coefficients from the angular momentum algebra, of terms similar to the two-level atom shifts for the different fine structure transitions from the state of interest. These terms are proportional to the squared transition dipole matrix elements $|\langle n'J'\|\hat{\vec{d}}\|nJ\rangle|^2$ and $1/\tilde{\Delta}$. $\tilde{\Delta}$ is a generalized detuning to the particular transition including counter rotating terms (no rotating wave approximation here) and the transition linewidth. The hyperfine splitting is neglected in this detuning.

The levels shifts are not given directly by $\langle i|\, V_{\text{eff}}\, |i\rangle$. Noting V_{hfs} the hyperfine interaction Hamiltonian, one has to diagonalize the total $V_{\text{hfs}}+V_{\text{eff}}$ Hamiltonian. Doing so, one obtain eigenstates mixing the $|nJFm_F\rangle$ states and their corresponding energies. The result is simplified when the perturbation is small compared to the hyperfine splitting. In this case, V_{eff} has the same expression where J is replaced by F and the susceptibilities are multiplied by coefficients depending on I, J and F. Conveniently, the scalar susceptibility remains independent on F (this holds when neglecting the hyperfine splitting in the expression of $\tilde{\Delta}$). This V'_{eff} can be diagonalized directly in a hyperfine state manifold. For pure π ($\zeta = 0$), or $\sigma_\pm$ ($\zeta = \pm 1$) polarization, it is already diagonal, the vector part is proportional to m_F and the tensor part has a m_F dependent component proportional to ${m_F}^2$ leading to a shift given by the experession

[5] $\alpha_{|i\rangle}$ is the susceptibility tensor for state $|i\rangle$ and $\vec{\epsilon}$ is the polarization of the electric field as defined previously.

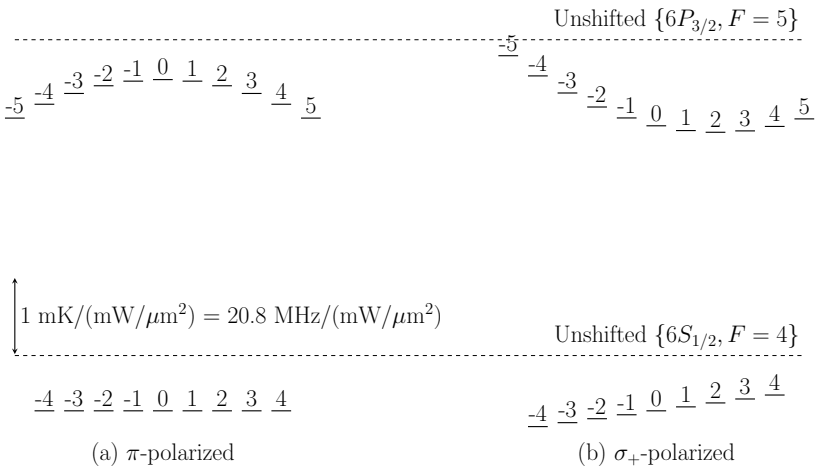

(a) π-polarized (b) σ_+-polarized

Figure 4.4: Illustration of m_F dependent polarizability for pure π (left) and σ_+ (right) polarization. The shifts are given for the ground $\{6S_1/2,F = 4\}$ and excited $\{6S_1/2,F = 5\}$ states of cesium and $\lambda = 935.2$ nm, using the polarizabilities computed in [Le Kien13b]. The total distance $\sim \hbar\omega_0$ between the ground and excited states is not to scale, and the conversion from standard units to mK/(mW/μm^2) assumes a plane wave in vacuum, i.e. $I = (1/2)c\epsilon_0 |E|^2$.

below and illustrated in Figure 4.4[6]:

$$\Delta E_{|nJFm_F\rangle} = -\frac{1}{4}|E|^2\left(\alpha^S_{nJF} + \zeta\alpha^V_{nJF}\frac{m_F}{2F} + \alpha^T_{nJF}\frac{(1-2\zeta^2)6m_F^2 + (3\zeta^2-1)2F(F+1)}{2F(2F-1)}\right).$$

For the curious, I give here the result of diagonalizing the tensor part of V'_{eff} for an electric field with $\vec{\epsilon} = \frac{1}{\sqrt{1+r^2}}(\vec{u}_x + ir\vec{u}_y)$, r being a real number varying from 0 to 1, and F=1. The eigenvectors are $\{|0\rangle, |1\rangle - |-1\rangle, |1\rangle + |-1\rangle\}$ with eigenvalues (up to a constant factor) 1, $\frac{r^2-2}{1+r^2}$ and $\frac{1-2r^2}{1+r^2}$. A different pair of states is degenerate for $r = 0$ (linear polarization) and r=1 (circular polarization). The eigenvectors do not depend on r for this example, but they do in general for arbitrary F. Also, note that the eigenvectors of the vector part are the elements of the initial basis $\{|0\rangle, |1\rangle, |-1\rangle\}$, the vector and tensor part are thus not simultaneously diagonal in those two simple basis.

Let's compare the general expression of V_{eff} to the simpler expression given before for the ground state of alkali atoms. The scalar term is obviously the same scalar term that we described before, but now all excited states can be taken into account when computing the scalar susceptibility. The vector term corresponds to the effective magnetic field introduced above, which lifts the angular momentum degeneracy. The last tensor term didn't appear above because it vanishes for $J = 0$ and $J = 1/2$. The latter condition is fulfilled for the ground states of alkali atoms, but importantly not for the $J = 3/2$ excited state of the D_2 line, which will thus experience a significant tensor shift.

[6]For pure σ polarization, one has to recall that $F_+F_- + F_-F_+ = 2(F_x^2 + F_y^2) = 2(\hat{F}^2 - F_z^2)$, where $F_\pm = F_x \pm iF_y$.

To summarize the result for the ground state of alkali atoms, there is no tensor shifts, the vector shift vanishes for linear polarization, and the scalar shift is very conveniently independent on F (as soon as the hyperfine splitting is neglected in $\tilde{\Delta}$) and m_F. For the excited state however, the tensor shift is significant and leads to an m_F dependent shift.

4.1.3 Back to the trap: ground-state coherence

The results that we just presented, the general expression of the light shifts as a function of the specific atomic state considered and the field polarization, are valid for both free-space or nanofiber-guided traps. A strong particularity of nanofiber guided beams and highly focused beams is a variation of polarization (and thus of trapping potentials) at subwavelength scale (subsection 1.1.2). Note that polarization can vary at wavelength scale in collimated free-space beam, even if this is usually avoided for far off-resonance dipole traps. This variation of polarization is responsible for example for sub-Doppler polarization-gradient cooling.

Now that we have a realistic description of the Stark shifts for cesium, we consider again a nanofiber-mediated dipole trap. Because our goal is not only to trap the atoms, but also to manipulate their quantum state[7] (i.e. for quantum memories) we must consider the coherence of the atomic state. A few concerns arise which I will introduce below, in particular because of the complex polarization structure of nanofiber-guided light.

- When trapping an atom in its ground state, because of the spatially dependent vector shifts, the different sublevels are trapped in different potentials. This means that the differential shift between two levels depends on the atomic position in the trap. An important consequence is the phase decoherence between such states during atomic motion.

- If we consider an atomic-ensemble-based experiment, the splitting of the different Zeeman levels will induce dephasing of the collective excitation (subsection 3.2.5). This will happen in general even if the atoms are cooled in the motional ground state as mentioned in [Lacroûte12], although in this case partial rephasing will be observed.

- Even without any vector shift, the different scalar shift for both hyperfine ground states will induce uncontrolled phase terms of hyperfine coherences.

- Another kind of decoherence may occur during atomic motion in the effective magnetic fields, referred to as "spin-flips" in [Le Kien13a]. This can be understood clearly in the context of magnetic traps. In such a trap, the magnetic field direction varies in space and the trapped levels, say the $m = +1/2$ state of a spin 1/2 particle, are considered to adiabatically follow the magnetic field direction. A problem occurs however if the center of the trap corresponds to a zero magnetic

[7] As an appetizer on the complexity, but also the rich possibilities of optical lattices with complex polarization patterns, [Deutsch98] provides the theoretical study of quantum-state manipulation in very similar configurations but using much simpler free-space propagating beams.

field. When the particle crosses this point, the magnetic field suddenly flips its direction, or, in the magnetic field "frame", the spin flips to the anti-trapped $m = -1/2$ state.

In a nanofiber trap, the flipped spin would not be anti-trapped in general because of the important scalar shift contribution[8]. But Zeeman coherences will be lost. For this "spin-flip" to happen, a condition is that the different levels are degenerate at some point in the trap (corresponding to the zero of magnetic field in the previous description). The adiabatic approximation, which decouples internal state and center of mass motion, actually breaks at this point. Using an external magnetic field can help to lift this degeneracy.

In principle a similar "spin-flip" may also arise because of the presence of a tensor shift. This effect in a dipole trap could be studied with a proper formalism such as the formalism mentioned in [Le Kien13a]. This would be closely linked to phenomena better known by chemical physicists [Mead87].

4.1.4 Driving optical transitions in a dipole trap: magic wavelengths

We now consider the consequence of the excited state trapping potential properties. If one wants to drive a particular transition from the ground state to an excited state, the fact that the excited state is trapped in a different potential will be an issue. Driving the transition induces a time-dependent force which will in general lead to heating. The transition will also in general be shifted and inhomogeneously broadened in the presence of differential scalar, vector and tensor shifts. The differential scalar shift may be canceled by using proper wavelengths (one of the so called "magic" wavelengths) where the scalar susceptibility is identical for the ground and excited state. When using such a wavelength the trap is "state insensitive" and the atomic center of mass motion is independent from the internal state. As reviewed in [Ye08], these magic wavelengths became an important tool for precision metrology[9] and for quantum state engineering in dipole traps, i.e. in cavity-quantum-electrodynamics experiments.

4.1.5 The chosen nanofiber trap

In our lab, we chose to implement the state-insensitive trap for $6S_{1/2} \leftrightarrow 6P_{3/2}$ transition proposed in [Lacroûte12, Ding12]. Both the differential scalar shifts and the vector shifts are canceled. Up to the quality of this cancellation and compared to an isolated atom, the only remaining shift and broadening are the tensor shifts in the excited state.

The scalar shift is canceled with the use of magic wavelengths, namely 686.3 nm (blue-detuned) and 935.2 nm (red-detuned) [Le Kien13b]. The optical lattice if formed by two counter-propagating quasi-linearly polarized (along a common axis, see Figure 4.5) red-detuned beams. **The vector shift is therefore canceled** thanks to the **standing wave** interference leading everywhere outside the fiber to a **linearly**

[8] The scalar shift could be canceled with the use of a proper wavelength. For example when $\Delta_2 = -2\Delta_1$ in Eq. (4.1.1).

[9] In a state-insensitive lattice for ^{87}Sr, the $^1S_0$ to $^3P_0$ has been measured with 10^{-15} accuracy [Boyd07].

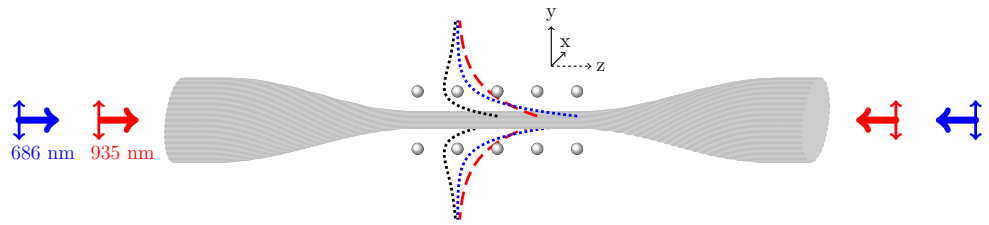

Figure 4.5: State-insensitive nanofiber dipole trap with two-color trapping beams. Two pairs of counter-propagating guided beams tuned at magic wavelengths (935 nm and 686 nm) are used, all quasi-linearly polarized along y. The red-detuned 935 nm beams are derived from a single laser to produce a standing wave. This standing wave has locally a linear polarization producing no vector shifts. On the other hand, the blue-detuned beams are detuned relatively to each other by a fraction of nanometer. This produces a rapidly translating standing wave (no vector shifts) averaging to a z-invariant repulsive potential.

polarized electric field (as detailed below). The blue detuned beams necessary for repulsion from the fiber surface are also quasi-linearly polarized along the same axis. Two counter-propagating beams are also used for vector shift cancellation. However, in order to avoid to superimpose a periodic structure with a different wavelength than the red detuned lattice, the two beams are detuned relative to each other. The translating standing wave simply averages for large enough detuning to a longitudinal invariant repulsive potential. For this, the detuning should be larger than the atomic motion characteristic frequencies and larger than the hyperfine splitting. The residual vector shift is proportional to the detuning, thus giving a higher limit to the desired detuning.

Overall, both the the vector shifts and differential scalar shifts between ground and excited states are canceled in this trapping scheme. The first are canceled by the use of standing waves and the second by the use of magic wavelengths.

This trap was implemented for the first time in [Goban12] with 0.4 mW in each red detuned beam and 5 mW in each blue detuned beam, resulting in trapping sites located 215 nm from the surface of a 430 nm diameter fiber with an estimated trap depth of 0.27 mK. The individual sites were arranged in two lines on both sides of the fiber. The two lines were made of regularly spaced traps, and in the harmonic approximation, the trapping frequencies were estimated to be 199 kHz, 273 kHz and 35 kHz in the respective radial, longitudinal and azimuthal directions. The relative detuning of the blue detuned beams was 382 GHz leading to a ground state residual vector broadening estimated to be 10 kHz and thus a collective excitation coherence limited to 100 μs. The tensor broadening in the excited state was about 700 kHz. A ground state hyperfine phase accumulation at a 30 Hz rate was expected for an atom cooled in the motional ground state, because of a residual differential scalar shift.

Linear polarization of the standing wave – As mentioned already, a linear polarization of the trapping light is obtained everywhere around the fiber by using a standing wave. This is done with the combination of two counter-propagating beams populating HE_{11} modes with identical quasilinear-polarization axis. The electric field

amplitude of the forward and backward beams are

$$\vec{E}_{fw} = (\vec{e}_t(x,y) + i\vec{e}_z(x,y))\frac{e^{i(-\omega t+\beta z)}}{2} + c.c.$$
$$\vec{E}_{bw} = (\vec{e}_t(x,y) - i\vec{e}_z(x,y))\frac{e^{i(-\omega t-\beta z)}}{2} + c.c.,$$

where $\vec{e}_t$ and $\vec{e}_z$ are real vectors, respectively in the transverse plane and along the fiber axis. The resulting standing wave interference is

$$\vec{E}_{\text{trap}} = \vec{E}_{fw} + \vec{E}_{bw} = (\vec{e}_t \cos\beta z - \vec{e}_z \sin\beta z)e^{-i\omega t} + c.c..$$

The polarization is indeed everywhere linear, and the trapping potential for the ground states is expressed as

$$V = -\frac{1}{4}\alpha^S_{nJF}\,|E|^2 = -\alpha^S_{nJF}\left(|\vec{e}_t|^2 + (\sin\beta z)^2(|\vec{e}_z|^2 - |\vec{e}_t|^2)\right).$$

Validity of the harmonic approximation – The harmonic approximation consists in considering the trapping potential as a parabola, as soon as the atomic motion stays close enough to the potential minimum. In a harmonic potential, the atomic motion is described by Fock states $|n\rangle$ of energy $E_n = (n+\frac{1}{2})\hbar\omega$, where n is a positive integer and ω is the trap frequency. The standard deviation of the position for state $|n\rangle$ is $\Delta z = \sqrt{n+\frac{1}{2}}a$ where

$$a = \sqrt{\frac{\hbar}{m\omega}},$$

and m denotes the atomic mass. To check the validity of the approximation, the real potential should be compared to the harmonic potential at a distance Δz from the minimum.

Along the longitudinal direction of our state-insensitive trap, the trapping potential for the ground state varies as $(\sin\beta_{\text{red}}z)^2$, where β_{red} is the wavenumber of the red detuned light[10]. The harmonic approximation $(\sin\beta_{\text{red}}z)^2 \sim (\beta_{\text{red}}z)^2$ results in a 10% error when $\beta_{\text{red}}z \sim \pi/6$ for example. This gives a limit to the spatial extension that atoms can have for the approximation to be valid. This limit can be expressed as a maximal value

$$n_{\max} = \left(\frac{\pi}{6a\beta_{\text{red}}}\right)^2 - \frac{1}{2}, \tag{4.1.2}$$

for n, and a maximal temperature

$$T_{\max} = E_{n_{\max}}/k_B = \left(\frac{\pi}{6a\beta_{\text{red}}}\right)^2 \hbar\omega/k_B. \tag{4.1.3}$$

Along the azimuthal direction, the trap varies as $(\sin\phi)^2$, with ϕ the azimuthal angle, so β_{red} should simply be replaced by $1/r_{\text{trap}}$, with r_{trap} the radial position of the trap. The radial dependence of the potential has a less practical expression involving the

[10] $\beta_{\text{red}} = 2\pi/\Lambda_{\text{red}}$, with $\Lambda_{\text{red}} = 898$ nm.

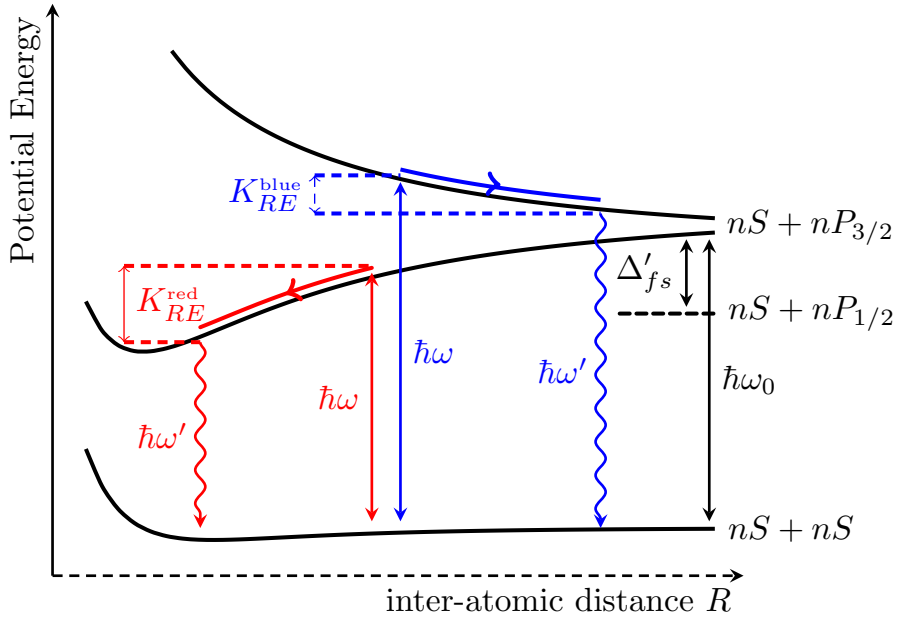

Figure 4.6: Schematic diagram showing the interaction adiabatic potentials for two atoms with ground state nS and excited state $nP_{3/2}$. The radiative escape mechanism in red-detuned optical molasses in illustrated in red: the atomic pair is promoted to an excited branch after absorbing a photon of energy $\hbar\omega$, it then acquires a kinetic energy K_{RE} before emitting a photon of energy $\hbar\omega' = \hbar\omega - K_{RE}$. The atoms can as well experience fine-structure-changing collisions, acquiring a kinetic energy Δ'_{fs}. Also, if using blue-detuned light (blue arrows), K_{RE} can be tailored such that only one atom escapes the trap (see subsection 4.2.2).

Bessel functions which describe both the red-detuned and blue-detuned evanescent fields, we thus use equations (4.1.2) and (4.1.3) for simplicity.

For the radial and longitudinal motion, we find $a \sim 20$ nm, $n_{\max} \sim 15$ and $T_{\max} \sim 200$ μK. The harmonic approximation can be reasonable. For the azimuthal motion $a = 47$ nm, $n_{\max} = 22$ and $T_{\max} \sim 38$ μK. The maximal temperature is closer but still higher than what was measured in our optical molasses (subsection 4.2.2).

4.1.6 Collisional blockade

We already mentioned that either zero or one atom are typically loaded in the trapping sites. This is because of the *collisional blockade* effect when loading our microscopic trapping sites from a MOT or an optical molasses.

Because of *light-assisted collisions* when the cooling light of a MOT and an optical molasses is turned on, if two atoms are loaded in a trapping site, they will rapidly expel each other out from the trap. The relevant collisional mechanism is described in [Gallagher89] and reviewed in [Weiner99]. Its role is studied in the context of loading dipole traps in [Kuppens00], and in the particular case of collisional blockade in subwavelength traps in [Schlosser02]. The van der Waals interactions underlying those collisions are reviewed in [Margenau39].

Those collisions can be understood from the following rapid discussion. Consider two atoms, one in the ground state $|g\rangle$ and one in the excited state $|e\rangle$. If the two atoms are infinitely far apart, the two states $|ge\rangle$ and $|eg\rangle$ are uncoupled and degenerate. However, as soon as the inter-atomic distance R gets smaller, van der Waals interactions appear (Figure 4.6).

The dipolar electric field created by one atom at the other atom position decays as $1/R^3$. The $-\vec{d}.\vec{E}$ interaction can thus be described with a Rabi frequency $\Omega \propto 1/R^3$ and, after diagonalization, to an energy splitting in $\pm\hbar\Omega/2$. The resulting adiabatic potentials, plotted as a function of R are two branches with energy $\pm\hbar\Omega/2 \propto \pm 1/R^3$ ($nS+nP_{3/2}$ branches). The length scale characterizing this $\pm 1/R^3$ interaction is on the order of $\lambda/2\pi$, it is thus very important in our subwavelength size trapping sites. Note that if the two atoms are in the ground state, perturbation theory must be derived to a higher order, and the resulting potential is of shorter range, in $-1/R^6$ ($nS + nS$ branch).

The most relevant mechanism for collisional blockade when loading microscopic dipole traps from an optical molasses or a MOT is the so called *radiative escape*. Because of the red-detuned cooling light, the two atoms can absorb a photon and be promoted to the $-1/R^3$ branch as illustrated in red in Figure 4.6. They are then mutually accelerated in the $-1/R^3$ potential, and if they have acquired sufficient kinetic energy K_{RE} before re-emitting a photon by spontaneous emission, they will escape the trap. Other mechanisms can be involved. *Fine-structure-changing collisions* are significant when the *trap depth* is increased from the mK scale (dipole trap) to the K scale (MOT): when the atoms get close enough, an alkali atom in $nP_{3/2}$ state may decay to $nP_{1/2}$ state and the D line fine splitting energy transferred to kinetic energy. For cesium for example, the fine splitting ($\frac{1}{2}\Delta'_{fs} \sim 400K$) is much higher that the typical trap depth.

4.1.7 Loading the trap

The main consequence of a detailed study of light-assisted collisions for loading the trap from a MOT is the following. In the loading process, the red detuning of the cooling beam should be increased, and the cooling and repumping power should be decreased. The loading efficiency will optimally reach 1/2 in such microscopic traps.

Higher loading efficiencies can be obtained with more complex procedures though, while keeping the subpoissonian statistics of the trap (at most one atom loaded). The kinetic energy acquired in collisions can be tuned such that a single atom is lost in the 2-body collisional process. This can be implemented using a blue-detuned beam with carefully chosen detuning. We can see in Figure 4.6 that the smaller the blue detuning, the smaller the acquired kinetic energy: for a small enough detuning, the acquired energy will lead to the loss of only one atom in the collisional process. 82.7% and 90% loading efficiencies are reported in [Grunzweig10] and [Lester15].

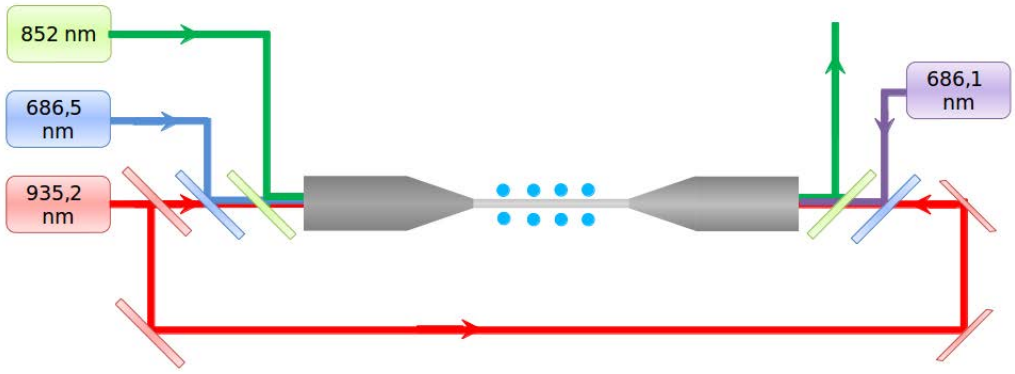

Figure 4.7: Laser beams for our two-color nanofiber trap. Two pairs of counter-propagating guided beams tuned at magic wavelengths (935 nm and 686 nm) are used, all quasi-linearly polarized along the same direction. The red-detuned beams are derived from a single laser to produce a standing wave. On the other hand, the blue-detuned beams are detuned relatively to each other by a fraction of nanometer.

Section summary

We have introduced in this section the principle of a nanofiber mediated two-color dipole trap. We described the dynamic Stark shifts and their consequences for building microscopic trapping sites on both sides of a nanofiber. A state-insensitive scheme with proper wavelengths and geometry is chosen. We also discussed the loading of a such a trap (at most one atom per trapping site) and the expected coherence in the trap.

4.2 Experimental realization

After having presented the theoretical concepts underlying the nanofiber dipole trap, we now turn to its experimental realization. The new elements of the experiment are three diode lasers generating the trapping lights, and the optical system used to handle all those different wavelengths in the same single-mode fiber as illustrated in Figure 4.7. We will present those elements before reporting our characterization of the trap.

4.2.1 Optical system

The red-detuned light (935 nm) is generated by a single commercial diode laser (Toptica DL Pro - 50 mW) and arranged as illustrated on Figure 4.8. The small 852 nm component of its spectrum is filtered out with a standard dichroïc mirror ($R > 99\%$ at 852 nm with $T > 85\%$ at 917 nm) to avoid any contamination at our signal wavelength. It is then divided into the two paths necessary to generate a standing wave. It is frequency controlled and timed by individual double-pass AOMs and coupled into polarization maintaining single-mode fibers (PMF). For better stability of the standing

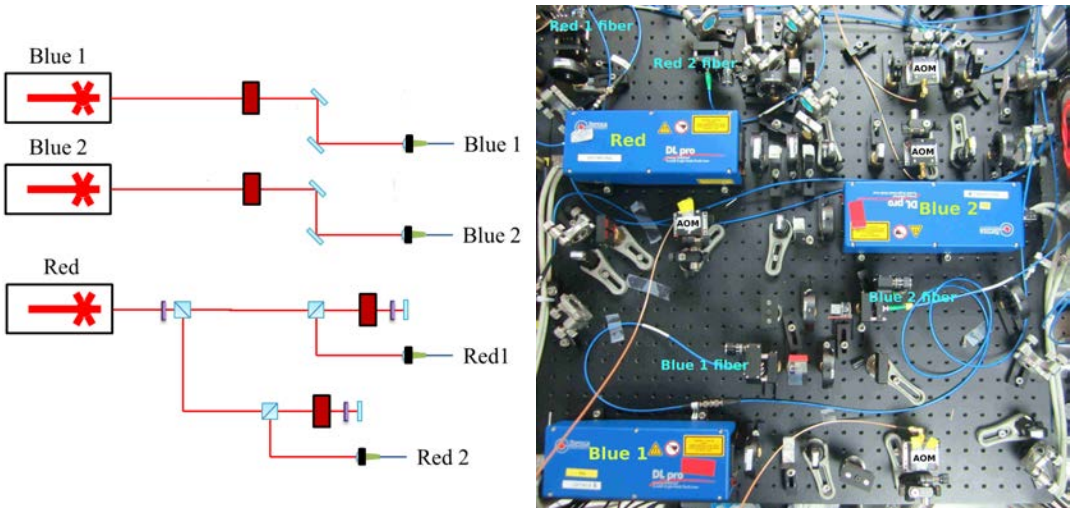

Figure 4.8: Optical arrangement of the dipole trap diodes at 935 nm and 686 nm. The red rectangles are the single-pass or double-pass AOMs. A non-negligible component at 852 nm in the red-detuned light is filtered out.

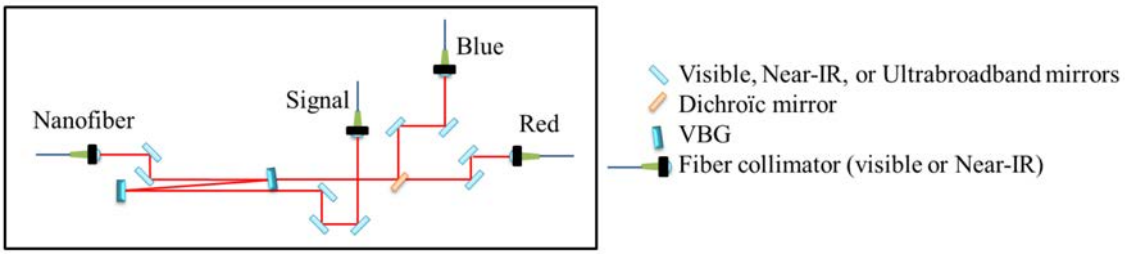

Figure 4.9: Wavelength-mixing breadboard. In the nanofiber, the three wavelengths, 852 nm (signal), 935 nm (red-detuned) and 686 nm (blue-detuned) are propagating. A pair of VBGs filters the signal path. All paths are used in both directions (each fiber is used both as an input and an ouput), at both sides of the nanofiber.

wave, the RF frequencies driving the AOMs are generated by a single VCO rather than two. After fiber coupling, 5 mW are available in each fiber.

The blue detuned light (686 nm) is generated by two different diode lasers (Toptica - 24 mW), because of the large targeted relative detuning. Similarly, each laser beam is coupled to optical fibers after single-pass AOMs. 10 mW are available in each fiber.

Mixing and filtering of the three wavelengths are done on two individual breadboards corresponding to both tails of the nanofiber. A first version of these breadboards was described in Adrien Nicolas's thesis [Nicolas14] before further development and implementation by Olivier Morin and Neil Corzo-Trejo. There are two main challenges here: achieving a high filtering efficiency such that 852 nm light, possibly single-photons, coming from the nanofiber can be detected with a large signal-to-noise ratio. We must also handle the three beams in order the superimpose them in the same, fiber-coupled mode, with independent control of polarization. The degrees of freedom

are intrinsically coupled and a careful procedure is necessary. The different optical elements obviously have different behaviour for the different wavelengths, polarizations, focusing, and optical axis alignment.

A simplified drawing is given in Figure 4.9. The nanofiber side of the mixing breadboard is a non-polarization maintaining single-mode fiber, identical to the fiber used for nanofiber fabrication. Aligned with broadband mirrors, the 852 nm component is reflected on two volume Bragg gratings (VBG[11]) setup for optimal reflectivity at 852 nm with efficient filtering of the red and blue detuned light. Here the wavefront should in principle be perfectly flat. The required filtering efficiency of 120 dB is achieved. The light reflected on the VBGs is then coupled to a PMF which can be connected to a detection or an input path. The 852 nm polarization is fixed in the 852-only path for optimal reflection on the VBGs. In the nanofiber part, it is setup using fibered polarization controller.

The blue and red detuned light arrive from two independent PMF fibers and adjustable lenses. Their polarizations are handled separately with a pair of waveplates and they are mixed on a regular dichroic mirror, before being transmitted through the VBGs and coupled into the common fiber. In our setup, we can lack power for the blue detuned light. Loss on this path should be reduced as much as possible. Of course, we also minimize losses on the 852 nm path in order to preserve the quantum state of the signal light before detection.

Overall we achieve 60% transmission through the signal path (or 70% if using only one VBG). 4 mW are finally available for each of the blue-detuned beams and 2 mW for each of the red-detuned beams.

4.2.2 Loading the trap

Once the trapping light is ready, it is left continuously on, and the trap is loaded with the sequence illustrated in Figure 4.10. First, the MOT is loaded with similar parameters than in the previous chapters. At time t_0 the magnetic field is shut-off and starts to decay. From t_0, and for 10 ms, the cooling and repumping beams of the MOT are modified following approximately exponential curves. The detuning of the cooling beam is increased from -2Γ to about -16Γ with a time constant of about 10 ms, and its power decreased, with a time constant of about 3.5 ms. The repumping power is decreased as well with a 10 ms time constant[12].

At time $t_1 = t_0+10$ ms, the MOT beams are completely shut-off and the dipole trap is considered loaded. The trapped atoms can be probed and the atomic state may be purified with an additional repumping pulse.

Note that if a probe is sent in the nanofiber just after loading, not only the trapped atoms but also the atoms released from the MOT are probed. During the loading stage, many atoms are kept trapped in an optical molasses, they are also much cooler than in our first experiments. They can in principle contribute to absorption for a few tens of milliseconds.

[11] Also referenced in [Goban12], these VBGs were designed by Optigrate to achieve a narrow high reflectivity window centered arround 852 nm, while other wavelengths are transmitted. The rejection of the undesired wavelengths is on the order of 70 to 90 dB with a ~ 1 nm bandwidth.

[12] The repumping decay time didn't seem critical up to now.

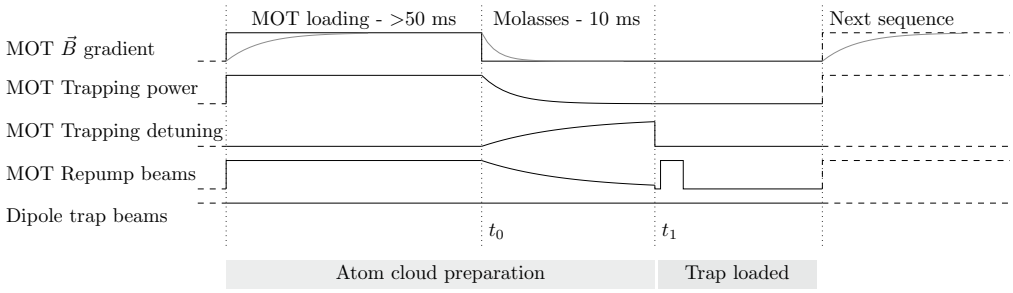

Figure 4.10: Typical dipole-trap loading sequence. Once the MOT is fully loaded the magnetic-field gradient is turned off and the dipole trap loaded by a transient molasses stage: the MOT-trapping-beams detuning is increased while their power is decreased, and the MOT-repump-beams power is ramped down.

The lower temperature obtained after the transient molasses stage was confirmed by time-of-flight measurements: the cloud is released and imaged after a varying expansion time[13]. The expansion speed is directly linked to the initial cloud temperature. Using this method, we measured temperatures of 370 ± 30 μK and 14 ± 3 μK before and after the molasses stage respectively.

As soon as this loading sequence is implemented, there is a first immediate result: the optical depth of a nanofiber-guided resonant probe increases drastically. For a rough figure, it is measured with a 3Γ detuned beam, and supposing an unbroadened Lorentzian absorption spectrum, estimated higher than 60 on the $\{6S_{1/2}, F = 4\} \rightarrow \{6P_{3/2}, F = 5\}$ transition.

4.2.3 Characterizing the trap

Unless mentioned otherwise, all the presented data are from March 2015 and are chosen here for their consistency with each other: they all correspond to the same nanofiber and the same experimental parameters, they were recorded in the first weeks following our first implementations of the dipole trap.

Absorption linewidth – First, we measure the absorption of a guided probe as a function of its detuning. The probe quasi-polarization is aligned along the trapping light polarization axis. The result is displayed on Figure 4.11. The absorption profile is plotted here for atoms which have stayed for a long or short time in the trap, i.e. 1 ms or 20 ms. After short times, this profile exhibits the typical plateau of high OD systems around zero detuning.

The result for the displayed curve is an OD probably larger than 100 after 1 ms in the trap. This high OD curve cannot be simply fitted to a Lorentzian profile. All data here are measured at low powers with photon-counting modules. Note that on this set of data, the error bars are much higher for the large positive detuning because of lower probing power in this region.

[13] A laser beam is shone on the cloud, and its position-dependent absorption recorded with a camera.

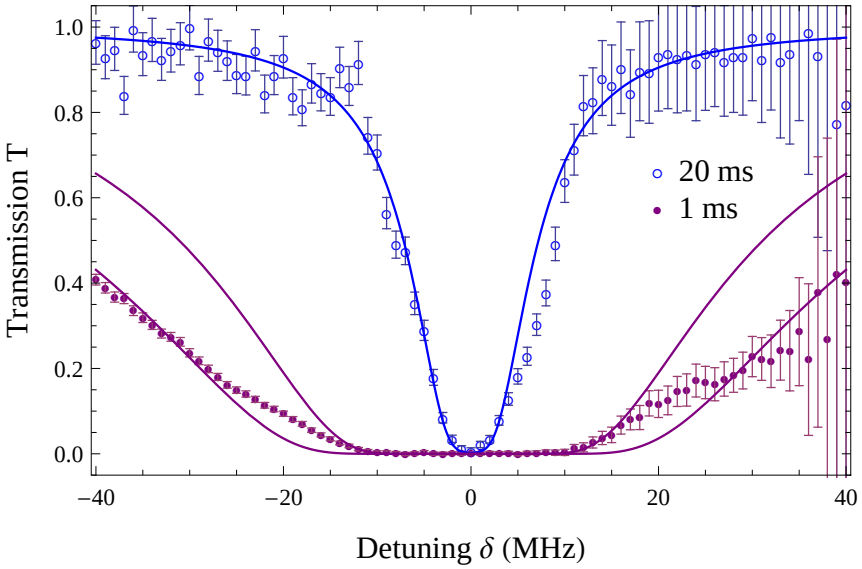

Figure 4.11: Absorption profiles when probing 1 ms or 20 ms after loading. The detuning is given relative to the $\{6S_{1/2},F=4\} \rightarrow \{6P_{3/2},F=5\}$ transition. The blue curve is a Lorentzian with OD = 6 and $\Gamma = 5.2$ MHz compatible with the data after 20 ms. The purple curves are Lorentzians with OD = 100 and OD = 200, and $\Gamma = 5.2$ MHz.

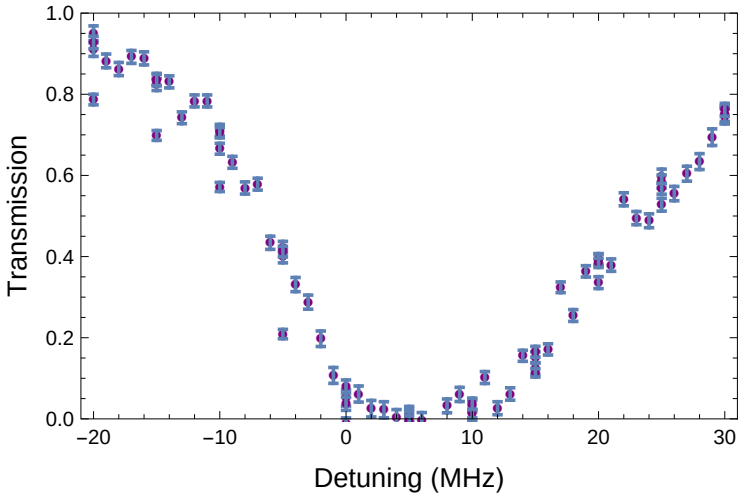

Figure 4.12: Absorption profile for a near resonant trap. Instead of the "magic" 935 nm wavelength, the red-detuned beams are tuned to 854.4 nm. The detuning of the probe is given relative to the $\{6S_{1/2},F=4\} \rightarrow \{6P_{3/2},F=5\}$ transition. The absorption line is shifted about +6MHz away from the unperturbed resonance. Data from October 2015.

Because of the state-insensitive trapping scheme, no shift and little asymmetry are visible. This can be compared to the results obtained with different trapping wavelengths as in Figure 4.12. For the latter, the "magic" red-detuned beams are

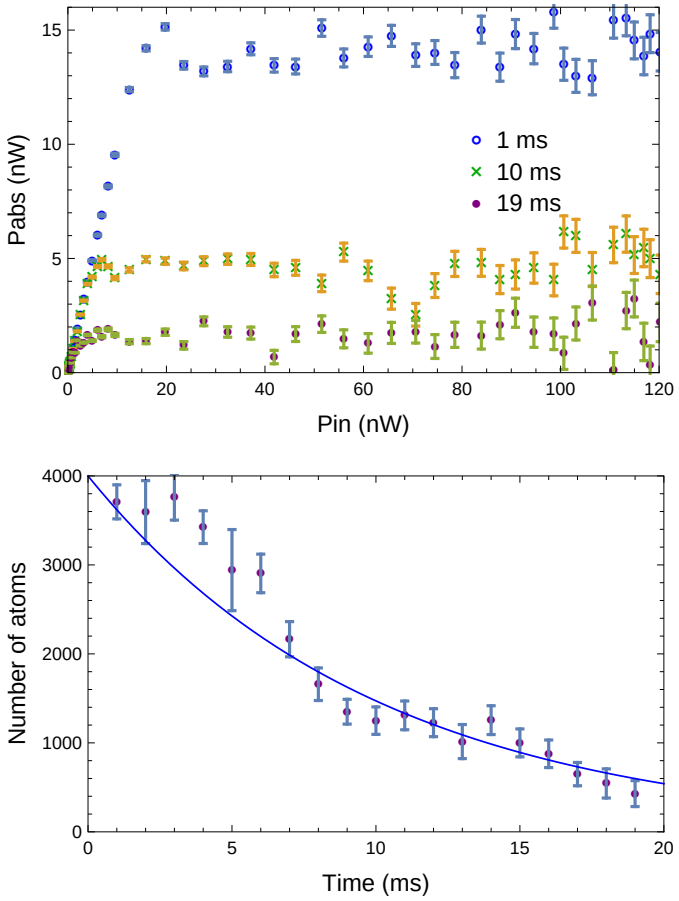

Figure 4.13: Top: Saturation of the absorbed power from a probe resonant on $\{6S_{1/2},F=4\} \rightarrow \{6P_{3/2},F=5\}$. The absorbed power ($P_{in}$-$P_{out}$) is given as a function of the input power. Bottom: Number of atoms derived with Eq. (2.3.1) as a function of time. The blue curve corresponds to an exponential decay with a 10 ms time constant.

replaced by beams with a wavelength of 854.4 nm, much closer to the D_2 resonance (the detuning is 2.05 nm). At this state-sensitive wavelength, the absorption line is clearly shifted to a larger frequency by about 6 MHz. The direction of the shift is expected. Since the trapping light is close to resonance, the two-level atom result is obtained: for red-detuned light, the ground state has lower energy and the excited state has a higher energy, the resonance is thus shifted to higher frequencies.

Saturation and number of atoms – Next, we measure saturation profiles such as in subsubsection 2.3.2.1. The number of trapped atoms can be estimated from such measurements. Now, the number of trapped atoms is a well defined quantity and can be derived directly from the absorbed power (recall Eq. (2.3.1)) in the saturated regime.

Figure 4.13 shows such saturation curves, for different trapping duration. The

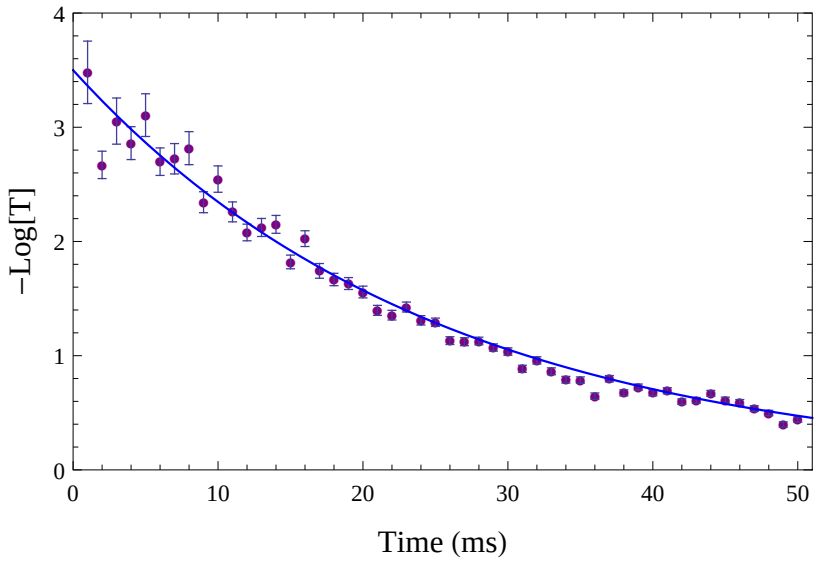

Figure 4.14: Transmission of a detuned probe as a function of time. The blue curve is an exponential decay with time constant 25 ms. The probe is detuned 15MHz away from the $\{6S_{1/2},F=4\} \rightarrow \{6P_{3/2},F=5\}$ transition. Data from June 2015.

derived number of atoms is plotted as a function of time. A few thousand atoms are trapped. The measured OD per atom is a few percent, lower than the 8% value reported by Goban et al. [Goban12], and similar to the values reported in [Vetsch10, Dawkins11][14] with a different trapping scheme.

Lifetime – The trap lifetime can be more directly measured by a simple absorption measurement plotted in log scale as a function of trapping time. The measurement can be done with a detuned probe for better signal to noise ratio at large optical depths. A result from June 2015 is plotted in Figure 4.14. The lifetime is improved to about 25 ms, the curve is well fitted by an exponential decay.

As a conclusion for this section, we implemented the nanofiber-mediated dipole trapped proposed in [Lacroûte12]. Thanks to the high optical depth obtained, and the suppression of transit-time broadening, we expect enhanced results in atomic ensemble-based protocols. We already observed EIT and memory signals similar to those described in chapter 3 in this configuration.

[14] In [Dawkins11] the on-resonance optical depth is deduced from a measurement of the phase-shift experienced by a detuned probe.

Chapter Conclusion

We described and implemented a light-matter interface in which atoms are trapped in individual sites in the vicinity of an optical nanofiber.

- We use a state-insensitive scheme: there are no differential scalar shifts between the ground and excited states of the D_2 line (using magic wavelengths 686 nm and 935 nm) and no vector shift (using linear local polarization of the trapping light).
- The individual trapping sites are arranged every $\lambda_{\mathrm{red}}/2$ in two lines on both sides of the 400 nm diameter fiber. Trapping frequencies of about 200 kHz and 30 kHz (azimuthal direction) and a ~ 0.3 mK trapping depth are expected.
- 4 mW are used in each blue detuned beam, and 0.5 mW in each red detuned beam. The blue detuned beams are detuned by a few 100 GHz relative to each other to avoid the superimposition of two lattices of different periodicity. All the polarization states are quasi-linearly polarized along the same axis.
- An efficient filtering system was setup, compatible with measurements at the single-photon level.
- We measured optical depth higher than 100 on the D_2 $\{F = 4\} \rightarrow \{F' = 5\}$ transition, corresponding to an OD per atom of a few percent. The lifetime for an atom in the trap is 25 ms.
- The coherence time is expected to be about 100 μs for a collective excitation of unpolarized Zeeman degenerate atoms. The ground state hyperfine coherence should persist for 30 ms at most for atoms cooled in the motional ground state.

The next experimental steps are the following:

- Quantum state purification (optical pumping) and control. Including the study of coherence in the trap.
- Implementing quantum-optics protocol based on atomic ensembles trapped around a nanofiber.
- Exploring other experimental ideas, including experiments in collaboration with LKB's optomechanics team. A nano-membrane in a fiber-coupled cavity will be connected to the nanofiber output. The atomic motion in the detuned light will thus be directly coupled to the membrane motion. Then, the membrane can for example be sympathetically cooled down by atomic cooling.

Conclusion

The main goal of this thesis was to start a new experiment involving nanofibers and cold atoms. This goal is reached. We now produce optical nanofibers in the lab, developed a full cold-atom physics environment and already reported important results obtained from this light-matter interface. The rich possibilities of this interface should allow to move towards quantum optics protocols, the main goal of the group with this experiment.

Nanofibers are produced using the flame brushing technique: standard fibers are heated and pulled until a subwavelength diameter is obtained. Light guided in these nanofibers is tightly focused and, thanks to a strong evanescent field, can interact efficiently with matter in its vicinity. We embedded such a nanofiber in a high-vacuum system. Then, a magneto-optically trapped ensemble of Cesium was prepared around the nanofiber, and allowed first ensemble-based experiments with nanofiber-guided light in our lab. More precisely, we observed electromagnetically-induced transparency, and realized a memory at the single-photon level for the light tightly confined by the nanofiber. More recently, we prepared an ensemble with higher optical depth (OD $\sim$ 100), and longer lifetime in the nanofiber vicinity. A few thousand atoms are now trapped in the individual potential wells created by detuned fiber-guided light beams. A two-color trapping scheme was implemented, with a "state-insensitive" variant which attempts to preserve the controlled coherence properties of isolated atoms, using well chosen wavelength and a linear local polarization of the electric field.

Different quantum-optics experiments we wish to implement with our new experimental setup are the building-blocks of the so-called DLCZ protocol [Duan01]. One of these building-blocks is the generation of heralded collective atomic excitations. As I explained in this manuscript, a single photon can be stored in an atomic ensemble using dynamic EIT. The information is stored as a collective excitation in the form:

$$|S\rangle = \sum_{i=1}^{N} |g_1,g_2,...,g_{i-1},s_i,g_{i+1},...,g_N\rangle \,.$$

As illustrated in Figure 4.15, there is another way to *write* such an excitation, based on photon detection. A detuned write beam is shone on the $|g\rangle \rightarrow |e\rangle$ transition. With a low probability, an atom is transferred to $|s\rangle$, emitting a photon (field 1) in a specific optical mode. If such a photon is detected, the creation of $|S\rangle$ is heralded. This long-lived excitation can then be transferred to a single-photon, with exactly the same technique as in the reading part of the dynamic-EIT memory: a *read* beam with the characteristics of the control beam of EIT, i.e. tuned on the $|s\rangle \rightarrow |e\rangle$ transition,

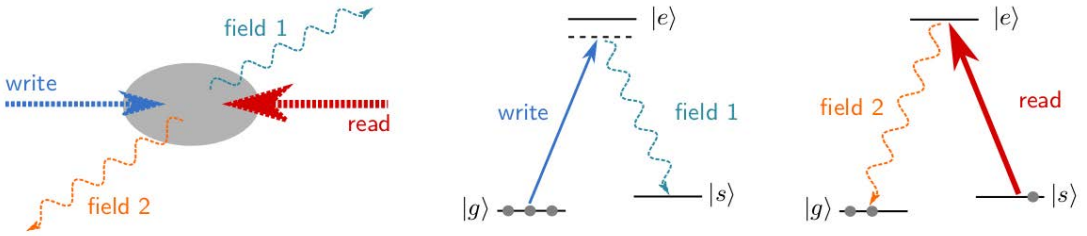

Figure 4.15: Ensemble-based single-photon generation. The write beam and detection of field 1 are first used for the heralded creation of a collective excitation. The read beam then triggers the emission a single photon propagating in EIT conditions.

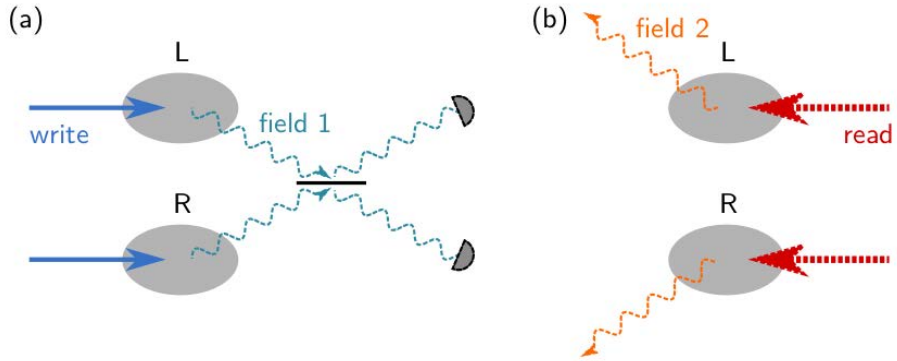

Figure 4.16: Creating entanglement between remote atomic ensembles. (a) Write beams are shined on both atomic ensembles. The detection of field 1 heralds entanglement amongst the two ensembles. (b) The entanglement can be analyzed after being transferred to an entangled photon pair.

in shone on the cloud. A single-photon is emitted and propagates out of the sample in EIT conditions and in a well-defined optical mode. Using such a protocol with a nanofiber would result in an all-fibered photon gun. The gun is loaded with the detection of a first nanofiber-guided photon, and triggered with the read beam.

This heralded collective excitation generation can easily be extended to the generation of entanglement between remote atomic ensembles. This entanglement is the ingredient of a quantum repeater, an important requirement of long-distance quantum communications. It can readily be implemented in our lab, using the two ensembles of the free-space and nanofiber experiments. As illustrated in Figure 4.16, this is done by mixing on a beam-splitter the heralding photon from both ensembles before detection. Elementary quantum networks can also be implemented, i.e. by generating a fiber-guided single-photon with a first ensemble, and storing it in a second ensemble using the dynamic-EIT memory presented in this thesis.

Very pleasantly, our nanofiber fabrication rig is already used for different applications that were not planned in the very beginning. Our optical nanofibers are used indeed by our neighbors in the lab, working in particular on the collection, by nanofibers, of single photons emitted from nanocrystals. They were also used as a platform for

fluid-structure interaction physics, and helped to understand better the properties of spider silk [Elettro15].

I should also mention different projects we have for our new experimental setup. One is the study of nanofiber-trapped atomic clouds described as a collection of discrete entities, rather than as a continuous medium. This includes the Bragg-mirror-like behavior of atomic arrays in a nanofiber vicinity [Le Kien14b, Chang12]. We also have an on-going collaboration with the optomechanics team of LKB, whose goal is to study the coupled vibrations of a nanomembrane in a fiber-coupled optical cavity, and atoms trapped close to a nanofiber. Since the mechanical elements (atom and membrane) are already fiber coupled in both teams, a simple fiber connection is possible. One of the main requirements is to match the oscillations frequencies of the atoms and the membrane. Indeed the atom-membrane coupling constant scales as

$$\omega_a \sqrt{\frac{N m_a}{m_m}} \sqrt{\frac{\omega_a}{\omega_m}} \mathcal{F},$$

where ω_a, ω_m, m_a and m_m are the atom and membrane vibration frequencies and masses, N is the number of atoms and $\mathcal{F}$ the optical-cavity finesse. It is clear in this formula that we should also maximize the number of trapped atoms such that the total atomic mass gets closer to the membrane effective mass. The mass mismatch can be compensated with a high finesse of the optical cavity, possibly with a 2D photonic-crystal nanomembrane [Makles15]. With such an atom-membrane motional coupling, cooling the atoms in their nanofiber trap would allow for example to cool the membrane, as demonstrated in a similar experiment recently [Jöckel15].

The present text was an attempt to build a coherent document, presenting most of the necessary tools needed to understand my work in the past few years. I tried however, not to over-describe ideas that were already very well presented elsewhere. I provided, as much as possible, as precise information as reasonable, which I hope, will be useful for the future research: both for the future of my own experiment, and for the ongoing work of the international research community.

Appendix A

Experiment control

A.1 Interfacing the experiment

A computer control is a very important ingredient, making possible otherwise over-challenging experiments.

The experiment built during my thesis is interfaced in the Python language. The hardest part as a beginner here, was to learn how to use - in Python - the interfacing tools provided with all the different instruments, something which became very easy and fast with some experience. The different interfaces are used together, both for changing the experiments parameters, and for data acquisition and display. This was realized thanks to remote control of different generators, of oscilloscopes[1] and of the FPGAs I will describe below.

My first try at experiment interfacing was actually the program for controlling and monitoring the nanofiber pulling rig. The code was written using the C++/Qt library for the graphical interface. A screenshot is given in Figure A.1.

One of the instruments we used was developed as a side project during my thesis and turned out to be a central part of our experiment control system: FPGAs, used both for 10 ns-resolution synchronization and time-stamp acquisition from photon detection events. The present appendix will give an introduction to these applications of FPGAs.

A.2 FPGAs as a tool for synchronization and time-stamp acquisition

One of the problem I had to solve during my thesis was the following. How should be handled the triggering events, the synchronization of the different ingredients of the experiment, with a sufficient precision. In our case a rather low resolution of about 10 ns was desired.

We would like here to generate a number of digital signals whose states can change at well defined times relative to each other, and with a resolution δt. These different signals will be used for example to turn on/off different laser beams controlled by

[1] Modern digital oscilloscopes are nothing else than an acquisition device with an advanced interface and a variety of integrated tools.

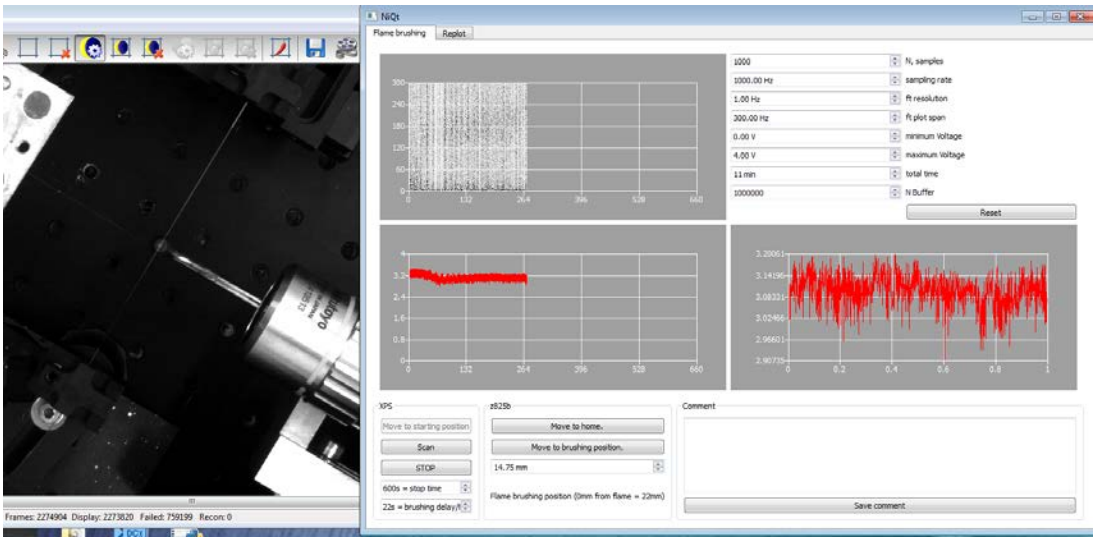

Figure A.1: Screenshot of the flame brushing interface. On the right is the Qt based interface (NiQt). Three plots are obtained from the photodiode signal. 1. bottom-right: photodiode output for the last second. 2. bottom-left: signal recorded since the beginning of the pulling. 3. top-left: spectrogram. Different parameters are setup on the bottom-left of the NiQt window. The different stages are initialized and the brushing process started with the different buttons.

acousto-optic modulators, or to trigger diverse analog signal acquisition or generation. Possible improvements include operating as a function of digital inputs, generating analog signals, or acquiring analog signals, analyzing them and reacting accordingly.

Regarding time scales, note here that during a nanosecond an electric signal propagates over about 30 cm. At this scale, it is thus important to take into account the nature and length of the cables, and to use adapted digital signal standards.

A.2.1 Different possible choices

The most immediate solution is to design a simple digital circuit tailored to our needs. A digital counter, triggered by a stable oscillator (a clock) should work. However the main flaw of this solution is its low adaptability: we need an easy way to reprogram our experimental sequences.

FPGA – A very flexible solution that has become inexpensive (<200 €) is the programming of a Field Programmable Gate Array (FPGA). In this digital circuit, individual logic gates can be rearranged indefinitely, unlike usual chips designed for a specific set of operations. The circuit is "drawn" in the form of text files whose information can be transferred to the FPGA chip. This possibility offers both the simplicity of basic logical circuits and the flexibility of reprogramming. FPGAs also have to advantage of being fast. It is easy to reach resolutions lower than 10 ns.

FPGA programming was introduced in our team by Sydney Burks [Burks10] when building the freespace memory experiment which is fully controlled using this solution.

However, expensive devices and softwares from National Instruments were used at that time. And the result, more complex, is not as fast as our present target. I myself started programming FPGAs as a side project during the first part of my PhD. They turned out to be cheap and fast synchronization systems based on simple ideas. They were rapidly used for another application with the contribution of Olivier Morin: acquiring data from photon-counting modules. I will describe these two applications in the following paragraphs.

Microprocessors – A different solution consists in using usual programmable systems, such as a personal computer or a microcontroller. These possibilities, as is, are not adapted to resolutions much smaller than microseconds, and cannot be used here.

Note that usual personal computers have very fast microprocessors. But they are commonly used with operating systems whose priority is user interface (when the mouse is moved, the user should see a result on the screen) and not well defined times. They can thus not be used for real time programming. However, "real time" operating systems such as RTLinux or FreeRTOS, which can handle precisely timed computations have been developed, but their speed do not correspond to our requirements.

In principle, a bare microprocessor and low level programming could be used for our purpose. Another rather straightforward solution would be to read our digital outputs directly from a fast-access memory, although the size of the memory might become rapidly inconvenient.

I did a few tests in this direction with the ARM processor of a Raspberry Pi computer, not as fast as more common personal computer processors, but with easily accessible programmable digital outputs. With a 700 MHz clock and a system based on an elementary counter, I obtained a resolution of about 60 ns. The solution should thus not completely be pushed aside.

Commercial solutions – They are different commercial solutions available. Examples are the Signadyne products, or the Spincore Pulseblaster which is very close to our needs, although we don't have any experience using it in the team.

A.2.2 FPGA programming

FPGAs can be bought as a chip already mounted on an electronic board facilitating common usage. We used in this thesis the Nexys 3 board from Digilent (Figure A.2), equipped with a Xilinx Spartan 6 FPGA. The board provides the possibility to configure the FPGA, interact with it, and transfer data via USB, a VHDC connector used to dispatch many digital outputs, displays and switches useful for debugging, and more...

An FPGA circuit is described by two files. The first one, written in a HDL (hardware description language), usually either verilog (*.v* files) or VHDL, describes the logical circuit itself, independently of the particular hardware. The second file (*.ucf*), gives the link between the inputs/outputs of the digital circuits and the pins of our particular FPGA chip.

Once these two source files (HDL and *.ucf*) are written, a configuration file (*.bit*) is compiled and can be consequently loaded to the FPGA. The source files are fed to

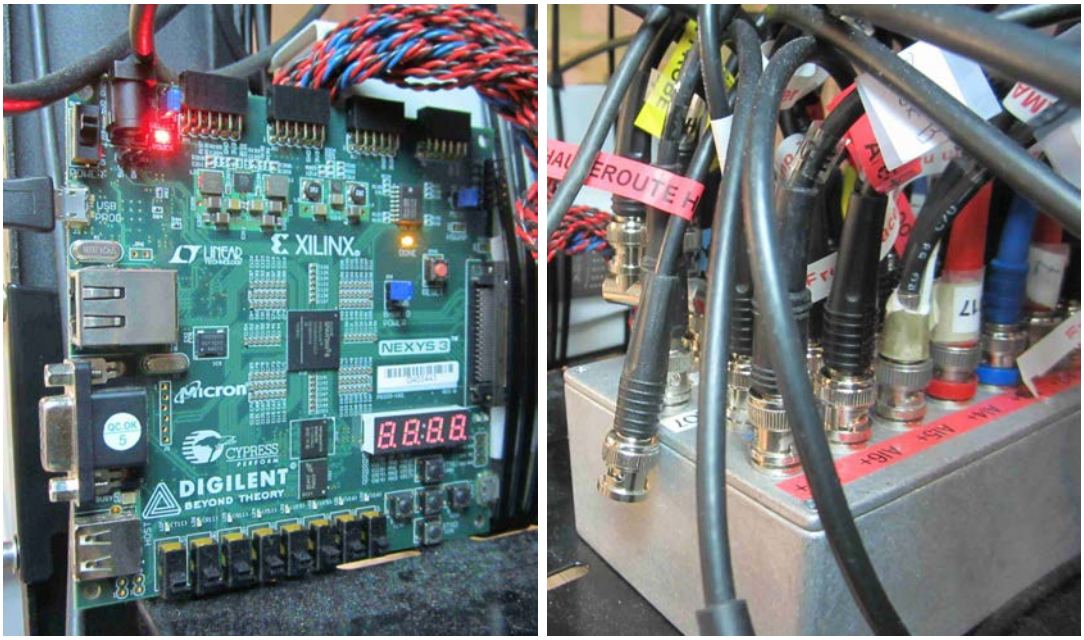

Figure A.2: Photo of an FPGA board used in the lab. On the left is the Digilent Nexys 3 board used as a synchronizer of the experiment. The central chip is the FPGA itself. We use a USB connector (left) for programming and remote control from a PC. The VHDC connector on the right of the board is dispatched in 32 BNC outputs which can be seen in the second picture (right).

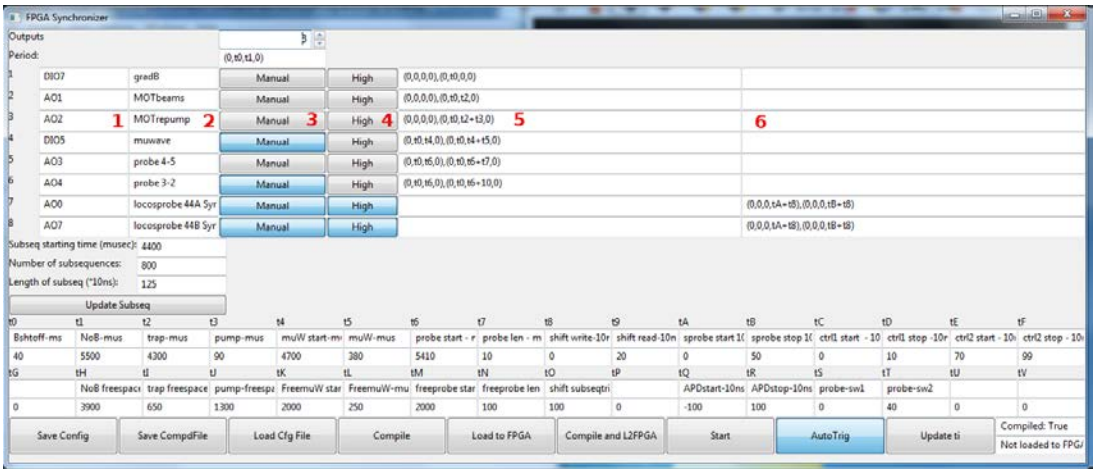

Figure A.3: Screenshot of the graphical interface for the FPGA-based synchronizer. For simplicity, we used a reduced number of outputs for this screenshot than what is actually used in experiments. Each output is controlled with a series of boxes in the outputs array (top half). The boxes for the third output are labeled here with red numbers. The first box is the label of the BNC connector corresponding to this output. For historical reasons, they have names that might suggest that there are analog channels (e.g. AO2), but they are actually all digital outputs. The second box describes the role of the output in the experiment (e.g. MOTrepump). The third and fourth boxes are buttons allowing to manually set the output value to high or low rather than running the experimental sequence. The fifth box allows to define the sequence: each pulse defined here will be repeated once per MOT cycle (The MOTrepump starts at time 0 and stops at time $t_0 + t_2 + t_3$, where t_0 is expressed in milliseconds and t2 and t3 in microseconds.). The last box is for the subsequence: each pulse defined here will be repeated in every subsequence (as shown in Figure 3.13). Here the MOTrepump is not used during the subsequence. Once the sequence is defined, the program is compiled and loaded to the FPGA. Different parameters can be updated without recompiling. The subsequence parameters for example (starting time, number of subsequences, period) are defined in the four lines just below the outputs array. We also typically use a set of 32 timing parameters: the *ti* numbers defined in the array in the bottom of the image. Note that the synchronizer can be configured and used entirely from the command line or external programs. This independent graphical interface allows easier definitions of the configurations saved in regular text files, or fast updates of the different parameters.

the proprietary compiling tools of the chip manufacturer. The required Xilinx tools are available online for free and can be used from the command line.

For our purpose, the digital circuit always has the same elements, but the sequences used in our experiments might change. I thus wrote a Python routine which, given a particular experimental sequence, automatically writes the verilog and *.ucf* files, compile them and load them to the FPGA. A few fancier features were also developed, such as a graphical interface (Figure A.3) for defining the experimental sequences and handling the many outputs, as well as the possibility to change some parameters of

the sequence without the need for recompiling (changing a specific pulse position or duration, activating or not a given output, or setting it to continuous rather than pulsed).

Below are brief descriptions of our designs and simple code examples. The full code and detailed description can be found online [webpage].

Synchronizer – Our synchronizer (or pulse generator) works on the following basis. During each clock cycle, a counter is incremented. The value of each output is changed whenever the counter reaches a desired value. In our case, we always run experiments cyclically: the counter is simply reseted when it has reached a value corresponding to the period of the experiment.

Here is an example of verilog file describing such a synchronizer:

```
module sync_main(
    ////////////////////////////////////////////////////
    // This file defines the synchronizer module sync_main.
    // Imagine a module as an electronic chip.
    // The "output wire" and "input wire" lines below are
    // declaring all the output and input pins of our chip.
    ////////////////////////////////////////////////////

    // 8 digital outputs
    output wire [7:0] outputs,

    // a clock (say a 100MHz oscillator) connected as input
    input wire clk
    );

    ////////////////////////////////////////////////
    // From now we describe what is inside the chip.
    ////////////////////////////////////////////////

    // A 32 bits memory, used to store our counter value.
    reg [31:0] counter;

    // A 8 bits memory, used to store the output values.
    reg [7:0] out;

    // The outputs wires are connected to the corresponding memory.
    assign outputs[7:0] = out[7:0];

    // The rest of the file says what should be done when
    // a clock input is switched from low voltage to high voltage.
    always@(posedge clk)
    begin
        // If the counter has reached a given value,
        // corresponding to the experimental period,
        // everything is reset.
        if(counter==1000000) // The sequence duration is 10ms.
            begin
                counter=0;
                out=0;
            end
        else
```

```
        // Otherwise the counter is incremented
        // and the outputs updated if required.
        begin
            counter = counter + 1;

            // Output 0 is programmed as a 500 ns pulse,
            // starting at t=10 microseconds.
            if(counter == 1000)
            begin
                // Adding 1 to a bit is equivalent to switching its value.
                out[0]=out[0]+1;
            end

            if(counter == 1050)
                begin
                    out[0]=out[0]+1;
                end

            // Output 1 is programmed as a 200 microseconds pulse,
            // starting at t=100 microseconds.
            if(counter == 10000)
            begin
                out[1]=out[1]+1;
            end

            if(counter == 30000)
            begin
                out[1]=out[1]+1;
            end
        // The other outputs aren't used here.
        end
    end
endmodule
```

And the *.ucf* counterpart for our FPGA board:

```
# The clock signal "clk" of our verilog file
# is connected to the pin "V10" of our FPGA chip.
NET "clk"            LOC = "V10" | IOSTANDARD = "LVCMOS33";
Net "clk" TNM_NET = sys_clk_pin;
TIMESPEC TS_sys_clk_pin = PERIOD sys_clk_pin 100000 kHz;

# The different outputs "outputs[i]" of our verilog file
# are connected to different pins of our FPGA chip
# (e.g. "A4" defined in the Xilink FPGA chip documentation).
# These pins are routed on our FPGA Board (Digilent Nexys 3)
# to the VHDC connector (defined in Nexys documentation).
NET "outputs<0>"         LOC = "A4" | IOSTANDARD = "LVCMOS33";
NET "outputs<1>"         LOC = "A5" | IOSTANDARD = "LVCMOS33";
NET "outputs<2>"         LOC = "B6" | IOSTANDARD = "LVCMOS33";
NET "outputs<3>"         LOC = "A3" | IOSTANDARD = "LVCMOS33";
NET "outputs<4>"         LOC = "A6" | IOSTANDARD = "LVCMOS33";
NET "outputs<5>"         LOC = "C7" | IOSTANDARD = "LVCMOS33";
NET "outputs<6>"         LOC = "C5" | IOSTANDARD = "LVCMOS33";
NET "outputs<7>"         LOC = "C8" | IOSTANDARD = "LVCMOS33";
```

An example of generated pulse is plotted in Figure A.4. In this simple example, for each redefinition of the experimental sequence, a new file has to be compiled. The

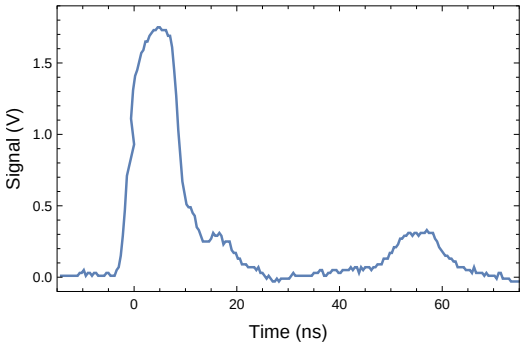

Figure A.4: A 10 ns pulse from our FPGA-based synchronizer. At this short time scale, it is clearly not an ideal square pulse.

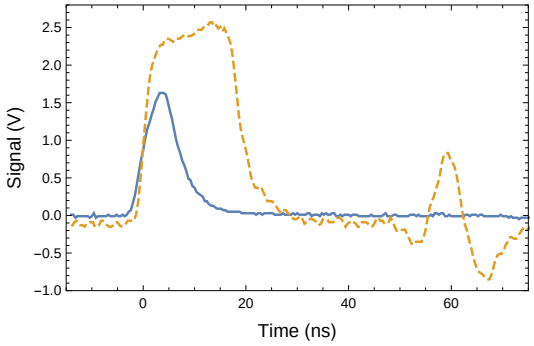

Figure A.5: APD detection pulse, before (solid line) and after shaping (dashed).

final version used in our lab takes profit of the USB communication capabilities of the board. Rather than comparing the counter value to fixed numbers, those number are stored in a small memory which can be changed by an external computer. This means than a USB interface must be implemented in the FPGA chip, which is a more complex circuit for someone not trained in digital circuit design. However, such an interface is available as a free software thanks to the work of Chris McClelland[2].

Time-stamp acquisition – Our time-stamp acquisition design is also based on a counter. An acquisition time interval is triggered by our synchronizer FPGA. During this interval the input voltage is recorded as a digital waveform, defined as 1 when the voltage is higher than a threshold value, and 0 otherwise. Before our acquisition device, the pulses from our single-photon counting modules (SPCM-AQR-14-FC) are amplified and shaped to a longer duration as shown in Figure A.5, using a simple op-amp-based analog circuit. The data is retrieved regularly and analyzed by an external computer. Rate of detections, histograms, or correlations are computed as a function of the different parameters of the experiment. This can be done with a graphical interface, compatible with acquisition from one channel (Figure A.6) or multiple channels.

Note that both for synchronization and time-stamp acquisition, we use 10 ns time increments for simplicity. We could in principle use a lower value although the nanosec-

[2]https://github.com/makestuff/libfpgalink

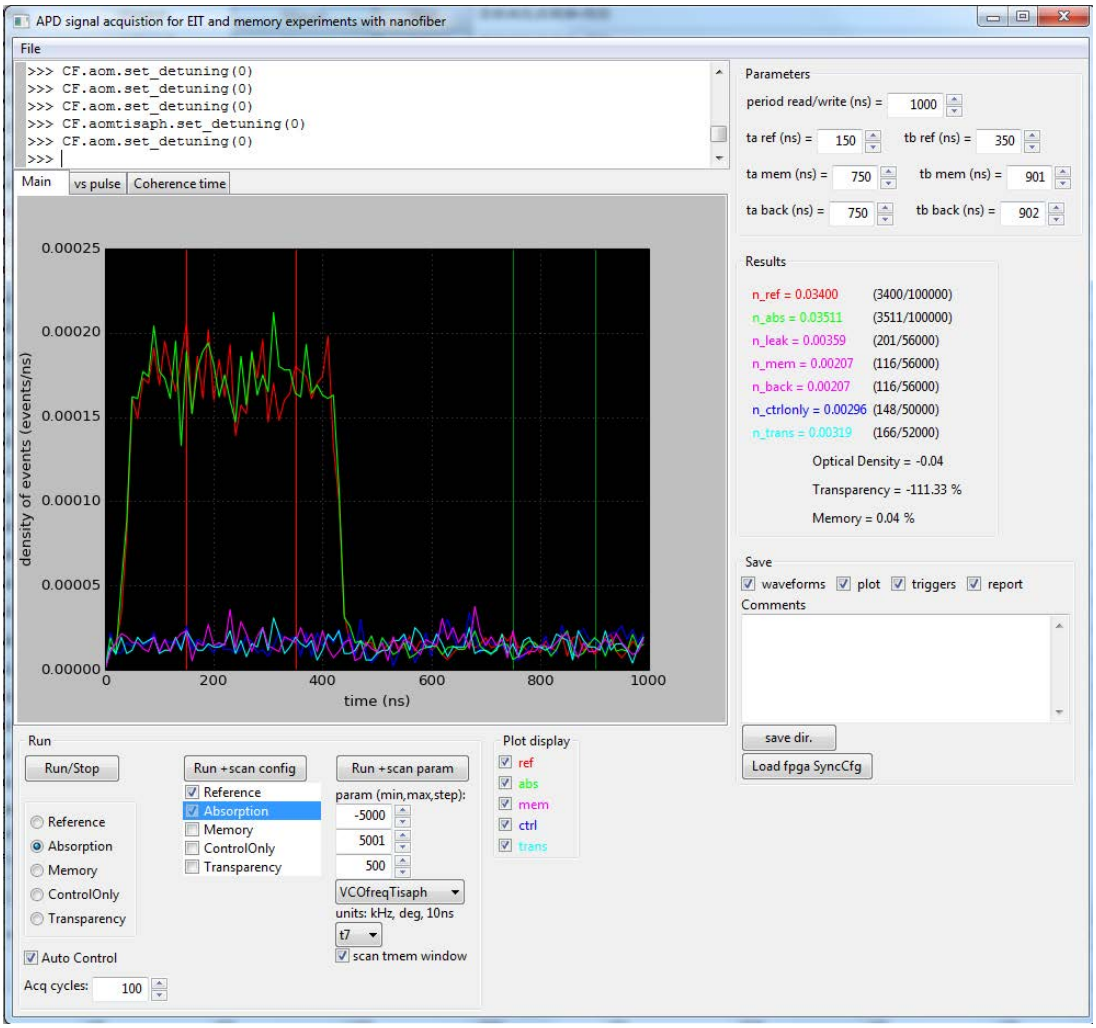

Figure A.6: Time-stamp acquisition interface used for memory experiments. Histograms built from APD detection events are plotted. The interface can automatically acquire data as a function of the different parameters of the experiment. The command line (top of the picture) allows to execute any desired python code. We also use a similar interface compatible with simultaneous acquisitions from 3 different APDs and correlations analysis.

ond time scale will not be reached with the hardware currently available. For every FPGA design used, the compiling tools give a limit on the maximum clock frequency which can be used with the target hardware. For very simple synchronizer designs or for our time-stamp-acquisition design for example, the minimal time increment is slightly smaller than 5 ns. For the designs we use in recent experiments, it is about 9 ns, but here some optimization would be possible. Using higher grade FPGAs can result to a speed improvement of a factor ~ 2, i.e. using Xilinx Zynq with the highest speed grade (-3).

For now we use the oscillators located on each Nexys 3 boards as clocks. The

independent boards (for the synchronizer or for the acquisition) thus accumulate a small timing error relative to each other. If this error becomes an issue in the experiment though, it is easy enough to use a single clock for all devices, as well as using a stabilized clock if better accuracy is required.

Chapter Conclusion

We have used FPGA boards as a cheap, simple enough and efficient way to synchronize an experiment and acquire time-stamps with a 10 ns resolution. Sources and more details are available online [webpage].

Appendix B

Magnetic fields

B.1 Measuring magnetic fields with Zeeman structure spectroscopy

As noted in chapter 3, a precise control of the magnetic field is required in our experiment. Atomic physics allows us to make a precise measurement of it via Zeeman-sublevel spectroscopy. Indeed, a magnetic field splits the Zeeman sublevels of the two hyperfine ground states of cesium. The energy splitting - which is proportionnal to the field - is measured with the method described in previous PhD thesis of the group [Giner13b, Veissier13] and summarized below. The method used is given in the first paragraph. Our results on magnetic field cancellation are detailed in the following paragraph.

B.1.1 Method for Zeeman-sublevel spectroscopy

The spectroscopy is done in the following way: atoms released from the MOT, initially in the $\{6S_{1/2},F=4\}$ state are transfered (via a magnetic dipole transition) to the $\{6S_{1/2},F=3\}$ state by a microwave pulse with frequency close the hyperfine splitting. The efficiency of the transfer is measured by probing the optical depth on $\{6S_{1/2},F=3\} \rightarrow \{6P_{3/2},F=2\}$ transition. It depends on the Zeeman splitting, the microwave frequency and the atomic Zeeman states involved as shown in Figure B.1. The timing sequence used is summarized in Figure B.2.

Plotting absorption as a function of the microwave frequency (Figure B.3) will typically lead in 15 peaks for non-zero magnetic field, more or less visible depending on the polarization of the microwaves magnetic field and on the possible imbalance in Zeeman-level populations. The minimal width of the peaks is usually limited by the duration of the microwave pulse (i.e. width $\sim 1/T \sim 10$ kHz). Larger width reflects the presence of gradients (in the probed volume) or variations of the field at the pulse length time-scale. For zero magnetic field, only a single central peak remains, its width allows to evaluate residual magnetic fields - which may be a residual offset, spatial gradients or time fluctuations.

Note that the optical probe propagates in free space using the same path than the control field of the EIT experiments (subsubsection 3.2.1.1). Indeed probing via the

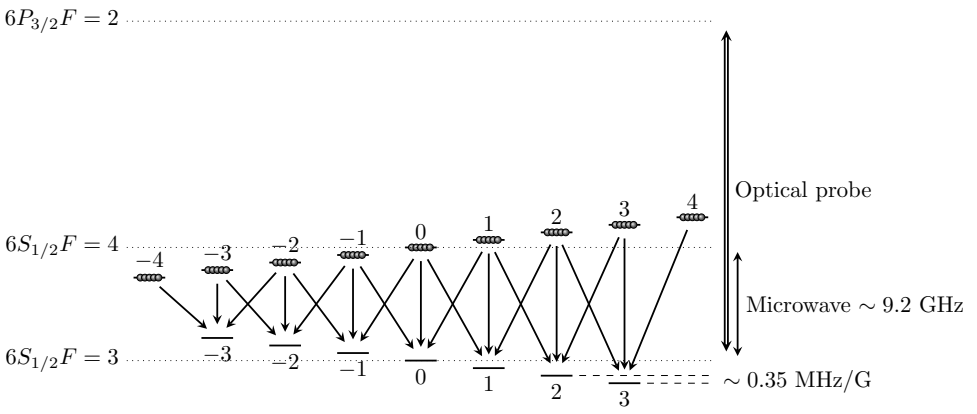

Figure B.1: Level diagram for Zeeman-sublevel spectroscopy.

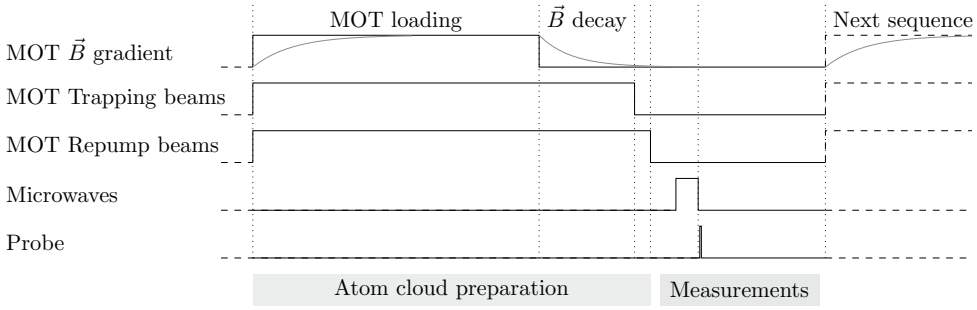

Figure B.2: Typical timing sequence for Zeeman-sublevel spectroscopy. The microwave pulse duration is chosen to generate approximately a π-pulse for the $m = 0 \rightarrow m = 0$ transition (typically 100 μs in our experiment) for optimal transfer of atoms in the $F = 3$ ground state. The pulse delay can be modified to measure the magnetic field at different times.

nanofiber led to very low signal to noise ratio: because of saturation (see subsubsection 2.3.2.1), very weak probes have to be used and longer integration time are thus required, possibly associated with detection in single-photon counting devices.

B.1.2 Canceling residual magnetic field offset and gradients in our experiment

The constant DC component of the $\vec{B}$ field and the time varying component are studied to optimize the fast cancellation of the magnetic field gradient used for the magneto-optical trap (MOT).

Shutting off the current in the MOT coils is done typically at the millisecond time scale. As during this time atoms are spreading and optical depth decreases, the shutting off time must be optimized to the lowest possible values. The circuit used, briefly described in subsection B.2.3 below, will typically take a few hundreds of microseconds. But unlike in the previous freespace EIT experiment of the group where

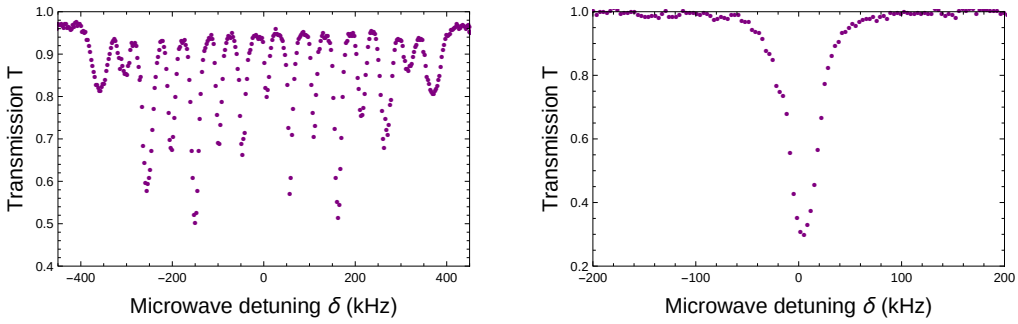

Figure B.3: Zeeman-sublevel spectroscopy. The transmission of the optical probe is plotted as a function of the microwave detuning from the cesium ground state hyperfine splitting. When a significant magnetic field remains (left), 15 peaks at most are visible, corresponding to the transitions of Figure B.1. The splitting between two adjacent peaks (here 50 kHz), is directly linked to the magnetic field value (here 140 mG). When the magnetic field is canceled (right), only one peak is visible.

the chamber is in glass, our vacuum chamber is made of stainless steel to allow for easier opening and insertion of nanofibers. This stainless steel chamber has a non negligible effect on magnetic fields. Indeed, during shutoff, eddy currents are generated in the chamber with long decay rates (tens of milliseconds) and create a residual magnetic field very unpractical here. After some optimization, using this circuit allowed us to make an experiment $\sim$ 4.4 ms after the beginning of the magnetic field shutoff. But time variations of the magnetic field remains. These variations might be canceled in the future. One of the possibility is to change the first MOT coils for smaller ones which does not respect the anti-Helmholtz criteria (see section B.2) but have a smaller mutual impedance when interacting with our vacuum chamber. Another direction - unsuccessful for now - is the use of an engineered shutoff of the current in the coils, including a negative impulsion which might be able to cancel the eddy currents. The solution actually adopted in the current setup is to work at longer times after turning off the MOT. This is made possible with further trapping of the atoms, either in an optical molasses or after being loaded in a dipole trap. Both of these schemes are described in chapter 4.

The DC (earth) residual field is cancelled using external pairs of bias coils aligned along 3 orthogonal axis. The residual magnetic field leads to a $\sim$ 30kHz central peak in the Zeeman spectroscopy (Figure B.3 right). This corresponds the residual fields smaller than 10 milligauss. Then central peak enlarges up to $\sim$ 100kHz during the full millisecond used for repeated experiments, which corresponds to 20 mG variations of the magnetic field.

B.2 Magnetic field coil design

Magnetic fields are produced by copper wires winded in coils outside the vacuum chamber. Three pairs of coils, ideally in Helmholtz configuration, are used for cancellation of the static surrounding magnetic field. Precise measurements of the cancellation are done with atomic spectroscopy as described in the previous section. An additional pair of coils, ideally in anti-Helmholtz configuration, produces the magnetic field gradient[1] required for the MOT.

We will consider in this appendix a few design considerations for these coils. The first part will introduce Helmholtz and anti-Helmholtz configurations. In a second part, we will consider the possibility to elongate a MOT in a preferred direction by using a different coil arrangement. We will then sum up the design considerations and give the characteristics of the final design used in our experiment.

B.2.1 Helmholtz and anti-Helmholtz configurations

Helmholtz and anti-Helmholtz configurations are arrangements for a pair of coils aimed at producing a nearly uniform magnetic field, or magnetic field gradient respectively. These configurations will be shortly described here.

We consider a system composed of two coaxial circular coils of identical radius R, each of them made of n turns, and separated by a distance d. The magnetic field produced by a single coil on its revolution axis is

$$\vec{B}(z) = \frac{\mu_0 n I}{2R} \frac{1}{(1+(z/R)^2)^{\frac{3}{2}}} \vec{u},$$

where z is the distance from the center of the coil and $\vec{u}$ is a unit vector parallel to the axis.

In the Helmholtz configuration, the two coils are carrying a current of same sign, so in the center a magnetic field is obtained whose gradient and all odd derivatives with respect to z are canceled by symmetry. The second derivative can be canceled as well by adjusting the distance d. One then obtains the Helmholtz configuration which gives a close to uniform magnetic field in the center and for which:

$$d = R,$$

and the magnetic field at the center of the system is:

$$\vec{B} = \frac{\mu_0 n I}{R} \frac{1}{(1+(d/2R)^2)^{\frac{3}{2}}} \vec{u}.$$

[1] Note that a *magnetic field gradient* is a rather imprecise term since a magnetic field is no a scalar, but a vector field. In the traditional MOT configuration with anti-Helmholtz coils, there are three axis of interest along which the laser beams are propagating. One is the coil revolution axis, and the other two are in the perpendicular plane. The magnetic field is null in the center, and when moving away along one of these axis, the magnetic field is pointing parallel to the axis. The given axis thus defines a quantization axis such that the circularly polarized light beams propagating along those axis can be described as $\sigma_\pm$ polarized. Care has to be taken when considering more complex coils arrangements with less symmetry such as proposed in subsection B.2.2.

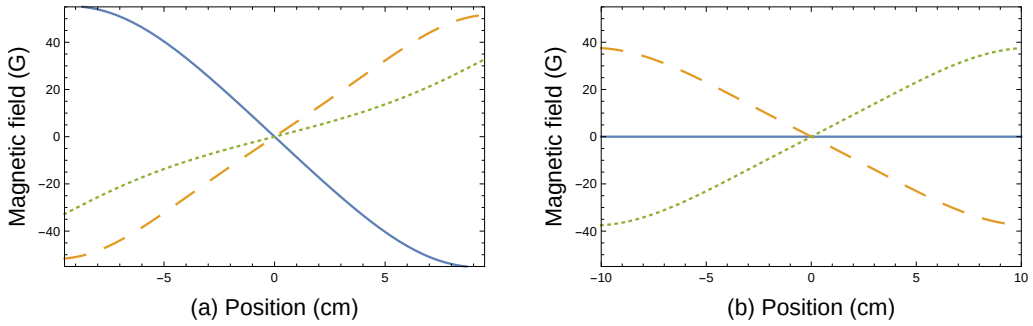

Figure B.4: Magnetic fields for an elongated MOT. The magnetic field along z, x and y axis are plotted in solid, dashed and dotted line respectively. For the two examples given, the magnetic field on a given axis is always parallel to this particular axis. (a) Elongated pair of rectangular coils with the parameters given in subsection B.2.4. The aspect ratio is 1.5 and the coils are close to anti-Helmholtz configuration. (b) 2D gradient with 2 pairs of coils. The four coils are 10×10 cm^2 squares and the two coils of a pair are 10 cm apart. Each coil is driven by 500 turns.A.

Another way to obtain a uniform magnetic field is to use a solenoid. This results is in a better uniformity but also a cumbersome setup with low optical access.

In the anti-Helmholtz configuration, the two coils are carrying opposite currents. All the even derivatives are canceled and d is chosen such that the third derivative cancels. A uniform magnetic field gradient is thus obtained. The configuration corresponds to:

$$d = \sqrt{3}R,$$

and, in the center:

$$\frac{\partial \vec{B}.\vec{u}}{\partial z} = \frac{\mu_0 n I}{R} \frac{-3\frac{d}{2R^2}}{(1+(d/2R)^2)^{\frac{5}{2}}}.$$

Even when the coils are not perfectly in Helmholtz/anti-Helmholtz configuration, the larger the coils compared to the volume of interest, the better the uniformity.

One might wonder what are the "Helmholtz" configuration for non circular coils. The answer for square coils for example is $d \sim 1.08R$ (Helmholtz) and $d \sim 1.10\sqrt{3}R$ (anti-Helmholtz) where $2R$ is now the square side's length.

B.2.2 Coils arrangement for an elongated MOT

In quantum memory experiments, absorption of a signal beam (optical depth) in a given direction is required to be as high as possible. One way to improve the optical depth of a cloud released from a MOT along this preferred direction is to create an elongated MOT. This can be done by modifying the coils design. Two solutions are summarized here and the resulting magnetic fields plotted in Figure B.4.

The first solution is to expand the coils shape in the direction of interest. For clarity, starting from the anti-Helmholtz configuration with square coils, let us note z the coils axis, y the perpendicular direction of elongation, and x the third direction.

In anti-Helmholtz configuration, the gradient along z is twice as large as the gradient along x and y. So the MOT is already not spherically symmetric. When expanding the coils in y direction the following happens: the gradient along y decreases progressively while the gradient along x gets gradually closer to the gradient along z as visible in Figure B.4a, this expansion will thus intuitively lead to a MOT expanded in the y direction. For an aspect ratio of 2 for example, the gradient along x is already 80% of the gradient along z, and the gradient along y is 6 times smaller.

The second solution is to use two identical pairs of coils rather than one, with axis respectively along x and y, and currents flowing in opposite directions. In this case the gradient is identical along x and y and exactly zero along z axis (Figure B.4b). This configuration is used in different experiments [Zhang12, Chen13, Yang12], including in the newest version of the free-space experiment of the team, as a tool to reach a very high optical depth.

B.2.3 Criteria considered for coil design

The different criteria for coils design in our experiment are listed below:

- Value of the target field (0.5 G for the compensation coils) or gradient (10 G/cm for the MOT).
- Uniformity of the magnetic field or gradient.
- Limited heating of the system.
- Space occupied (enough optical access should be left).
- Short cut-off time of the MOT gradient. The electronic circuit used was designed by Jean-Pierre Okpisz and is described in [Giner13b]. The coil is discharged - via transistors - in an external resistor, the main limitation being the high voltage $L\frac{dI}{dt}$ created by fast current decrease at the poles or an inductor.

The main parameters that can be adjusted are the following:

- the radius R of the coils,
- the number of turns n,
- the copper wire section area s (and its diameter δ)

Using the following equations:

- The dissipated power is $P = \rho I^2$ where $\rho = nr$, $r \propto R/s$ being the per-turn electrical resistance.
- The volume of a winded coil $V = 2\pi Rns$.
- The inductance of a coil is close to $L = n^2 l$ where l is the per-turn inductance. It is given by:
$$l = \mu_0 R(ln(\frac{16R}{\delta} - 1.75))$$
(Kirchoff's law approximated for $\frac{\delta}{R} \ll 1$ [Rosa12]).

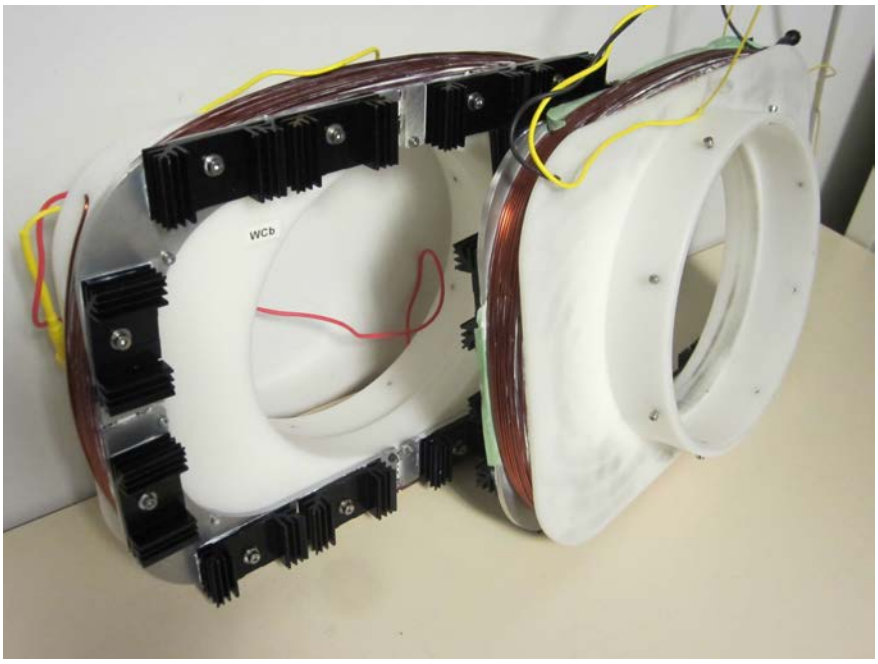

Figure B.5: Coils for the MOT magnetic field gradient.

For a constant field or gradient, the dissipated power can be decreased by increasing either the number of turns or the wire section s. Note however that larger wires are harder to wind. The result is the same in term of volume, but the current I is smaller in the first case and the inductance (and hence the shut-off time) is smaller in the second case.

B.2.4 Final design

The first coil design we built is elongated with ratio 1.5 and rather big in order to reach the anti-Helmholtz conditions. A picture is given in Figure B.5. The smallest side is 19 cm long, and the distance between the coils 16.5 cm. 9 G/cm are obtained at 8 A with 172 turns as plotted in Figure B.4a. The inductance of the two coils in position is 26 mH. 88 W are dissipated with 1.6 mm diameter wire. The dissipated power is dispatched on 12 heat sinks of thermal resistance 6.8 K/W: the steady state temperature is estimated to 75°C and measured around 90°C when the experiment is running cyclically.

The coil structure is made of plastic material in order to avoid magnetic sensitive metals. The specific material chosen, ertacetal, can experience rather high temperatures. Smaller aluminum parts are used on the external part for heat conduction towards the heat sinks. The structure is designed to fit directly on the large windows of the vacuum chamber. It can be removed and put back into position easily in a reproducible way when the front window is opened for a nanofiber transfer into vacuum.

A smaller design from the previous experiment (the rectangular coils from [Giner13b] figure III.9) has also been used as an attempt to decrease the eddy currents amplitude.

An even smaller design, discarding both the ideas of elongated coils and anti-Helmholtz criteria is planned for the future.

Appendix C

Transferring a nanofiber into vacuum protocol

C.1 Parts needed during operation

- Handling the fiber
  - Vacuum fiber-holder, clamps and screws
  - Swagelok-feedthrough Teflon part
  - 2 (+spares) sheaths for fiber guiding from the main window to the swagelok feedthroughs
  - Fiber-tail guides to be placed in front of the main window (U-shaped copper wires)
  - Splicing tools
  - Laser source, detector and continuous monitoring device
- Parts for the large window
  - Spare screws (M8-35mm) and washers
  - Anti-seize grease
  - Annealed gaskets
- Dispensers
  - Cesium dispensers
  - Can opener
- Pumping
  - Turbopump and related (KF flexible tube, KF clamps, KF seals)
  - Handle for angle valve
- Cleaning and storage

  - Clean clothes : masks, gloves, hats, shirts, shoes
  - Alcohol, lens paper, cotton swabs
  - Material for temporary storage of: large window, greasy-screws storage, Swagelok nuts, vacuum-fiber-holder screws and clamps
  - Aluminum foil

- Tools
  - Wrench for opening the large window (13mm)
  - Torque wrench for closing the large window (13mm)
  - Wrench for Swagelok feedthrough (11mm)
  - Wrench for nitrogen input (14mm)
  - Hex key for vacuum holder fixing
  - Pliers for cesium dispensers
  - Hex key for M6 screws
  - Some blank paper, some tape
  - Helper for Swagelok feedthrough closing (adjustable wrench)

- Fiber-pulling-rig side
  - Alcohol and lens paper
  - UHV glue and UV LED
  - Manual stages for fiber holder approach under the just fabricated nanofiber

C.2 To be prepared days before operation

- Reread this protocol together and make all the decisions.
- Clean vacuum components and tools.
- Make some space (including enough space for opening/closing the angle valve).
- Remove the front breadboard, including the front MOT coil and the back-reflection mirror fixed on this breadboard. It is OK to leave the compensation coils in place.
- Protect everything that stays there.
- Connect nitrogen Swagelok input.
- Clean the room.

C.3 Protocol

C.3.1 Getting ready

- Wear clean clothes.
- Make sure everything is removed correctly (breadboard, etc...) and clean.
- Make sure everything left is protected.
- Turn on both clean air laminar flows (nanofiber fabrication and main optical table).
- Have a storing zone for large window ready.
- Have a storing place for swagelok nuts and rings, for vacuum fiber holder (and its clamps and screws).

C.3.2 First stage

In parallel: someone is making a fiber while the rest of the team prepares the vacuum system.

C.3.2.1 Break-vacuum team

1. Open the nitrogen bottle : 1.2 bar abs.
2. Close the gate valve.
3. Open the angle valve (slowly in the beginning).
4. Break old-fiber tails close to Swagelok feedthroughs. Open Swagelok feedthroughs : untighten then remove, save nuts in a clean place.
5. Clean old-fiber tails.
6. Open large window :
    - Take care of grease.
    - Store screws (and washers) apart for later reuse.
    - Remove all screws and their washers before opening window. The window itself should be hold in place (one person holding the window while another is taking off the 3 last screws, and takes care of the gasket when the window is removed).
    - Store the window in the cleanest possible way.
7. (Increase nitrogen pressure to increase the flow.)
8. Take the nanofiber holder outside of the chamber (untighten the screws, take the holder, pull the fiber tails).

9. Save the fiber holder in a clean way.
10. Cleaning if possible (remove some grease left by the screws on the chamber, remove dust from the window).
11. Change cesium dispensers (open stored dispensers box, take old dispensers away, use pliers to prepare new ones, put them in the chamber, close dispenser box - nitrogen will be added later on).
12. Insert clean sheaths into fiber Swagelock (beware of the grease), leave the large window ends inside the chamber for now.
13. Prepare some fiber-tails guides in front of the chamber.
14. Wait for the fiber.

C.3.2.2 Make-a-fiber solo

1. Different from usual fabrication : make it with extra tail-length (1m on each side), more cleaning (clean the whole fiber), systematically use gloves.
2. Get the fiber vacuum holder ready.
3. Glue the fiber on fiber vacuum holder.
4. Open magnetic v-groove clamps.
5. Do not disconnect input laser or measuring connector.
6. Fiber is ready, wait for vacuum to be ready, monitor (and record) transmission, leave the laminar flux on.

C.3.3 Second stage

When fiber and vacuum are ready. 3 persons are needed for the first step.

1. When fiber ready on holder, put holder in vacuum. Done in a smart synchronous translation for 3 people :
   - Someone takes the holder for a translation directly to the chamber. Left arm under the fiber-reserve side of the fiber, grabs the measuring side of the holder. Right arm grabs the fiber reserve side of the holder.
   - Second person is on the measuring side and holds the connector.
   - Third person is on the fiber reserve side, and holds this side of the fiber.
2. Check fiber transmission
3. First tail (detector side)
   (a) Disconnect measuring connector.
   (b) Re-clean the fiber tail.

(c) Insert the free extremity of the fiber in its sheath and pull the fiber and sheath through the swagelok part.

(d) Remove the sheath and clean the fiber's tail

(e) Add the Teflon part, and close swagelok connection (do not tighten the connection yet, this will be done later while monitoring transmission).

(f) Reconnect the connector and recheck transmission.

(g) Remove the fiber-guide from the optical table.

4. Second tail (laser side)

(a) Cut laser side of the fiber.

(b) Clean the fiber tail.

(c) Insert the free extremity of the fiber in its sheath and pull the fiber and sheath through the swagelok part.

(d) Add the Teflon part, and close swagelok connection (do not tighten the connection yet, this will be done later while monitoring transmission).

(e) Re-splice laser side of the fiber.

(f) Check transmission through the fiber.

(g) Remove the fiber-guide from the optical table.

(h) From now on, monitor continuously the transmission through the fiber.

5. Fix fiber holder on the rails.

6. (decrease nitrogen pressure to 1.2 bar abs.)

7. Close large window.

8. Close angle valve.

9. Tighten the swagelok feedthroughs, while monitoring the transmission through the fiber. Do not over-tighten: stop before you need to use some strength, the Teflon part should not be squeezed out of the swagelok nut (around the fiber) – it should be squeezed though.

C.3.4 Third and last stage

Pump and finalize.

1. Disconnect nitrogen.

2. Optional : perform some leak detection.

3. Connect the turbopump.

4. Start the turbopump to empty the tube going to the angle valve, then stop the turbo pump before opening the angle valve, then start the turbopump again.

5. Check if tightening the swagelok a bit more can improve the measured pressure.

6. Dispensers baking: 2.5A for 30min.
7. Use nitrogen to fill the cesium dispenser container et re-close container.
8. Test whether the dipole trap light (with the proper power) can be guided through the fiber.
9. When turbo pump has pumped enough (half a day), open gate valve then close angle valve.
10. Write detailed notes.

Bibliography

[Abraham98] Abraham, E. R. and E. A. Cornell. Teflon feedthrough for coupling optical fibers into ultrahigh vacuum systems. *Appl Opt*, 37(10):1762–1763, Apr 1998. (cited in p. 34)

[Agarwal78] Agarwal, G. S. Quantum statistical theory of optical-resonance phenomena in fluctuating laser fields. *Phys. Rev. A*, 18:1490–1506, Oct 1978. URL http://dx.doi.org/10.1103/PhysRevA.18.1490. (cited in p. 65)

[Aoki10] Aoki, Takao. Fabrication of Ultralow-Loss Tapered Optical Fibers and Microtoroidal Resonators. *Japanese Journal of Applied Physics*, 49(11R):118001, 2010. URL http://stacks.iop.org/1347-4065/49/i=11R/a=118001. (cited in p. 15)

[Arimondo96] Arimondo, Ennio. Relaxation processes in coherent-population trapping. *Phys. Rev. A*, 54:2216–2223, Sep 1996. URL http://dx.doi.org/10.1103/PhysRevA.54.2216. (cited in p. 65)

[Balykin04] Balykin, V. I., K. Hakuta, F. Le Kien, J. Q. Liang, and M. Morinaga. Atom trapping and guiding with a subwavelength-diameter optical fiber. *Physical Review A*, 70(1):011401, July 2004. URL http://dx.doi.org/10.1103/PhysRevA.70.011401. (cited in p. 4)

[Béguin14] Béguin, J.-B., E. M. Bookjans, S. L. Christensen, H. L. Sørensen, J. H. Müller, E. S. Polzik, and J. Appel. Generation and Detection of a Sub-Poissonian Atom Number Distribution in a One-Dimensional Optical Lattice. *Phys. Rev. Lett.*, 113:263603, Dec 2014. URL http://dx.doi.org/10.1103/PhysRevLett.113.263603. (cited in p. 4)

[Birks92] Birks, Timothy A. and Youwei W. Li. The Shape of Fiber Tapers. *Journal of Lightwave Technology*, 10:4, April 1992. (cited in p. 16)

[Black91] Black, R.J., S. Lacroix, F. Gonthier, W.M. Henry, W.J. Stewart, and J.D. Love. Tapered single-mode fibres and devices. *IEE Proceedings*, 138:5, October 1991. (cited in p. 16)

[Boller91] Boller, K.-J., A. Imamoğlu, and S. E. Harris. Observation of electromagnetically induced transparency. *Phys. Rev. Lett.*, 66:2593–2596, May 1991. URL http://dx.doi.org/10.1103/PhysRevLett.66.2593. (cited in p. 65)

[Boyd07] Boyd, Martin M., Andrew D. Ludlow, Sebastian Blatt, Seth M. Foreman, Tetsuya Ido, Tanya Zelevinsky, and Jun Ye. ^{87}Sr Lattice Clock with Inaccuracy below 10^{-15}. *Phys. Rev. Lett.*, 98:083002, Feb 2007. URL http://dx.doi.org/10.1103/PhysRevLett.98.083002. (cited in p. 104)

[Brambilla04] Brambilla, Gilberto, Vittoria Finazzi, and David Richardson. Ultra-low-loss optical fiber nanotapers. *Opt. Express*, 12(10):2258–2263, May 2004. URL http://dx.doi.org/10.1364/OPEX.12.002258. (cited in p. 3)

[Brambilla10] Brambilla, G. Optical Fibre Nanowires and Microwires: a Review. *Journal of Optics*, 12:043001, March 2010. (cited in p. 3)

[Burks10] Burks, Sidney. *Towards A Quantum Memory For Non-Classical Light With Cold Atomic Ensembles*. Theses, Université Pierre et Marie Curie - Paris VI, October 2010. URL https://tel.archives-ouvertes.fr/tel-00699270. (cited in p. 122)

[Candéla11] Candéla, Yves. *Silica microcavities : Fibre excitation of whispering gallery modes and coupling with Silicon nanocrystals*. Ph.D. thesis, Université Pierre et Marie Curie - Paris VI, 2011. URL https://tel.archives-ouvertes.fr/tel-00658670. (cited in p. 15)

[Carvalho04] Carvalho, P. R. S., Luís E. E. de Araujo, and J. W. R. Tabosa. Angular dependence of an electromagnetically induced transparency resonance in a Doppler-broadened atomic vapor. *Phys. Rev. A*, 70:063818, Dec 2004. URL http://dx.doi.org/10.1103/PhysRevA.70.063818. (cited in p. 89)

[Chang07] Chang, D. E., A. S. Sørensen, E. A. Demler, and M. D. Lukin. A single-photon transistor using nanoscale surface plasmons. *Nature Physics*, 3:807–812, November 2007. 0706.4335, URL http://dx.doi.org/10.1038/nphys708. (cited in p. 55)

[Chang12] Chang, D E, L Jiang, A V Gorshkov, and H J Kimble. Cavity QED with atomic mirrors. *New Journal of Physics*, 14(6):063003, 2012. URL http://stacks.iop.org/1367-2630/14/i=6/a=063003. (cited in p. 119)

[Chang14] Chang, Darrick E., Vladan Vuletic, and Mikhail D. Lukin. Quantum nonlinear optics - photon by photon. *Nat Photon*, 8(9):685–694, September 2014. ISSN 1749-4885. URL http://dx.doi.org/10.1038/nphoton.2014.192. (cited in p. 4 and 49)

[Chen13] Chen, Yi-Hsin, Meng-Jung Lee, I-Chung Wang, Shengwang Du, Yong-Fan Chen, Ying-Cheng Chen, and Ite A. Yu. Coherent Optical Memory with High Storage Efficiency and Large Fractional Delay. *Phys. Rev. Lett.*, 110:083601, Feb 2013. URL http://dx.doi.org/10.1103/PhysRevLett.110.083601. (cited in p. 136)

[Choi11] Choi, Kyung Soo. *Coherent control of entanglement with atomic ensembles Citation*. Ph.D. thesis, California Institute of Technology, 2011. (cited in p. 89)

[Dalibard13] Dalibard, J. Des cages de lumière pour les atomes: la physique des pièges et des réseaux optiques. Cours 1: Le potentiel dipolaire. Leçons au Collège de France. available online at http://www.phys.ens.fr/ dalibard/CdF/2013/cours1.pdf, May 2013. URL http://www.phys.ens.fr/~dalibard/CdF/2013/cours1.pdf. (cited in p. 97)

[Dawkins11] Dawkins, S. T., R. Mitsch, D. Reitz, E. Vetsch, and A. Rauschenbeutel. Dispersive Optical Interface Based on Nanofiber-Trapped Atoms. *Physical Review Letters*, 107(24):243601, December 2011. URL http://dx.doi.org/10.1103/PhysRevLett.107.243601. (cited in p. 115)

[Deutsch98] Deutsch, Ivan H. and Poul S. Jessen. Quantum-state control in optical lattices. *Phys. Rev. A*, 57:1972–1986, Mar 1998. URL http://dx.doi.org/10.1103/PhysRevA.57.1972. (cited in p. 103)

[Ding12] Ding, D., A. Goban, K. S. Choi, and H. J. Kimble. Corrections to our results for optical nanofiber traps in Cesium. *ArXiv e-prints*, December 2012. 1212.4941. (cited in p. 95 and 104)

[Duan01] Duan, L.-M., M. D. Lukin, J. I. Cirac, and P. Zoller. Long-distance quantum communication with atomic ensembles and linear optics. *Nature*, 414(6862):413–418, November 2001. ISSN 0028-0836. URL http://dx.doi.org/10.1038/35106500. (cited in p. 76 and 117)

[Elettro15] Elettro, Hervé. *Elastocapillary windlass: from spider silk to smart actuators*. Theses, UPMC, July 2015. URL http://hal.upmc.fr/tel-01200518. (cited in p. 119)

[Fleischhauer00] Fleischhauer, M. and M. D. Lukin. Dark-State Polaritons in Electromagnetically Induced Transparency. *Phys. Rev. Lett.*, 84:5094–5097, May 2000. URL http://dx.doi.org/10.1103/PhysRevLett.84.5094. (cited in p. 73, 74, and 76)

[Fleischhauer05] Fleischhauer, Michael, Atac Imamoglu, and Jonathan P. Marangos. Electromagnetically induced transparency: Optics in coherent media. *Rev. Mod. Phys.*, 77:633–673, Jul 2005. URL http://dx.doi.org/10.1103/RevModPhys.77.633. (cited in p. 57, 64, and 65)

[Gallagher89] Gallagher, Alan and David E. Pritchard. Exoergic collisions of cold Na*-Na. *Phys. Rev. Lett.*, 63:957–960, Aug 1989. URL http://dx.doi.org/10.1103/PhysRevLett.63.957. (cited in p. 107)

[Garcia-Fernandez11] Garcia-Fernandez, R., W. Alt, F. Bruse, C. Dan, K. Karapetyan, O. Rehband, A. Stiebeiner, U. Wiedemann, D. Meschede, and A. Rauschenbeutel. Optical nanofibers and spectroscopy. *Applied Physics B-lasers and Optics*, 105(1):3–15, October 2011. URL http://dx.doi.org/10.1007/s00340-011-4730-x. (cited in p. 15)

[Giner13a] Giner, L., L. Veissier, B. Sparkes, A. S. Sheremet, A. Nicolas, O. S. Mishina, M. Scherman, S. Burks, I. Shomroni, D. V. Kupriyanov, P. K. Lam, E. Giacobino, and J. Laurat. Experimental investigation of the transition between Autler-Townes splitting and electromagnetically-induced-transparency models. *Phys. Rev. A*, 87:013823, Jan 2013. URL http://dx.doi.org/10.1103/PhysRevA.87.013823. (cited in p. 84)

[Giner13b] Giner, Lambert. *Etude de la Transparence Electromagnétiquement Induite dans un ensemble d'atomes froids et application aux mémoires quantiques.* Theses, Université Pierre et Marie Curie - Paris VI, May 2013. (cited in p. 1, 32, 37, 131, 136, and 137)

[Goban12] Goban, A., K. S. Choi, D. J. Alton, D. Ding, C. Lacroûte, M. Pototschnig, T. Thiele, N. P. Stern, and H. J. Kimble. Demonstration of a State-Insensitive, Compensated Nanofiber Trap. *Phys. Rev. Lett.*, 109:033603, Jul 2012. URL http://dx.doi.org/10.1103/PhysRevLett.109.033603. (cited in p. 4, 26, 95, 100, 105, 111, and 115)

[Goban15] Goban, Akihisa. *Strong atom-light interactions along nanostructures: Transition from free-space to nanophotonic interfaces.* Ph.D. thesis, California Institute of Technology, 2015. (cited in p. 55)

[Gouraud15] Gouraud, B., D. Maxein, A. Nicolas, O. Morin, and J. Laurat. Demonstration of a Memory for Tightly Guided Light in an Optical Nanofiber. *Phys. Rev. Lett.*, 114:180503, May 2015. URL http://dx.doi.org/10.1103/PhysRevLett.114.180503. (cited in p. 21, 47, and 79)

[Grimm00] Grimm, Rudolf, Matthias Weidemüller, and Yurii B. Ovchinnikov. Optical Dipole Traps for Neutral Atoms. volume 42 of *Advances In Atomic, Molecular, and Optical Physics*, pages 95 – 170. Academic Press, 2000. URL http://dx.doi.org/10.1016/S1049-250X(08)60186-X. (cited in p. 97)

[Grunzweig10] Grunzweig, T., A. Hilliard, M. McGovern, and M. F. Andersen. Near-deterministic preparation of a single atom in an optical microtrap. *Nat Phys*, 6(12):951–954, December 2010. ISSN 1745-2473. URL http://dx.doi.org/10.1038/nphys1778. (cited in p. 108)

[Hammerer10] Hammerer, Klemens, Anders S. Sørensen, and Eugene S. Polzik. Quantum interface between light and atomic ensembles. *Rev. Mod. Phys.*, 82:1041–1093, Apr 2010. URL http://dx.doi.org/10.1103/RevModPhys.82.1041. (cited in p. 57 and 76)

[Hendrickson09] Hendrickson, S. M., T. B. Pittman, and J. D. Franson. Nonlinear transmission through a tapered fiber in rubidium vapor. *J. Opt. Soc. Am. B*, 26(2):267–271, Feb 2009. URL http://dx.doi.org/10.1364/JOSAB.26.000267. (cited in p. 4)

[Hoffman14] Hoffman, J. E., S. Ravets, J. A. Grover, P. Solano, P. R. Kordell, J. D. Wong-Campos, L. A. Orozco, and S. L. Rolston. Ultrahigh transmission optical nanofibers. *AIP Advances*, 4(6):067124, 2014. URL http://dx.doi.org/10.1063/1.4879799. (cited in p. 15, 21, and 22)

[Hoffman15] Hoffman, Jonathan E., Fredrik K. Fatemi, Guy Beadie, Steven L. Rolston, and Luis A. Orozco. Rayleigh scattering in an optical nanofiber as a probe of higher-order mode propagation. *Optica*, 2(5):416–423, May 2015. URL http://dx.doi.org/10.1364/OPTICA.2.000416. (cited in p. 15 and 16)

[Jenkins06] Jenkins, S. D., D. N. Matsukevich, T. Chanelière, A. Kuzmich, and T. A. B. Kennedy. Theory of dark-state polariton collapses and revivals. *Phys. Rev. A*, 73:021803, Feb 2006. URL http://dx.doi.org/10.1103/PhysRevA.73.021803. (cited in p. 90)

[Jenkins12] Jenkins, S. D., T. Zhang, and T. A. B. Kennedy. Motional dephasing of atomic clock spin waves in an optical lattice. *Journal of Physics B: Atomic, Molecular and Optical Physics*, 45(12):124005, 2012. URL http://stacks.iop.org/0953-4075/45/i=12/a=124005. (cited in p. 88 and 90)

[Jones14] Jones, D. E., J. D. Franson, and T. B. Pittman. Saturation of atomic transitions using subwavelength diameter tapered optical fibers in rubidium vapor. *J. Opt. Soc. Am. B*, 31(8):1997–2001, Aug 2014. URL http://dx.doi.org/10.1364/JOSAB.31.001997. (cited in p. 50)

[Jöckel15] Jöckel, Andreas, Aline Faber, Tobias Kampschulte, Maria Korppi, Matthew T. Rakher, and Philipp Treutlein. Sympathetic cooling of a membrane oscillator in a hybrid mechanical–atomic system. *Nat Nano*, 10(1):55–59, January 2015. ISSN 1748-3387. URL http://dx.doi.org/10.1038/nnano.2014.278. (cited in p. 119)

[Kato15] Kato, Shinya and Takao Aoki. Strong Coupling between a Trapped Single Atom and an All-Fiber Cavity. *Phys. Rev. Lett.*, 115:093603, Aug 2015. URL http://dx.doi.org/10.1103/PhysRevLett.115.093603. (cited in p. 4)

[Klimov04] Klimov, V. V. and M. Ducloy. Spontaneous emission rate of an excited atom placed near a nanofiber. *Phys. Rev. A*, 69:013812, Jan 2004. URL http://dx.doi.org/10.1103/PhysRevA.69.013812. (cited in p. 55)

[Kuppens00] Kuppens, S. J. M., K. L. Corwin, K. W. Miller, T. E. Chupp, and C. E. Wieman. Loading an optical dipole trap. *Phys. Rev. A*, 62:013406, Jun 2000. URL http://dx.doi.org/10.1103/PhysRevA.62.013406. (cited in p. 107)

[Lacroûte12] Lacroûte, C, K S Choi, A Goban, D J Alton, D Ding, N P Stern, and H J Kimble. A state-insensitive, compensated nanofiber trap. *New Journal of Physics*, 14(2):023056, 2012. URL http://stacks.iop.org/1367-2630/14/i=2/a=023056. (cited in p. 95, 103, 104, and 115)

[Le Kien04] Le Kien, F., V. I. Balykin, and K. Hakuta. Atom trap and waveguide using a two-color evanescent light field around a subwavelength-diameter optical fiber. *Physical Review A*, 70(6):063403, December 2004. URL http://dx.doi.org/10.1103/PhysRevA.70.063403. (cited in p. 95)

[Le Kien05] Le Kien, F., S. D. Gupta, V. I. Balykin, and K. Hakuta. Spontaneous emission of a cesium atom near a nanofiber: Efficient coupling of light to guided modes. *Physical Review A*,

72(3):032509, September 2005. URL http://dx.doi.org/10.1103/PhysRevA.72.032509. (cited in p. 5 and 55)

[Le Kien09] Le Kien, Fam and K. Hakuta. Slowing down of a guided light field along a nanofiber in a cold atomic gas. *Physical Review A*, 79(1):013818, January 2009. URL http://dx.doi.org/10.1103/PhysRevA.79.013818. (cited in p. 53, 57, and 84)

[Le Kien13a] Le Kien, Fam, P. Schneeweiss, and A. Rauschenbeutel. State-dependent potentials in a nanofiber-based two-color trap for cold atoms. *Phys. Rev. A*, 88:033840, Sep 2013. URL http://dx.doi.org/10.1103/PhysRevA.88.033840. (cited in p. 95, 103, and 104)

[Le Kien13b] Le Kien, Fam, Philipp Schneeweiss, and Arno Rauschenbeutel. Dynamical polarizability of atoms in arbitrary light fields: general theory and application to cesium. *The European Physical Journal D*, 67(5):92, 2013. ISSN 1434-6060. URL http://dx.doi.org/10.1140/epjd/e2013-30729-x. (cited in p. 95, 97, 99, 101, 102, and 104)

[Le Kien14a] Le Kien, Fam and A. Rauschenbeutel. Anisotropy in scattering of light from an atom into the guided modes of a nanofiber. *Physical Review A*, 90(2):023805, August 2014. URL http://dx.doi.org/10.1103/PhysRevA.90.023805. (cited in p. 55)

[Le Kien14b] Le Kien, Fam and A. Rauschenbeutel. Propagation of nanofiber-guided light through an array of atoms. *Phys. Rev. A*, 90:063816, Dec 2014. URL http://dx.doi.org/10.1103/PhysRevA.90.063816. (cited in p. 55 and 119)

[Le Kien15] Le Kien, Fam and A. Rauschenbeutel. Electromagnetically induced transparency for guided light in an atomic array outside an optical nanofiber. *Phys. Rev. A*, 91:053847, May 2015. URL http://dx.doi.org/10.1103/PhysRevA.91.053847. (cited in p. 57)

[Lee15] Lee, J, J A Grover, J E Hoffman, L A Orozco, and S L Rolston. Inhomogeneous broadening of optical transitions of 87 Rb atoms in an optical nanofiber trap. *Journal of Physics B: Atomic, Molecular and Optical Physics*, 48(16):165004, 2015. URL http://stacks.iop.org/0953-4075/48/i=16/a=165004. (cited in p. 4)

[Leon-Saval04] Leon-Saval, S. G., T. A. Birks, W. J. Wadsworth, P. St.J. Russell, and M. W. Mason. Supercontinuum generation in submicron fibre waveguides. *Optics Express*, 12:13, June 2004. (cited in p. 3)

[Lester15] Lester, Brian J., Niclas Luick, Adam M. Kaufman, Collin M. Reynolds, and Cindy A. Regal. Rapid Production of Uniformly Filled Arrays of Neutral Atoms. *Phys. Rev. Lett.*, 115:073003, Aug 2015. URL http://dx.doi.org/10.1103/PhysRevLett.115.073003. (cited in p. 108)

[Lu Ding10] Lu Ding, Sara Ducci Giuseppe Leo, Cherif Belacel and Ivan Favero. Ultralow loss single-mode silica tapers manufactured by a microheater. *Applied optics*, 49:13, May 2010. (cited in p. 15)

[Lützler12] Lützler, C. Fabrication of Optical Microfibers. 2012. (cited in p. 21)

[Makles15] Makles, K., T. Antoni, A. G. Kuhn, S. Deléglise, T. Briant, P.-F. Cohadon, R. Braive, G. Beaudoin, L. Pinard, C. Michel, V. Dolique, R. Flaminio, G. Cagnoli, I. Robert-Philip, and A. Heidmann. 2D photonic-crystal optomechanical nanoresonator. *Opt. Lett.*, 40(2):174–177, Jan 2015. URL http://dx.doi.org/10.1364/OL.40.000174. (cited in p. 119)

[Margenau39] Margenau, H. Van der waals forces. *Rev. Mod. Phys.*, 11:1–35, Jan 1939. URL http://dx.doi.org/10.1103/RevModPhys.11.1. (cited in p. 107)

[Matsukevich06] Matsukevich, D. N., T. Chanelière, S. D. Jenkins, S.-Y. Lan, T. A. B. Kennedy, and A. Kuzmich. Observation of Dark State Polariton Collapses and Revivals. *Phys. Rev. Lett.*, 96:033601, Jan 2006. URL http://dx.doi.org/10.1103/PhysRevLett.96.033601. (cited in p. 90)

[Mead87] Mead, C. Alden. Molecular Kramers degeneracy and non-Abelian adiabatic phase factors. *Phys. Rev. Lett.*, 59:161–164, Jul 1987. URL http://dx.doi.org/10.1103/PhysRevLett.59.161. (cited in p. 104)

[Mishina11] Mishina, O. S., M. Scherman, P. Lombardi, J. Ortalo, D. Felinto, A. S. Sheremet, A. Bramati, D. V. Kupriyanov, J. Laurat, and E. Giacobino. Electromagnetically induced transparency in an inhomogeneously broadened Λ transition with multiple excited levels. *Phys. Rev. A*, 83:053809, May 2011. URL http://dx.doi.org/10.1103/PhysRevA.83.053809. (cited in p. 73)

[Mitsch14a] Mitsch, R., C. Sayrin, B. Albrecht, P. Schneeweiss, and A. Rauschenbeutel. Exploiting the local polarization of strongly confined light for sub-micrometer-resolution internal state preparation and manipulation of cold atoms. *Phys. Rev. A*, 89:063829, Jun 2014. URL http://dx.doi.org/10.1103/PhysRevA.89.063829. (cited in p. 12)

[Mitsch14b] Mitsch, R., C. Sayrin, B. Albrecht, P. Schneeweiss, and A. Rauschenbeutel. Quantum state-controlled directional spontaneous emission of photons into a nanophotonic waveguide. *Nature Communications*, 5, December 2014. URL http://dx.doi.org/10.1038/ncomms6713. (cited in p. 12)

[Morrissey09] Morrissey, Michael J., Kieran Deasy, Yuqiang Wu, Shrabana Chakrabarti, and Síle Nic Chormaic. Tapered optical fibers as tools for probing magneto-optical trap characteristics. *Review of Scientific Instruments*, 80(5):053102, 2009. URL http://dx.doi.org/10.1063/1.3117201. (cited in p. 4)

[Nagai14] Nagai, Ryutaro and Takao Aoki. Ultra-low-loss tapered optical fibers with minimal lengths. *Opt. Express*, 22(23):28427–28436, Nov 2014. URL http://dx.doi.org/10.1364/OE.22.028427. (cited in p. 15)

[Nayak09] Nayak, Kali Prasanna. *Optical Nanofibers for Manipulating Atoms and Photons*. Theses, University of Electro-Communications, 2009. URL http://ir.lib.uec.ac.jp/infolib/user_contents/9000000344/9000000344.pdf. (cited in p. 4)

[Nicolas14] Nicolas, Adrien. *Optical quantum memories with cold atomic ensembles: a free space implementation for multimode storage, or a nanofiber-based one for high collection efficiency*. Theses, Université Pierre et Marie Curie, September 2014. URL https://tel.archives-ouvertes.fr/tel-01095100. (cited in p. 1, 37, 73, 89, and 110)

[Novikova07] Novikova, Irina, Alexey V. Gorshkov, David F. Phillips, Anders S. Sørensen, Mikhail D. Lukin, and Ronald L. Walsworth. Optimal Control of Light Pulse Storage and Retrieval. *Phys. Rev. Lett.*, 98:243602, Jun 2007. URL http://dx.doi.org/10.1103/PhysRevLett.98.243602. (cited in p. 87)

[Orucevic07] Orucevic, Fedja, Valérie Lefèvre-Seguin, and Jean Hare. Transmittance and near-field characterization of sub-wavelength tapered optical fibers. *Opt. Express*, 15(21):13624–13629, Oct 2007. URL http://dx.doi.org/10.1364/OE.15.013624. (cited in p. 21)

[Parigi15] Parigi, Valentina, Vincenzo D'Ambrosio, Christophe Arnold, Lorenzo Marrucci, Fabio Sciarrino, and Julien Laurat. Storage and retrieval of vector beams of light in a multiple-degree-of-freedom quantum memory. *Nat Commun*, 6:–, July 2015. URL http://dx.doi.org/10.1038/ncomms8706. (cited in p. 63)

[Patnaik02] Patnaik, A. K., J. Q. Liang, and K. Hakuta. Slow light propagation in a thin optical fiber via electromagnetically induced transparency. *Physical Review A*, 66(6):063808, December 2002. URL http://dx.doi.org/10.1103/PhysRevA.66.063808. (cited in p. 4, 57, and 79)

[Peters12] Peters, Thorsten, Benjamin Wittrock, Frank Blatt, Thomas Halfmann, and Leonid P. Yatsenko. Thermometry of ultracold atoms by electromagnetically induced transparency. *Phys. Rev. A*, 85:063416, Jun 2012. URL http://dx.doi.org/10.1103/PhysRevA.85.063416. (cited in p. 89)

[Petersen14] Petersen, Jan, Jürgen Volz, and Arno Rauschenbeutel. Chiral nanophotonic waveguide interface based on spin-orbit interaction of light. *Science*, 346(6205):67–71, 2014. http://www.sciencemag.org/content/346/6205/67.full.pdf, URL http://dx.doi.org/10.1126/science.1257671. (cited in p. 12)

[Raczyński13] Raczyński, A., J. Zaremba, and S. Zielińska-Kaniasty. *Light Propagation in Optically Dressed Media, Open Systems, Entanglement and Quantum Optics*. InTech, 2013. URL http://dx.doi.org/10.5772/55830. (cited in p. 73 and 74)

[Ravets13] Ravets, S., J. E. Hoffman, P. R. Kordell, J. D. Wong-Campos, S. L. Rolston, and L. A. Orozco. Intermodal energy transfer in a tapered optical fiber: optimizing transmission. *J. Opt. Soc. Am. A*, 30(11):2361–2371, Nov 2013. URL http://dx.doi.org/10.1364/JOSAA.30.002361. (cited in p. 15 and 16)

[Reitz13] Reitz, D., C. Sayrin, R. Mitsch, P. Schneeweiss, and A. Rauschenbeutel. Coherence Properties of Nanofiber-Trapped Cesium Atoms. *Physical Review Letters*, 110(24):243603, June 2013. URL http://dx.doi.org/10.1103/PhysRevLett.110.243603. (cited in p. 95)

[Rosa12] Rosa, E. B. and F. W. Grover. Formulas and tables for the calculation of mutual and self-inductance (revised). *Bulletin of the Bureau of Standards*, 8:1–287, 1912. (cited in p. 136)

[Sagué07] Sagué, G., E. Vetsch, W. Alt, D. Meschede, and A. Rauschenbeutel. Cold-Atom Physics Using Ultrathin Optical Fibers: Light-Induced Dipole Forces and Surface Interactions. *Phys. Rev. Lett.*, 99:163602, Oct 2007. URL http://dx.doi.org/10.1103/PhysRevLett.99.163602. (cited in p. 4 and 53)

[Sayrin15] Sayrin, C., C. Clausen, B. Albrecht, P. Schneeweiss, and A. Rauschenbeutel. Storage of fiber-guided light in a nanofiber-trapped ensemble of cold atoms. *Optica*, 2(4):353–356, Apr 2015.

URL http://dx.doi.org/10.1364/OPTICA.2.000353. (cited in p. 79 and 80)

[Scherman12] Scherman, Michael. *Electromagneically induced transparency and quantum memories on the D2 line of cesium : effect of the inhomogeneous broadening in a multilevel atomic structure.* Theses, Université Pierre et Marie Curie - Paris VI, March 2012. URL https://tel.archives-ouvertes.fr/tel-00815517. (cited in p. 37)

[Schlosser01] Schlosser, Nicolas, Georges Reymond, Igor Protsenko, and Philippe Grangier. Sub-poissonian loading of single atoms in a microscopic dipole trap. *Nature*, 411(6841):1024–1027, June 2001. ISSN 0028-0836. URL http://dx.doi.org/10.1038/35082512. (cited in p. 96)

[Schlosser02] Schlosser, N., G. Reymond, and P. Grangier. Collisional Blockade in Microscopic Optical Dipole Traps. *Phys. Rev. Lett.*, 89:023005, Jun 2002. URL http://dx.doi.org/10.1103/PhysRevLett.89.023005. (cited in p. 107)

[Shan13] Shan, Liye, Gilles Pauliat, Guillaume Vienne, Limin Tong, and Sylvie Lebrun. Stimulated Raman scattering in the evanescent field of liquid immersed tapered nanofibers. *Applied Physics Letters*, 102(20):201110, 2013. URL http://dx.doi.org/10.1063/1.4807170. (cited in p. 3)

[Sheremet10] Sheremet, A. S., L. V. Gerasimov, I. M. Sokolov, D. V. Kupriyanov, O. S. Mishina, E. Giacobino, and J. Laurat. Quantum memory for light via a stimulated off-resonant Raman process: Beyond the three-level Λ-scheme approximation. *Phys. Rev. A*, 82:033838, Sep 2010. URL http://dx.doi.org/10.1103/PhysRevA.82.033838. (cited in p. 73)

[Snyder83] Snyder, Allan W. and John D. Love. *Optical Waveguide Theory.* Chapman & Hall, 1983. (cited in p. 5, 6, and 7)

[Sorensen14] Sorensen, H. L., E. S. Polzik, and J. Appel. Heater Self-Calibration Technique for Shape Prediction of Fiber Tapers. *Journal of Lightwave Technology*, 32:1886–1891, May 2014. 1312.3840, URL http://dx.doi.org/10.1109/JLT.2014.2314319. (cited in p. 15)

[Spillane08] Spillane, S. M., G. S. Pati, K. Salit, M. Hall, P. Kumar, R. G. Beausoleil, and M. S. Shahriar. Observation of Nonlinear Optical Interactions of Ultralow Levels of Light in a Tapered Optical Nanofiber Embedded in a Hot Rubidium Vapor. *Phys. Rev. Lett.*, 100:233602, Jun 2008. URL http://dx.doi.org/10.1103/PhysRevLett.100.233602. (cited in p. 4)

[Steck] Steck, Daniel A. Quantum and Atom Optics. available online at http://steck.us/teaching. (cited in p. 37, 66, and 101)

[Steck98] Steck, Daniel A. Cesium D Line Data. available online at http://steck.us/alkalidata, 1998. (cited in p. 39 and 52)

[Stiebeiner10] Stiebeiner, Ariane, Ruth Garcia-Fernandez, and Arno Rauschenbeutel. Design and optimization of broadband tapered optical fibers with a nanofiber waist. *Opt. Express*, 18(22):22677–22685, Oct 2010. URL http://dx.doi.org/10.1364/OE.18.022677. (cited in p. 15)

[Sumetsky06] Sumetsky, M. How thin can a microfiber be and still guide light? *Opt. Lett.*, 31(7):870–872, Apr 2006. URL http://dx.doi.org/10.1364/OL.31.000870. (cited in p. 10)

[Tong03] Tong, Limin, Rafael R. Gattass, Jonathan B. Ashcom, Sailing He, Jingyi Lou, Mengyan Shen, Iva Maxwell, and Eric Mazur. Subwavelength-diameter silica wires for low-loss optical wave guiding. *Nature*, 426:816–819, December 2003. (cited in p. 3)

[Veissier13] Veissier, Lucile. *Quantum memory protocols in large cold atomic ensembles*. Theses, Université Pierre et Marie Curie - Paris VI, December 2013. URL https://tel.archives-ouvertes.fr/tel-00977307. (cited in p. 1, 37, 79, and 131)

[Vetsch10] Vetsch, E., D. Reitz, G. Sagué, R. Schmidt, S. T. Dawkins, and A. Rauschenbeutel. Optical Interface Created by Laser-Cooled Atoms Trapped in the Evanescent Field Surrounding an Optical Nanofiber. *Phys. Rev. Lett.*, 104:203603, May 2010. URL http://dx.doi.org/10.1103/PhysRevLett.104.203603. (cited in p. 4, 95, 100, and 115)

[Vetsch12] Vetsch, E., S.T. Dawkins, R. Mitsch, D. Reitz, P. Schneeweiss, and A. Rauschenbeutel. Nanofiber-Based Optical Trapping of Cold Neutral Atoms. *Selected Topics in Quantum Electronics, IEEE Journal of*, 18(6):1763–1770, Nov 2012. ISSN 1077-260X. URL http://dx.doi.org/10.1109/JSTQE.2012.2196025. (cited in p. 26)

[Ward14] Ward, J. M., A. Maimaiti, Vu H. Le, and S. Nic Chormaic. Contributed Review: Optical micro- and nanofiber pulling rig. *Review of Scientific Instruments*, 85(11):111501, 2014. URL http://dx.doi.org/10.1063/1.4901098. (cited in p. 15)

[Warken07] Warken, F. Ultra thin glass fibers as a tool for coupling light and matter. 2007. (cited in p. 21)

[webpage] webpage. www.nsup.org/~gouraud/phd.html. (cited in p. 2, 21, 71, 126, and 130)

[Weiner99] Weiner, John, Vanderlei S. Bagnato, Sergio Zilio, and Paul S. Julienne. Experiments and theory in cold and ultracold collisions. *Rev. Mod. Phys.*, 71:1–85, Jan 1999. URL http://dx.doi.org/10.1103/RevModPhys.71.1. (cited in p. 107)

[Wilcut Connolly09] Wilcut Connolly, Elizabeth. *Experiments with Toroidal Microresonators in Cavity QED*. Ph.D. thesis, California Institute of Technology, 2009. (cited in p. 15)

[Yang12] Yang, Liu, Wu Jing-Hui, Shi Bao-Sen, and Guo Guang-Can. Realization of a Two-Dimensional Magneto-optical Trap with a High Optical Depth. *Chinese Physics Letters*, 29(2):024205, 2012. URL http://stacks.iop.org/0256-307X/29/i=2/a=024205. (cited in p. 136)

[Ye08] Ye, Jun, H. J. Kimble, and Hidetoshi Katori. Quantum State Engineering and Precision Metrology Using State-Insensitive Light Traps. *Science*, 320(5884):1734–1738, 2008. http://www.sciencemag.org/content/320/5884/1734.full.pdf, URL http://dx.doi.org/10.1126/science.1148259. (cited in p. 104)

[Zhang12] Zhang, Shanchao, J. F. Chen, Chang Liu, Shuyu Zhou, M. M. T. Loy, G. K. L. Wong, and Shengwang Du. A dark-line two-dimensional magneto-optical trap of 85Rb atoms with high optical depth. *Review of Scientific Instruments*, 83(7):073102, 2012. URL http://dx.doi.org/10.1063/1.4732818. (cited in p. 136)

[Zhao09] Zhao, Bo, Yu-Ao Chen, Xiao-Hui Bao, Thorsten Strassel, Chih-Sung Chuu, Xian-Min Jin, Jorg Schmiedmayer, Zhen-Sheng Yuan, Shuai Chen, and Jian-Wei Pan. A millisecond quantum memory for scalable quantum networks. *Nat Phys*, 5(2):95–99, February 2009. ISSN 1745-2473. URL http://dx.doi.org/10.1038/nphys1153. (cited in p. 89)

Baptiste GOURAUD **11 Février 2016**

Sujet : Des nanofibres optiques comme interface entre lumière guidée et atomes froids
Un outil pour l'optique quantique

Résumé : Cette thèse a consisté à mettre en place une nouvelle expérience utilisant des atomes froids en interaction avec la lumière guidée par une nanofibre optique. Nous avons tout d'abord développé un banc de fabrication de nanofibres. En chauffant et étirant une fibre optique commerciale, on obtient un cylindre de silice de 400 nm de diamètre. La lumière guidée dans ces nanofibres est fortement focalisée sur toute la longueur de la fibre et exhibe de forts champs évanescents, ce qui permet d'obtenir une grande profondeur optique avec un faible nombre d'atomes. Après avoir inséré une nanofibre au milieu d'un nuage d'atomes, nous avons observé le phénomène de lumière lente dans les conditions de transparence électromagnétiquement induite. Nous avons aussi stoppé la lumière guidée et mémorisé l'information qu'elle contenait. Nous avons montré que ce protocole de mémoire optique fonctionne pour des impulsions lumineuses contenant moins d'un photon en moyenne. Ce système pourra donc être utilisé comme une mémoire quantique, un outil essentiel pour les futurs réseaux de communication quantique. Enfin, nous avons piégé les atomes dans un réseau optique au voisinage de la nanofibre grâce à de la lumière guidée par celle-ci. Par rapport à notre première série d'expériences, le nuage ainsi obtenu a un temps de vie plus long (25 ms) et interagit plus fortement avec la lumière guidée (OD $\sim$ 100). Ce nouveau système devrait permettre d'implémenter efficacement d'autres protocoles d'optique quantique, comme la génération de photons uniques et l'intrication de deux ensembles atomiques distants.

Cette thèse est rédigée en langue anglaise.

Mots clés : nanofibre optique, atomes froids, optique quantique, mémoire quantique, communication quantique, transparence électromagnétiquement induite, piège dipolaire

Subject : Optical Nanofibers Interfacing Cold Atoms
A Tool for Quantum Optics

Résumé : We built a new experiment using cold atoms interacting with the light guided by an optical nanofiber. We first developed a nanofiber manufacturing bench. By heating and stretching a commercial optical fiber, a silica cylinder of 400 nm diameter is obtained. The light guided in these nanofibers is strongly focused over the whole length and exhibits strong evanescent fields. We then prepared a vacuum chamber and the laser system necessary for the manipulation of cold atoms. After inserting a nanofiber amid a cloud of cold atoms, we observed the phenomenon of slow light under the conditions of electromagnetically induced transparency: the light guided by the fiber is slowed down to a speed 3000 times smaller than its usual speed. We also stored the light guided by an optical fiber. After several microseconds, the information stored as a collective atomic excitation could be retrieved in the fiber. We have shown that this optical memory works for light pulses containing less than one photon on average. This system may therefore be used as a quantum memory, an essential tool for future quantum communication networks. Finally, we trapped atoms in an array in the vicinity of the nanofiber thanks to the light guided by the latter. Compared to our first set of experiments, the resulting cloud has a longer lifetime (25 ms) and interacts more strongly with the guided light (OD $\sim$ 100). This new system should allow to efficiently implement other quantum optics protocols, such as the generation of single photons, or the entanglement of two remote atomic ensembles.

This thesis is written in English.

Keywords : optical nanofiber, subwavelength optical fiber, nanowaveguide, quantum optics, quantum memory, cold atoms, quantum communication, electromagnetically-induced transparency, dipole trap